NASA TECHNICAL MEMORANDUM

NASA TM X-2099

NASA TM X-2099

EFFECT OF NOZZLE LATERAL SPACING ON AFTERBODY DRAG AND PERFORMANCE OF TWIN-JET AFTERBODY MODELS WITH CONVERGENT NOZZLES AT MACH NUMBERS UP TO 2.2

by Donald L. Maiden and Jack F. Runckel

Langley Research Center
Hampton, Va. 23365

NATIONAL AERONAUTICS AND SPACE ADMINISTRATION • WASHINGTON, D. C. • OCTOBER 1970

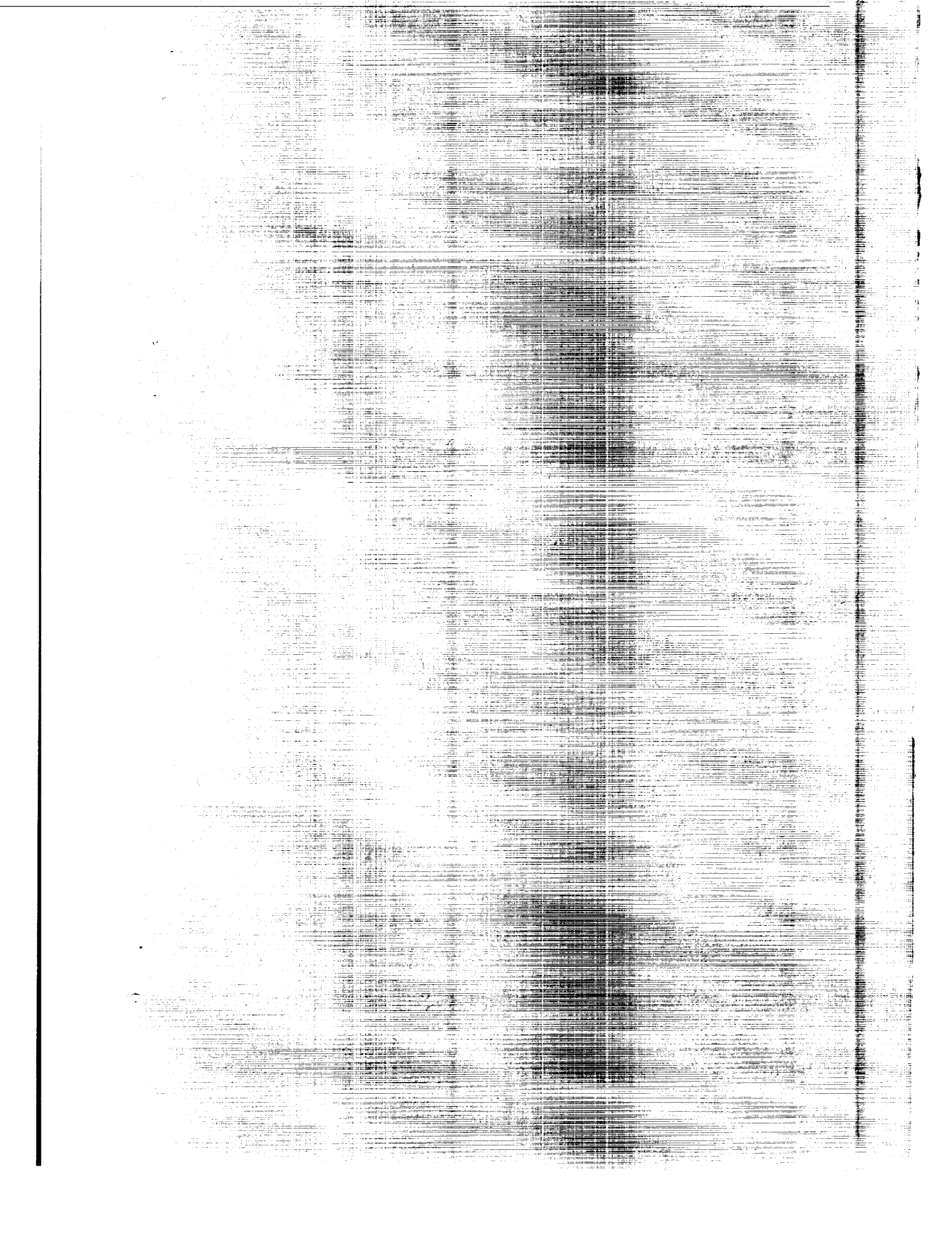

1. Report No.	2. Government Accession No.	3. Recipient's Catalog No.
NASA TM X-2099		

4. Title and Subtitle	5. Report Date
EFFECT OF NOZZLE LATERAL SPACING ON AFTERBODY DRAG AND PERFORMANCE OF TWIN-JET AFTERBODY MODELS WITH CONVERGENT NOZZLES AT MACH NUMBERS UP TO 2.2	October 1970
	6. Performing Organization Code
7. Author(s)	8. Performing Organization Report No.
Donald L. Maiden and Jack F. Runckel	L-7192
	10. Work Unit No.
9. Performing Organization Name and Address	720-03-11-01
NASA Langley Research Center Hampton, Va. 23365	11. Contract or Grant No.
	13. Type of Report and Period Covered
12. Sponsoring Agency Name and Address	Technical Memorandum
National Aeronautics and Space Administration Washington, D.C. 20546	14. Sponsoring Agency Code

15. Supplementary Notes

16. Abstract

Twin-jet afterbody models were investigated by using two balances to measure the thrust minus afterbody drag and the afterbody drag, separately, at static conditions and at Mach numbers up to 2.2 for a constant angle of attack of 0^{o}. Hinged-flap convergent nozzles were tested at dry- and afterburner-power settings with a high-pressure air system used to simulate jet-total-pressure ratios up to 21.0. Equal nondimensional area distributions were maintained as the nozzle lateral spacing was varied. In addition to the lateral-spacing study, afterbodies with recessed blunt bases were investigated, and the effects of exposing primary nozzle flaps to free-stream flow were examined. The results indicate an increase in afterbody axial-force (drag) coefficient with increased lateral spacing for the shrouded and unshrouded configurations for subsonic and supersonic Mach numbers, with the exception of the shrouded dry-power nozzle configurations at subsonic Mach numbers (for which the trend was opposite).

17. Key Words (Suggested by Author(s))	18. Distribution Statement
Jet effects Twin-jet afterbody models Afterbody drag	Unclassified – Unlimited

19. Security Classif. (of this report)	20. Security Classif. (of this page)	21. No. of Pages	22. Price*
Unclassified	Unclassified	141	$3.00

*For sale by the Clearinghouse for Federal Scientific and Technical Information
Springfield, Virginia 22151

EFFECT OF NOZZLE LATERAL SPACING ON AFTERBODY DRAG AND PERFORMANCE OF TWIN-JET AFTERBODY MODELS WITH CONVERGENT NOZZLES AT MACH NUMBERS UP TO 2.2

By Donald L. Maiden and Jack F. Runckel
Langley Research Center

SUMMARY

An investigation has been conducted to determine the effect of nozzle lateral spacing on the drag and performance of twin-engine afterbody configurations with hinged-flap convergent nozzles at static conditions and at Mach numbers ranging from 0.6 to 2.2. Two lateral spacings of the nozzle exits were studied, with identical longitudinal cross-sectional-area distributions and fineness ratios maintained as the spacing was varied. Three afterbody types consisting of a basic shrouded configuration, an exposed-nozzle-flap configuration, and a shrouded configuration having a blunt-base interfairing terminating forward of the nozzle exits were studied. Two nozzle power settings were used – the dry-power setting corresponding to minimum throat area and the maximum-augmented-power setting corresponding to maximum throat area. The jet-total-pressure ratio was varied from 1.0 (jet off) to approximately 21 depending on the Mach number.

The results indicate (1) that the close-spaced-nozzle-exit configurations had lower afterbody axial-force (drag) coefficient than the wide-spaced-nozzle-exit configurations, with the exception of the shrouded dry-power nozzle configurations at subsonic Mach numbers (for which the trend was opposite) and (2) that the addition of cross-sectional area generally increased afterbody drag subsonically, but decreased afterbody drag supersonically. Differences may occur in determining the forces on the afterbody if only shroud drag, which does not include the annulus drag of the afterbody, is considered. The correlation between theoretically and experimentally determined supersonic wave drag was good for the close-spaced-nozzle afterbody configurations and fair for the wide-spaced-nozzle afterbody configurations.

INTRODUCTION

Twin-engine multimission aircraft require careful integration of the airframe with the engines in order to provide high performance over a wide speed range. Engines

installed in the fuselage offer the advantage of compactness and alleviation of the one-engine-out stability problem. However, the afterbody-nozzle arrangement for this type of configuration can be quite sensitive to the mutual nozzle-airframe interactions (refs. 1 to 4). Therefore, attention has been directed toward the twin-jet aircraft back-end problem in order to examine the effects of axial location of jet exits along the body (ref. 5), the effects of afterbody shape and type, and the effects of lateral spacing of the nozzle exits (ref. 6).

As part of a program on engine-nozzle—aircraft-afterbody integration, the Langley Research Center is evaluating the performance of various twin jet nozzles installed near the rear of model fuselages. Reference 5 reports the results of the initial investigation and describes an air-powered, twin-jet afterbody model which has provisions for making separate measurements of the combined exhaust thrust minus drag and the external afterbody drag. The present investigation shows the effects of nozzle lateral spacing for hinged-flap convergent nozzles which were tested with and without the flaps exposed aft of the hinge point. Afterbodies having a minimum wave-drag shape with the same cross-sectional-area distributions and fineness ratios were designed for both close and wide spacings of the nozzles.

Some previous investigations have indicated that afterbodies with recessed or blunt bases may achieve low drag with twin propulsion nozzles at the rear of the fuselage (refs. 7 and 8). This type of afterbody was also examined in the present investigation for both close and wide spacings by additions to the interfairing between the engine nacelles.

The investigation was conducted in the Langley 16-foot transonic tunnel at Mach numbers from 0.6 to 1.3 with nozzle throat areas corresponding to dry power (minimum throat area) and maximum augmented power (maximum throat area) and in the Langley 4- by 4-foot supersonic pressure tunnel at Mach numbers of 2.0 and 2.2 with the nozzles at the maximum-augmented-power setting. Jet-total-pressure ratio was varied from 1.0 (jet off) to approximately 8 in the transonic facility and to approximately 21 in the supersonic tunnel. All configurations were tested at zero angle of attack.

SYMBOLS

Aerodynamic coefficients are based on $q_\infty A_{max}$.

A cross-sectional area, m^2

$A_{an} = A_b - A_t$

A_b base area of one nozzle shroud (see fig. 3), m^2

A_{eng} engine-tailpipe maximum cross-sectional area, m^2

A_{max} maximum cross-sectional area of afterbody, m^2

A_s inside cross-sectional area of afterbody at hinge point, m^2

A_{seal} cross-sectional area enclosed by seal strip, m^2

A_t throat area of one nozzle, m^2

$C_{A,a}$ axial-force coefficient of afterbody including force on nozzle-base annuli, positive downstream

$C_{A,an}$ axial-force coefficient of nozzle-base annuli

$C_{A,f}$ skin-friction axial-force coefficient

$C_{A,s}$ shroud axial-force coefficient excluding force on nozzle-base annuli

$C_{D,w}$ supersonic wave-drag coefficient

C_p local-pressure coefficient, $\frac{p_l - p_\infty}{q_\infty}$

$C_{p,b}$ base-pressure coefficient, $\frac{p_b - p_\infty}{q_\infty}$

$C_{T,i}$ aerodynamic ideal-thrust coefficient, $\frac{F_i}{q_\infty A_{max}}$

d_b internal base diameter of nozzle shroud, m

d_{eng} diameter of engine-tailpipe maximum cross section (fig. 6), m

d_{equ} equivalent diameter corresponding to maximum cross-sectional area of afterbody, m

d_s internal diameter of shroud at cutoff point (fig. 7), m

d_t nozzle-throat diameter, m

F_A external axial force (drag), positive downstream, N

$F_{A,a}$ axial force on afterbody including force on nozzle-base annuli, N

$F_{A,an}$ force on nozzle-base annuli, N

$F_{A,s}$ shroud axial force excluding force on nozzle-base annuli, N

$F_{bal,a}$ force measured by drag balance, positive downstream (fig. 3), N

$F_{bal,j}$ force measured by thrust-minus-drag balance, positive upstream (fig. 3), N

F_i ideal thrust for complete isentropic expansion of jet flow,

$$\dot{m}_j\sqrt{\frac{2\gamma}{\gamma - 1} RT_{t,j}\left[1 - \left(\frac{p_\infty}{p_{t,j}}\right)^{\frac{\gamma-1}{\gamma}}\right]}, \text{ N}$$

$F_{i,c}$ ideal convergent-nozzle thrust, $\dot{m}_j\sqrt{\frac{2\gamma}{\gamma + 1} RT_{t,j}} + A_t\left(p_e - p_\infty\right)$, N

F_j jet (gross) thrust, positive upstream, N

h afterbody height at maximum cross section (fig. 4(a)), m

l length of model measured from nose (fig. 1), 134.62 cm

l_a afterbody length measured from seal station (fig. 1), 50.80 cm

l_f length of nozzle flaps (fig. 7), m

M free-stream Mach number

$\dot{m}_i$ ideal mass-flow rate, kg/s

$\dot{m}_j$ measured mass-flow rate, kg/s

p_b base pressure, N/m^2

p_e nozzle-exit static pressure, N/m^2

p_{es} static pressure at external seal station (fig. 3), N/m^2

p_f flap annulus pressure, N/m^2

p_i internal static pressure (fig. 3), N/m^2

p_l local static pressure, N/m^2

$p_{t,j}$ jet total pressure, N/m^2

p_∞ free-stream or ambient static pressure, N/m^2

q_∞ free-stream dynamic pressure, N/m^2

R gas constant ($\gamma = 1.4$), $287.3 \frac{N\text{-}m}{kg\text{-}^oK}$

r radius, m

S_w surface wetted area, m^2

s spacing distance between engine-nozzle center lines (fig. 4(a)), m

s/d_{eng} lateral spacing ratio based on engine-tailpipe diameter

s/d_t lateral spacing ratio based on nozzle-throat diameter

$T_{t,j}$ jet stagnation temperature, ^oK

w body width at maximum cross section (fig. 4(a)), m

x distance from nose to orifice location, m

γ ratio of specific heats

A bar over a symbol denotes an average condition.

APPARATUS AND METHODS

Wind Tunnels

The present investigation was conducted in the Langley 16-foot transonic tunnel and the Langley 4- by 4-foot supersonic pressure tunnel. The Langley 16-foot transonic tunnel is a single-return, atmospheric wind tunnel with an octagonal test section and continuous air exchange. The tunnel has a continuously variable speed range from Mach 0.20 to Mach 1.30. The Langley 4- by 4-foot supersonic pressure tunnel is a single-return, continuous-flow wind tunnel with a stagnation-pressure range from 0.2758×10^5 N/m^2 to 2.0684×10^5 N/m^2 and a stagnation-temperature range from 310.9° K to 322.2° K. By the use of interchangeable nozzle blocks, the tunnel Mach number can be varied from 1.25 to 2.2.

Model and Support System

A sketch of the strut-supported model with a twin-turbofan engine simulator used in the investigation is presented in figure 1, and a photograph of a typical model is shown in figure 2.

The afterbody shell (or shroud) of the model began 83.82 cm from the nose and was attached to a drag balance which was attached in tandem to a thrust-minus-drag balance as shown in figure 3. An annular clearance gap between the afterbodies and nozzles was required to prevent fouling of the afterbody drag balance. A teflon strip inserted into grooves machined into the afterbody shell and forebody (see fig. 3) was used as a seal to prevent internal flow in the model. The teflon strip, because of its low coefficient of friction, minimized restraint on the two balances. To insure a turbulent boundary layer over the afterbody shell, a 0.30-cm-wide transition strip of No. 100 carborundum grit was fixed 2.54 cm from the nose of the model.

The twin-turbofan-engine simulator utilized high-pressure air to simulate the exhaust of a twin-jet configuration. Compressed air was supplied to the model through pipes in the strut and passed through eight orifice nozzles into a low-pressure plenum chamber (see fig. 1). The orifice nozzles were located perpendicular to the longitudinal axis of the model to eliminate transfer of axial momentum. From the plenum chamber the air was passed through the tailpipe-nozzle system to simulate the exhaust of a twin-jet configuration. (See top view in fig. 1.)

A sketch giving dimensions for the six afterbodies used in this investigation is presented in figure 4. All afterbody configurations had the same nozzle-exit axial location for a given power setting. Two lateral spacings between engine-nozzle center lines were selected. The close spacing was determined by the minimum practical clearance between parallel tailpipes; in terms of a nondimensional spacing ratio based on engine-tailpipe

diameter, this spacing was 1.07. The wide spacing represented the maximum available spread between the tailpipes and was limited to the confines of the maximum width of an existing model.

Afterbody-nozzle geometric ratios are given in table I for all configurations, with spacing ratios in terms of engine-tailpipe diameter and nozzle-throat diameter. The basic afterbody geometry is represented by afterbody configurations 1 and 2, which had the same longitudinal distribution of cross-sectional area (see fig. 5) and shrouded convergent flap nozzles. The basic afterbody shrouds were cut off at the flap hinge point to form afterbody configurations 3 and 4 and thereby obtain comparisons of shrouded and unshrouded nozzle flaps. Filling in the channel on close-spaced-nozzle afterbody configuration 1 with flat top and bottom fairings terminating with a blunt base at the location of the hinge point of the nozzle resulted in the formation of afterbody configuration 5, which had an alternate axial area distribution and a recessed blunt base. Also, afterbody modifications were made on wide-spaced-nozzle afterbody configuration 2 to form afterbody configuration 6, which had the same alternate area distribution. The area distribution of afterbody configurations 1 and 2 shown in figure 5 between $\frac{x}{l} = 0.6$ and $\frac{x}{l} = 1.0$ was calculated by a computer program for axisymmetric bodies adapted from reference 9 and is representative of a minimum wave-drag body at a Mach number of 1.000001 with the restraint of a given forebody geometry, afterbody length, base area, and an infinite cylindrical exhaust plume. The area distribution of the basic afterbody configurations (1 and 2) was made equivalent to the area distribution of an axisymmetric minimum-wave-drag body. Therefore, afterbody configurations 5 and 6 represent a deviation from the theoretically predicted area distribution for minimum wave drag.

A sketch presenting the geometry and instrumentation of the hinged-flap convergent nozzle is given in figure 6. Two power settings were investigated. The maximum-augmented-power or afterburner-power setting is denoted as nozzle configuration A, and the dry-power or military-power setting is denoted as nozzle configuration D. The convergent nozzles were designed for use with air as a fluid medium ($\gamma = 1.4$). The ratio of augmented-power throat area to dry-power throat area was 2.5.

Instrumentation

External static-pressure orifices were located on the afterbodies as shown in figure 4. Pressure distributions were obtained on all afterbodies along generally axial rows on the top and bottom model center lines, at the top of the right nacelle, and on the left side and part way down on the nacelle toward the interfairing (see fig. 4). The pressure orifices were intended to indicate the flow characteristics over the afterbody model and to aid in interpreting the force-measurement results; however, the distribution of

orifices was not complete enough to determine afterbody pressure drag. Internal pressures were measured in the afterbody cavity at 10 internal orifice locations. Eight external static pressures were measured at orifices located on both sides of the seal gap between the forebody and afterbody (see fig. 3). These pressure measurements were used for axial-force corrections. The total pressure and stagnation temperature of the jet flow were measured in each tailpipe at locations indicated in figure 1.

Forces and moments on the parts of the model under consideration (see fig. 3) were measured by several balances. A five-component main balance was used to measure thrust minus afterbody drag. Forces and moments on the afterbody shell were measured with a tandem-mounted two-component auxiliary balance in the Langley 16-foot transonic tunnel and similarly with a six-component balance in the 4- by 4-foot supersonic pressure tunnel. An electronic turbine flowmeter was used to measure the air-mass-flow rate to the nozzles.

Data obtained in the Langley 16-foot transonic tunnel were recorded simultaneously on magnetic tape and were reduced to coefficient form by use of a computer. Approximately five frames of data were taken over a time period of 1 second for each data point and the average value was used for computations. Data obtained in the Langley 4- by 4-foot supersonic pressure tunnel were transmitted to self-balancing potentiometers, digitized, and punched into computer cards. An electrically actuated scanning valve was used for measuring and recording the internal and external afterbody pressures.

Tests

Tests were conducted in the Langley 16-foot transonic tunnel at Mach numbers from 0 to 1.3 and in the Langley 4- by 4-foot supersonic pressure tunnel at Mach numbers of 2.0 and 2.2 at a stagnation pressure of 1.213×10^5 N/m^2 and at a stagnation temperature of 310.9° K. The angle of attack was restricted to a constant value of 0° during the entire investigation. Reynolds number based on model length varied from approximately 17.27×10^6 at $M = 0.6$ to 17.49×10^6 at $M = 1.3$ in the Langley 16-foot transonic tunnel and from 16.75×10^6 at $M = 2.0$ to 16.47×10^6 at $M = 2.2$ in the Langley 4- by 4-foot supersonic pressure tunnel. The ratio of jet total pressure to free-stream static pressure was varied from 1.0 (jet off) to approximately 21 depending on Mach number.

DATA REDUCTION

The recorded data were used to compute standard force and pressure coefficients. The external-seal and internal pressure forces on the afterbodies were obtained by multiplying the difference between the average pressure (external seal or internal) and free-stream static pressure by the affected projected area normal to the model axis.

The gross thrust minus the afterbody axial force was obtained directly by the thrust-minus-drag balance (see fig. 3). This performance term was computed as follows:

$$F_j - F_{A,a} = F_{bal,j} + \left(\bar{p}_{es} - p_\infty\right)\left(A_{max} - A_{seal}\right) + \left(\bar{p}_i - p_\infty\right)A_{seal} \tag{1}$$

The forces sensed by the balance and included in the term $F_{bal,j}$ are nozzle thrust, afterbody external and internal axial forces transferred to the thrust-minus-drag balance through the tandem-mounted drag balance, and internal axial forces on the nozzle system.

Afterbody axial force was obtained directly from the tandem-mounted drag balance (see fig. 3). Included in the afterbody-axial-force term $F_{A,a}$ for the shrouded configurations is the force acting on the physical-afterbody-base area and on the area of the annulus between the inside of the afterbody and the nozzle throat. (See fig. 7.) For the unshrouded configurations the force acting on the physical-afterbody-base area and on the area of the annulus between the inside of the afterbody and the tailpipe at the hinge-point station is included in the afterbody-axial-force term. Because of the aspiration in the internal cavity between the afterbody shell and the nozzle-tailpipe system, the internal pressure just aft of the hinge point of the nozzle flap was of a lower value than the internal pressure forward of that point on the shrouded configurations. Therefore, the area over which the internal pressures act was divided at the hinge point of the nozzle and assigned to the appropriate pressure. The afterbody axial force for the shrouded nozzle configuration was computed from the equation

$$F_{A,a} = F_{bal,a} - \left(\bar{p}_{es} - p_\infty\right)\left(A_{max} - A_{seal}\right) - \left(\bar{p}_i - p_\infty\right)\left(A_{seal} - A_s\right) - \left(\bar{p}_f - p_\infty\right)\left(A_s - 2A_t\right) \tag{2a}$$

and the afterbody axial force for the exposed nozzle configuration was computed from the equation

$$F_{A,a} = F_{bal,a} - \left(\bar{p}_{es} - p_\infty\right)\left(A_{max} - A_{seal}\right) - \left(\bar{p}_i - p_\infty\right)\left(A_{seal} - 2A_{eng}\right) \tag{2b}$$

The internal-pressure correction terms used in the force equations can be large, as was reported in reference 5. The order of magnitude of this correction can be equal to the drag-balance readings.

The shroud axial force consists of the pressure and viscous forces on the afterbody shell including the small physical annuli bases and was obtained by subtracting the force on the nozzle-base annuli from the afterbody axial force – that is,

$$F_{A,s} = F_{A,a} - F_{A,an} \tag{3}$$

Jet thrust is obtained for the shrouded configuration by combining equations (1) and (2a) as follows:

$$F_j = \left(F_j - F_{A,a}\right) + F_{A,a} \tag{4}$$

Nozzle drag resulting from exposing the hinged flaps to free-stream flow could not be determined because of the absence of orifices in the thin nozzle flaps. This nozzle drag is included in the thrust-minus-drag performance term, and therefore internal performance $\left(F_j/F_i\right)$ for the exposed-hinged-flap configurations is not presented herein. A total-pressure rake was used to survey the jet-total-pressure distribution at the exit of the convergent nozzles, and the jet-total-pressure probe reading was corrected to the integrated value of jet total pressure at the exit. The mean value of jet total pressure at the exit was used to calculate the ideal thrust for complete isentropic expansion of the jet flow for the convergent nozzles.

Afterbody external skin-friction drag (used for theoretical wave-drag comparisons) was calculated by using the Frankl and Voishel equation for compressible, turbulent flow on a flat plane. (See ref. 10.)

RESULTS

The results of the investigation are presented in the following figures:

DISCUSSION

Pressure Measurements on the Afterbodies

Figure 8 presents typical pressure distributions obtained on configuration 1D, the shrouded close-spaced-nozzle configuration with the dry-power setting. The top and bottom center-line rows show good agreement at subsonic speeds and fair agreement at transonic speeds. The agreement of these pressure distributions indicates that interference effects caused by the wake of the support strut were small. Support-strut effects are discussed in detail in reference 11. The cause of the increase in pressure at x/l of about 0.9 is unknown since the interfairing channel had a smooth contour and seemingly smooth progression. Jet operation generally had a small detrimental effect on the rearmost pressure orifice locations for the dry-power setting. Figure 9 shows pressure distributions obtained on configuration 1A, the shrouded close-spaced-nozzle configuration with the maximum-augmented-power setting. Increasing the ratio of jet total pressure to free-stream pressure increased the pressure coefficient over the last 5 to 10 percent of the afterbody.

Figures 10 and 11 show similar results (to figs. 8 and 9) for the basic shrouded wide-spaced afterbody with dry-power and maximum-augmented-power settings (configurations 2D and 2A, respectively). The peak negative pressure coefficient occurs on the side row (row 6) at the rear of the nacelle, where the maximum local boattailing exists. The most forward orifice of row 8 also indicates a low-pressure peak, which is also observed on other wide-spaced-nozzle configurations at the same location. Inspection of the afterbody revealed a high local rate of change of surface slope at this particular location. The local high suction pressures emphasize that smooth gentle changes on local boattail curvature must be maintained to keep afterbody pressure drag to a minimum.

The pressure distributions for the afterbody with the exposed-flap close-spaced nozzles (afterbody configuration 3) were about the same as those for basic shrouded afterbody configuration 1. Thus, pressure-distribution data for afterbody configuration 3 are not presented. However, the afterbody with the exposed-flap wide-spaced nozzles (afterbody configuration 4) does show differences, even for the dry-power setting (see fig. 12). The inside row at the rear of the nacelle (row 5) does not exhibit the tendency to recover pressure. Afterbody configuration 5, the shrouded close-spaced-nozzle configuration with a blunt base, indicated no tendency toward pressure recovery on the body except on the blunt base at a Mach number of 0.90 for dry power and jet-on conditions (see fig. 14). The shrouded wide-spaced-nozzle configuration with interfairing modification (afterbody configuration 6), which had the same longitudinal area distribution as configuration 5, had more local curvatures, and the pressure distribution over the afterbody resembles that of basic wide-spaced-nozzle configuration 2.

Base Pressures

The variation of base-pressure coefficient with jet-total-pressure ratio is presented in figure 18 for blunt-base afterbody configurations 5 and 6 at several Mach numbers. For the dry-power setting the jet effect is unfavorable in that lower base-pressure coefficients are obtained as the jet-total-pressure ratio is increased (see fig. 18). For the maximum-augmented-power setting, the jet effect is generally unfavorable except at the highest jet-pressure ratios. The trend of the variation of base-pressure coefficient with jet-pressure ratio shown in figures 18(a) and 18(b) is similar to results found in reference 12 for a twin-jet configuration with a blunt base and dry- or augmented-power setting.

Afterbody Axial-Force Coefficients

Variation with jet-pressure ratio.- The effect of jet operation on afterbody axial-force (drag) coefficients are shown in figures 19 and 20. The plots for each Mach number are arranged with dry-power results in the left column and augmented-power results in the right column and with close-spaced-nozzle results at the top and wide-spaced-nozzle results at the bottom. The effect of cutting off the basic shrouds of afterbody configurations 1 and 2 to form the cutoff-shroud configurations with exposed nozzle flaps (afterbody configurations 3 and 4, respectively) is shown in figure 19. Mixed results occur with jet operation. Results for the close-spaced-nozzle configurations with the dry-power setting indicate that the afterbody axial-force coefficient for exposed-nozzle-flap configuration 3D is always lower than for fully shrouded configuration 1D, probably because the exposed-flap configurations are shorter and because of jet aspiration in the nozzle-base region of the basic shrouded configuration. The wide-spaced-nozzle configurations with the dry power show the same trend as their close-spaced-nozzle counterparts at $M = 0.60$, but

the effects are smaller. A reverse effect is seen above $M = 0.70$; shrouded configuration 2D has lower values of $C_{A,a}$ than configuration 4D from $M = 0.80$ up to $M = 0.95$. At transonic speeds the cutoff-shroud configurations have much lower values of $C_{A,a}$ than the basic configurations for the dry-power setting. With the augmented-power setting, fully shrouded configurations 1A and 2A have lower $C_{A,a}$ than cutoff-shroud configurations 3A and 4A, respectively, at subsonic speeds; at supersonic speeds, the differences are generally small and crossovers in axial-force-coefficient levels occur at pressure ratios of the order of 4 to 10 depending on Mach number.

The results of altering the area distribution of basic shrouded configurations 1 and 2 by the addition of fuselage interfairing (configurations 5 and 6) is shown in figure 20, where the comparison plot layout is the same as in figure 19. The data for afterbody configurations 1 and 2 are repeated from figure 19 as a basis for comparison. For the dry-power setting the basic shrouded configurations generally have the lower afterbody axial-force coefficient for both the close and wide spacing. This trend holds for the maximum-augmented-power setting at subsonic speeds. The axial-force-coefficient trends with jet-pressure ratio for afterbody configuration 5 are similar to the axial-force-coefficient variation of the blunt base model of reference 12. For the maximum-augmented-power setting at supersonic speeds (figs. 20(d) and 20(e)), afterbody configuration 6 generally had lower axial-force coefficients above a jet-pressure ratio of 4.5 than basic wide-spaced-nozzle configuration 2, whereas the close-spaced configurations show only small differences in axial-force-coefficient level.

Effect of Mach number.- The variation of afterbody axial-force coefficient with Mach number, for the schedule of jet-total-pressure ratio for a turbofan engine shown in figure 21, is summarized in figure 22 for all configurations. Some conflicting trends in the data are observed at subsonic speeds. Of the shrouded configurations with the dry-power setting (1D, 2D, 5D, and 6D), wide-spaced-nozzle configurations 2D and 6D generally exhibit the lower afterbody axial-force coefficients (figs. 22(a) and 22(c)). Of the cutoff-shroud configurations (3D and 4D), however, close-spaced-nozzle configuration 3D produced the lower values (fig. 22(b)). At subsonic speeds and with maximum augmented power, close-spaced-nozzle configurations 1A and 3A had lower afterbody axial-force coefficients than their wide-spaced-nozzle counterparts, configurations 2A and 4A (figs. 22(a) and 22(b)); for the modified-interfairing configurations the opposite trend was true, with wide-spaced-nozzle configuration 6A having lower values than close-spaced-nozzle configuration 5A (fig. 22(c)). At supersonic speeds all the close-spaced-nozzle configurations had the lower afterbody axial-force coefficients for both power settings. Shadowgraphs of several afterbodies are shown in figures 38 to 41 for varied pressure ratios at Mach 2.0 and 2.2.

Effect of lateral spacing on afterbody axial-force coefficient.- In previous discussions of nozzle-lateral-spacing effects, several spacing ratios have been proposed. The separation distance between engine nozzles could be chosen, with touching nozzles having a spacing distance of 0. The lateral spacing selected in the present paper is the distance between engine-nozzle center lines s. The minimum value of s is 1.0 nozzle diameter. Two reference parameters are apparent for defining a nondimensional spacing ratio – the engine-nozzle diameter and the nozzle-throat diameter. Because the jet plume is the source of the interference axial-force increment, perhaps the more meaningful parameter is the nozzle-exit diameter. With the convergent nozzle of the present investigation, the throat diameter sizes the jets, so a lateral spacing ratio of s/d_t has been selected. Use of d_t as the reference parameter ties the lateral spacing ratio directly to the engine power setting – that is, the nozzle throat size.

The effect of lateral spacing on the afterbody axial-force coefficient $C_{A,a}$ is presented in figure 23 for several Mach numbers at scheduled pressure ratios. For subsonic speeds and the dry-power setting, the effect of increasing lateral spacing is to decrease $C_{A,a}$ for the shrouded afterbody configurations (1, 2, 5, and 6) and to increase $C_{A,a}$ for the unshrouded, or exposed-nozzle, afterbody configurations (3 and 4). The increase in afterbody axial-force coefficient with spacing ratio s/d_t for the unshrouded configurations is consistent with the results obtained in reference 13 at $M = 0.8$. For supersonic speeds and the dry-power setting, the effect of increased lateral spacing is an increase in the afterbody axial-force coefficient, or afterbody drag coefficient, for all configurations.

With the nozzle throat set at the maximum-augmented-power position, the effect was generally an increase of afterbody axial-force coefficient with an increase in lateral spacing both subsonically and supersonically with the exception of the recessed-blunt-base afterbody configurations (5 and 6) subsonically. (The jet effects on base drag were less unfavorable for wide-spaced-nozzle configuration 6 than for close-spaced-nozzle configuration 5.)

Since the division of forces between afterbodies and nozzles has become more arbitrary in recent years (refs. 2, 5, and 14), it is necessary to define the external axial force charged to the airframe and that charged to the nozzles. For the shrouded configurations of the present investigation, nozzle-base annuli exist between the shroud base and the nozzle throat. Afterbody axial-force coefficient includes the pressure and viscous forces on the afterbody from A_{max} down to $2A_t$, and this definition is consistent with the definition in reference 5 in that the nozzle-base-annulus drag is included in the afterbody external drag. The magnitude of $C_{A,an}$ for the shrouded configurations is given in figure 24, which shows the variation with Mach number at jet-off conditions. Basic shrouded afterbody configurations 1 and 2 have thrust forces on the annuli at subsonic speeds as

does the wide-spaced-nozzle configuration with the added interfairing (afterbody configuration 6). The wide-spaced-nozzle dry-power configurations have the highest transonic drag levels. By subtracting the axial-force coefficient of the nozzle-base annuli $C_{A,an}$, as shown in figure 24, from the afterbody axial-force coefficient $C_{A,a}$, the axial-force coefficient of the afterbody shroud or shell including the small physical base of the shell $\left(C_{A,s}\right)$ is obtained.

Shroud Axial-Force Coefficients

The variation of shroud axial-force (drag) coefficient with Mach number for the jet-off condition is presented in figure 25. Figure 25 shows that when the nozzle-base-annulus axial-force coefficient resulting from the dry-power and maximum-augmented-power settings is removed from the afterbody axial-force coefficient for a common afterbody, the resulting shroud axial-force coefficient $C_{A,s}$ is approximately the same for the given afterbody regardless of power setting.

Variation with jet-pressure ratio.- The variation of shroud axial-force coefficient with jet-total-pressure ratio is presented in figures 26 and 27 for several Mach numbers and the two power settings. The plot layout in figures 26 and 27 is similar to that in figures 19 and 20. The effect of cutting off the basic nozzle shrouds of configurations 1 and 2 to form exposed-nozzle-flap configurations 3 and 4 is shown in figure 26. Generally, the exposed-flap dry-power configurations had lower shroud axial-force coefficient than did the shrouded dry-power configurations, but the opposite trend is indicated for the maximum-augmented-power setting at subsonic Mach numbers. These trends are probably due to jet effects, which are unfavorable to the shrouded configurations utilizing dry power and favorable for the maximum-augmented-power setting. The unfavorable jet effects are caused by the jet aspirating the rear region of the shroud boattail for the dry-power setting, and the favorable effects are caused by the convergent-nozzle underexpansion of exhaust flow creating positive pressures over the shroud boattail.

The effects of interfairing modification on the basic configurations are shown in figure 27. As a result of unfavorable jet interference on the base-pressure drag of the blunt-base configurations, the basic configurations indicate less shroud axial-force coefficient for the most part. However, the blunt-base afterbody with the close-spaced dry-power nozzles does show slightly less shroud axial-force coefficient at high transonic and low supersonic Mach numbers for the lower jet-pressure ratios. The blunt-base afterbody with the wide-spaced maximum-augmented-power nozzles shows less shroud axial-force coefficient supersonically at jet-pressure ratios above 4.0, the difference increasing with increased jet-total-pressure ratio.

Effect of Mach number.- The variation of the shroud axial-force coefficient with Mach number for a typical jet-pressure-ratio schedule (see fig. 21) is presented in

figure 28 for all configurations. For the dry-power setting the exposed-nozzle-flap configurations exhibit the lowest shroud axial-force coefficient, as a result of the adverse effect of the jet upon the base pressure on the shrouded configurations. Favorable jet effects on the close-spaced-nozzle recessed-blunt-base configuration with the dry-power setting reduce the shroud axial-force coefficient below the basic-shrouded-afterbody values as high subsonic speeds (M = 0.95) are approached. For the maximum-augmented-power setting, the basic shrouded configurations exhibit the lowest values of shroud axial-force coefficient subsonically, with the exposed-nozzle-flap configurations having somewhat higher values. At the same power setting supersonically, the effect of shrouds is relatively small, with the recessed-blunt-base configuration exhibiting a slight reduction in shroud drag at Mach 2.2, which is due to an increase in base pressures caused by underexpansion of exhaust flow at the high pressure ratios required for supersonic speeds.

Comparison of measured and theoretical wave-drag coefficients.- Supersonic wave-drag coefficients of afterbody configurations 1, 2, 5, and 6 with the convergent nozzles operating at the jet-total-pressure ratio of 1.89 are presented in figure 30 as functions of Mach number. The experimental values of $C_{D,w}$ were obtained by subtracting the skin-friction axial-force coefficient presented in figure 29 from the respective shroud axial-force coefficient obtained at a jet-total-pressure ratio of 1.89. In addition, the base-drag coefficient of each configuration having a recessed blunt base was subtracted from the shroud axial-force coefficient. Also shown in figure 30 are the values of afterbody wave-drag coefficient as obtained from axisymmetric and three-dimensional wave-drag theories by applying the assumption of infinite cylindrical jet plumes. Wave-drag calculations predict shroud drag with good accuracy for the close-spaced-nozzle afterbodies and with only fair accuracy for the wide-spaced-nozzle afterbodies. It is interesting to note that for the close-spaced-nozzle afterbody configuration, the axisymmetric wave-drag theory predictions (ref. 9) were closer to measured values for Mach numbers 1.2 and 1.3, while at Mach numbers 2.0 and 2.2 the three-dimensional wave-drag theory provided better correlation. For the wide-spaced-nozzle afterbody configurations, the measured values were higher than the values predicted by either theory.

Effect of lateral spacing on shroud axial-force coefficient.- The effect of lateral spacing ratios on the shroud axial-force coefficient $C_{A,s}$ is presented in figure 31. For the dry-power setting the shroud axial-force coefficient increases with increasing spacing ratio at all Mach numbers for all configurations. This effect is in contrast with the results shown in figure 23 for the variation of afterbody axial-force coefficient with spacing ratio, since the jet exhaust can influence the nozzle-base-annulus region differently for the various nozzle-afterbody configurations. Generally for the maximum-augmentated-power setting, little change in shroud axial-force coefficient occurred with changes in the spacing ratio at subsonic speeds; however, at supersonic speeds the

coefficient increased with increases in the lateral spacing. Because only two spacings were used, a linear variation is shown between the extremes.

Effect of power setting.- The effect of power setting – that is, convergent-nozzle throat size – is shown in figure 32 for some representative Mach numbers at the scheduled jet-pressure ratio. Variation of both the shroud axial-force coefficient and the afterbody axial-force coefficient with jet size $\left(A_t\right)$ are shown for the test configurations. Increasing the sonic jet size decreases the axial-force coefficient in all cases because of the expected larger favorable jet interference and the reduction in base annulus. Straight lines connecting the data points for dry-power and maximum-augmented-power settings are shown solid for the basic close-spaced-nozzle configuration (1) and broken for the basic wide-spaced-nozzle configuration (2) to indicate the trend with power setting since only two nozzle-throat sizes were used. The relation between the axial-force coefficients and the power parameter $2A_t/A_{max}$ is not necessarily linear for intermediate-augmented-power settings, as shown in reference 13. The least favorable effects of jet size on afterbody axial-force coefficient occur with the cutoff-shroud configurations (3 and 4) because the nozzle-exit plane is downstream of the shroud terminus. To facilitate conversion of aerodynamic coefficients to propulsion coefficients involving nozzle thrust ratios, figure 33 has been prepared. The variation of aerodynamic ideal-thrust coefficient with jet-pressure ratio is given for the dry- and maximum-augmented-power settings.

Performance Characteristics

Thrust-minus-drag ratio.- The variations of thrust-minus-drag ratio with jet-total-pressure ratio and Mach number for all afterbody-nozzle configurations are shown in figure 34. The thrust-minus-drag ratio of all configurations generally increases with increases in jet-total-pressure ratio, as expected since the jet thrust increases rapidly relative to the external drag $\left(F_A\right)$ of the afterbody.

Thrust-minus-drag variations with Mach number for a typical jet-total-pressure-ratio schedule of a turbofan engine (see fig. 21) is presented in figure 35. Decreases in performance due to increased nozzle lateral spacing are shown for the dry-power configurations at transonic speeds. Other variations in performance shown are due to configuration differences. As Mach number increases toward unity, a decrease in performance is indicated for all configurations, but shrouded configuration 6D shows the greatest decrease. Generally, the basic shrouded configurations had the highest performance subsonically. Supersonically, only slight differences are shown for the maximum-augmented-power setting.

Nozzle internal performance.- The variation of internal performance F_j/F_i with jet-pressure ratio and Mach number is presented in figures 36 and 37 for the dry-power

setting and maximum-augmented-power setting, respectively, for afterbody configurations 1, 2, 5, and 6. Also shown at the lowest and highest Mach numbers presented is the ratio of ideal convergent-nozzle thrust to ideal isentropic thrust $F_{i,c}/F_i$. Values of F_j/F_i at jet-total-pressure ratios below 2 generally appear to be greater than unity because of less accuracy of instrumentation in the lower range of forces, pressures, and flow rates. Also presented is the mass-flow ratio $\dot{m}_j/\dot{m}_i$ for each power setting and Mach number.

CONCLUDING REMARKS

An investigation of the effect of nozzle lateral spacing on the drag and performance of twin-jet afterbodies utilizing hinged-flap convergent nozzles was conducted at Mach numbers from 0.6 to 2.2. Two nozzle-exit lateral spacings were studied for three afterbody types, with identical longitudinal cross-sectional-area distributions and fineness ratios maintained as the spacing was varied. The three types consisted of a basic shrouded configuration, an exposed-nozzle-flap configuration, and a shrouded configuration having a blunt-base interfairing terminating forward of the nozzle exit. Two nozzle power settings were used – the dry-power setting corresponding to minimum throat area and the maximum-augmented-power setting corresponding to maximum throat area. The jet-total-pressure ratio was varied from 1.0 (jet off) to approximately 21 depending on the Mach number.

At Mach numbers from 0.6 to 0.95, the effect of lateral spacing of the nozzle exits on afterbody drag and performance was varied. For the basic shrouded configurations at the dry-power setting, afterbody axial-force (drag) coefficient was generally decreased with increased lateral spacing. The opposite trend was exhibited for the maximum-augmented-power setting. For the exposed-nozzle-flap configurations afterbody drag increased for an increase in lateral spacing for both power settings. For the shrouded recessed-blunt-base configuration at both power settings, afterbody drag decreased with increased lateral spacing.

At Mach numbers from 1.2 to 1.3 and 2.0 to 2.2, decreasing the lateral spacing of the nozzle exits generally decreases afterbody drag and increases thrust minus drag for all test configurations at both power settings.

An important conclusion of this investigation is that differences may occur in determining the forces on the afterbody if only shroud drag, which does not include the annulus drag of the afterbody, is considered. Shroud axial-force (drag) coefficient generally increases with increased lateral spacing for both power settings, all configurations, and all Mach numbers herein.

Comparisons of experimental wave-drag measurements with calculated supersonic wave drag as obtained from axisymmetric and three-dimensional theories indicate good agreement for the close-spaced-nozzle afterbody configurations and only fair agreement for the wide-spaced-nozzle afterbody configurations.

Langley Research Center,
National Aeronautics and Space Administration,
Hampton, Va., July 16, 1970.

REFERENCES

1. Runckel, Jack F.: Jet-Exit and Airframe Interference Studies on Twin-Engine-Fuselage Aircraft Installations. NASA TM X-1274, 1966.

2. Schmeer, James W.; Lauer, Rodney F., Jr.; and Berrier, Bobby L.: Performance of Blow-In-Door Ejector Nozzles Installed on a Twin-Jet Variable-Wing-Sweep Fighter Airplane Model. NASA TM X-1383, 1967.

3. Wilmoth, Richard G.; Norton, Harry T., Jr.; and Corson, Blake W., Jr.: Effect of Engine-Interfairing Modifications on the Performance of a Powered Twin-Jet Fighter-Airplane Model at Mach 1.20. NASA TM X-1534, 1968.

4. Corson, Blake W., Jr.; and Runckel, Jack F.: Exploratory Studies of Aircraft Afterbody and Exhaust-Nozzle Interaction. NASA TM X-1925, 1969.

5. Berrier, Bobby Lee; and Wood, Frederick H., Jr.: Effect of Jet Velocity and Axial Location of Nozzle Exit on the Performance of a Twin-Jet Afterbody Model at Mach Numbers up to 2.2. NASA TN D-5393, 1969.

6. Mercer, Charles E.; and Berrier, Bobby L.: Effect of Afterbody Shape, Nozzle Type, and Engine Lateral Spacing on the Installed Performance of a Twin-Jet Afterbody Model. NASA TM X-1855, 1969.

7. Leiss, Abraham: Free-Flight Investigation of Effects of Simulated Sonic Turbojet Exhaust on the Drag of Twin-Jet Boattail Bodies at Transonic Speeds. NACA RM L56D30, 1956.

8. Langfelder, Helmut: Low-Drag Installation of Twin Propulsion Nozzles in the Rear of the Fuselage for Transonic and Supersonic Flight. Aerodynamics of Power Plant Installation, Pt. I, AGARDograph 103, Oct. 1965, pp. 195-216.

9. Harris, Roy V., Jr.: An Analysis and Correlation of Aircraft Wave Drag. NASA TM X-947, 1964.

10. Shapiro, Ascher H.: The Dynamics and Thermodynamics of Compressible Fluid Flow. Vol. II. Ronald Press Co., c.1954.

11. Compton, William B., III; and Runckel, Jack F.: Jet Effects on the Boattail Axial Force of Conical Afterbodies at Subsonic and Transonic Speeds. NASA TM X-1960, 1970.

12. Nicoloff, G. B.; and Norell, R. G.: Incremental Afterbody Drag for a 1/18 Scale Fuselage Afterbody Model at Mach Numbers 0.75, 0.90 and 1.22. GDC-ERR-1329, Gen. Dyn./Convair, Dec. 1968.

13. Migdal, D.; Miller, E. H.; and Schnell, W. C.: An Experimental Evaluation of Exhaust Nozzle/Airframe Interference. AIAA Pap. No. 69-430, June 1969.

14. Corson, Blake W., Jr.; and Schmeer, James W.: Summary of Research on Jet-Exit Installations. NASA TM X-1273, 1966.

TABLE I.- AFTERBODY-NOZZLE GEOMETRY

Ratio	Afterbody configuration 1	Afterbody configuration 2	Afterbody configuration 3	Afterbody configuration 4	Afterbody configuration 5	Afterbody configuration 6
Geometry independent of power setting						
$2A_b/A_{max}$	0.36	0.36	0.47	0.47	0.36	0.36
$2A_{eng}/A_{max}$	0.407	0.407	0.407	0.407	0.407	0.407
l/d_{equ}	7.03	7.03	7.03	7.03	7.03	7.03
s/d_{eng}	1.07	1.82	1.07	1.82	1.07	1.82
S_w, m^2	0.3082	0.3395	0.2946	0.3260	0.3015	0.3346
Geometry for dry-power setting (hinged flap closed)						
$2A_{an}/A_{max}$	0.24	0.24	0.06	0.06	0.24	0.24
$2A_t/A_{max}$	0.12	0.12	0.12	0.12	0.12	0.12
s/d_t	1.97	3.35	1.97	3.35	1.97	3.35
Geometry for maximum-augmented-power setting (hinged flap open)						
$2A_{an}/A_{max}$	0.06	0.06	0.06	0.06	0.06	0.06
$2A_t/A_{max}$	0.30	0.30	0.30	0.30	0.30	0.30
s/d_t	1.25	2.12	1.25	2.12	1.25	2.12

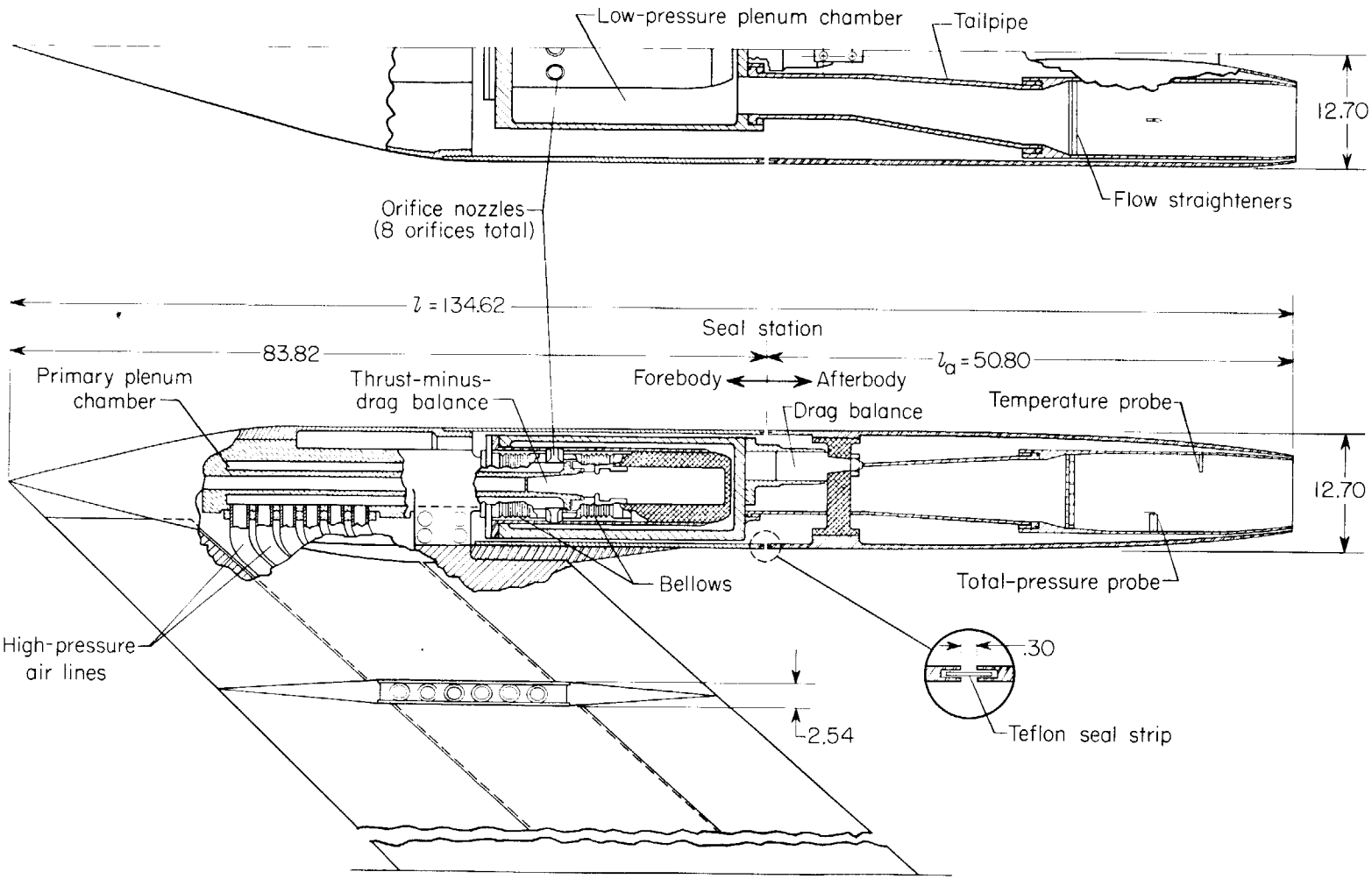

Figure 1.- Sketch of air-powered twin-jet model, with afterbody configuration 2 represented. (All dimensions are in cm.)

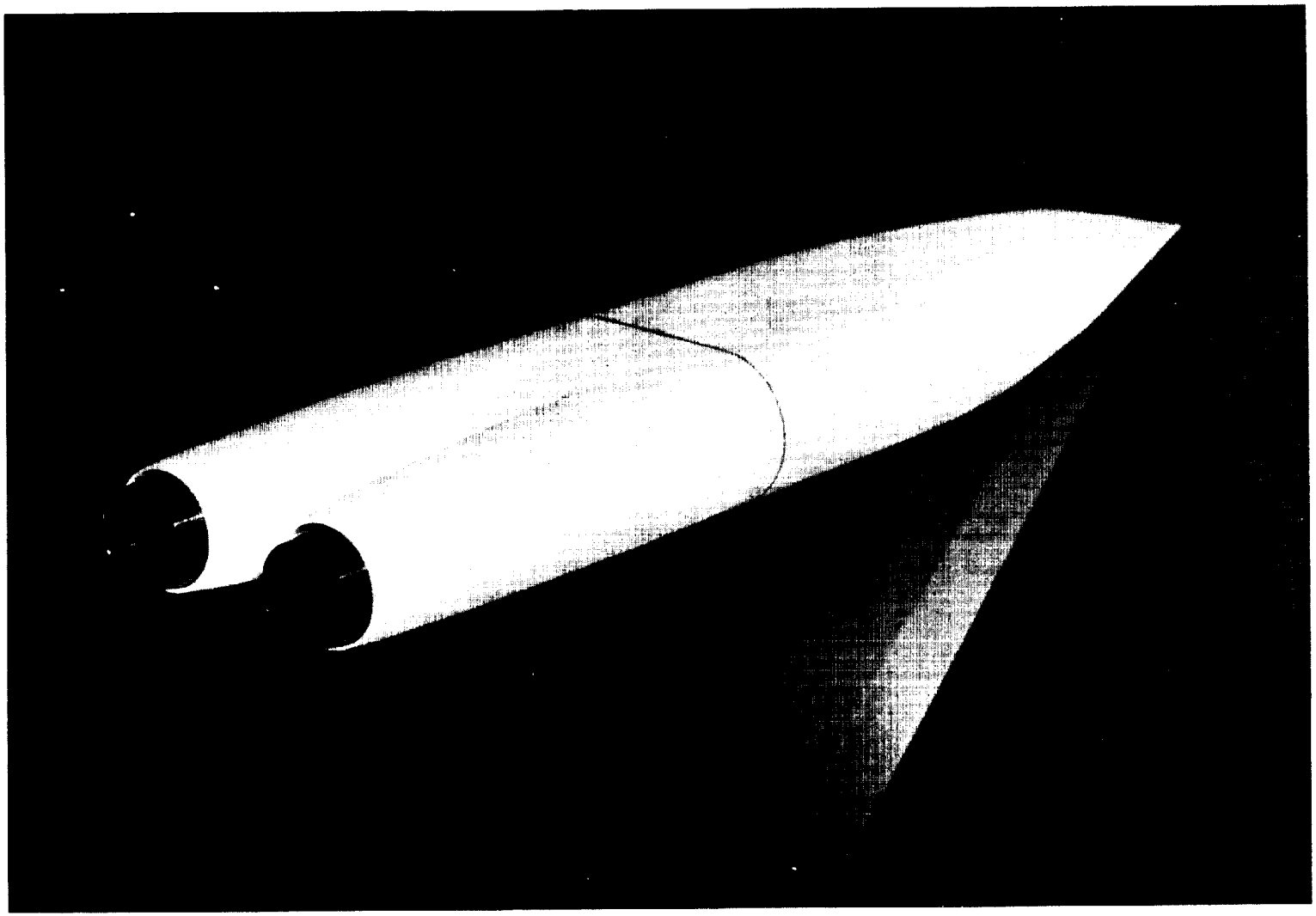

(a) Typical model installation in Langley 16-foot transonic tunnel. L-69-2775

Figure 2.- Photographs of twin-jet afterbody models.

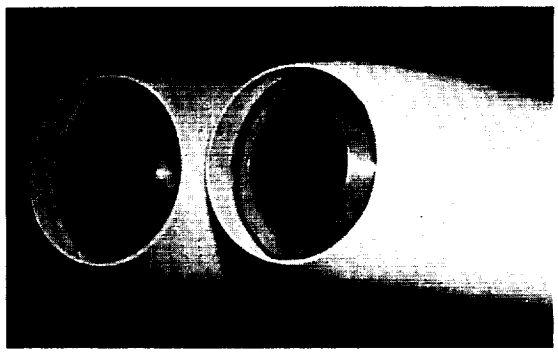

1D

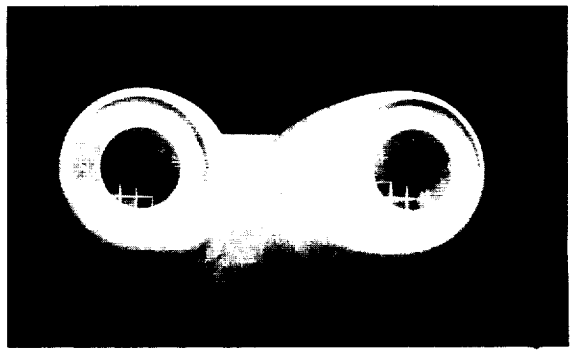

2D

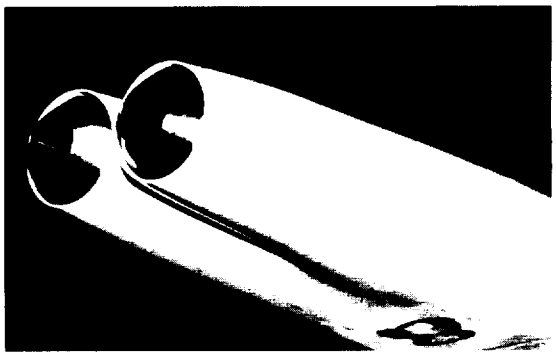

3D

4D

5D

6D

(b) Afterbody configurations with dry-power nozzles installed. L-70-1684

Figure 2.- Continued.

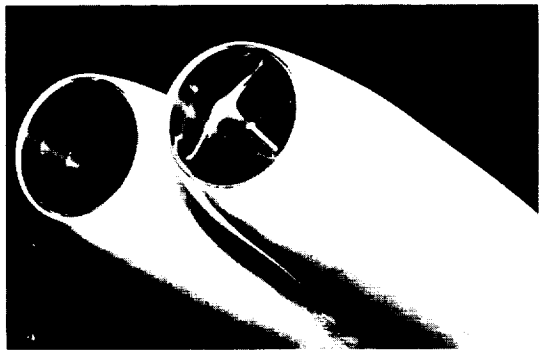

1A

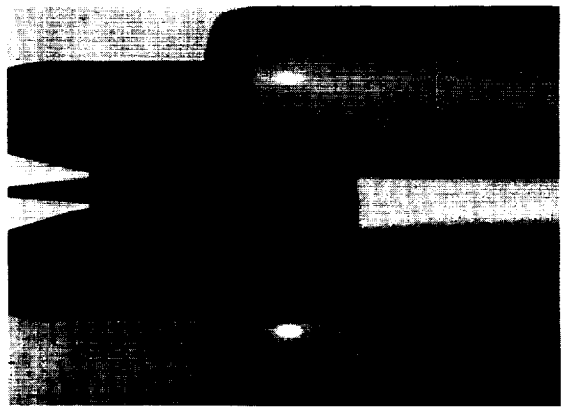

2A

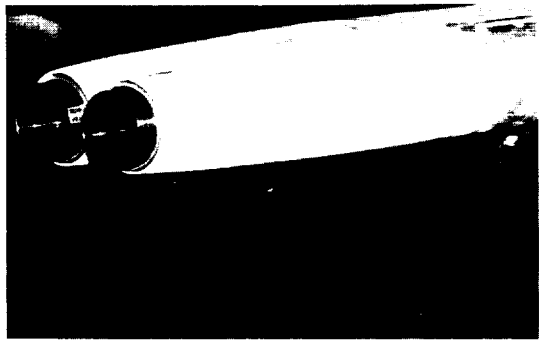

3A

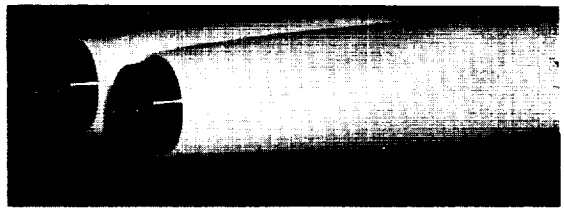

4A

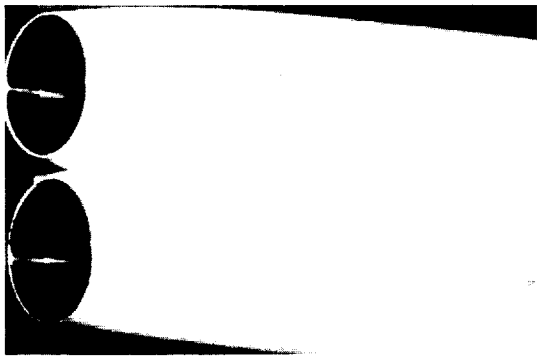

5A

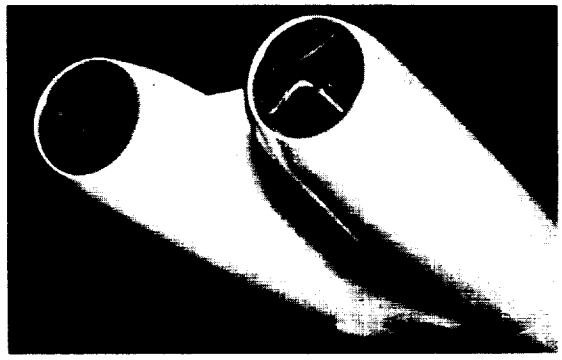

6A

(c) Afterbody configurations with maximum-augmented-power nozzles installed. L-70-1685

Figure 2.- Concluded.

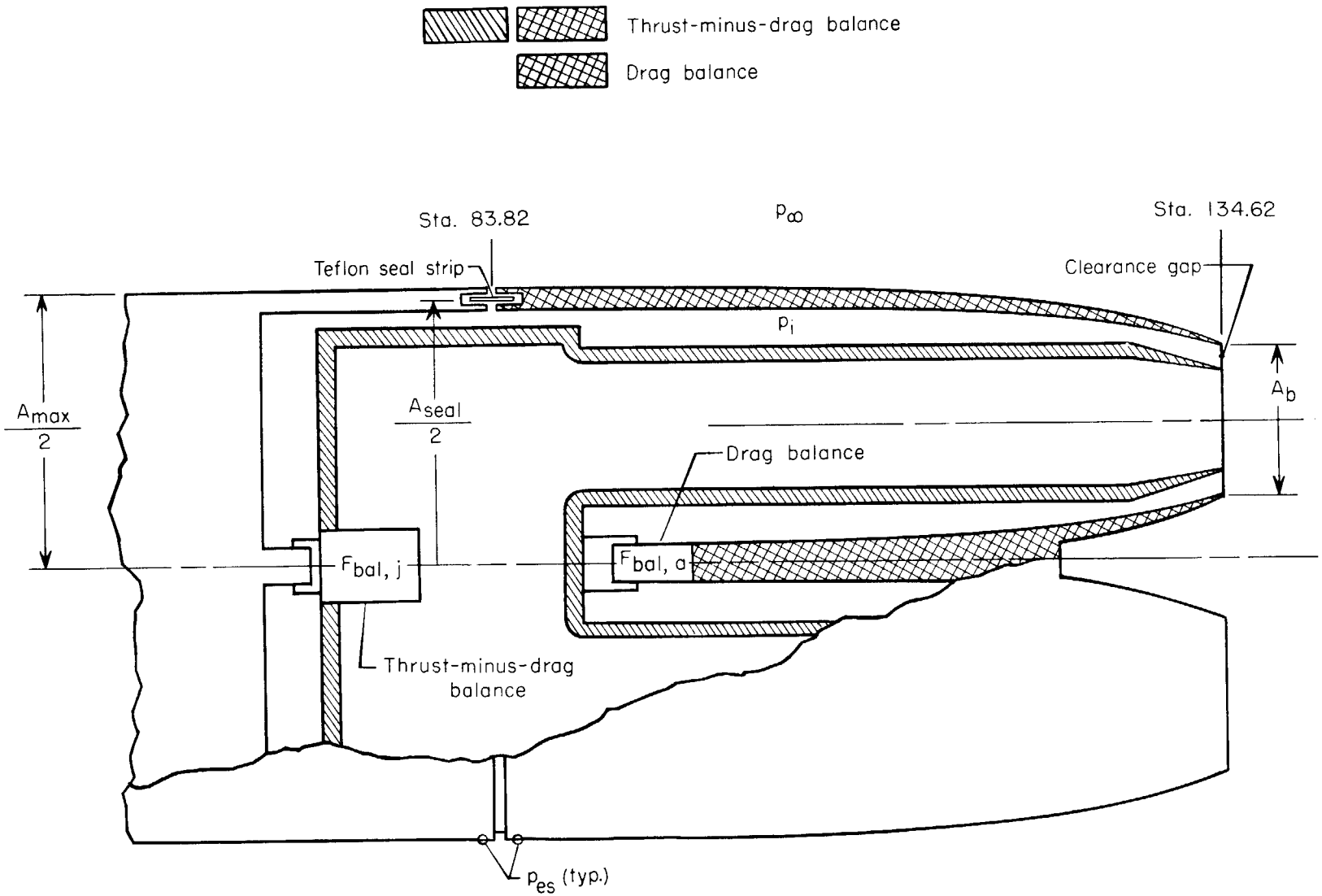

Figure 3.- Schematic sketch showing arrangement of two force balances.

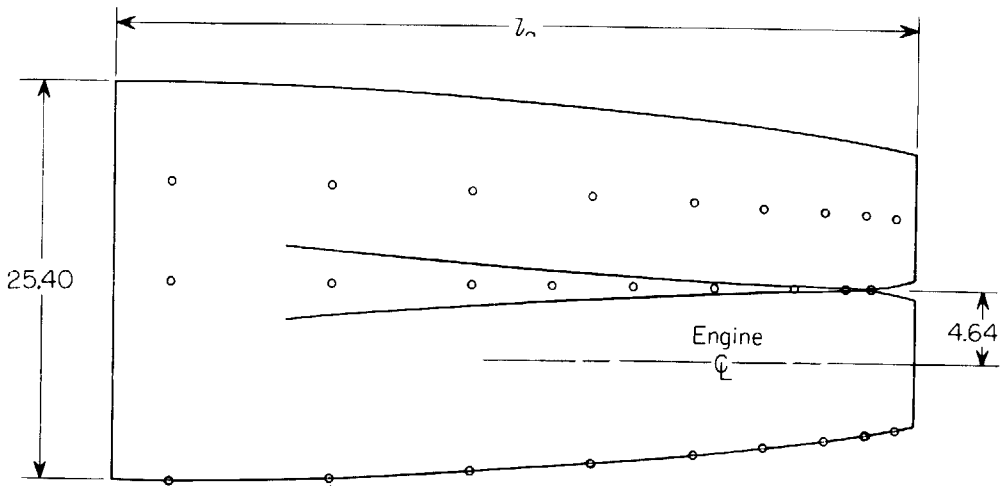

$\frac{x}{l}$	Row			
	1	2	3	4
0.651	X	X	X	X
.726	X	X		X
.792	X	X	X	X
.830	X			
.849		X		X
.868	X			
.890		X		X
.905	X		X	
.929		X		X
.943	X			
.957		X		X
.967	X		X	
.976		X		X
.980	X			
.990		X		X

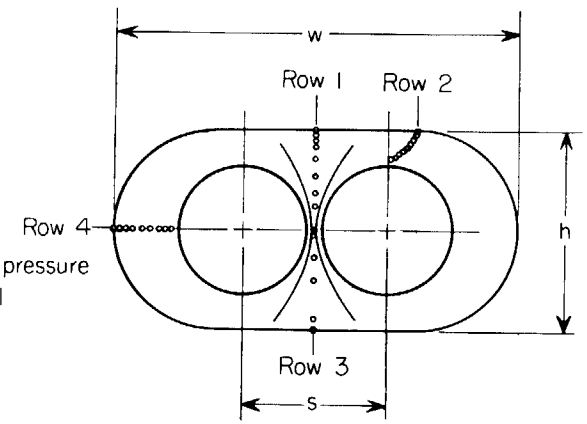

(a) Afterbody configuration 1.

Figure 4.- Sketch giving orifice locations on afterbody configurations. (All dimensions are in cm.)

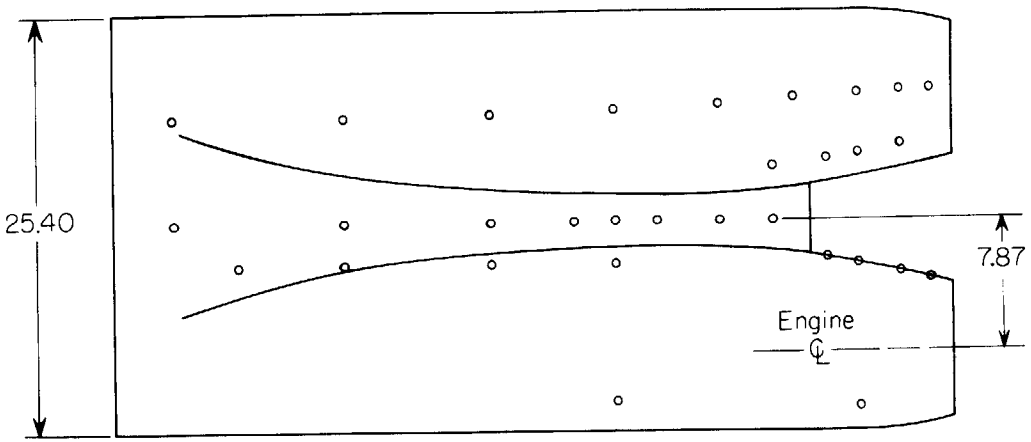

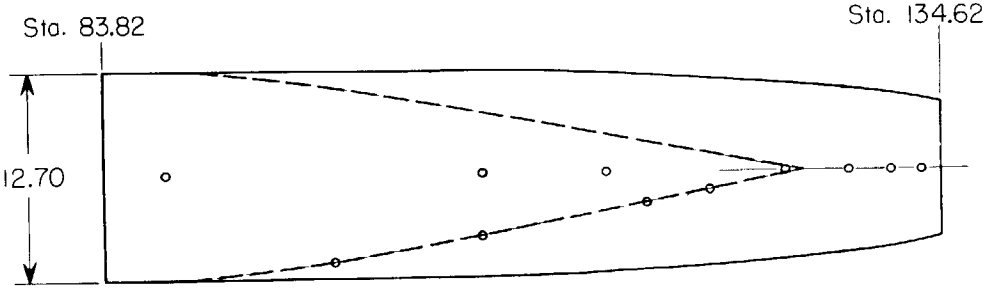

$\frac{x}{l}$	Row							
	1	2	3	4	5	6	7	8
0.651	X		X			X		
.679								X
.726	X		X	X				X
.792	X		X	X		X		X
.830	X							
.849	X		X			X	X	X
.868	X			X				
.896	X		X	X				
.919	X	X						
.929			X			X		
.943		X			X			
.959		X	X		X	X	X	
.976		X	X		X	X		
.990			X		X	X		

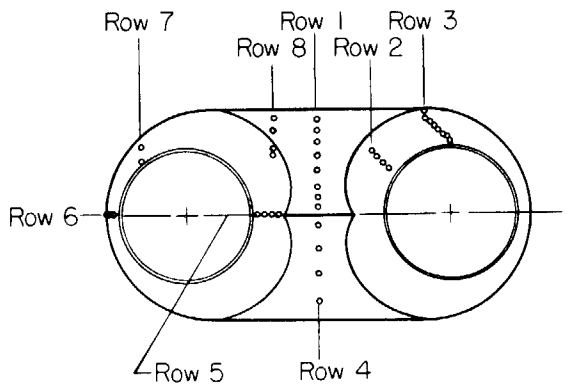

(b) Afterbody configuration 2.

Figure 4.- Continued.

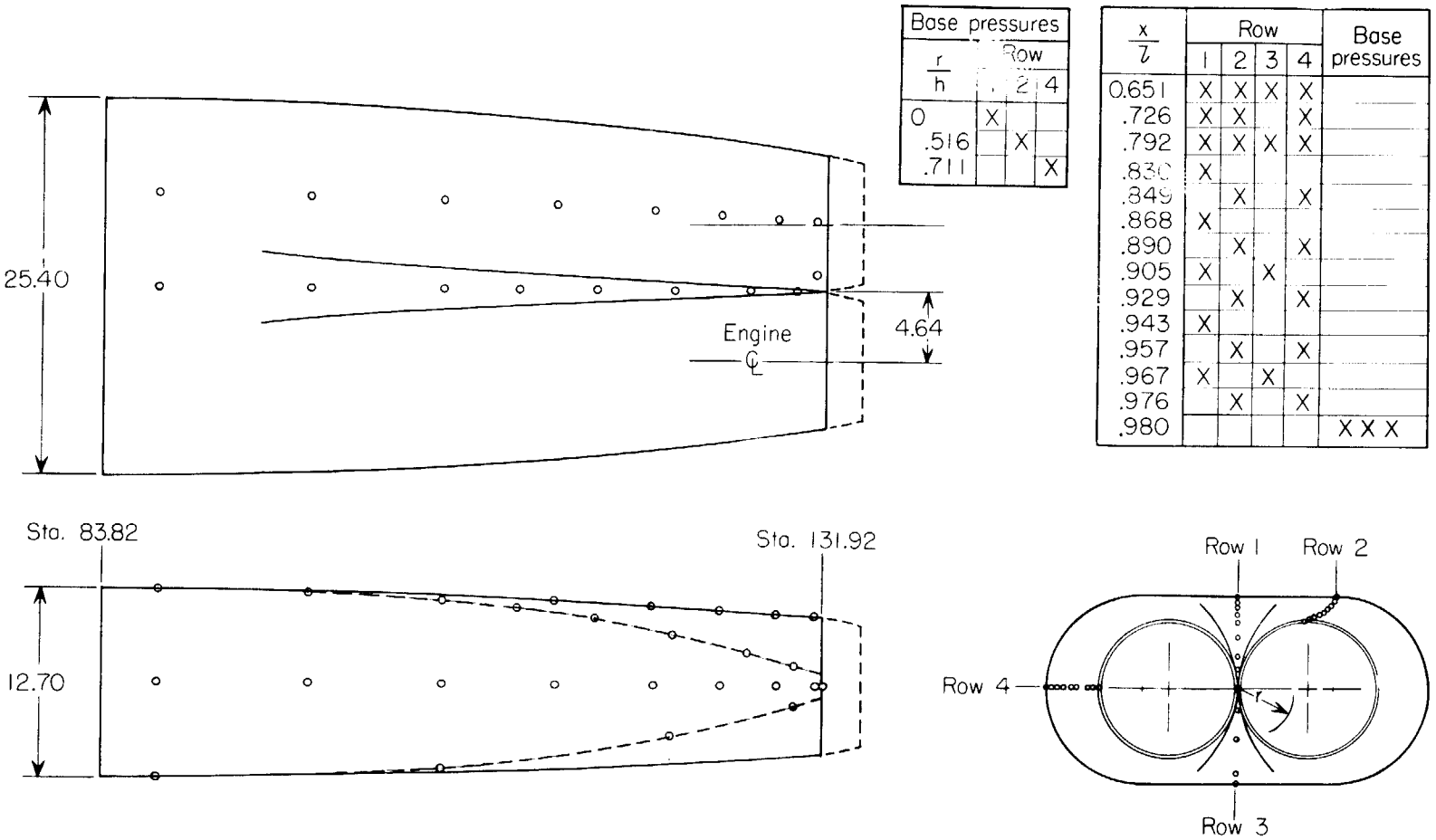

(c) Afterbody configuration 3.

Figure 4.- Continued.

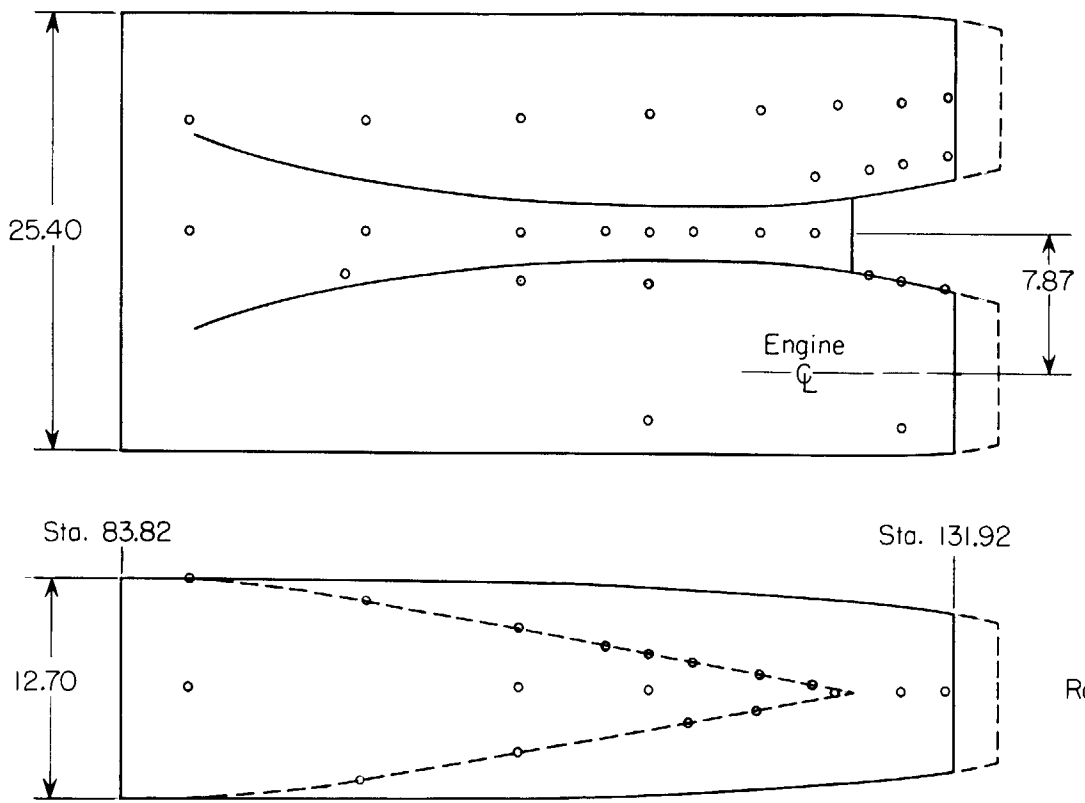

$\frac{x}{\ell}$	Row							
	1	2	3	4	5	6	7	8
0.651	X				X	X		
.679								X
.726	X		X		X			X
.792	X		X		X	X		X
.830					X			
.849	X				X	X	X	X
.868			X		X			
.896	X		X		X			
.919				X	X			
.929	X					X		
.943		X		X				
.959	X	X		X		X	X	
.976	X	X		X		X		
.980	X	X				X		

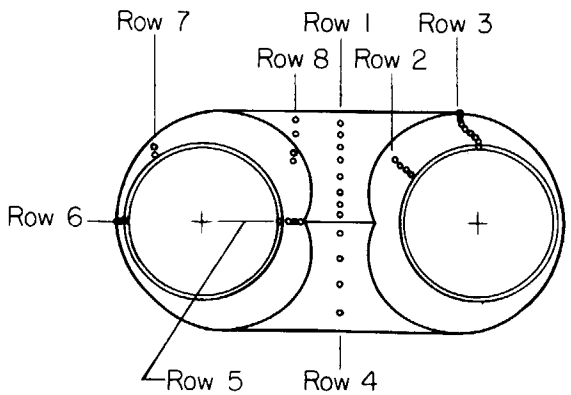

(d) Afterbody configuration 4.

Figure 4.- Continued.

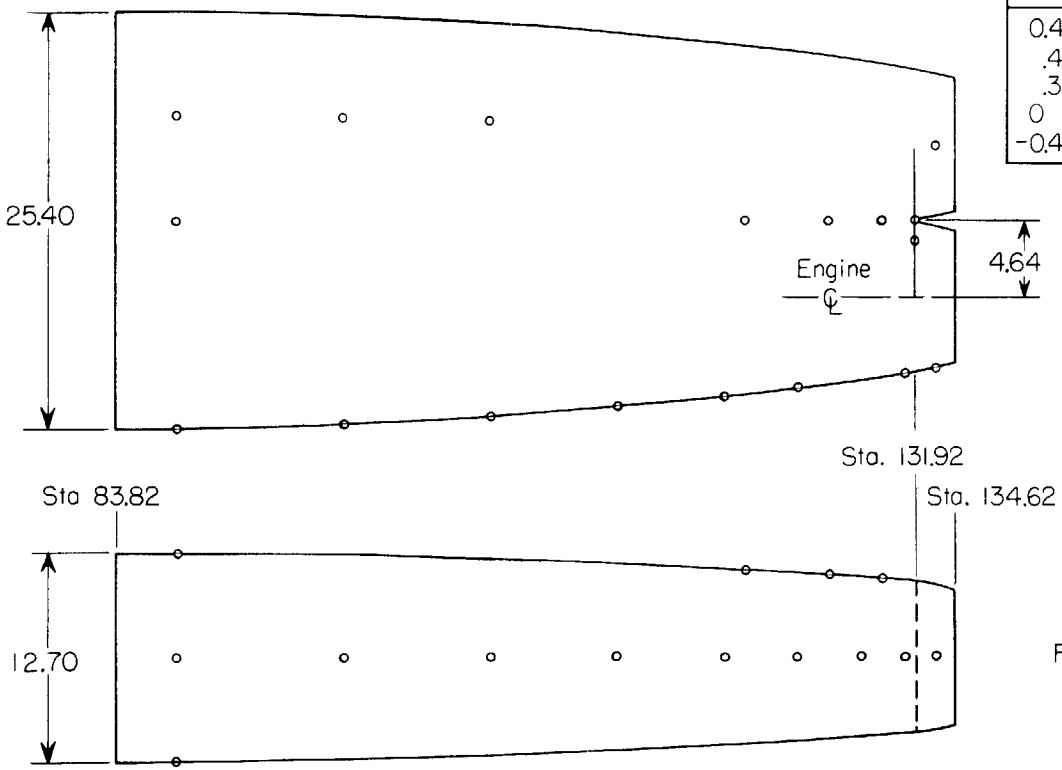

Base pressures		
$\frac{r}{h}$	Row	
	3	5
0.475	X	
.437		X
.306	X	
0	X	
-0.413	X	

$\frac{x}{l}$	Row				
	1	2	3	4	5
0.651	X	X	X	X	
.726		X		X	
.792		X		X	
.849				X	
.890				X	
.905	X				
.929				X	
.943	X				
.957				X	
.967	X				
.976				X	
.980			XXXX		X
.990		X		X	

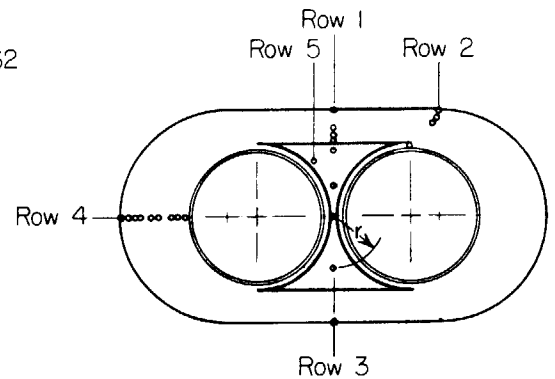

(e) Afterbody configuration 5.

Figure 4.- Continued.

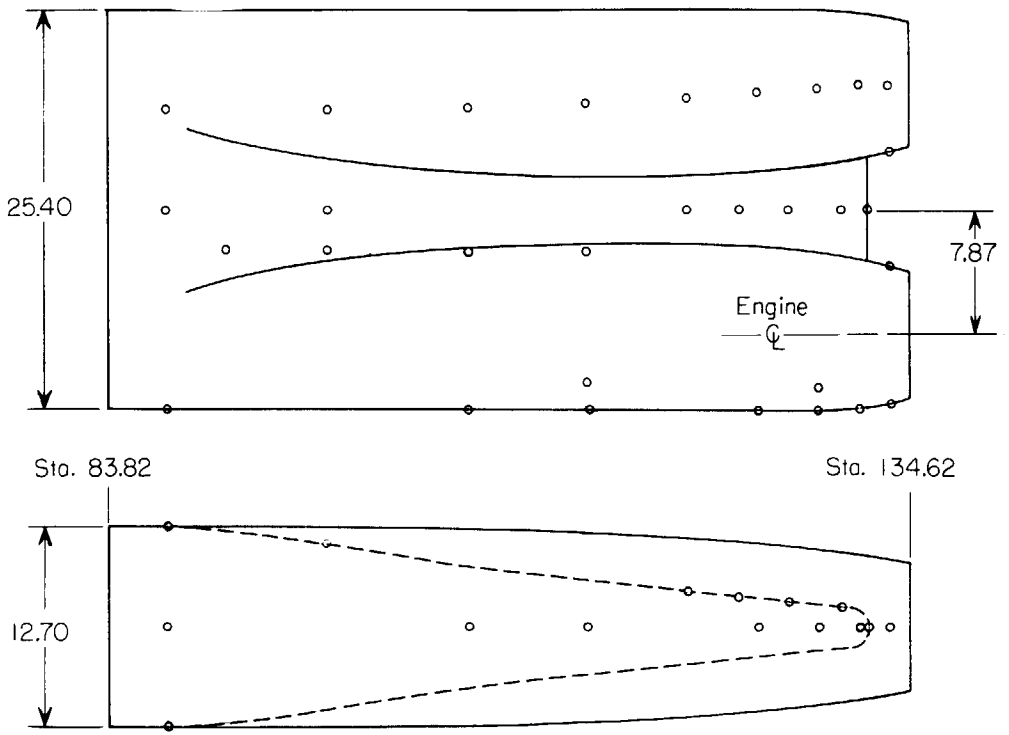

$\frac{x}{l}$	Row							
	1	2	3	4	5	6	7	8
0.651	X		X	X		X		
.679								X
.726	X		X					X
.792			X			X		X
.830								
.849			X			X	X	X
.868								
.896	X		X					
.919	X	X						
.929			X			X		
.943	X	X						
.959		X	X			X	X	
.967	X					X		
.976		X	X			X		
.980	X							
.990			X		X			

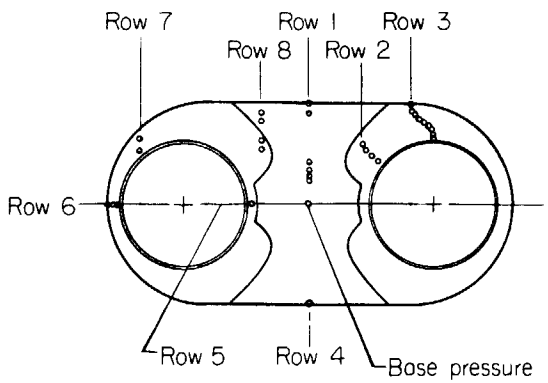

(f) Afterbody configuration 6.

Figure 4.- Concluded.

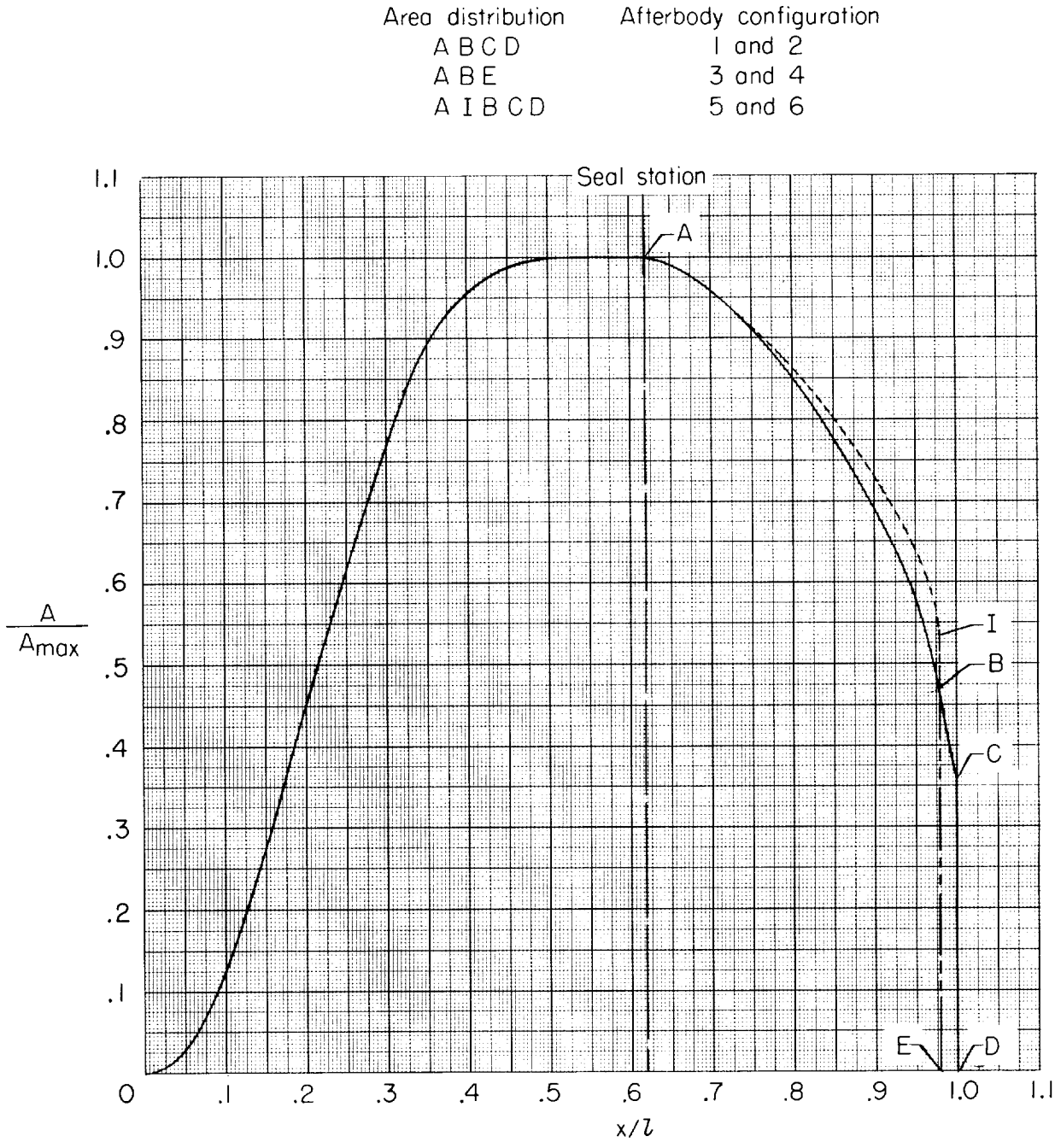

Figure 5.- Area distributions of twin-jet afterbody configurations. A_{max} = 287.90 cm^2.

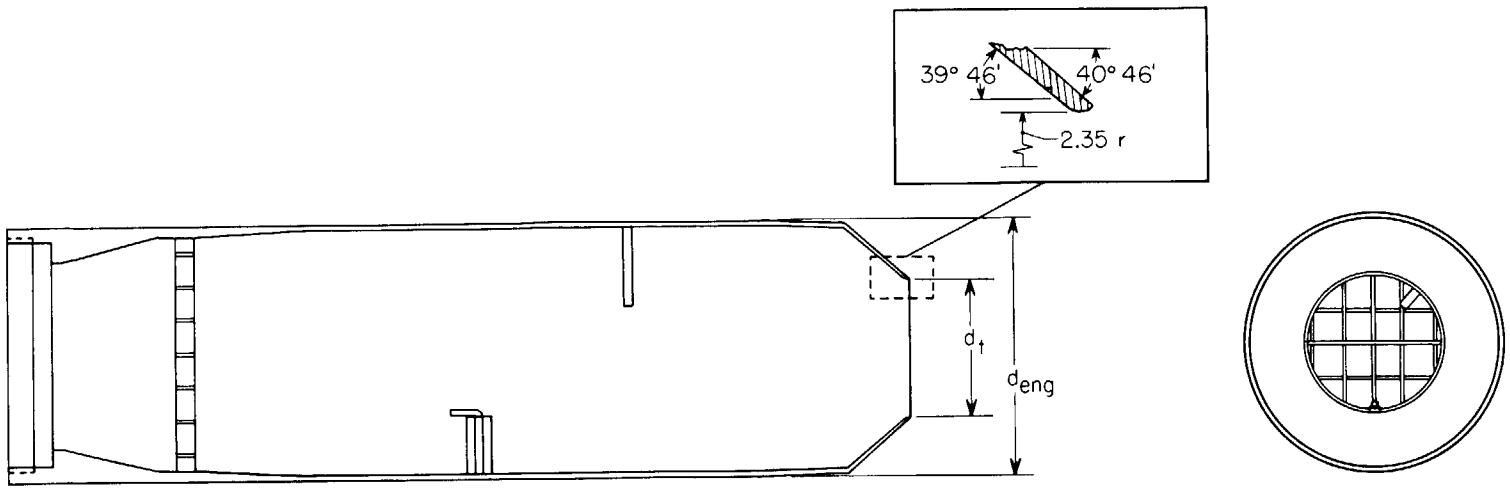

(a) Dry-power configuration.

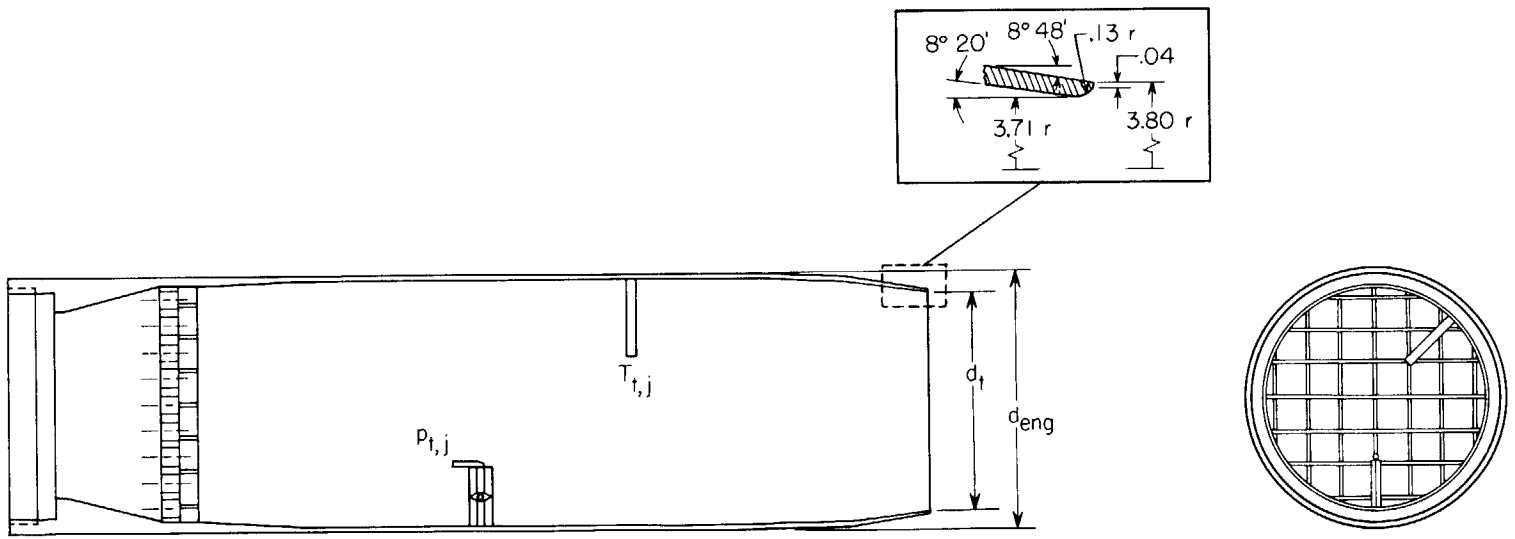

(b) Maximum-augmented-power configuration.

Figure 6.- Sketch of nozzle configurations. (All dimensions are in cm.)

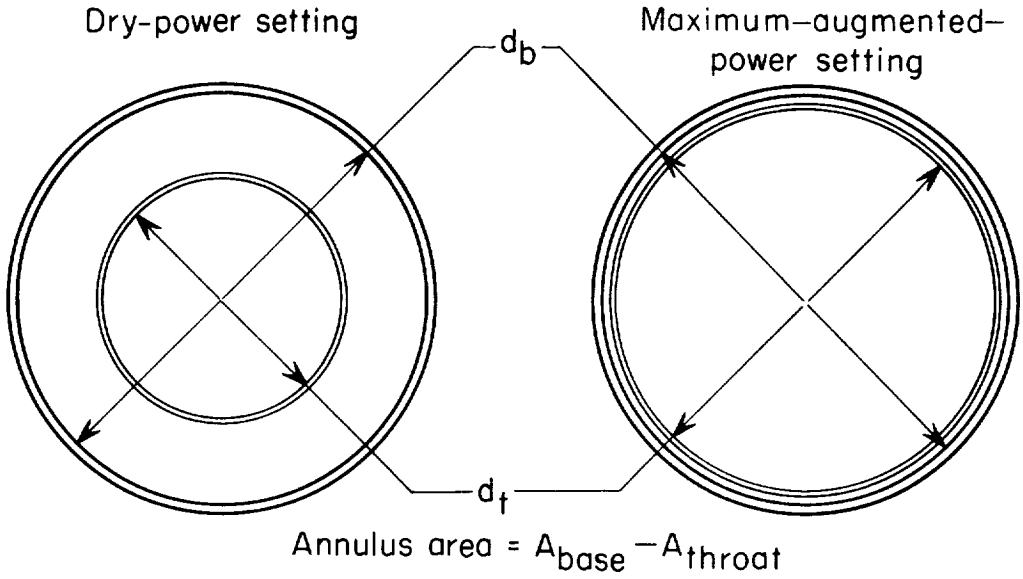

	d_b	d_s	l_f	d_t
Dry	7.95	8.78	2.69	4.69
Afterburner	7.95	8.78	2.12	7.42

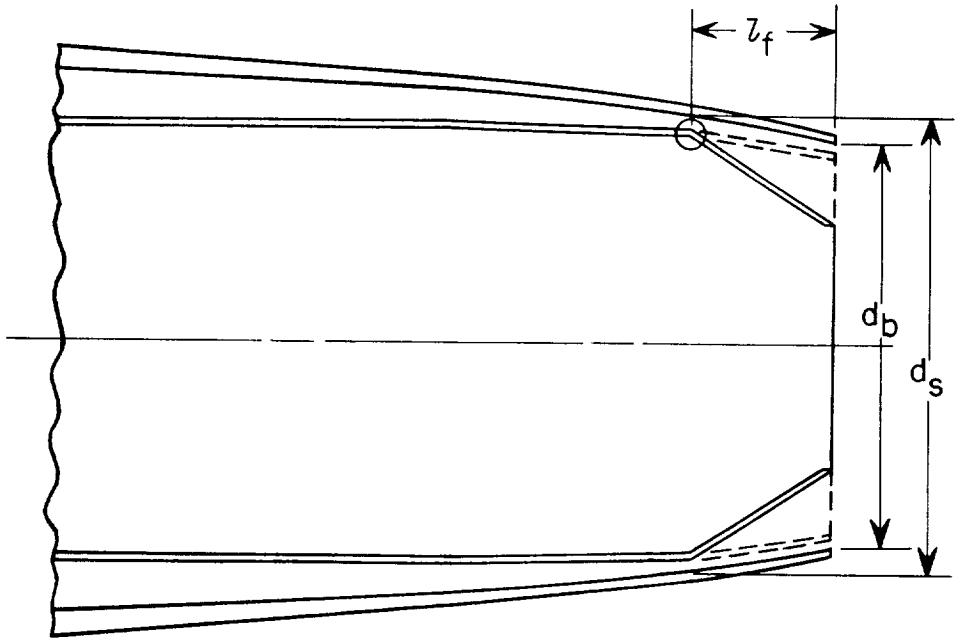

Figure 7.- Sketch of nozzle and shroud installation. (All dimensions are in cm.)

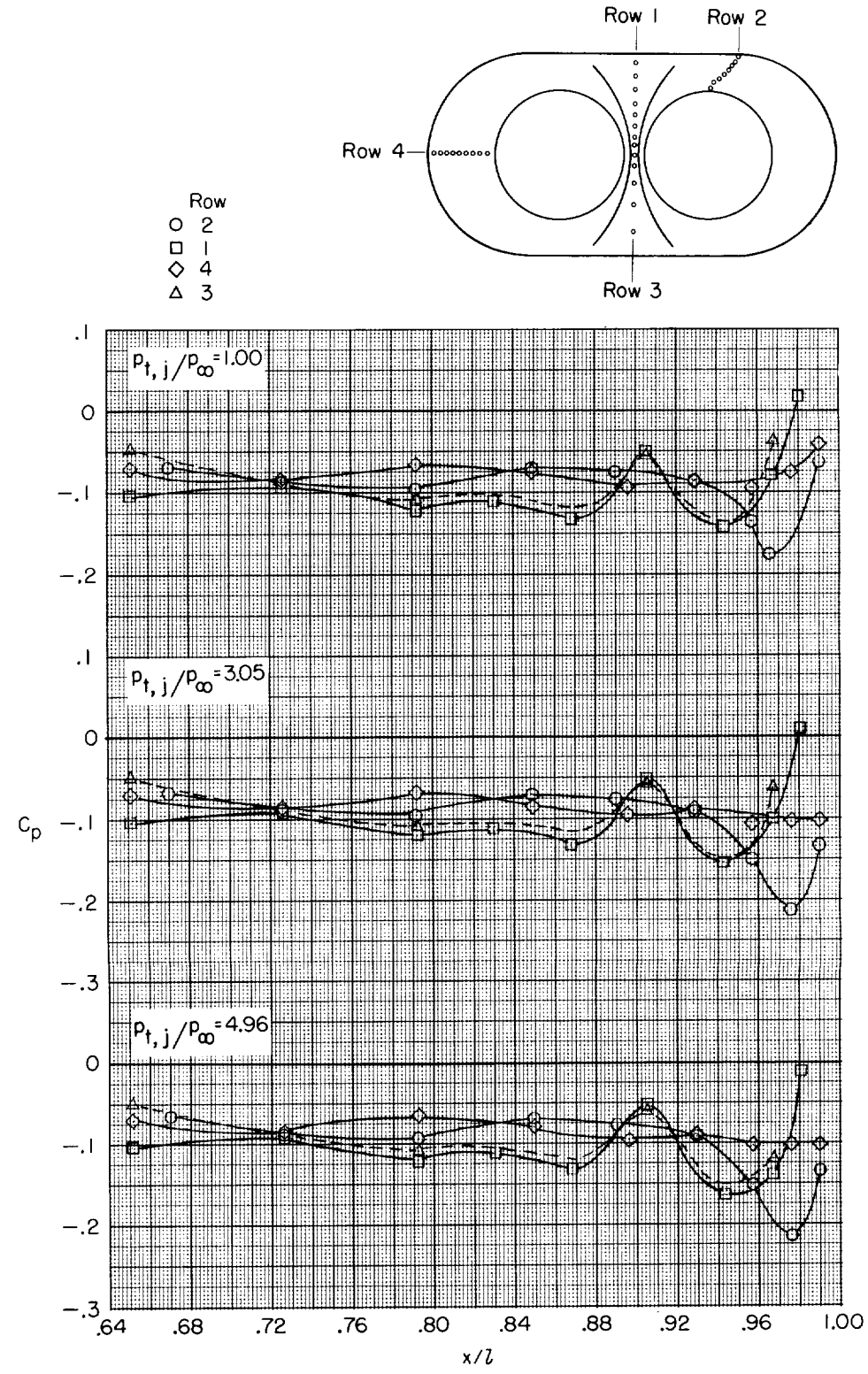

(a) M = 0.60.

Figure 8.- Longitudinal pressure distribution on configuration 1D at several pressure ratios and Mach numbers.

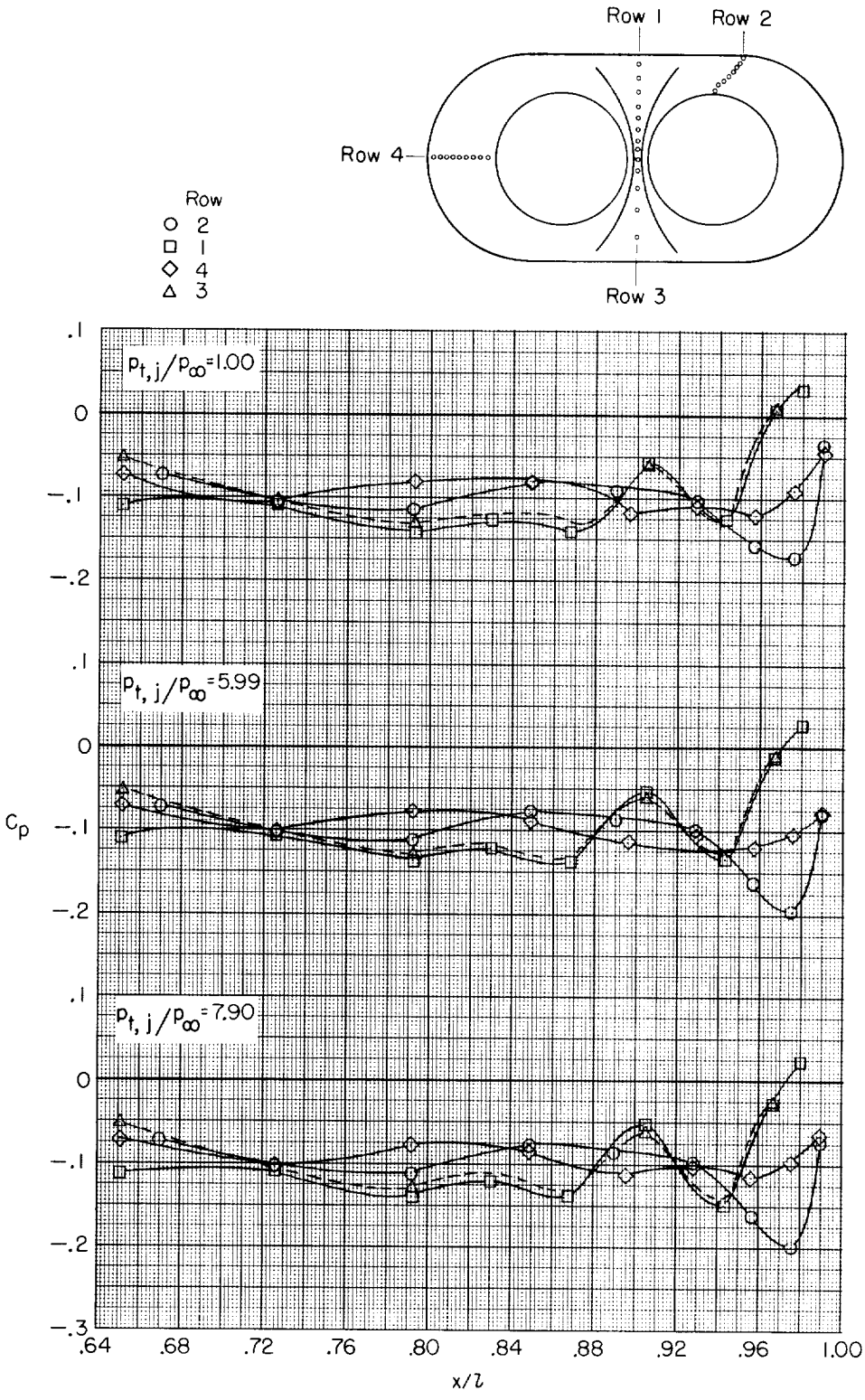

(b) M = 0.90.

Figure 8.- Continued.

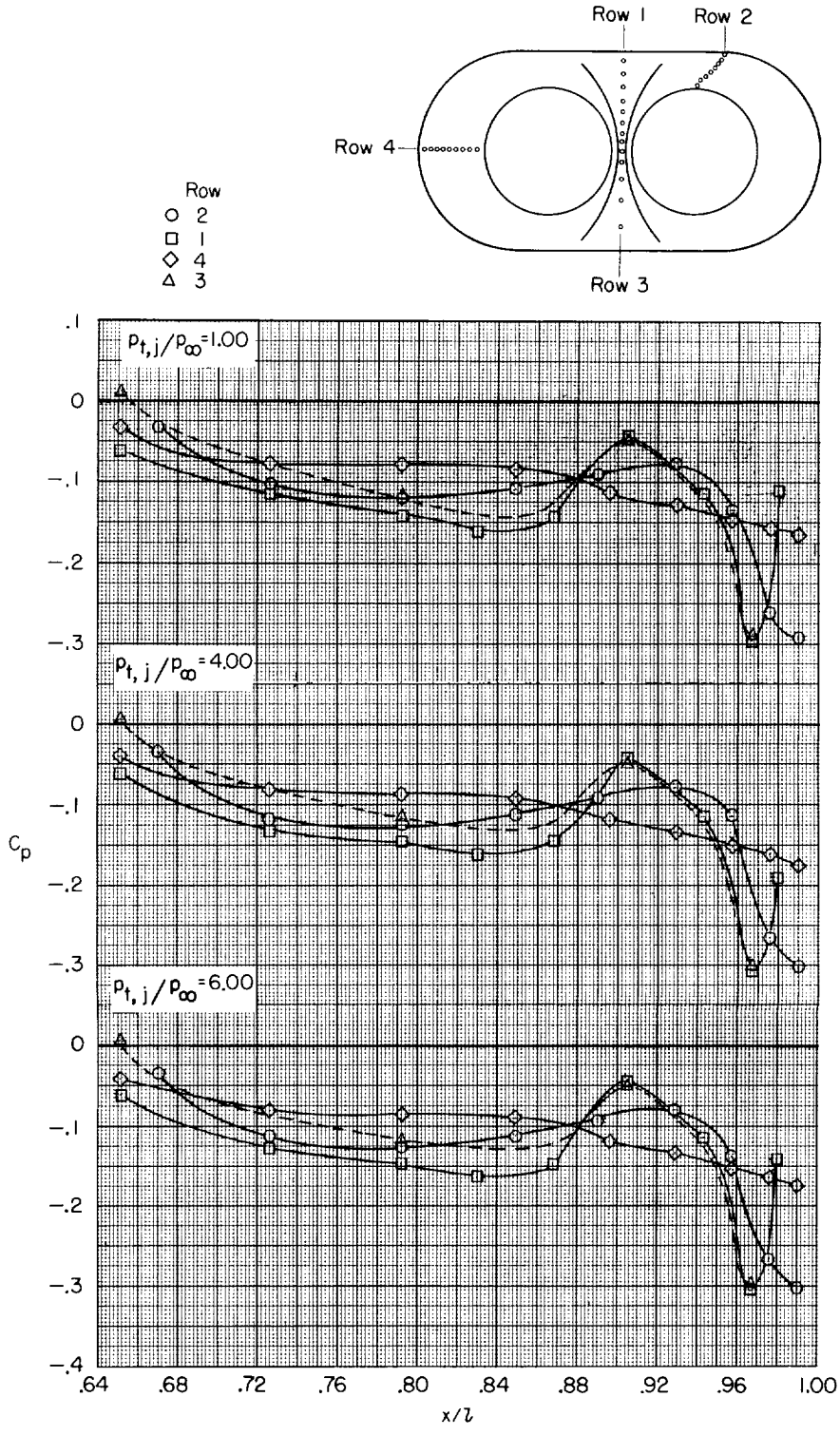

(c) M = 1.30.

Figure 8.- Concluded.

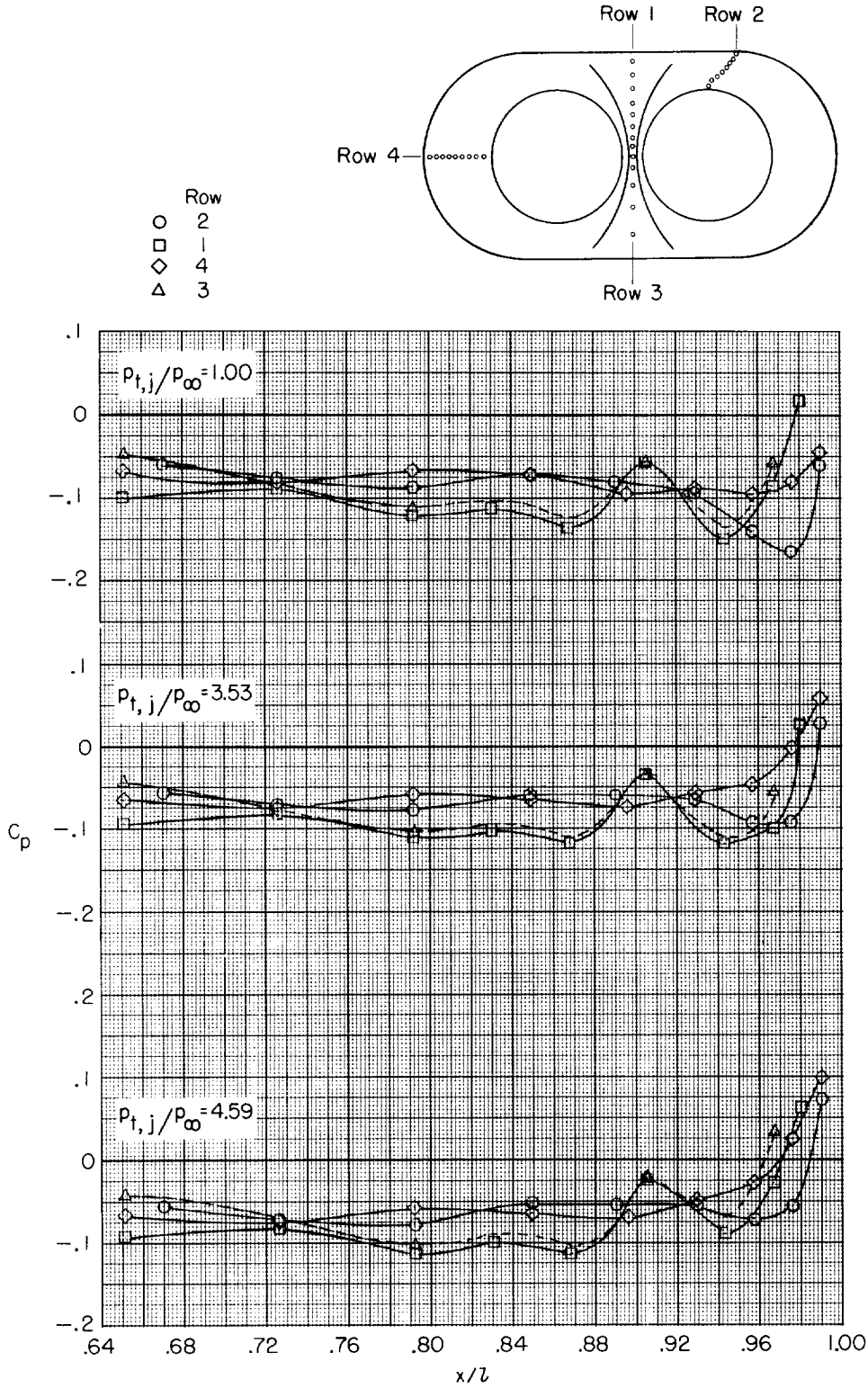

(a) M = 0.60.

Figure 9.- Longitudinal pressure distribution on configuration 1A at several pressure ratios and Mach numbers.

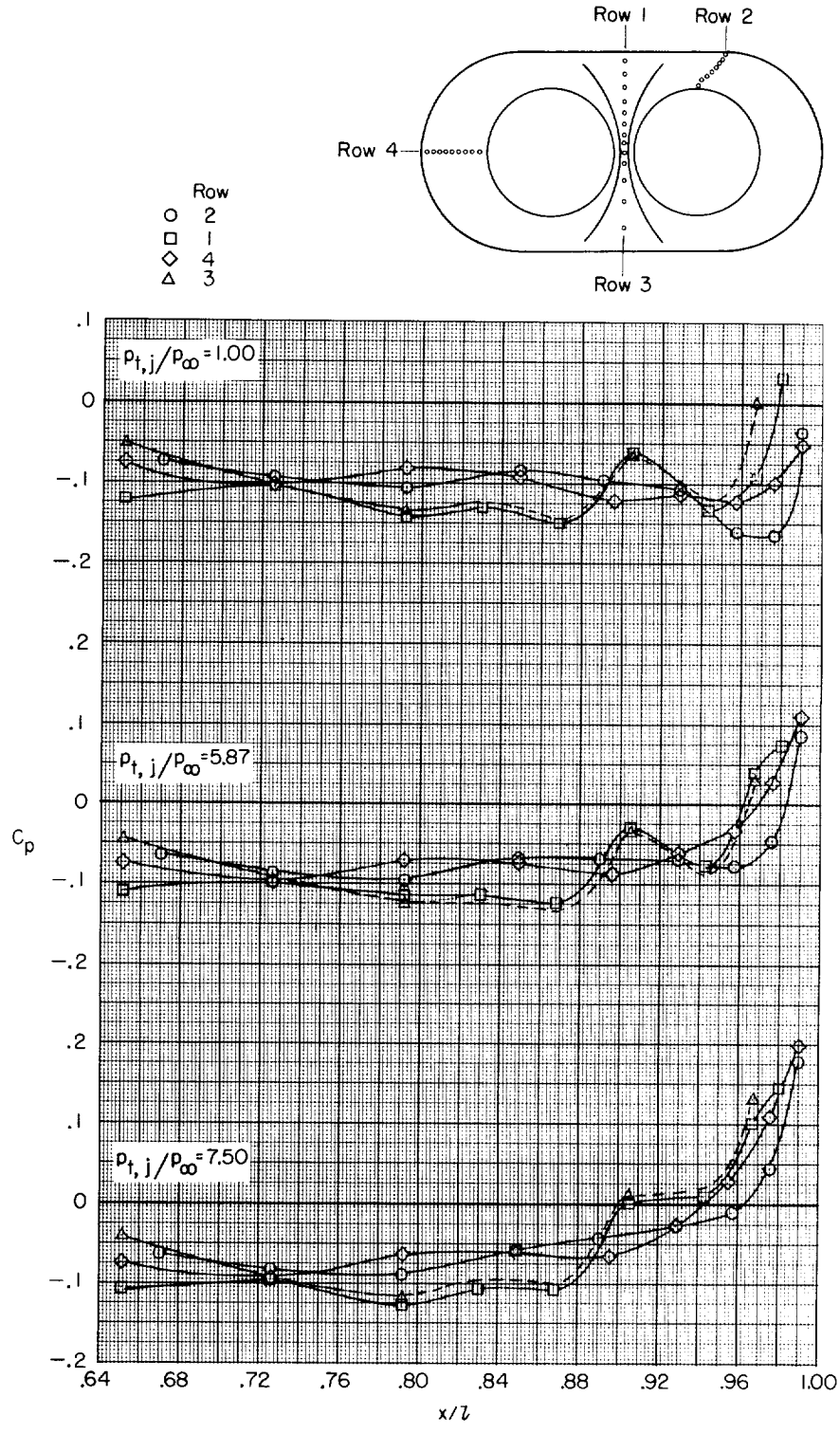

(b) M = 0.90.

Figure 9.- Continued.

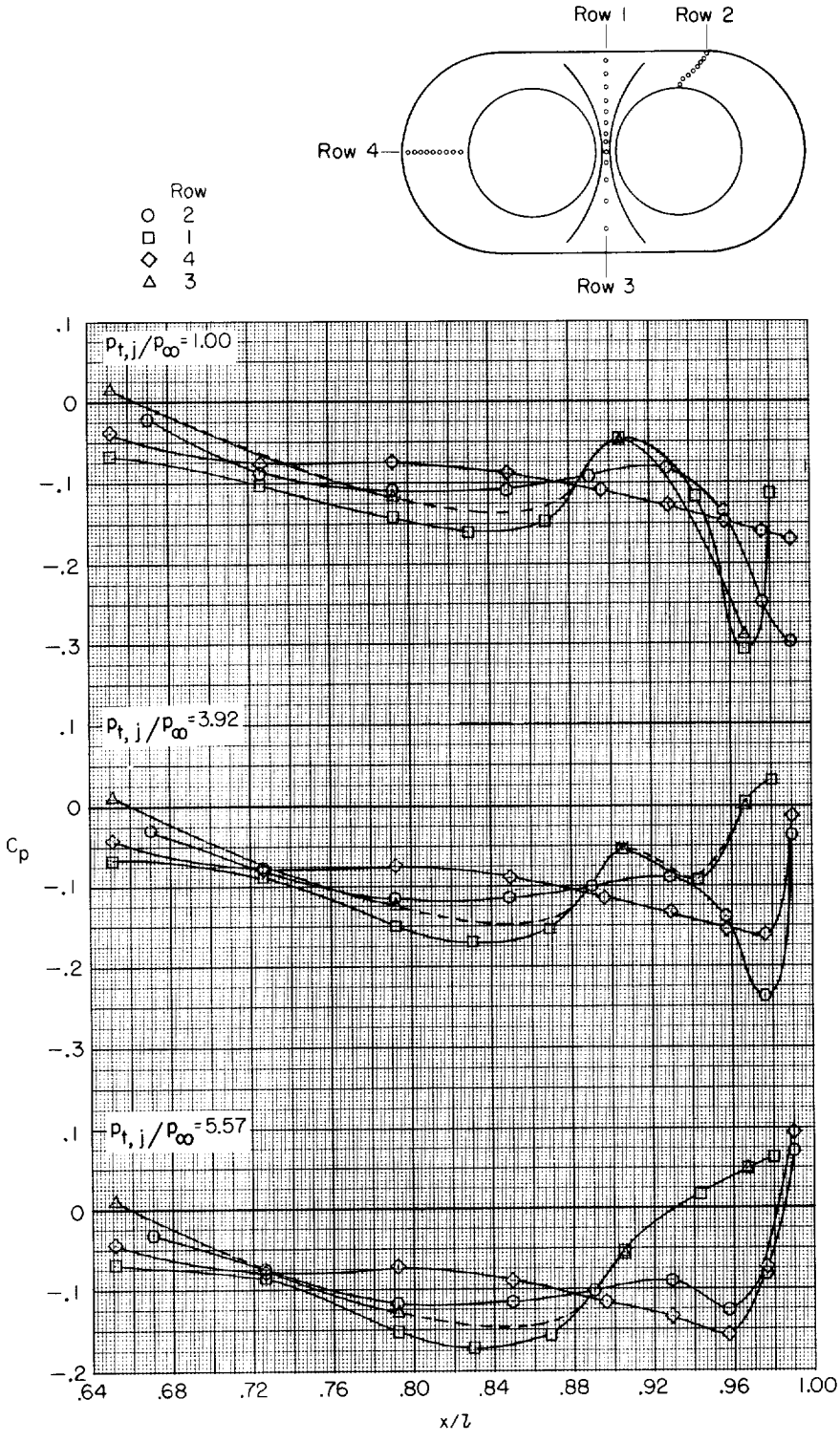

(c) M = 1.30.

Figure 9.- Concluded.

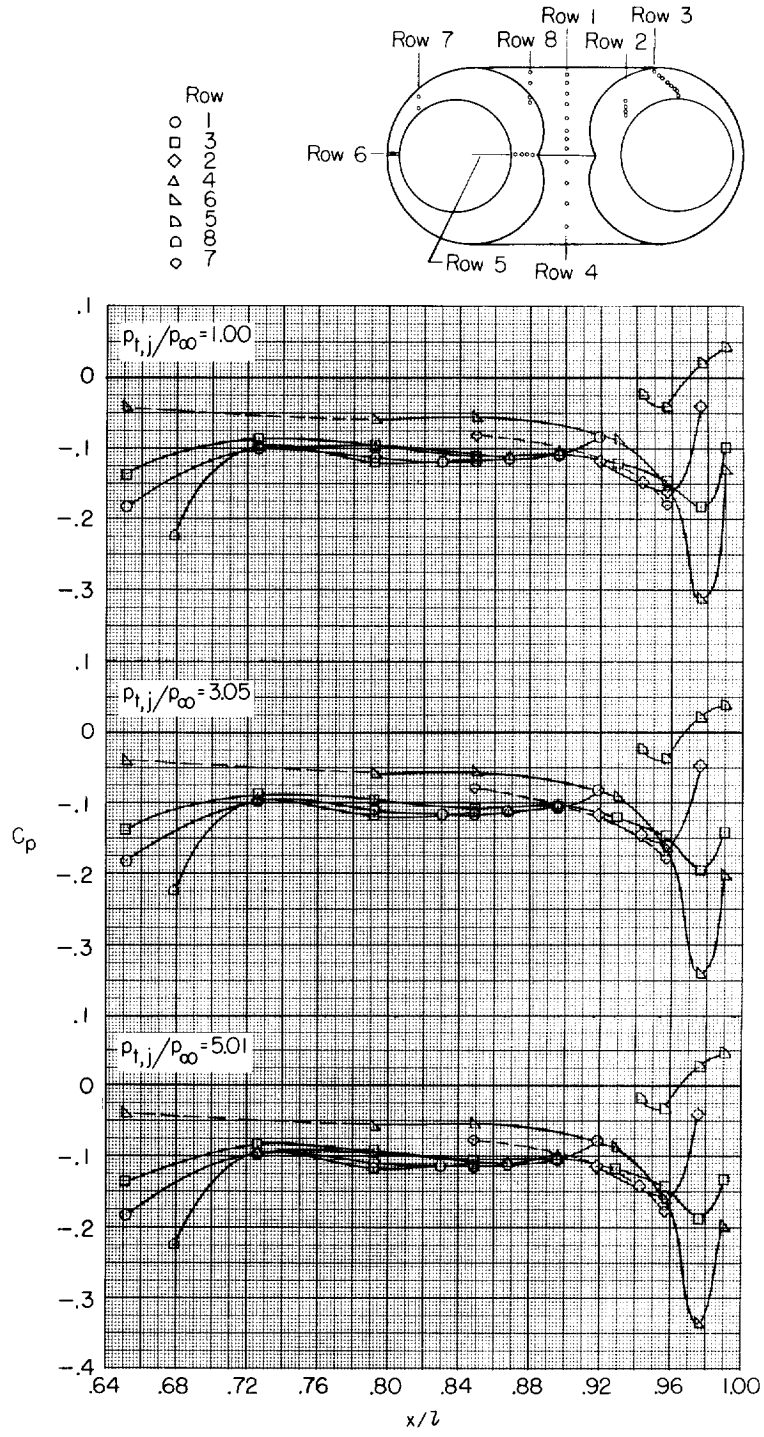

(a) M = 0.60.

Figure 10.- Longitudinal pressure distribution on configuration 2D at several pressure ratios and Mach numbers.

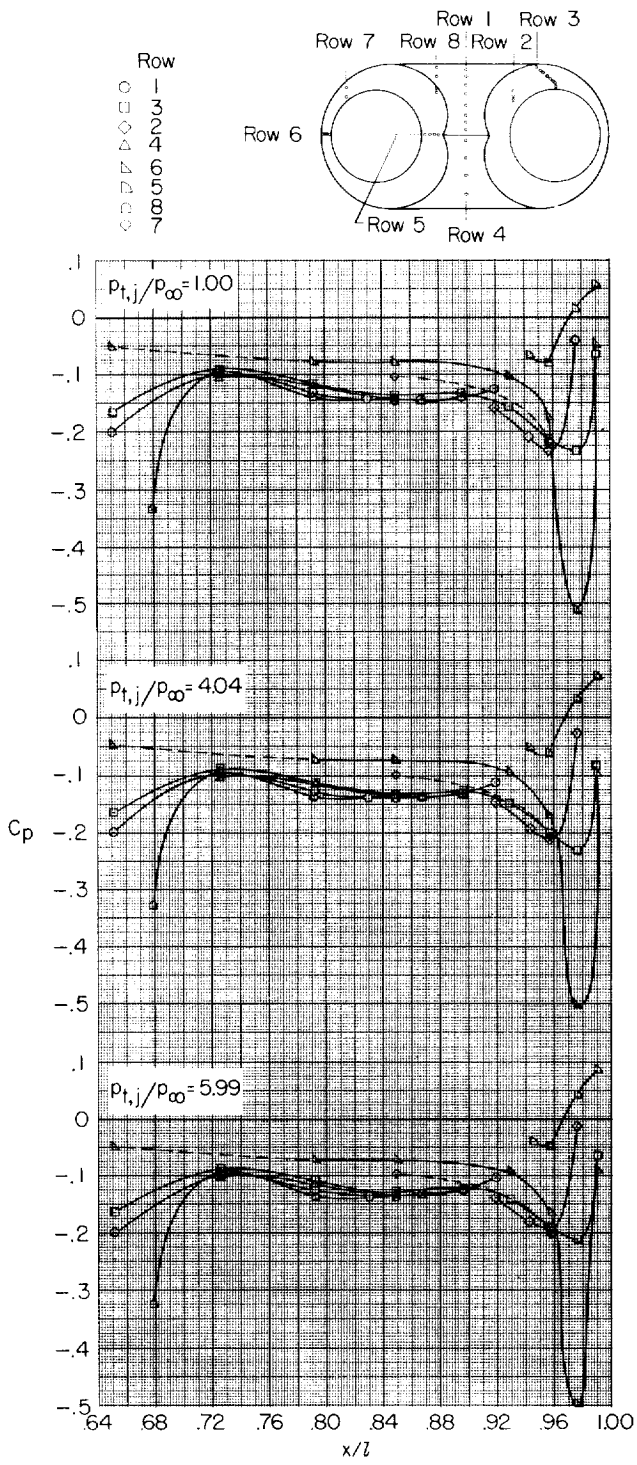

(b) M = 0.90.

Figure 10.- Continued.

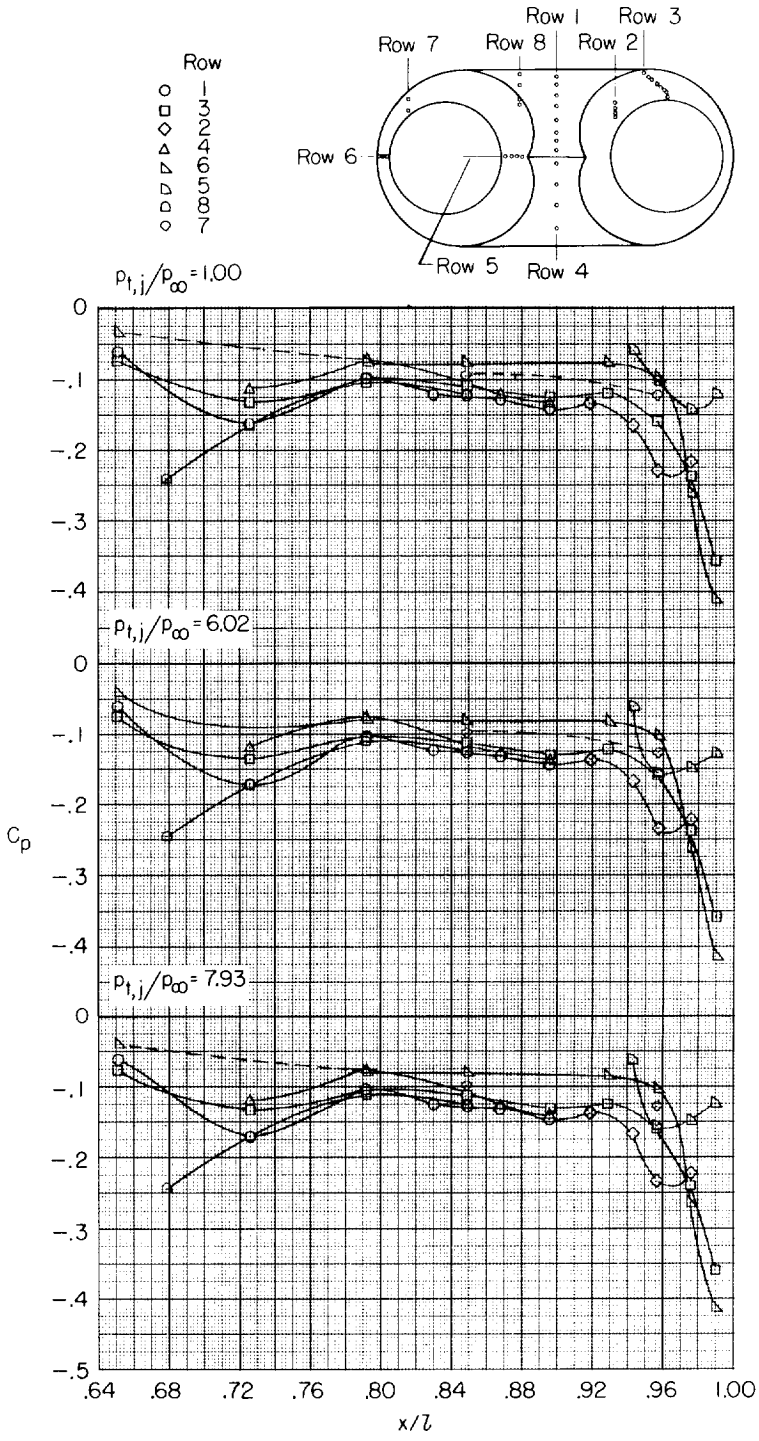

(c) M = 1.30.

Figure 10.- Concluded.

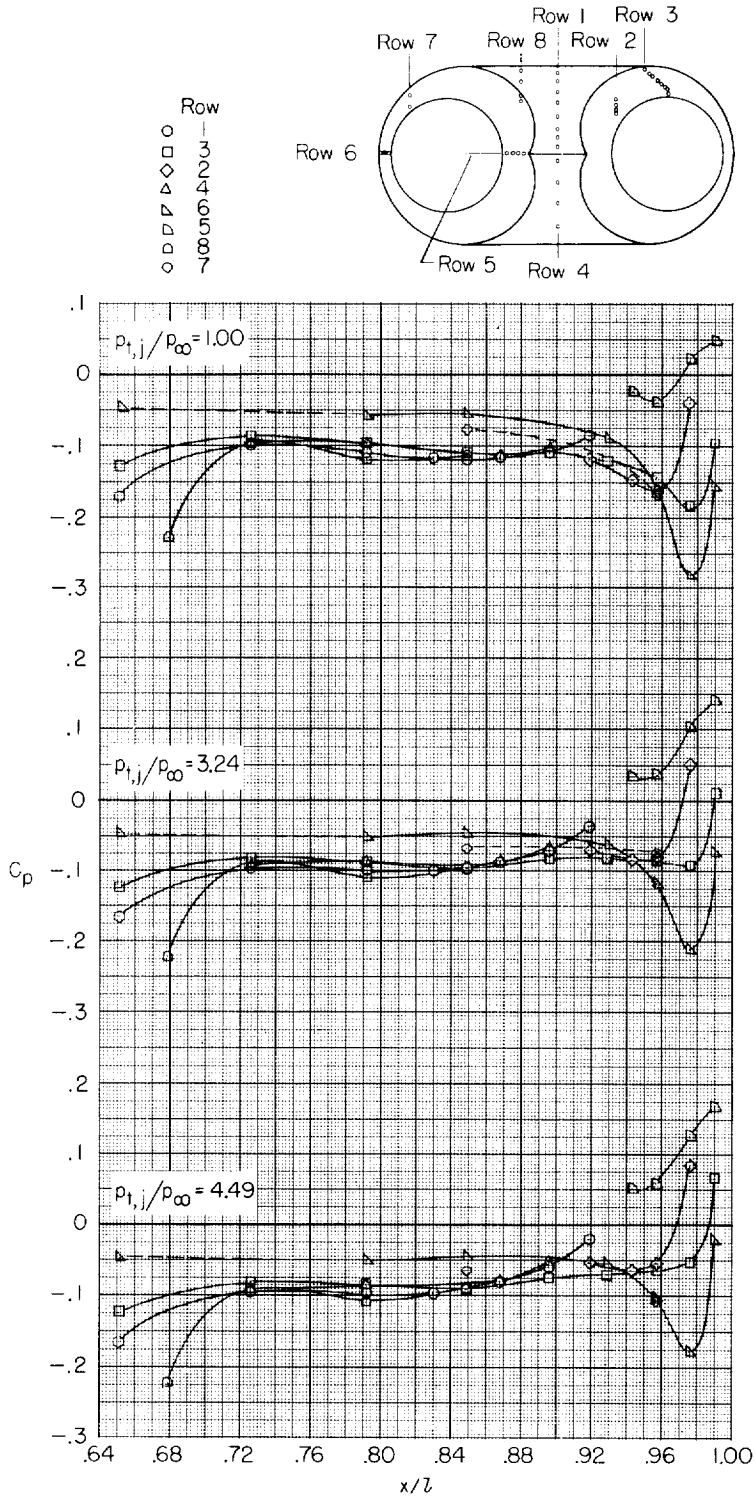

(a) M = 0.60.

Figure 11.- Longitudinal pressure distribution on configuration 2A at several pressure ratios and Mach numbers.

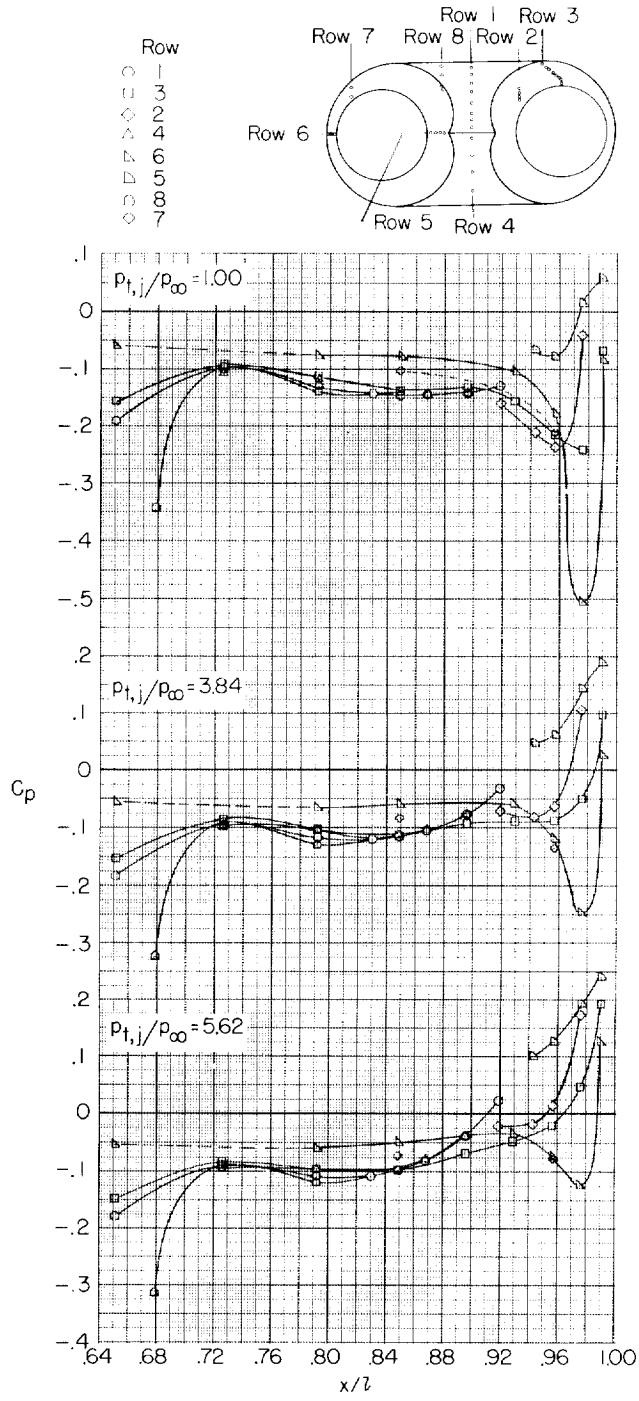

(b) M = 0.90.

Figure 11.- Continued.

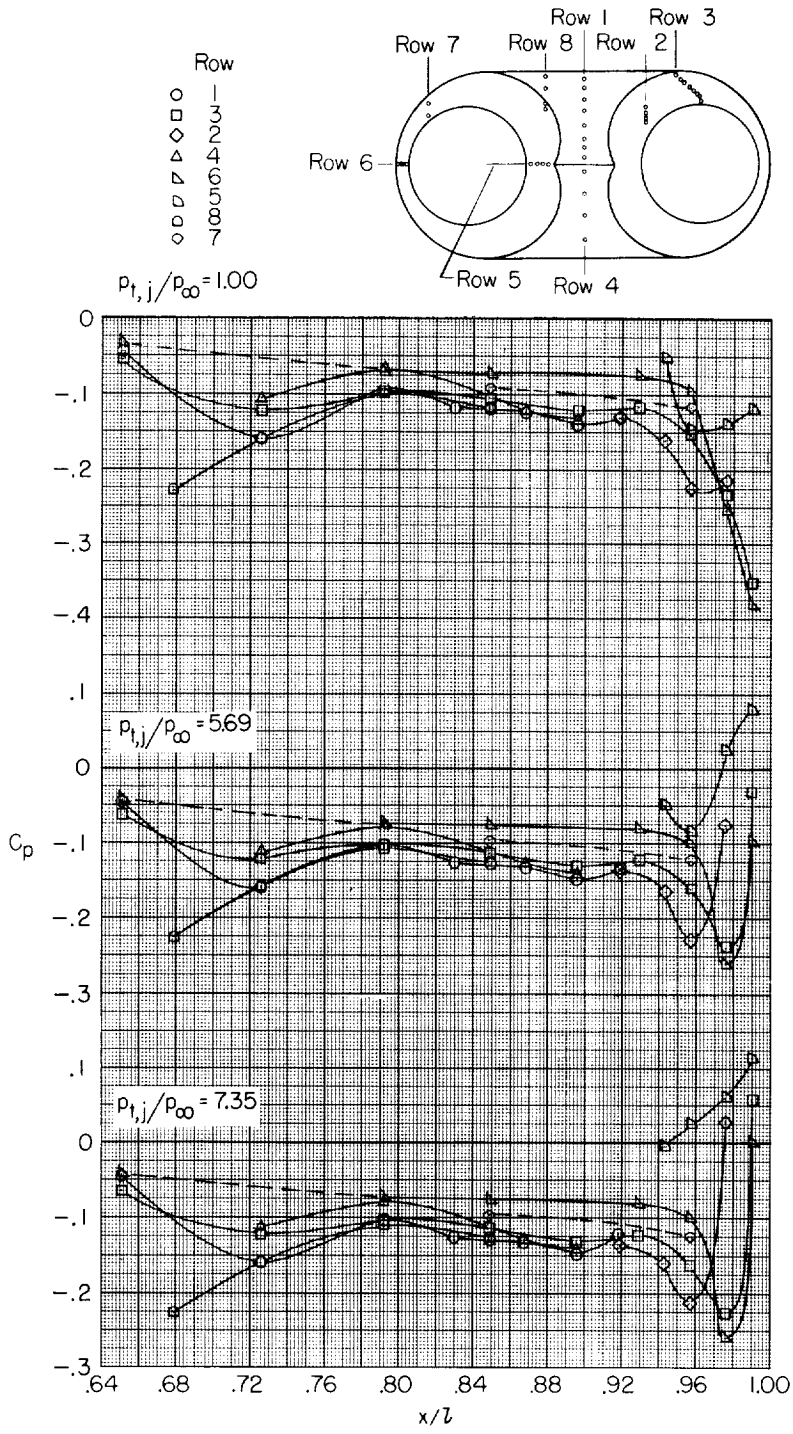

(c) M = 1.30.

Figure 11.- Concluded.

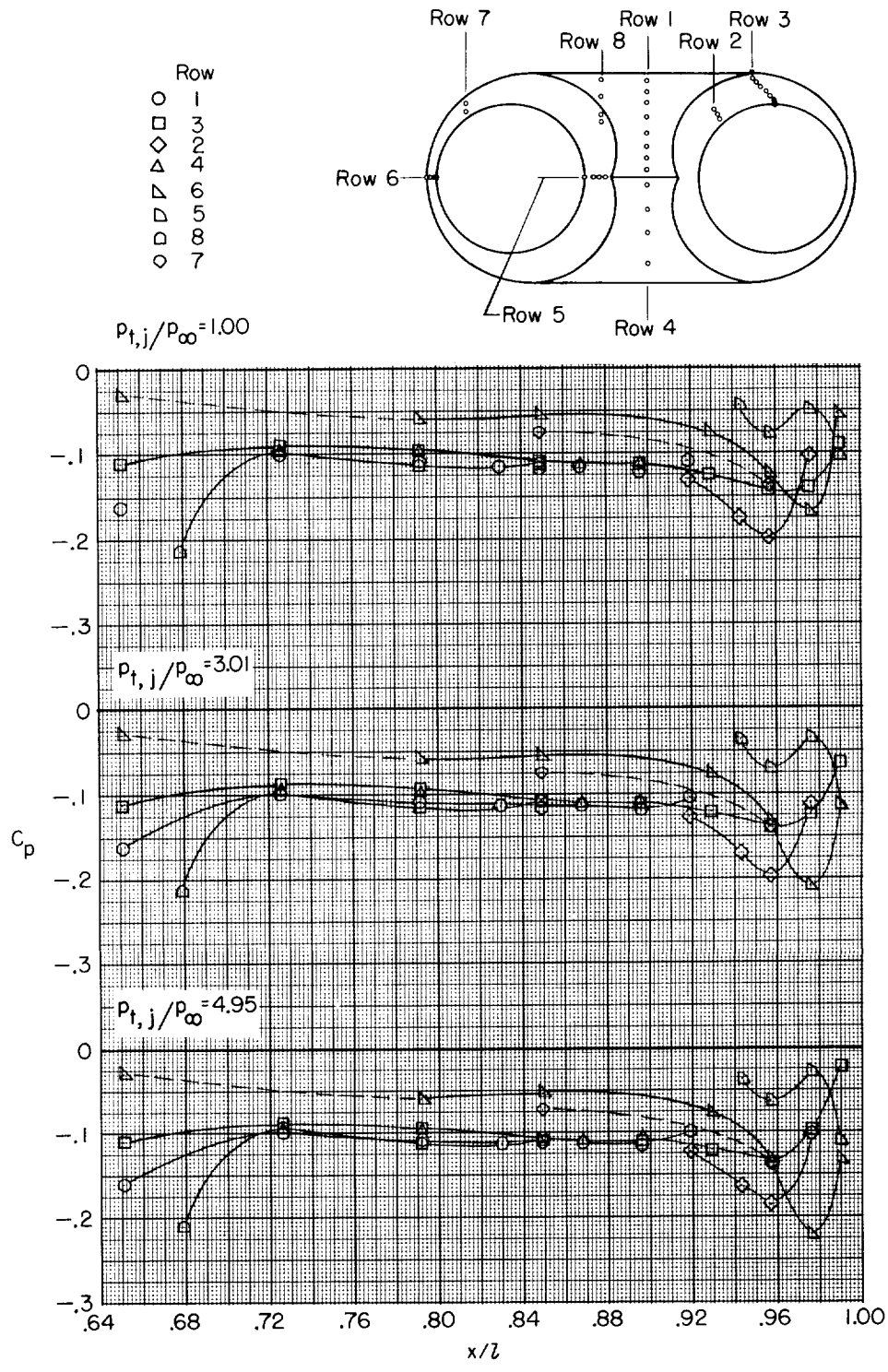

(a) M = 0.60.

Figure 12.- Longitudinal pressure distribution on configuration 4D at several pressure ratios and Mach numbers.

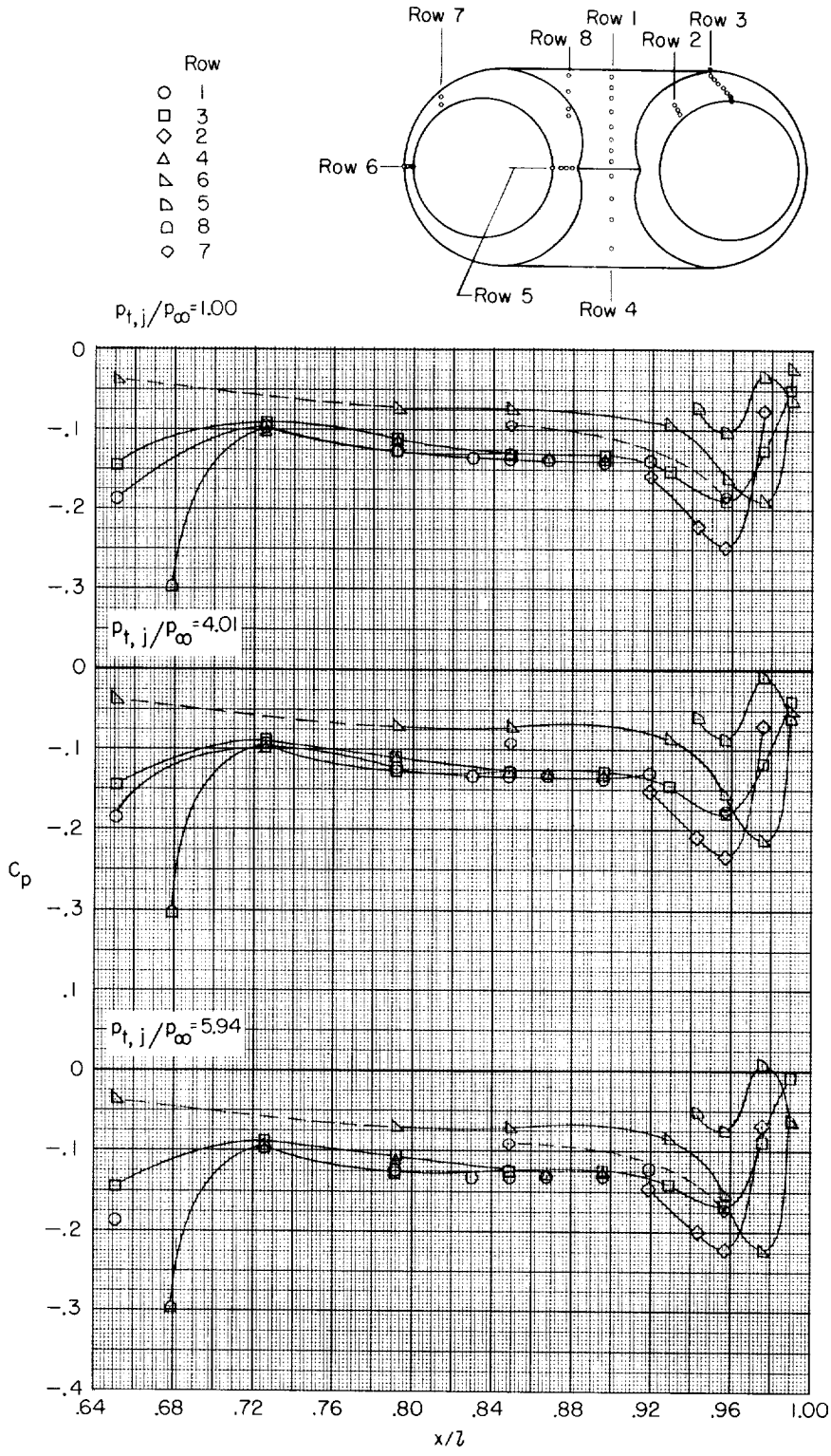

(b) M = 0.90.

Figure 12.- Continued.

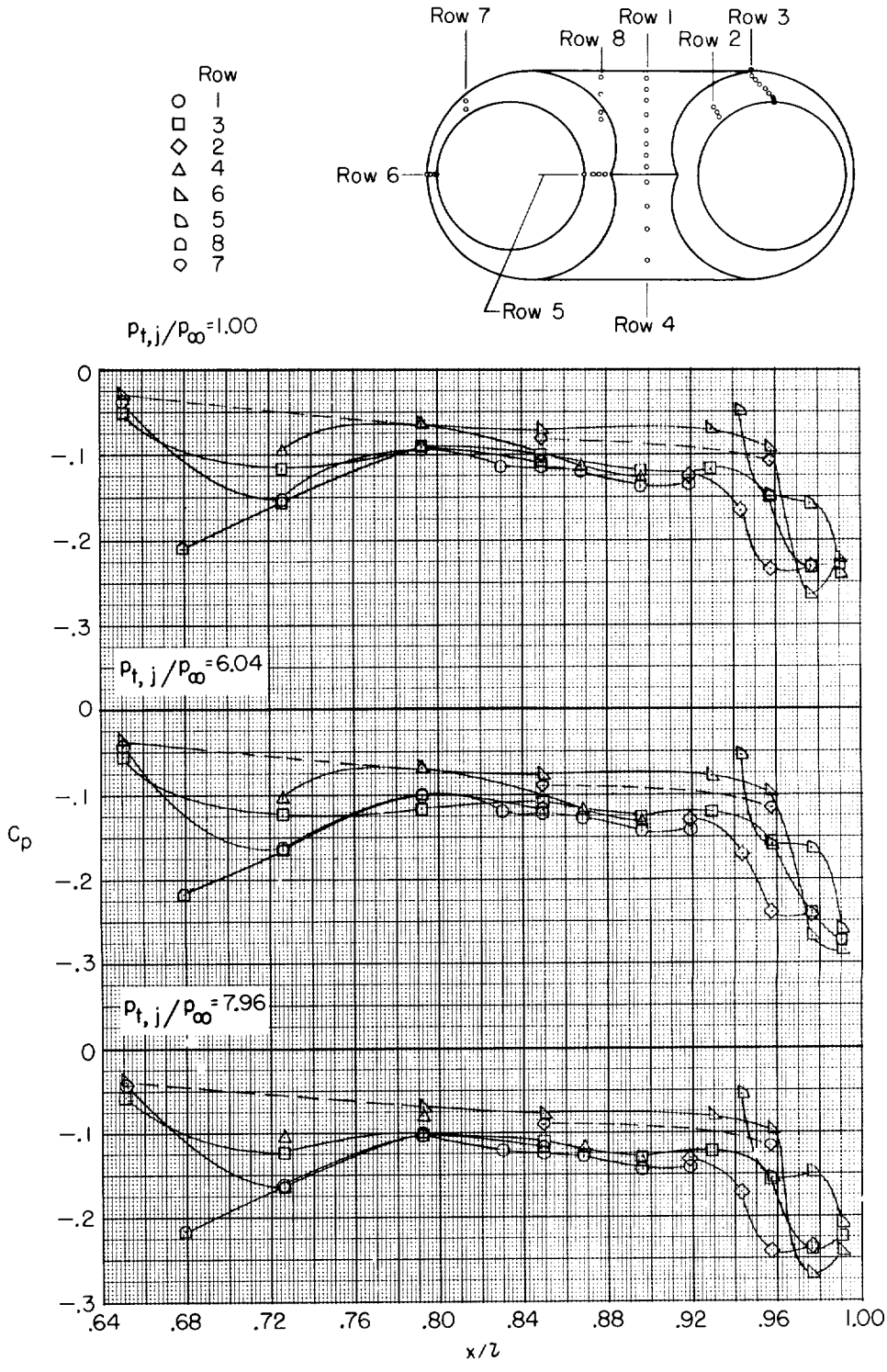

(c) M = 1.30.

Figure 12.- Concluded.

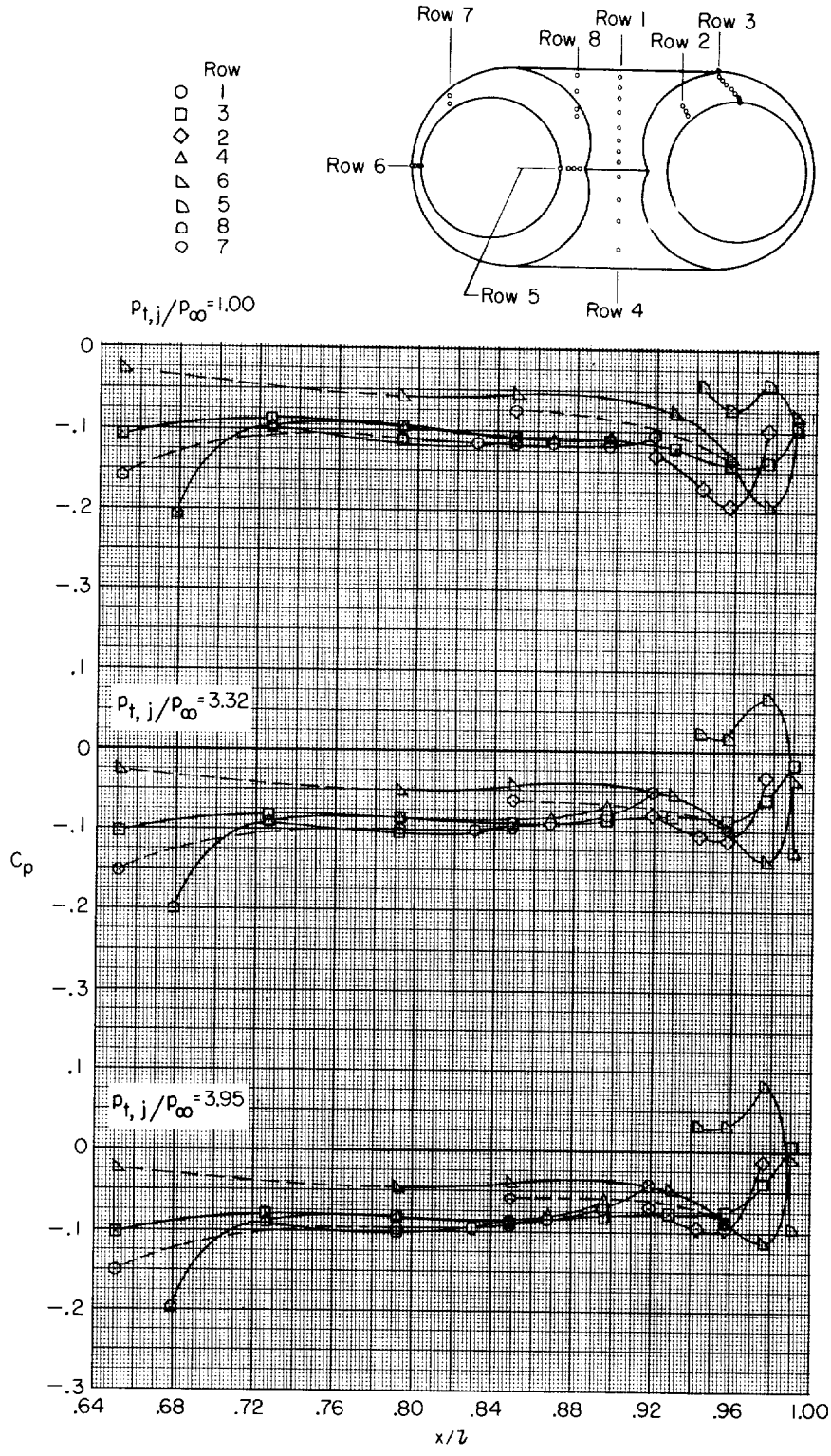

(a) M = 0.60.

Figure 13.- Longitudinal pressure distribution on configuration 4A at several pressure ratios and Mach numbers.

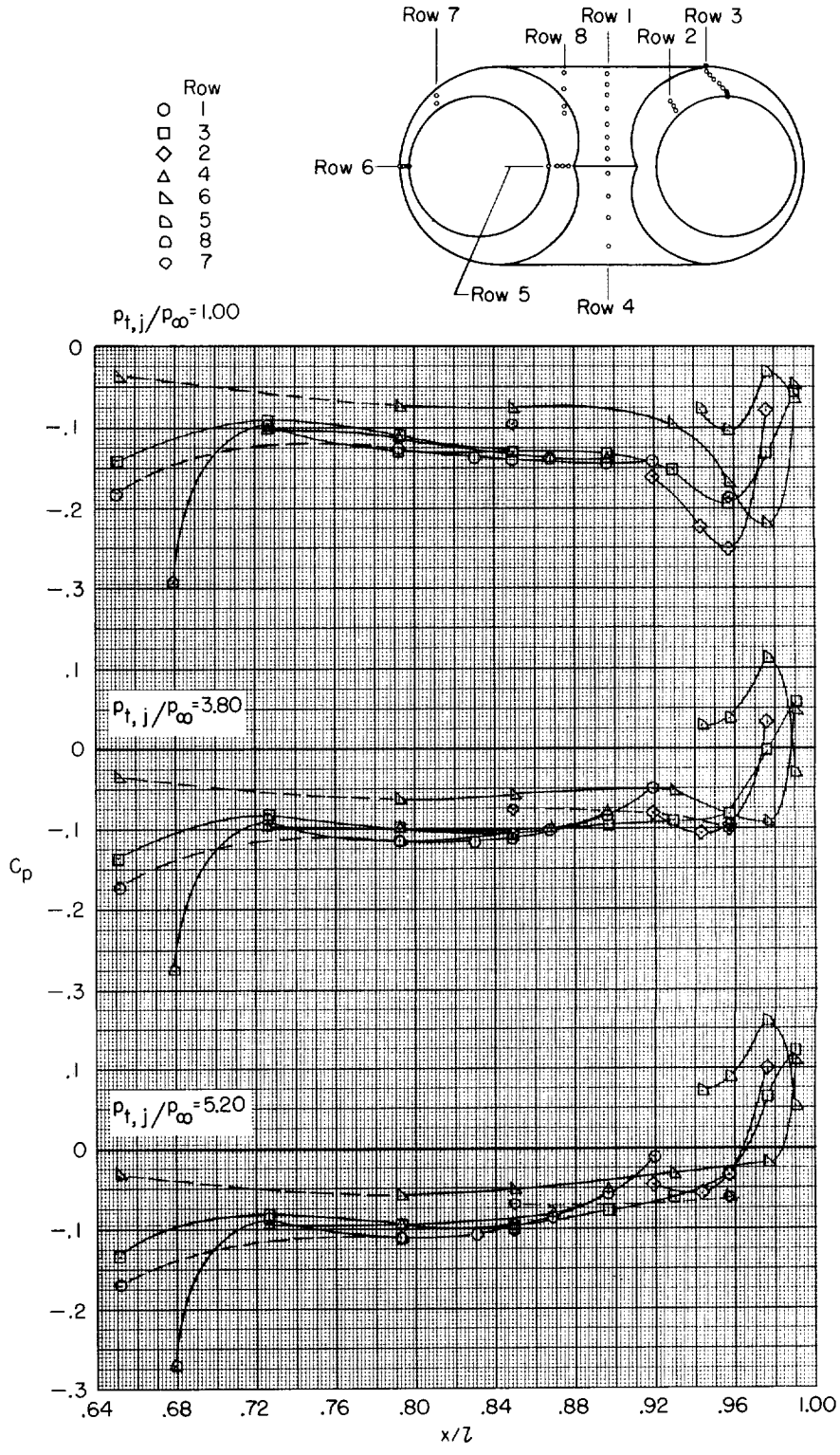

(b) M = 0.90.

Figure 13.- Continued.

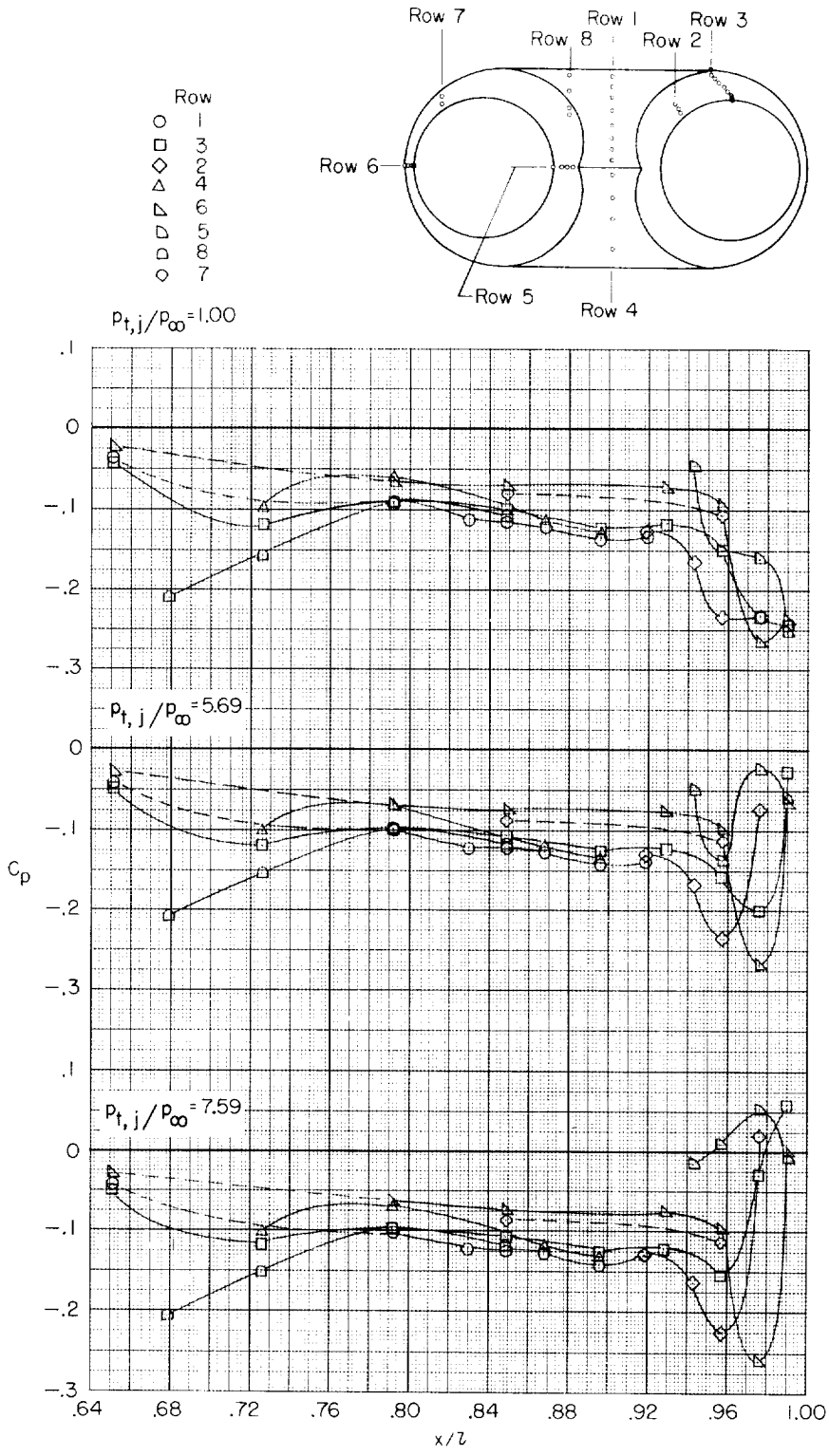

(c) M = 1.30.

Figure 13.- Concluded.

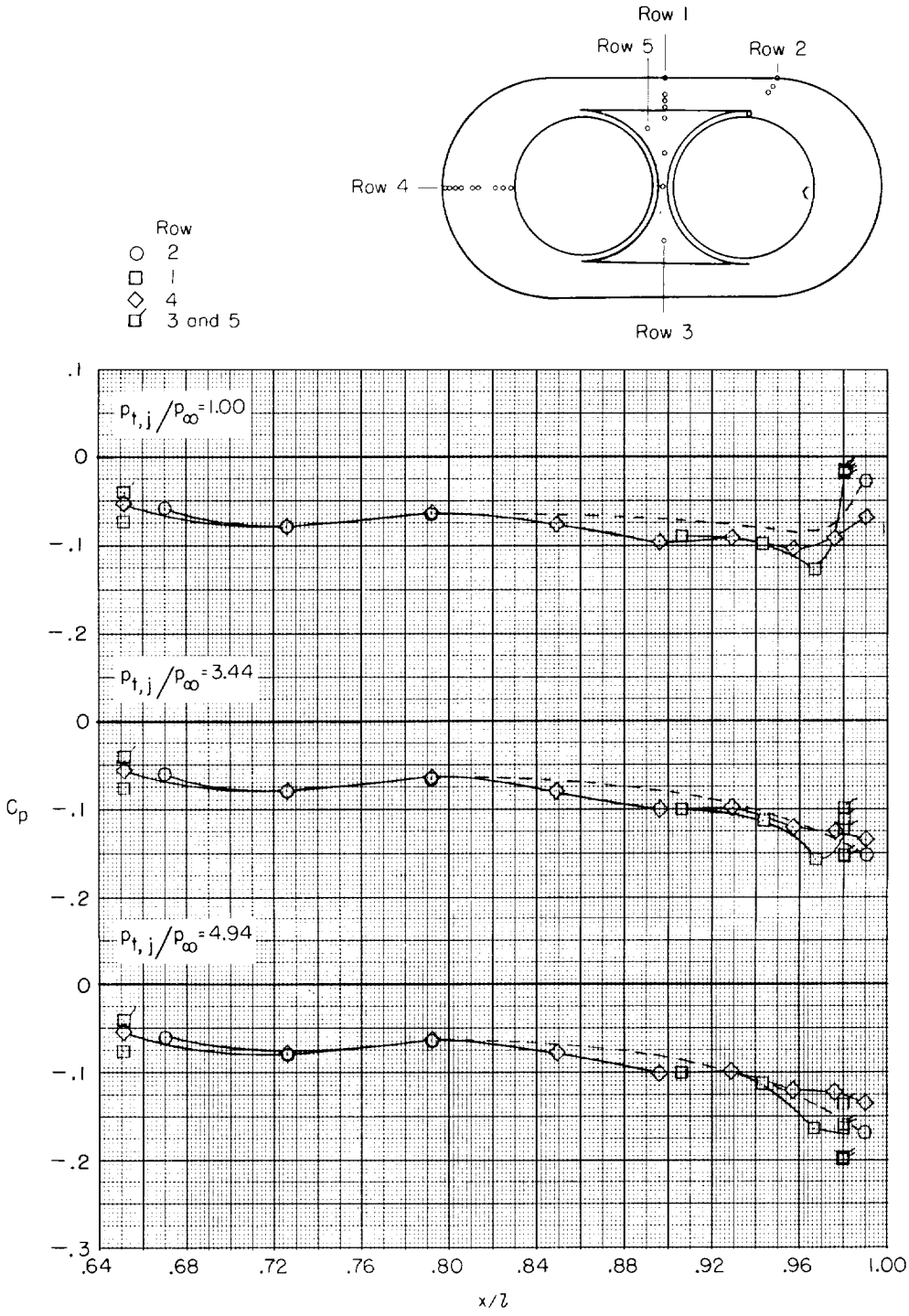

(a) M = 0.60.

Figure 14.- Longitudinal pressure distribution on configuration 5D at several pressure ratios and Mach numbers.

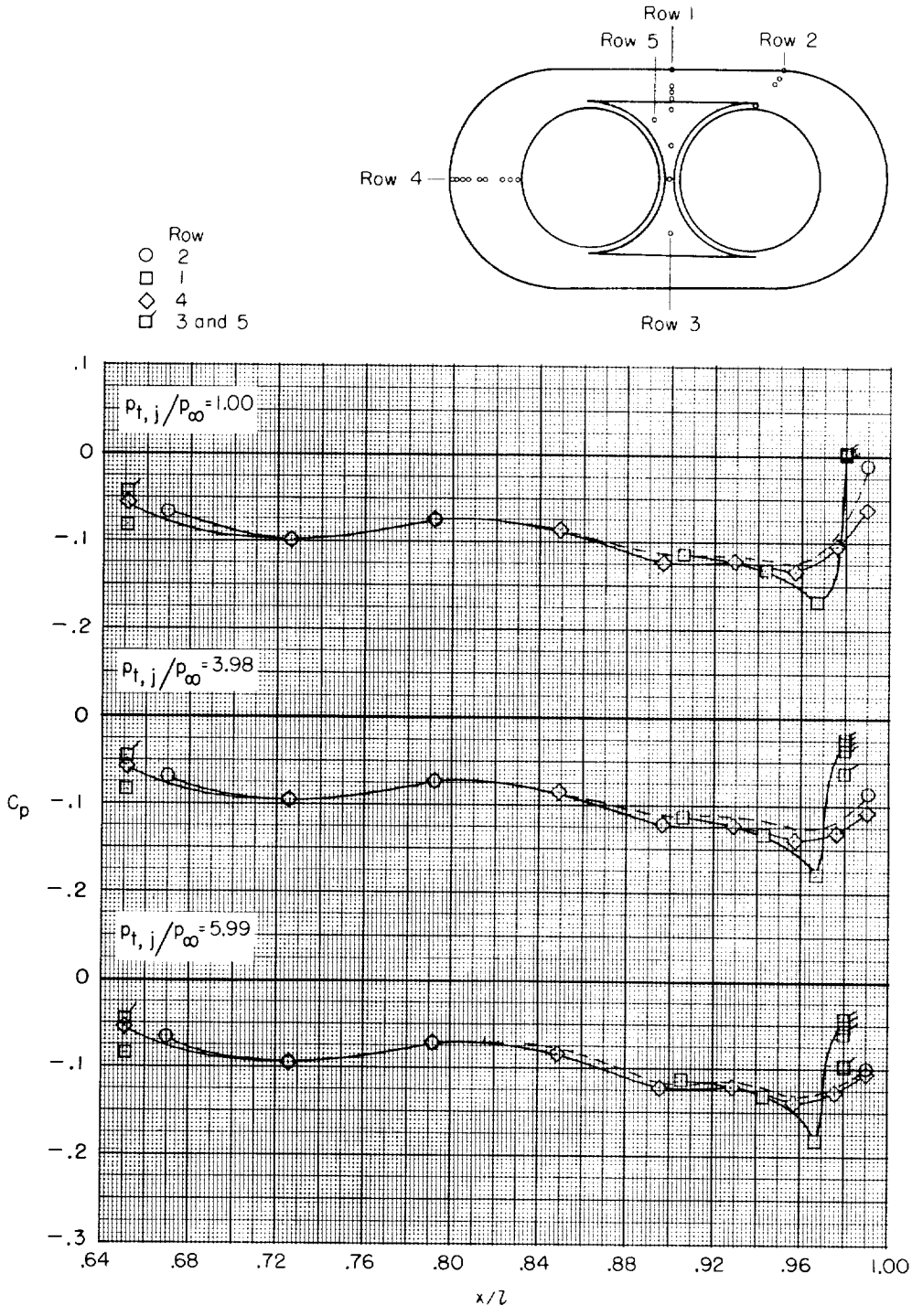

(b) M = 0.90.

Figure 14.- Continued.

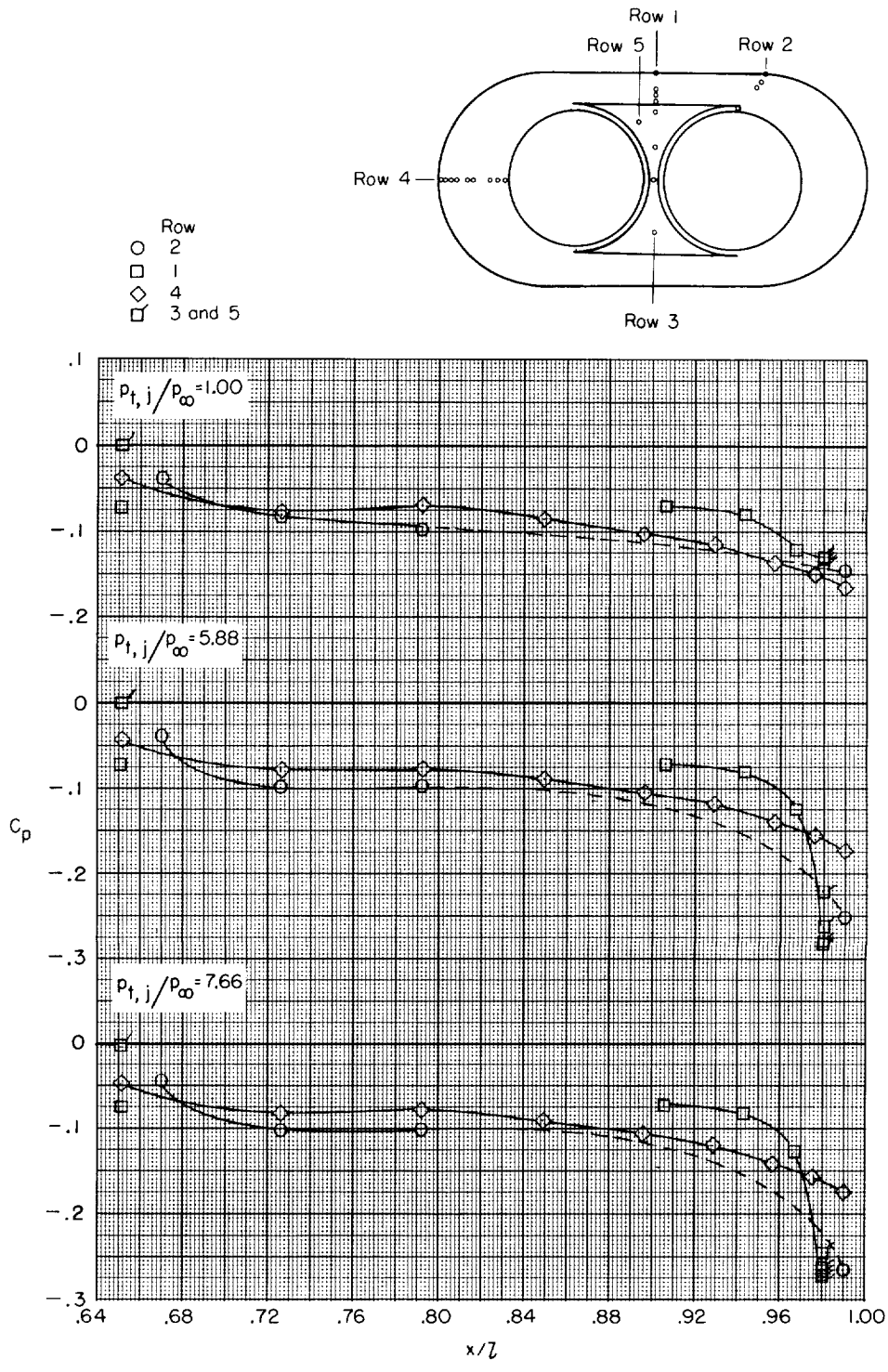

(c) M = 1.30.

Figure 14.- Concluded.

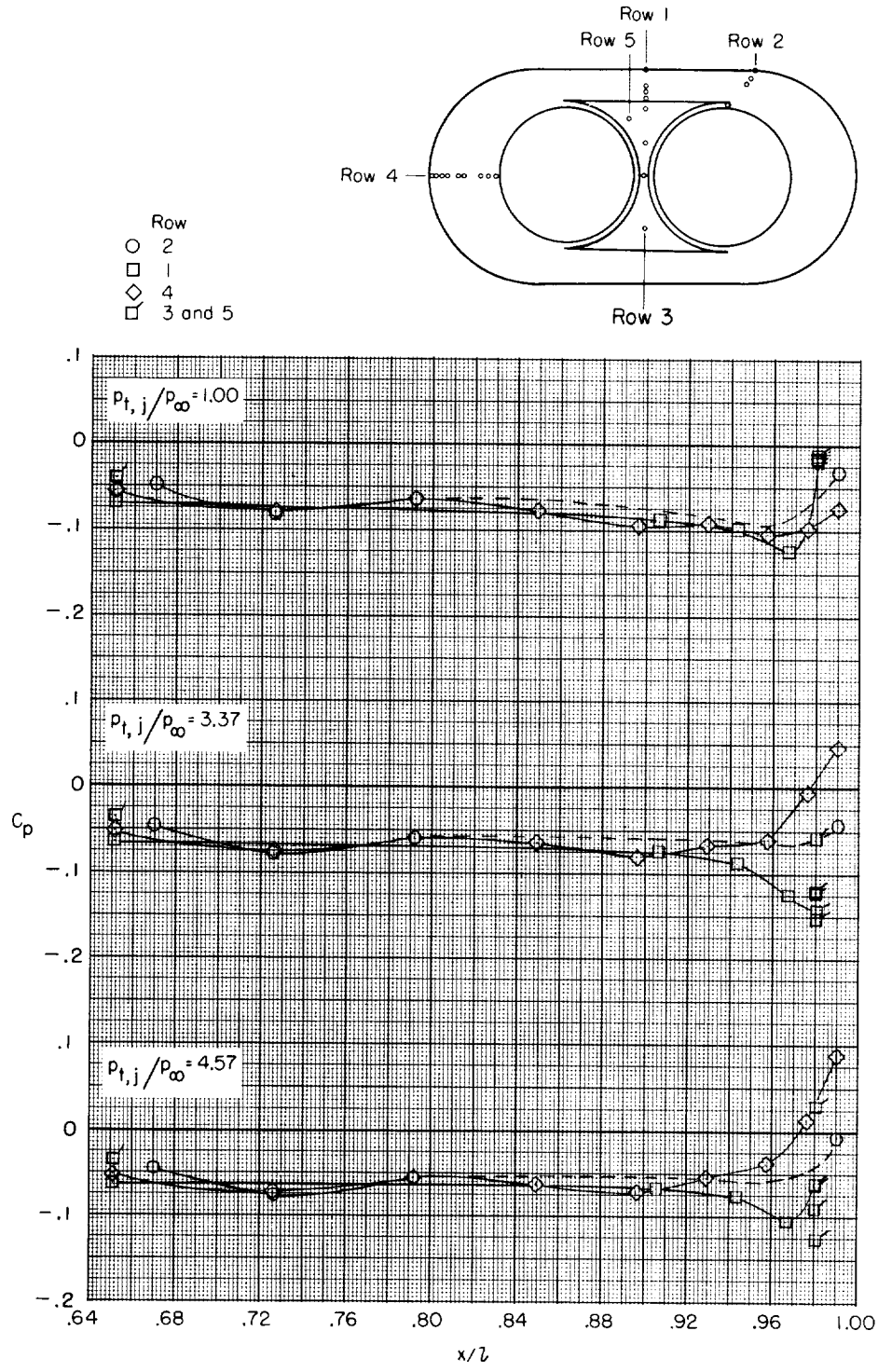

(a) M = 0.60.

Figure 15.- Longitudinal pressure distribution on configuration 5A at several pressure ratios and Mach numbers.

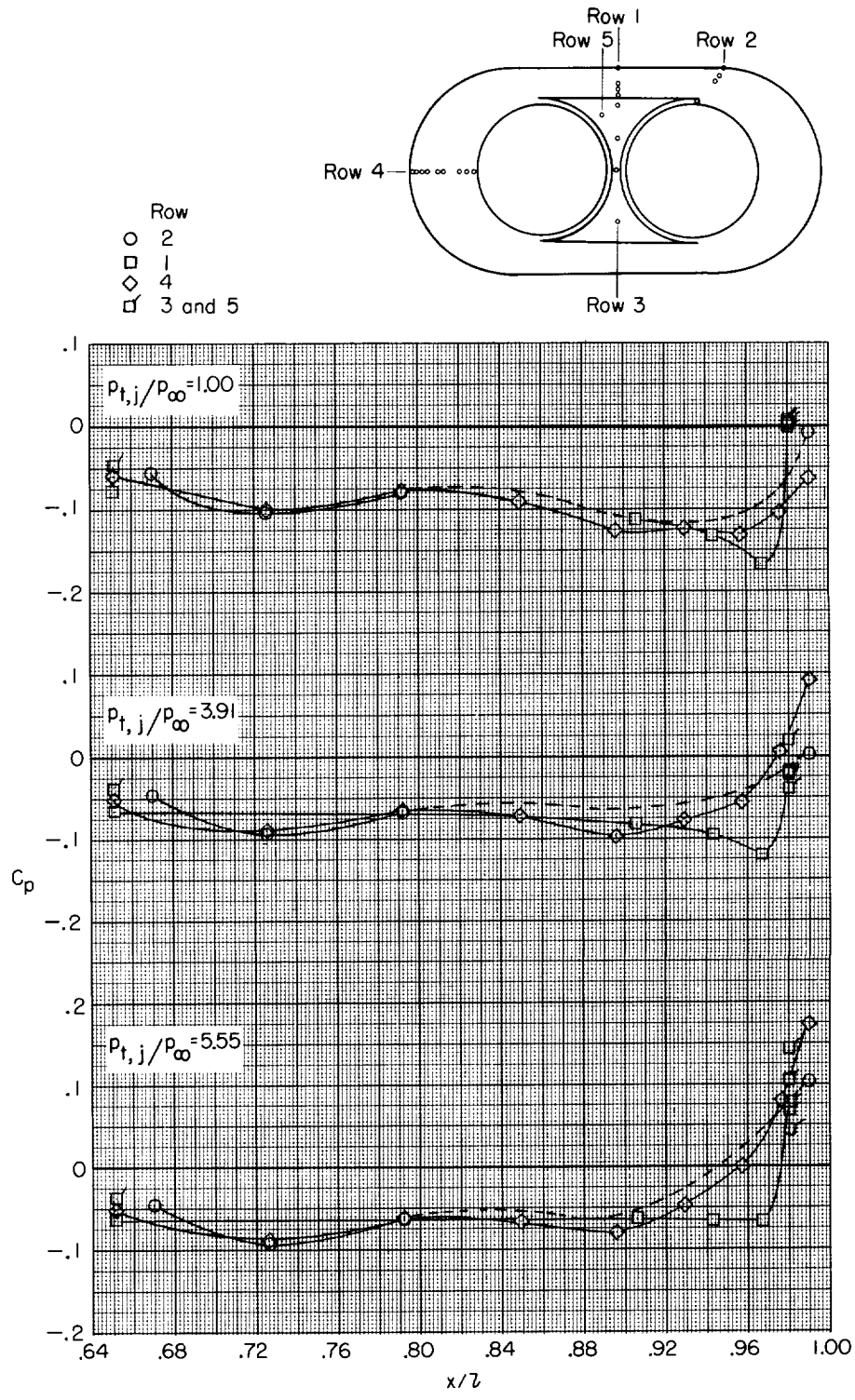

(b) M = 0.90.

Figure 15.- Continued.

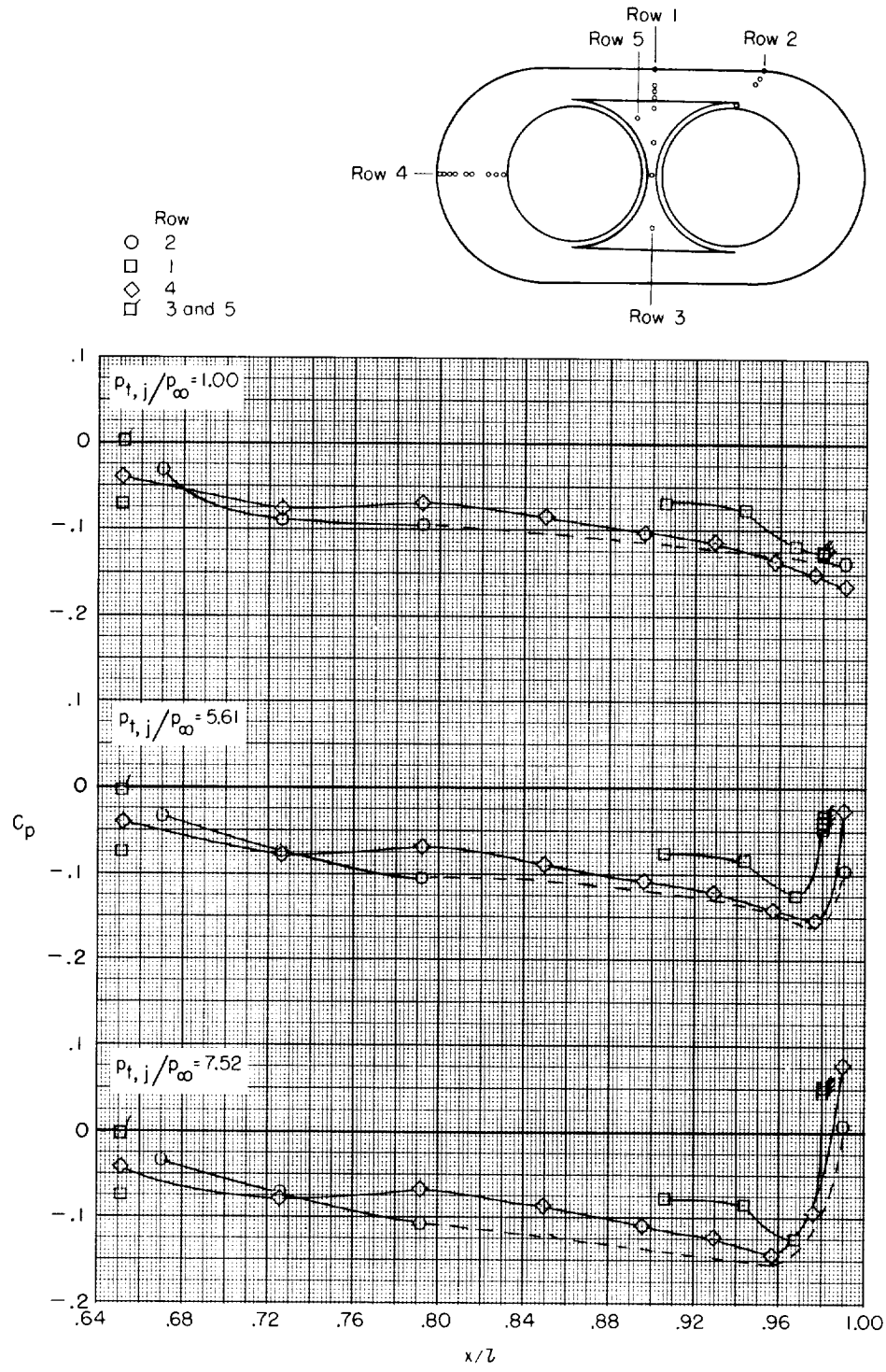

(c) M = 1.30.

Figure 15.- Concluded.

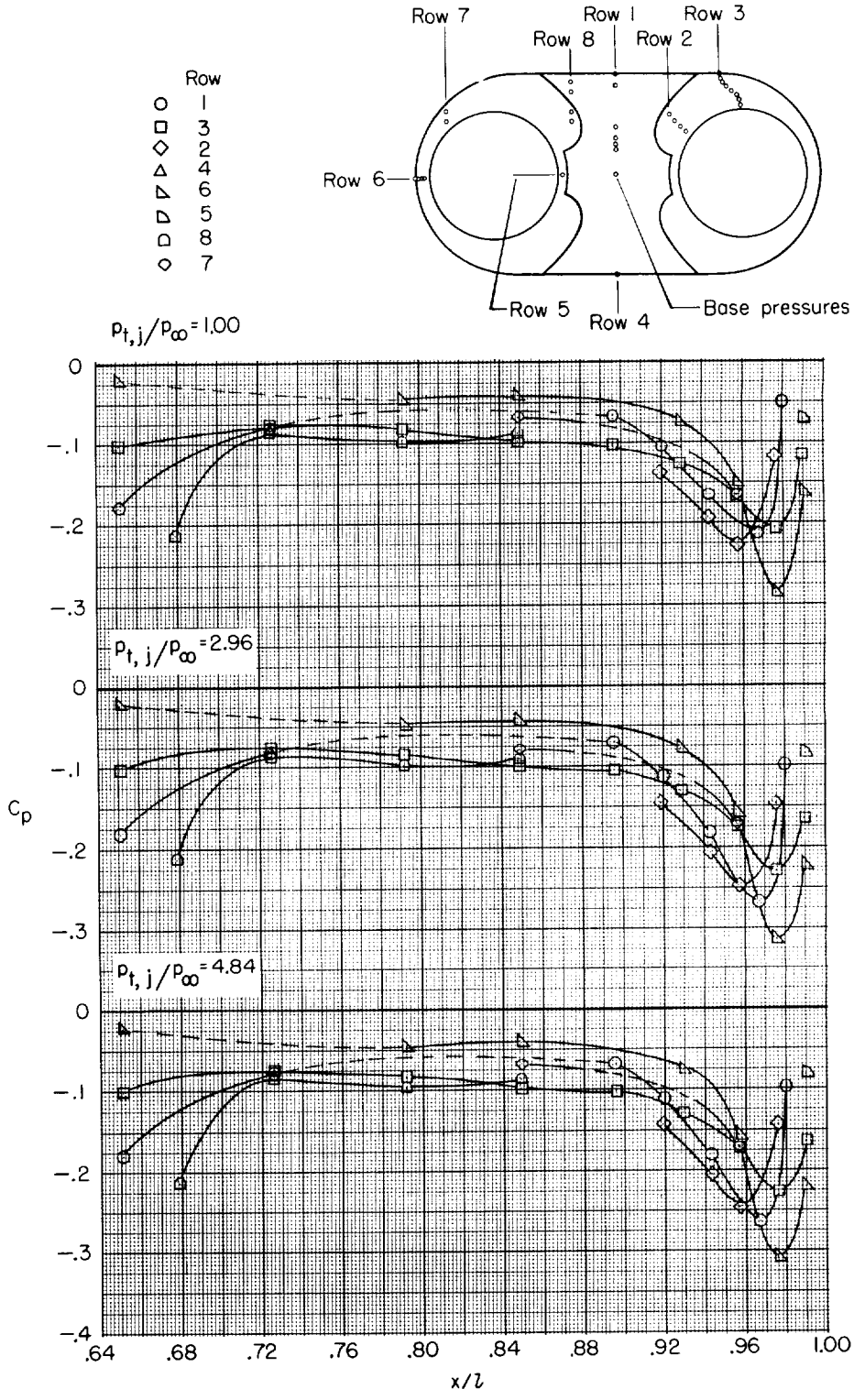

(a) M = 0.60.

Figure 16.- Longitudinal pressure distribution on configuration 6D at several pressure ratios and Mach numbers.

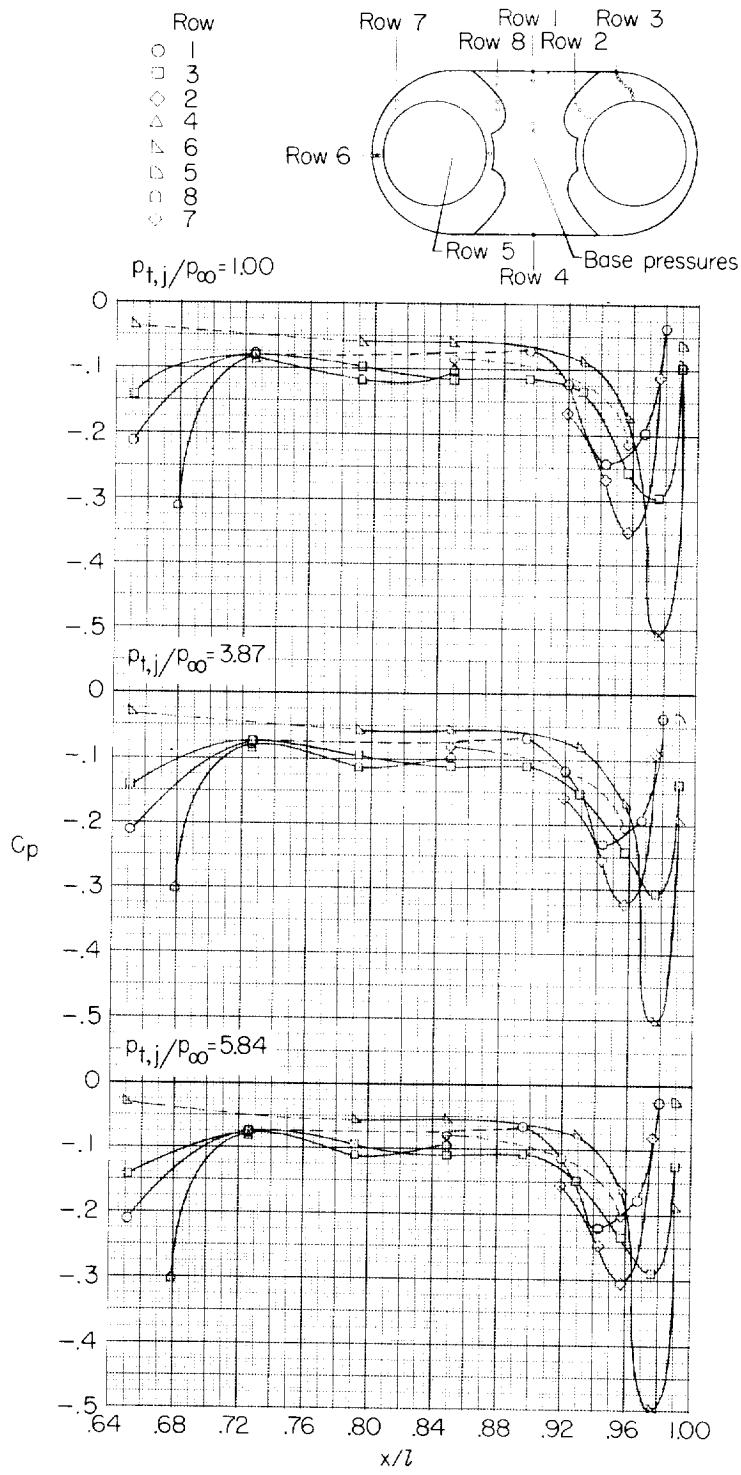

(b) M = 0.90.

Figure 16.- Continued.

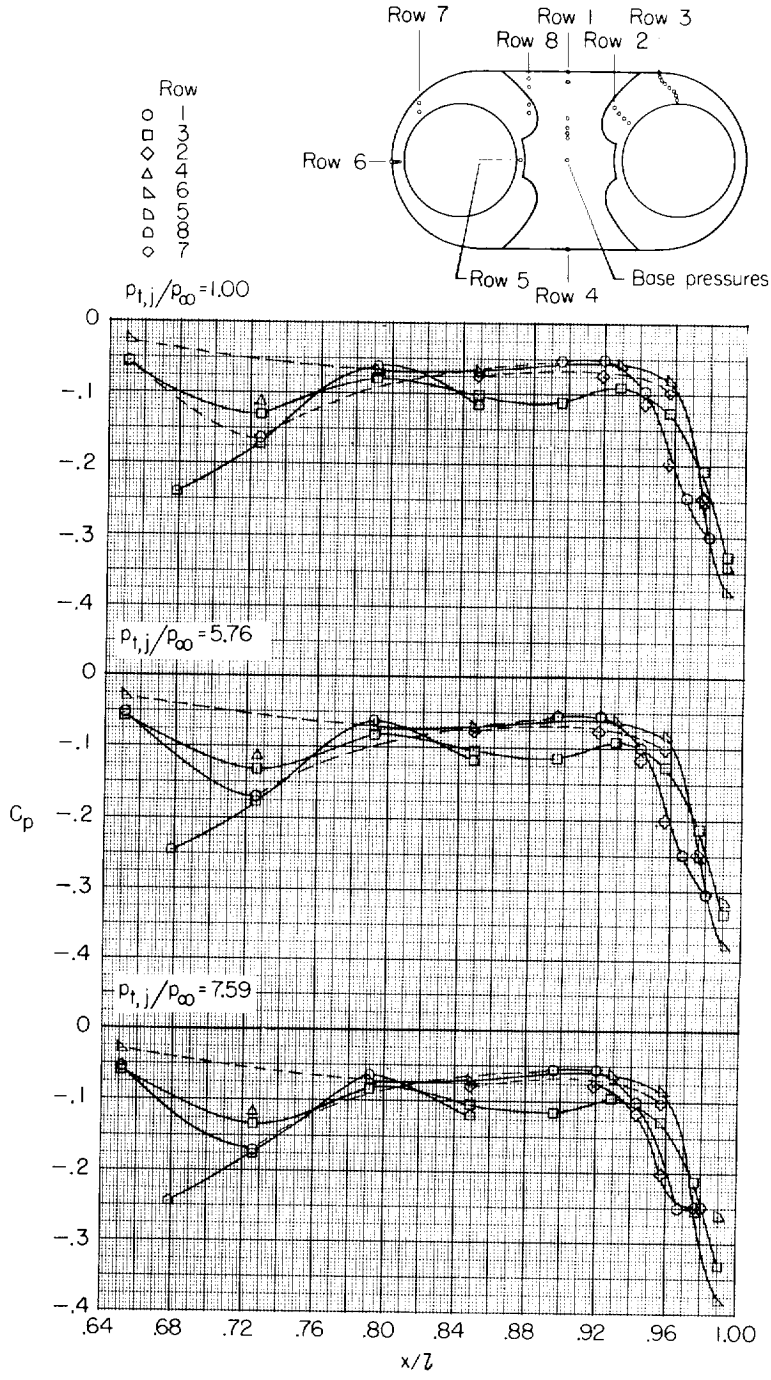

(c) M = 1.30.

Figure 16.- Concluded.

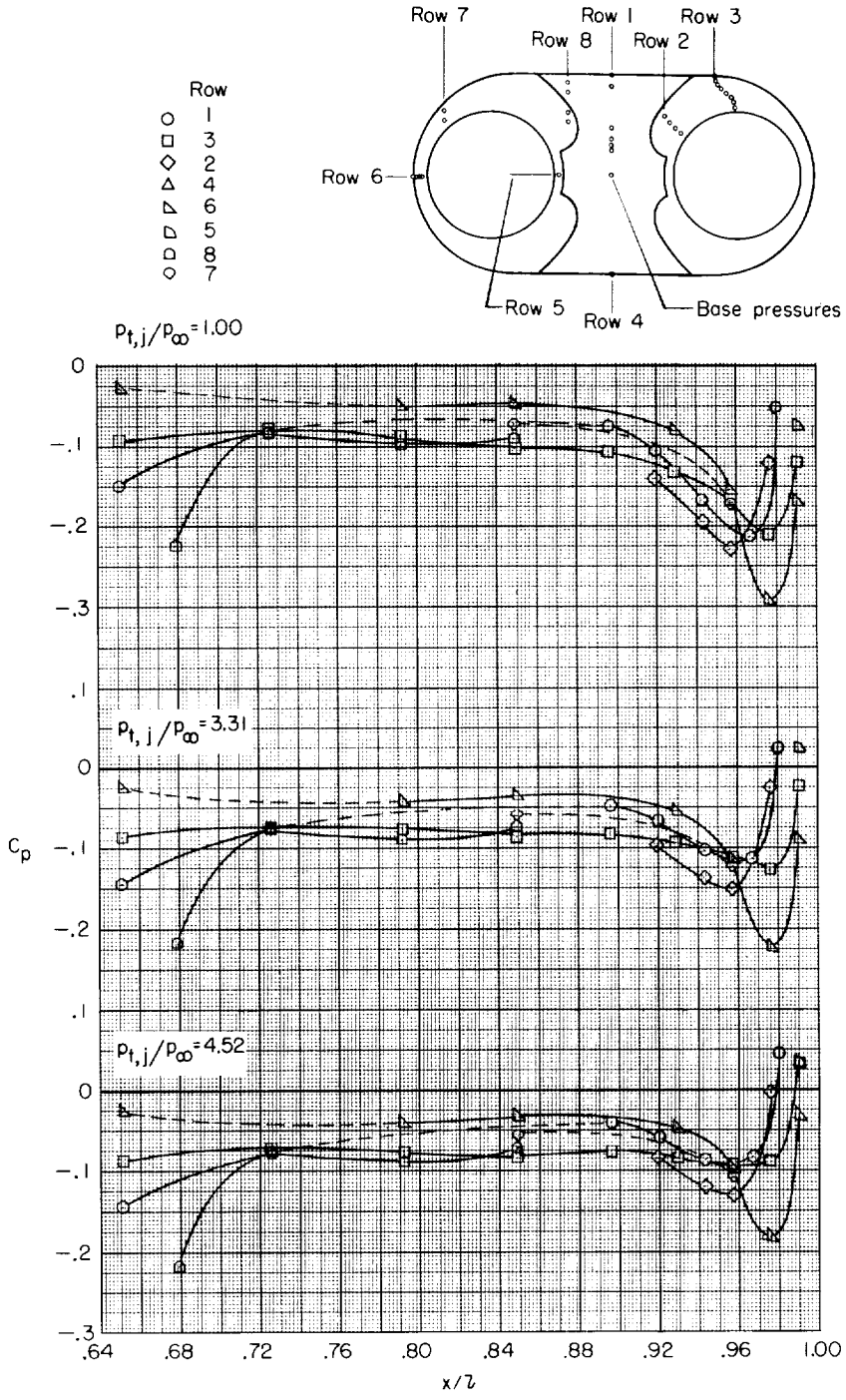

(a) M = 0.60.

Figure 17.- Longitudinal pressure distribution on configuration 6A at several pressure ratios and Mach numbers.

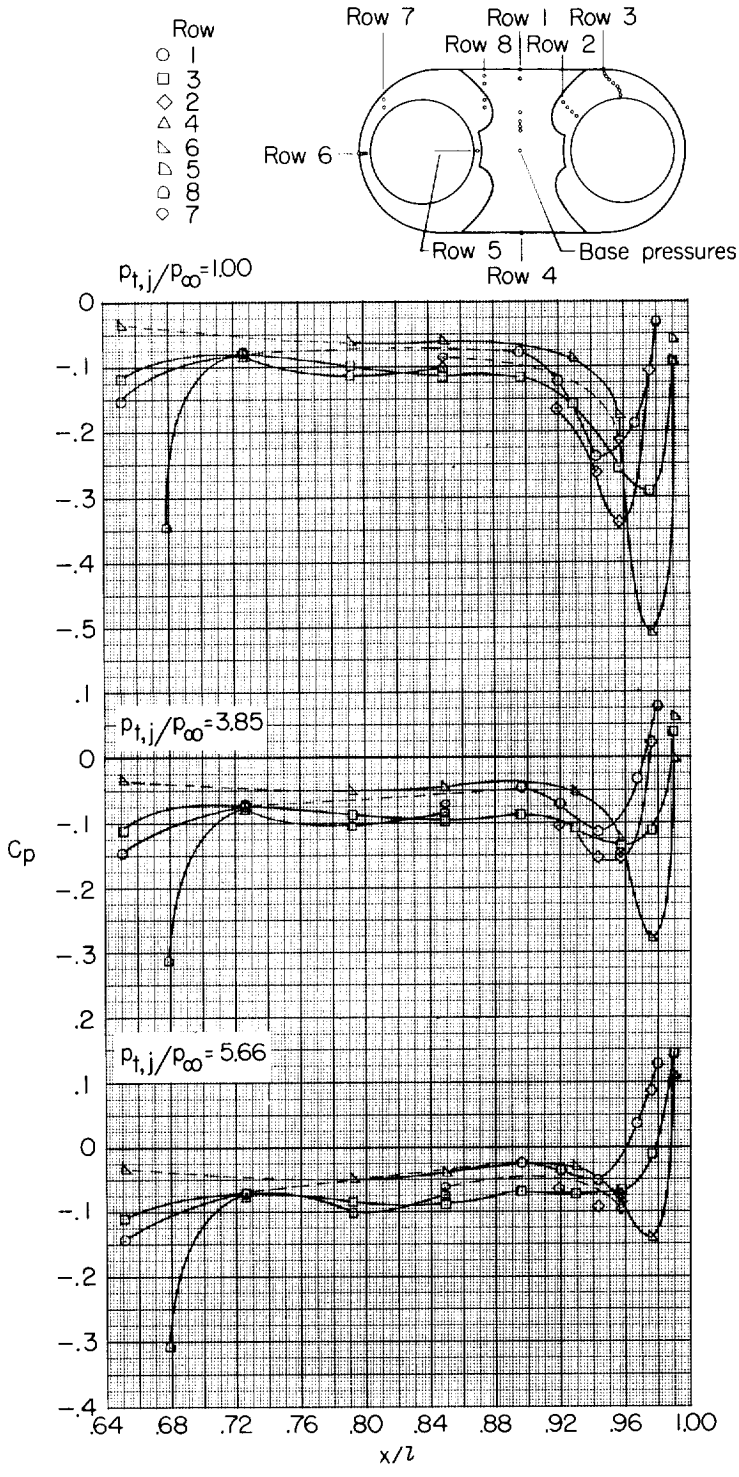

(b) M = 0.90.

Figure 17.- Continued.

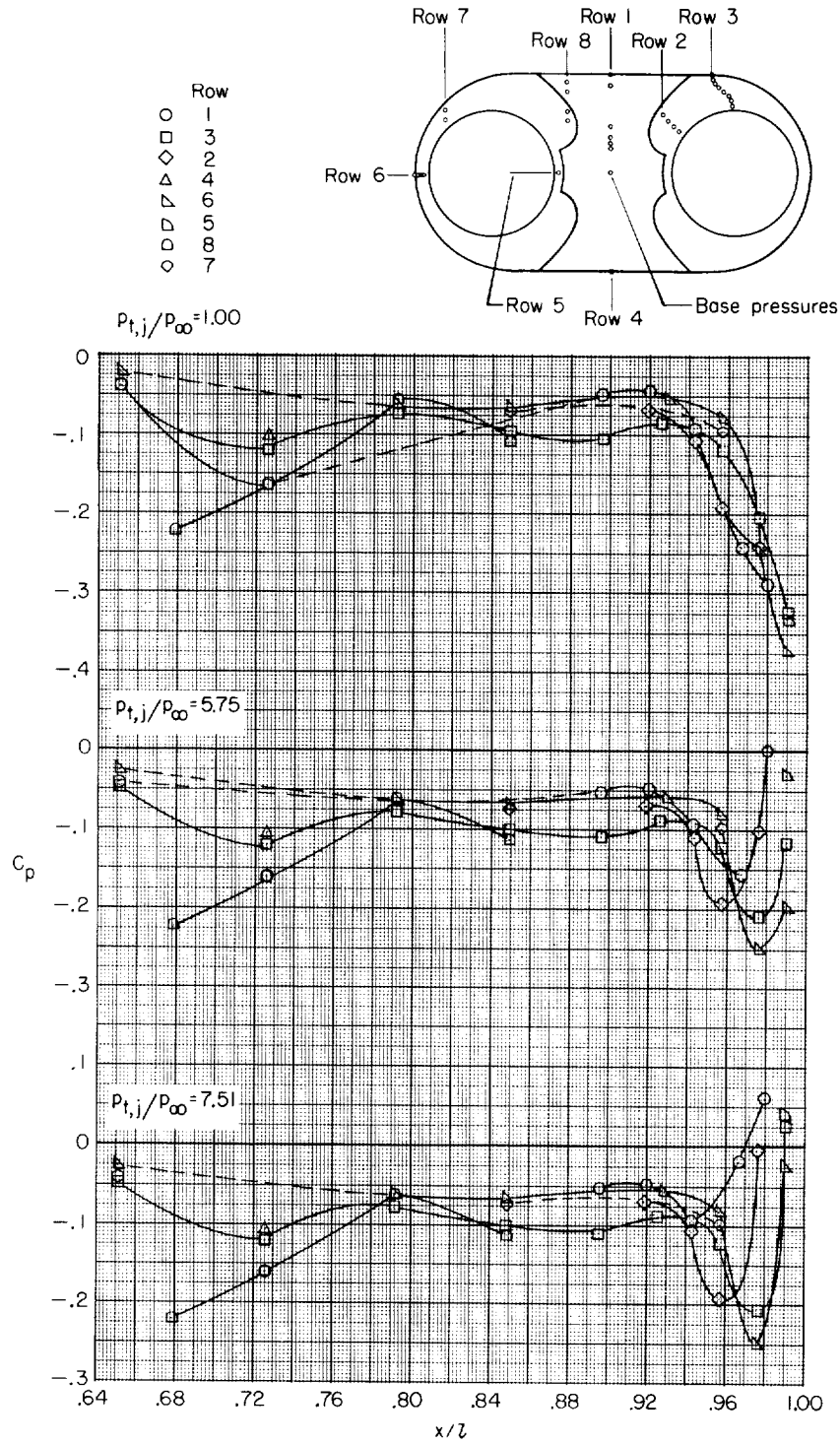

(c) M = 1.30.

Figure 17.- Concluded.

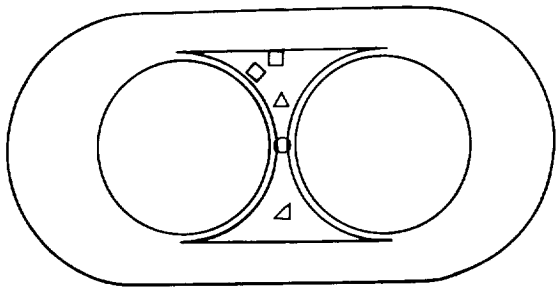

Base-pressure orifice locations

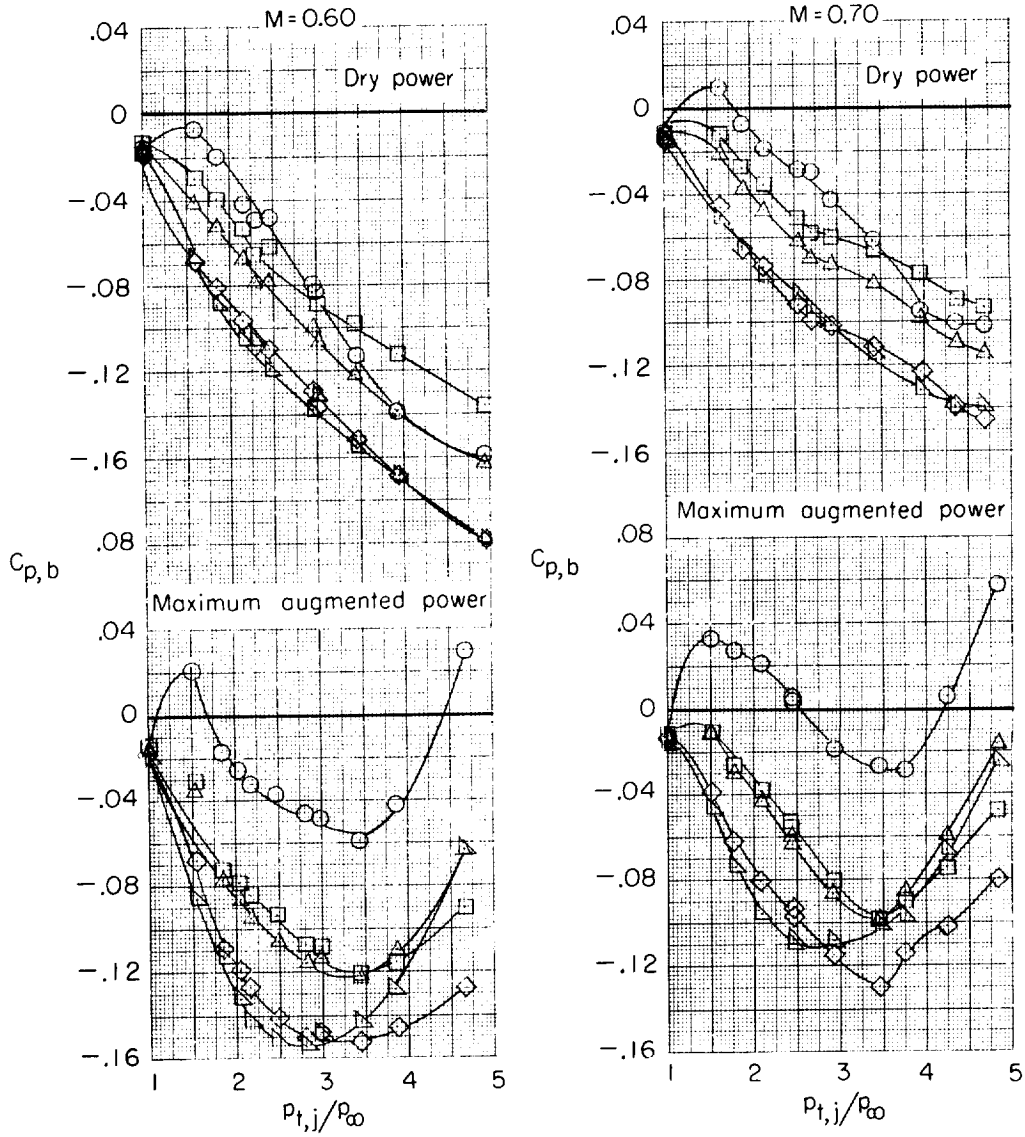

(a) M = 0.60 and 0.70; afterbody configuration 5.

Figure 18.- Variation of base-pressure coefficient with jet-total-pressure ratio at several Mach numbers for blunt-base afterbody configurations 5 and 6.

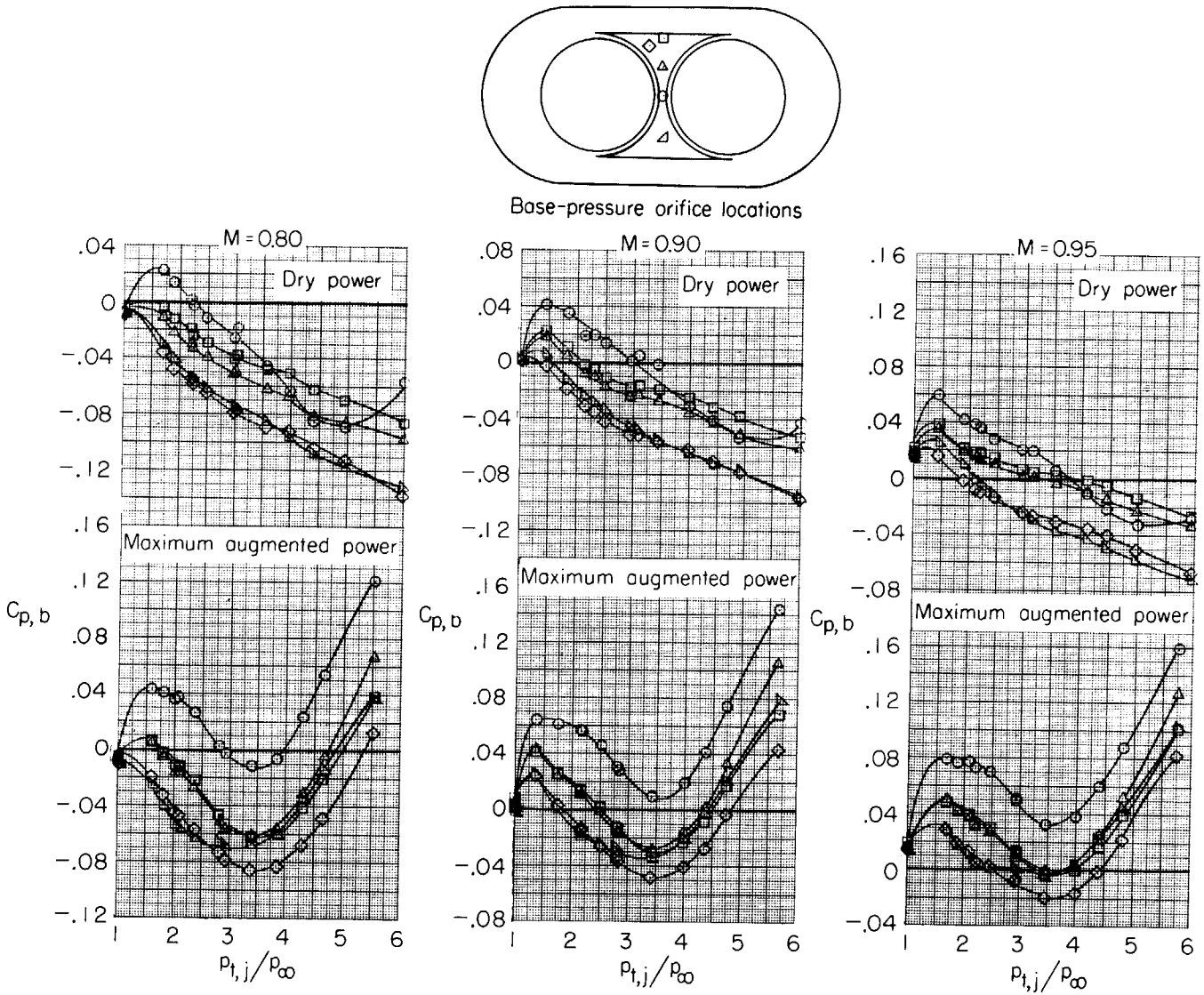

(b) M = 0.80, 0.90, and 0.95; afterbody configuration 5.

Figure 18.- Continued.

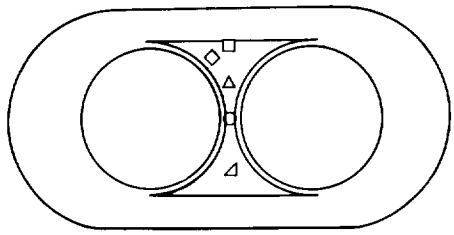

Base-pressure orifice locations

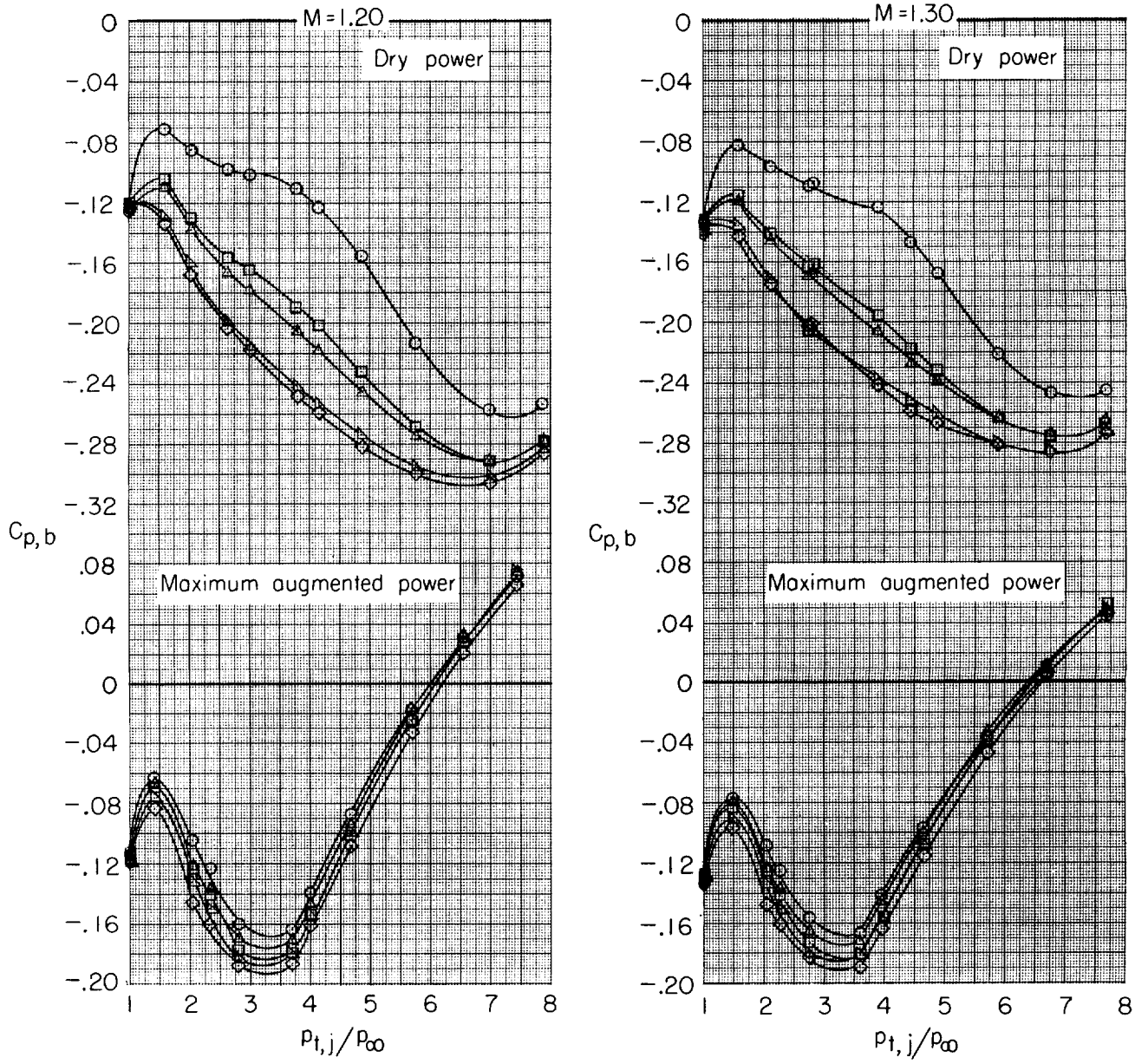

(c) M = 1.20 and 1.30; afterbody configuration 5.

Figure 18.- Continued.

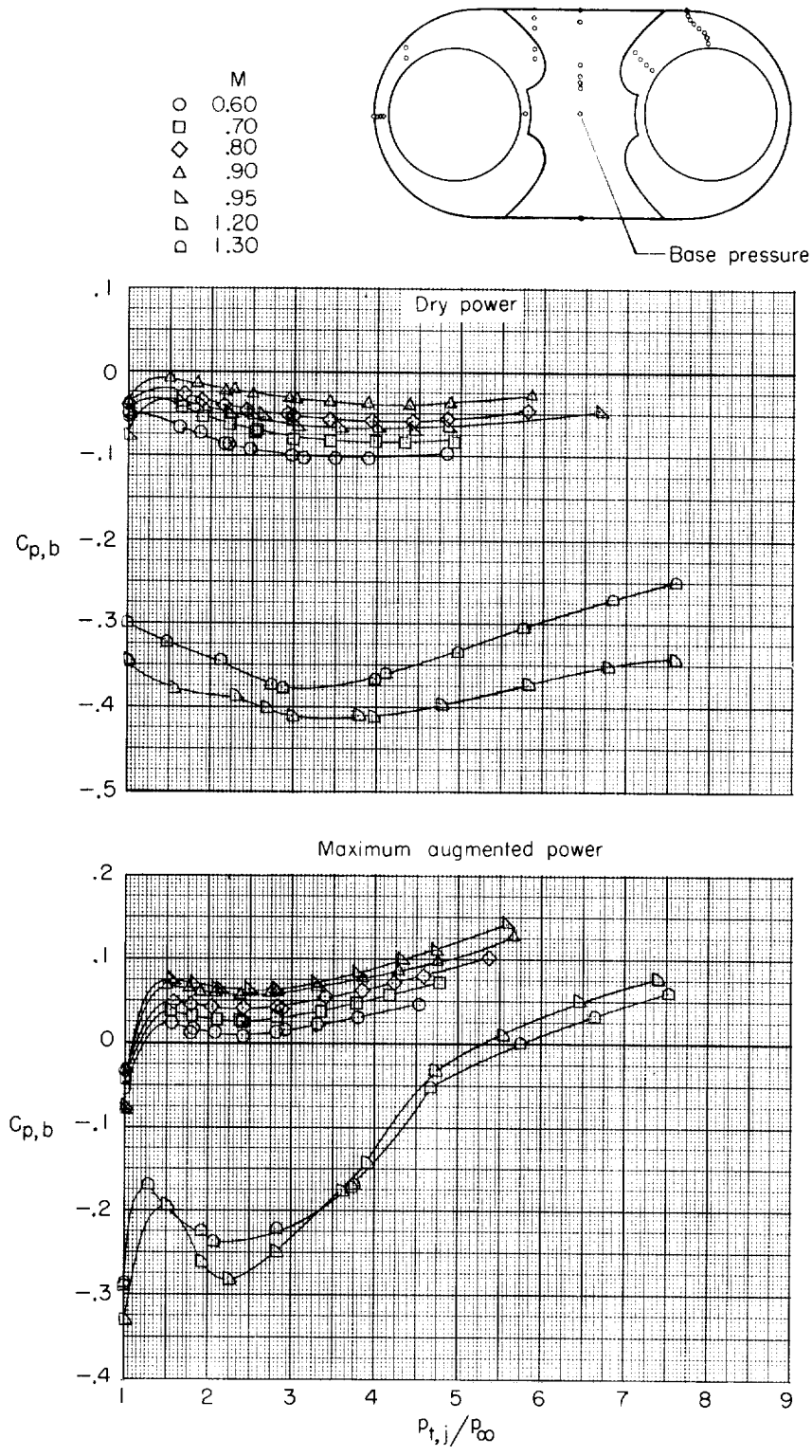

(d) Afterbody configuration 6.

Figure 18.- Continued.

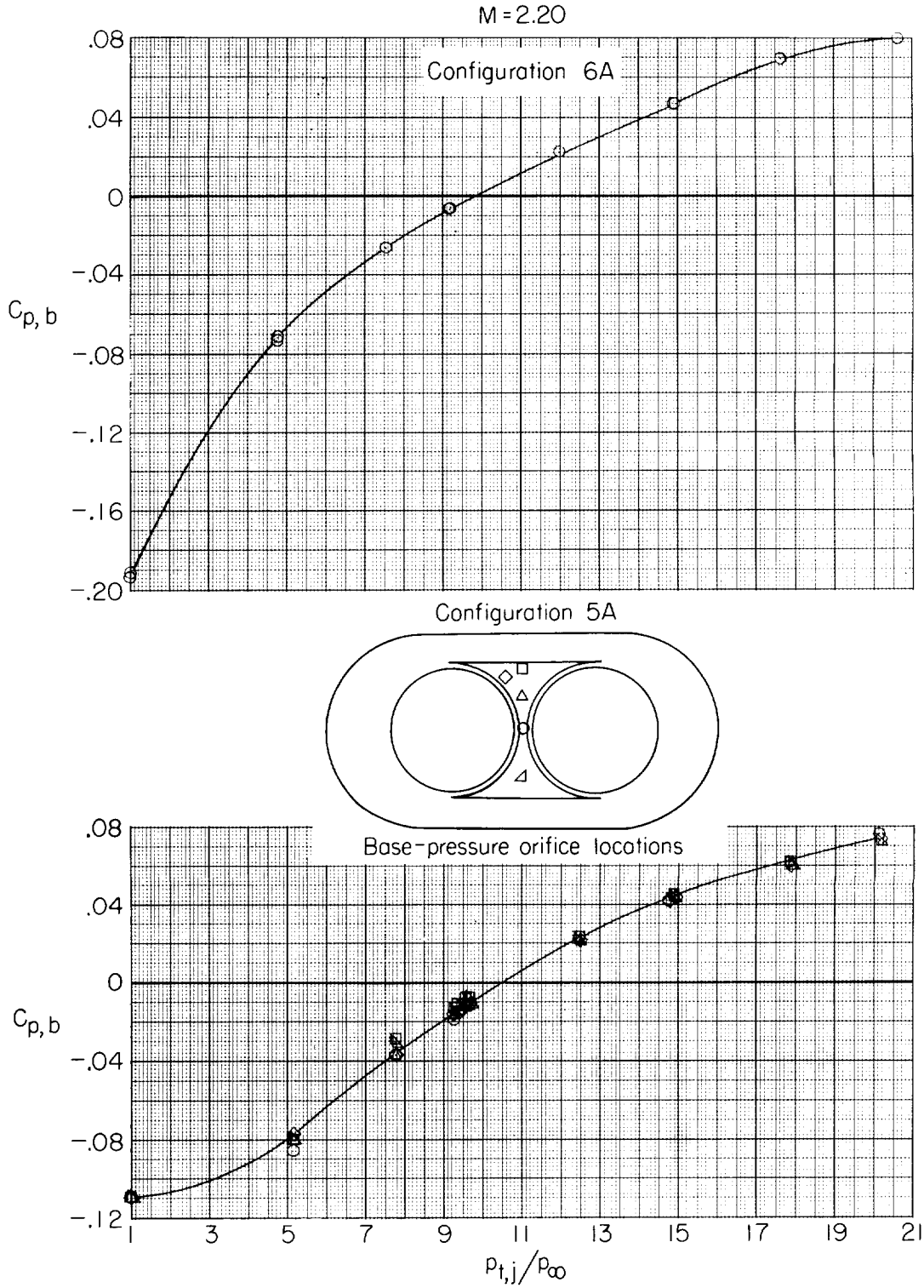

(e) M = 2.20; afterbody configurations 5 and 6.

Figure 18.- Concluded.

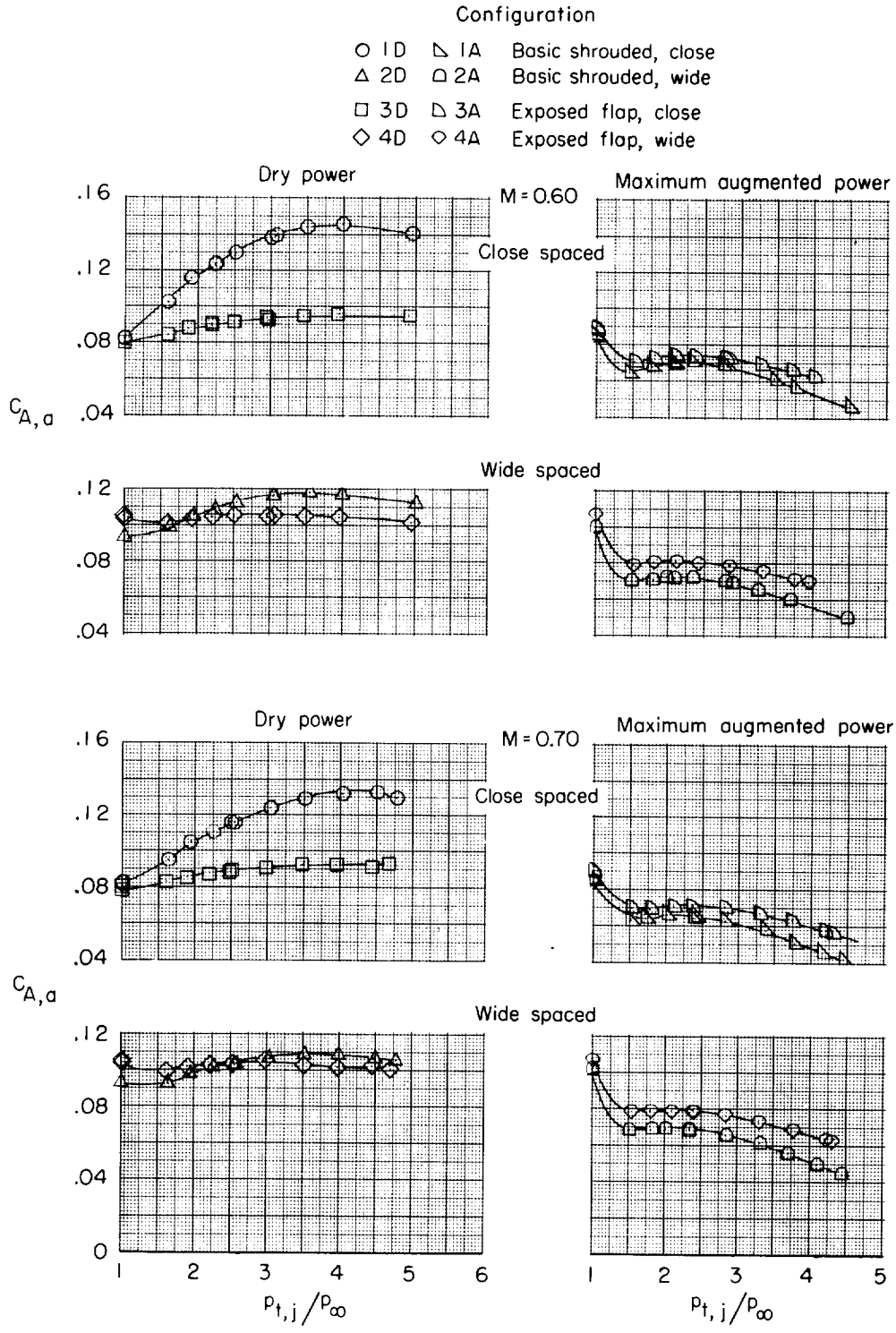

(a) M = 0.60 and 0.70.

Figure 19.- Variation of afterbody axial-force coefficient with jet-total-pressure ratio for afterbody configurations 1, 2, 3, and 4 at both power settings.

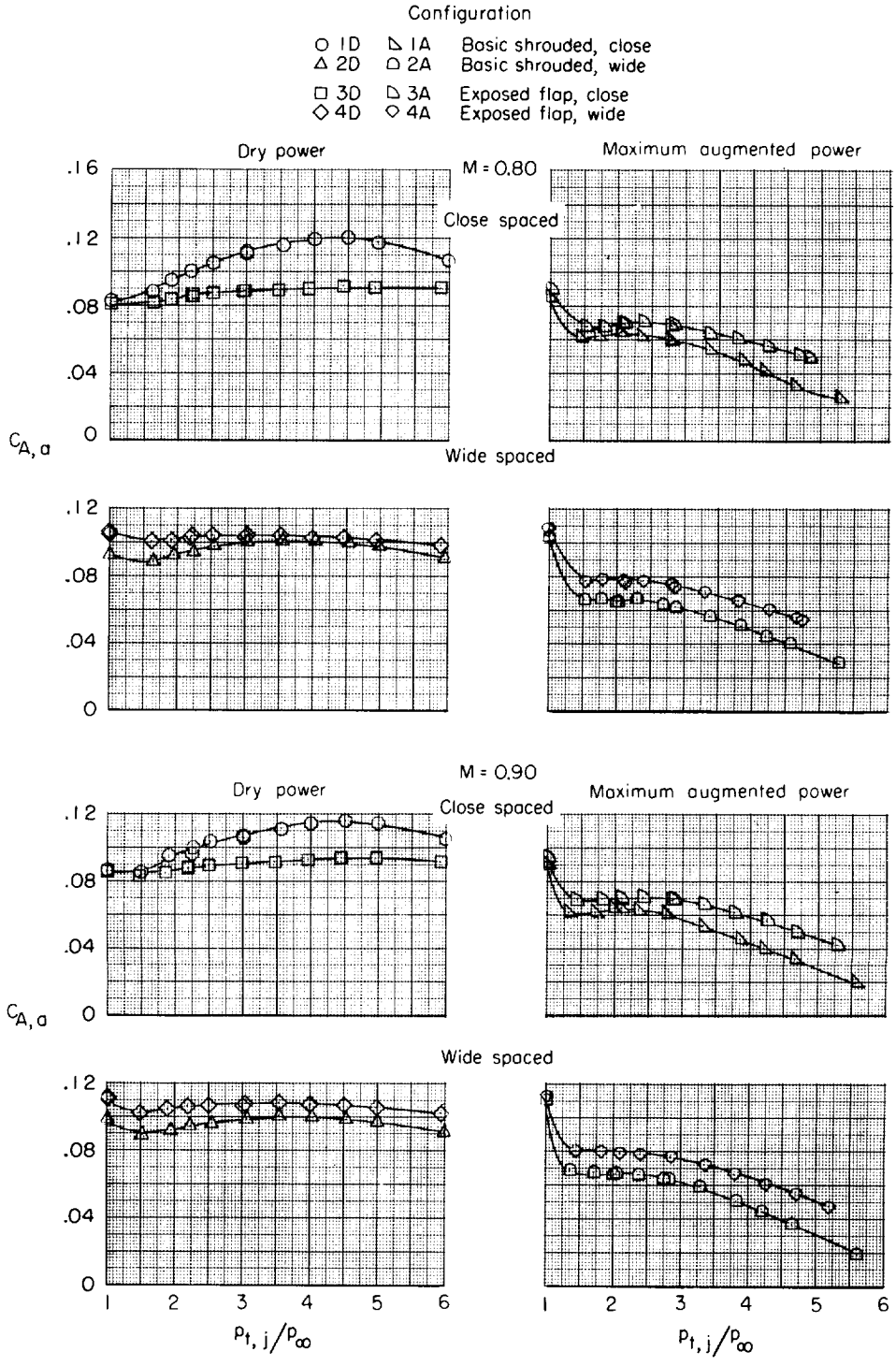

(b) M = 0.80 and 0.90.

Figure 19.- Continued.

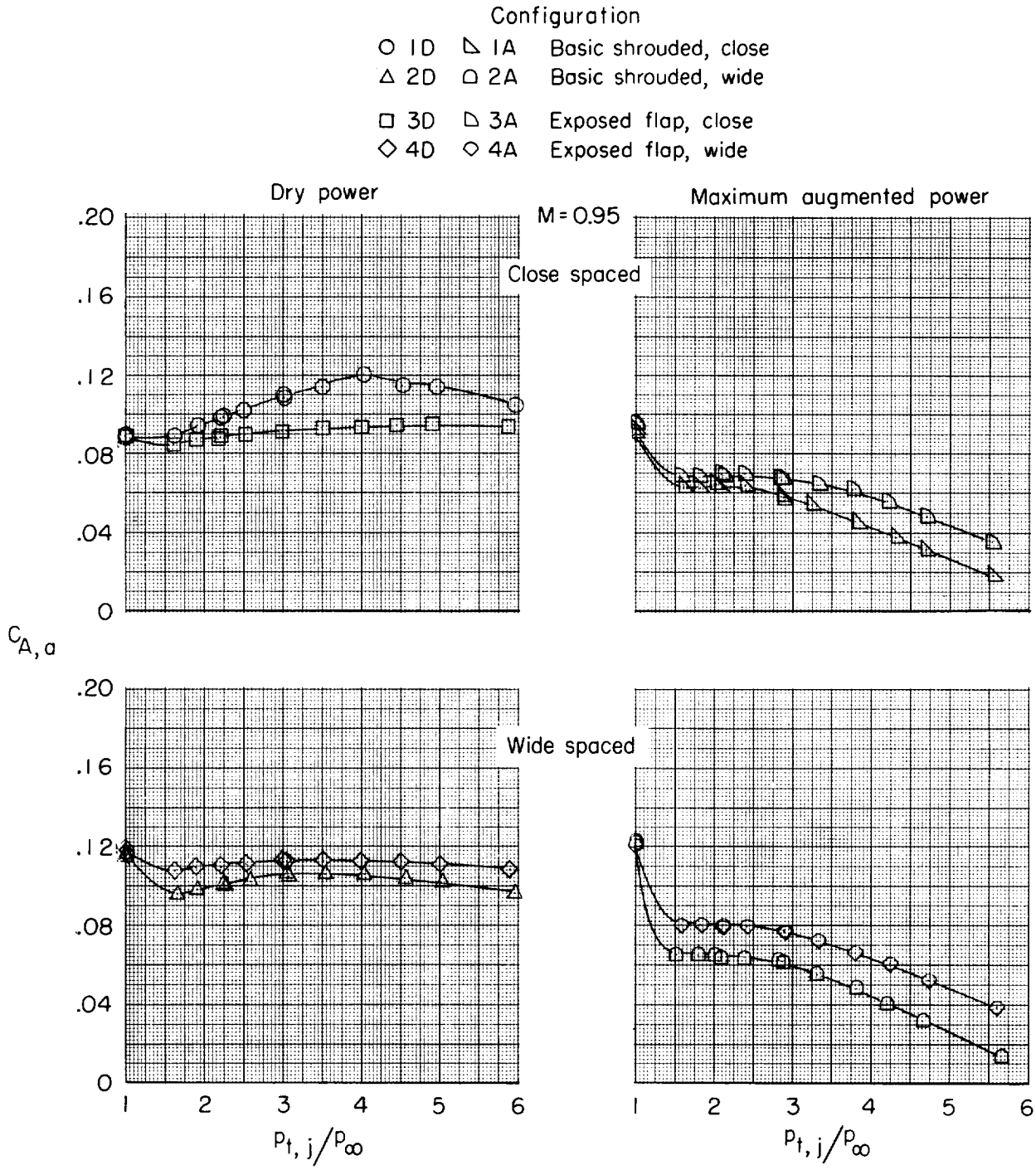

(c) M = 0.95.

Figure 19.- Continued.

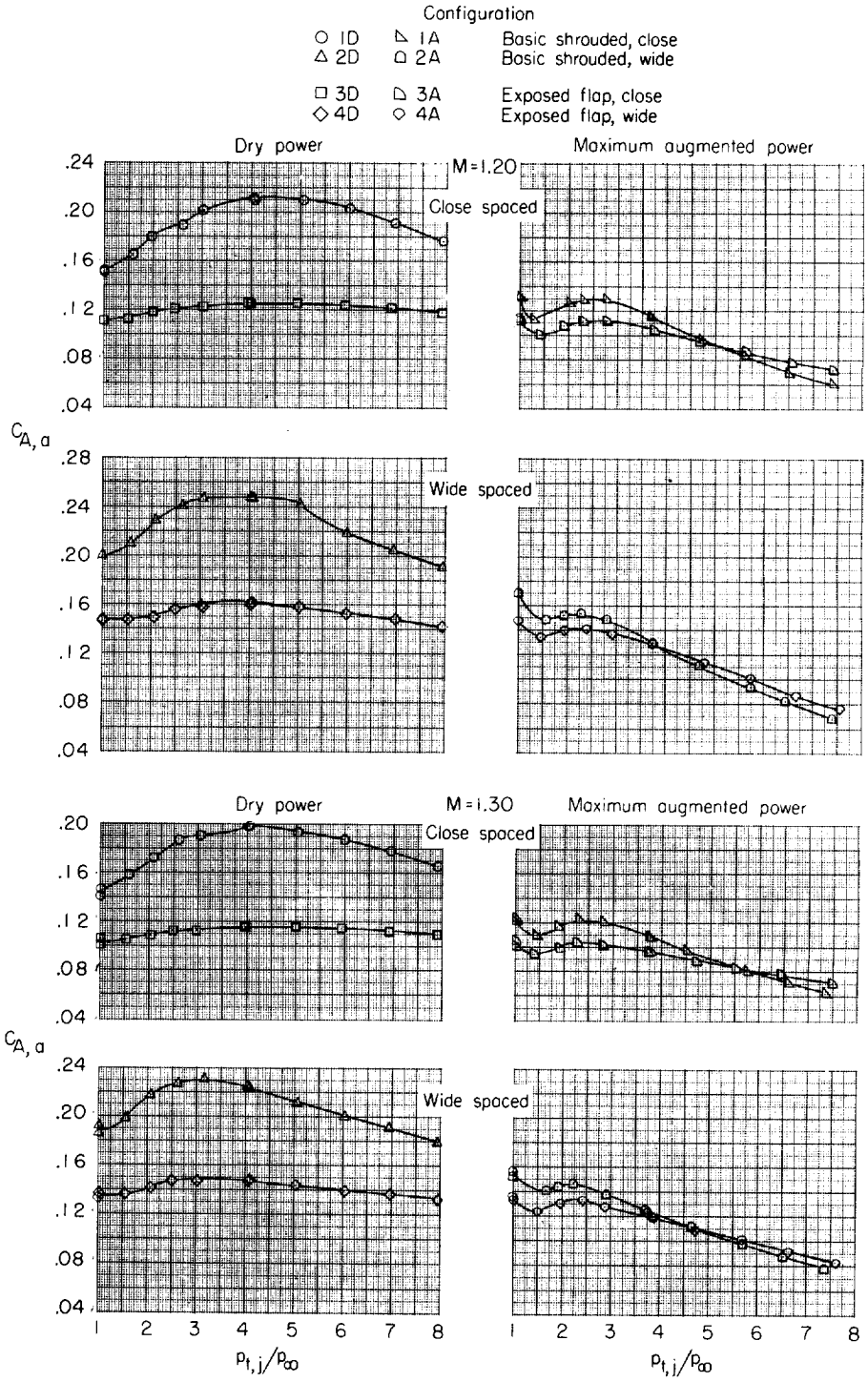

(d) M = 1.20 and 1.30.

Figure 19.- Continued.

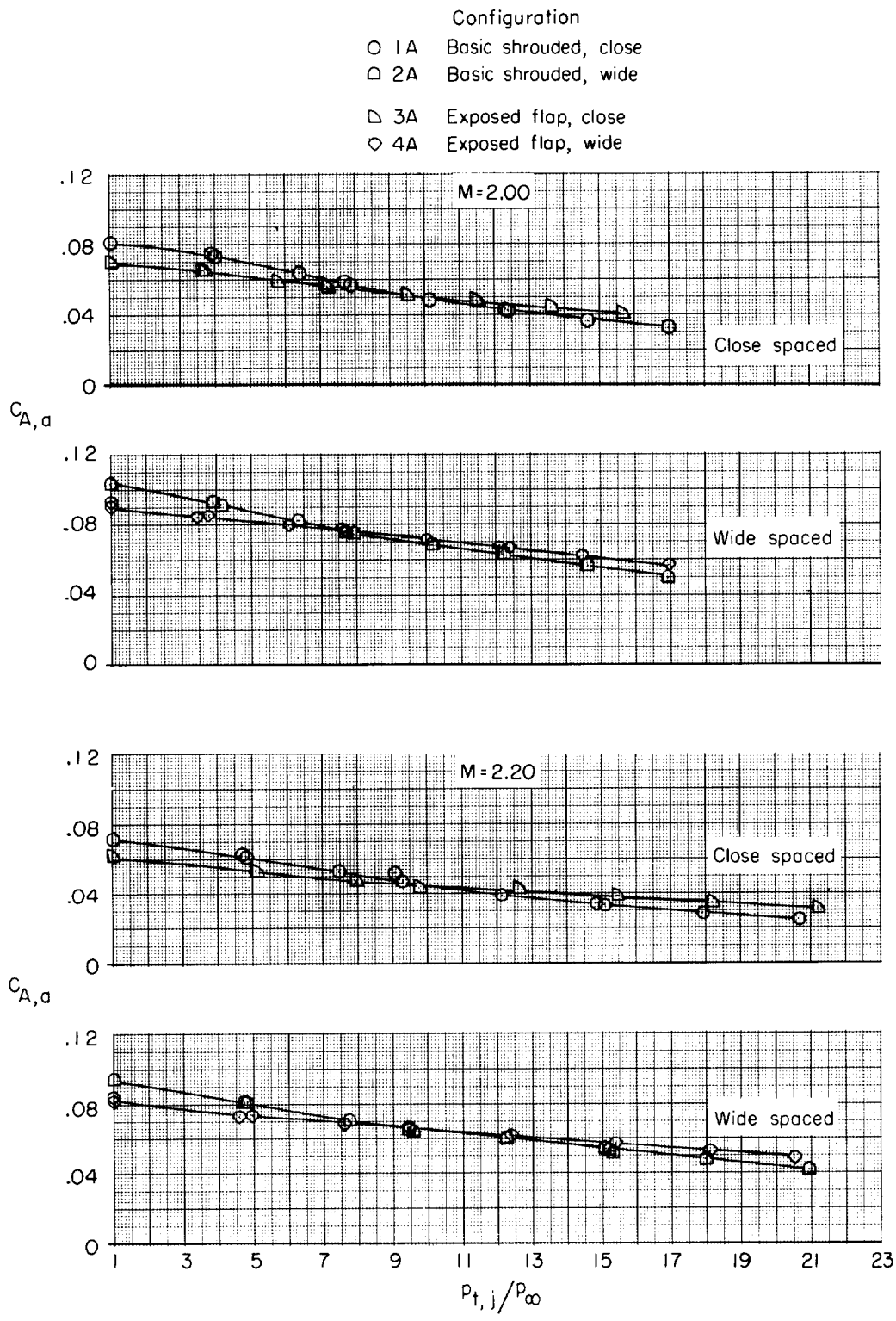

(e) M = 2.00 and 2.20.

Figure 19.- Concluded.

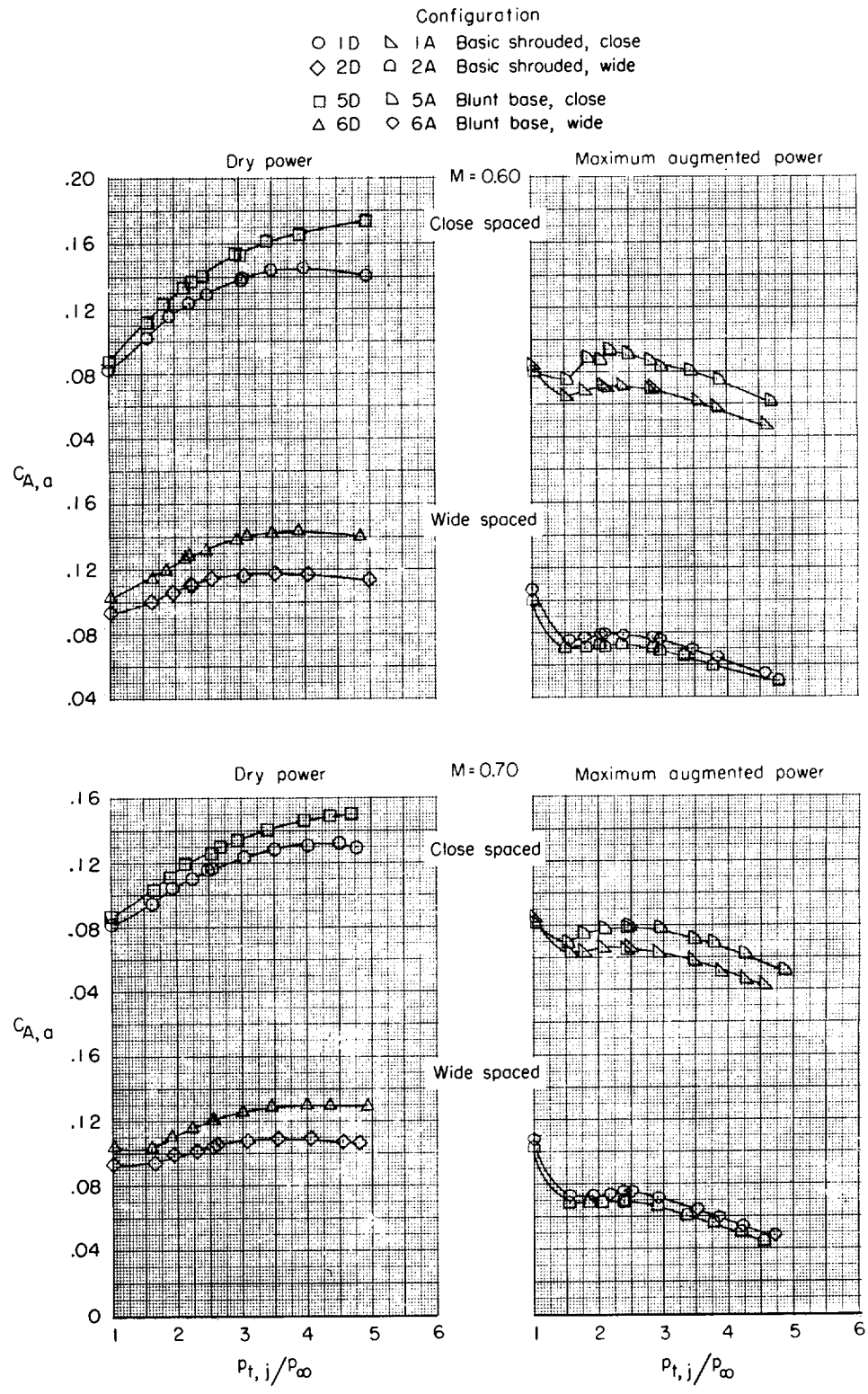

(a) M = 0.60 and 0.70.

Figure 20.- Variation of afterbody axial-force coefficient with jet-total-pressure ratio for afterbody configurations 1, 2, 5, and 6 at both power settings.

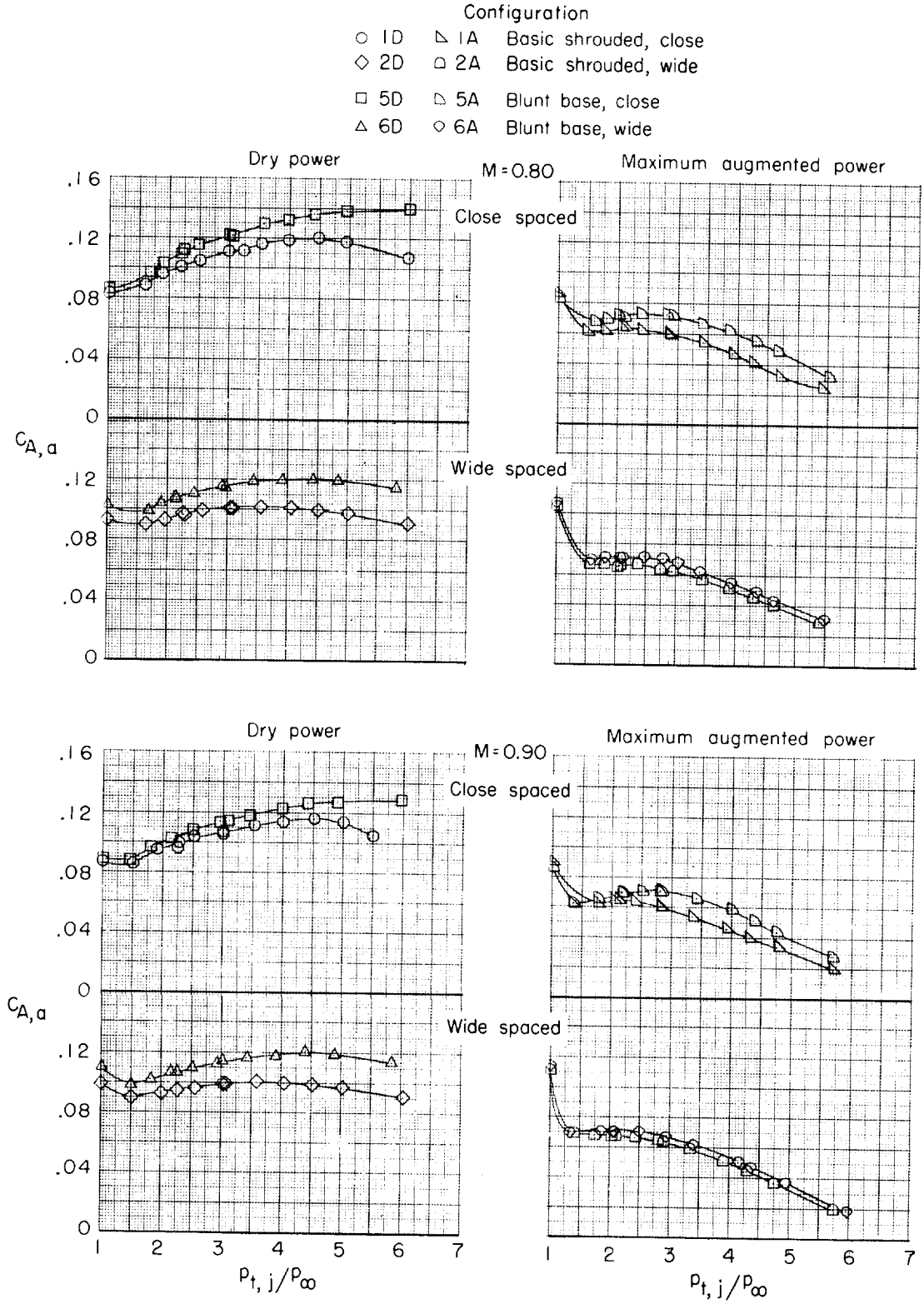

(b) M = 0.80 and 0.90.

Figure 20.- Continued.

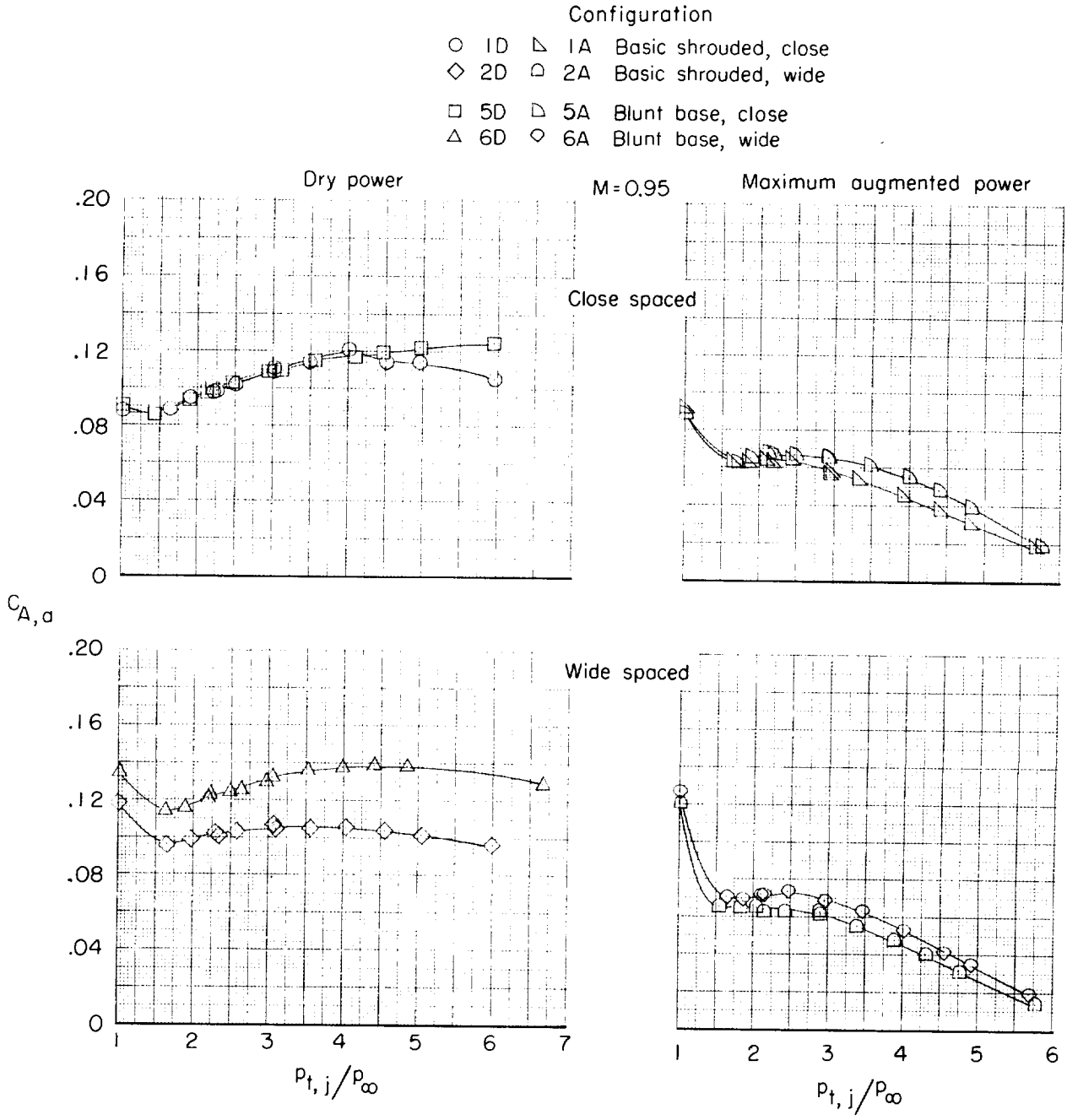

(c) M = 0.95.

Figure 20.- Continued.

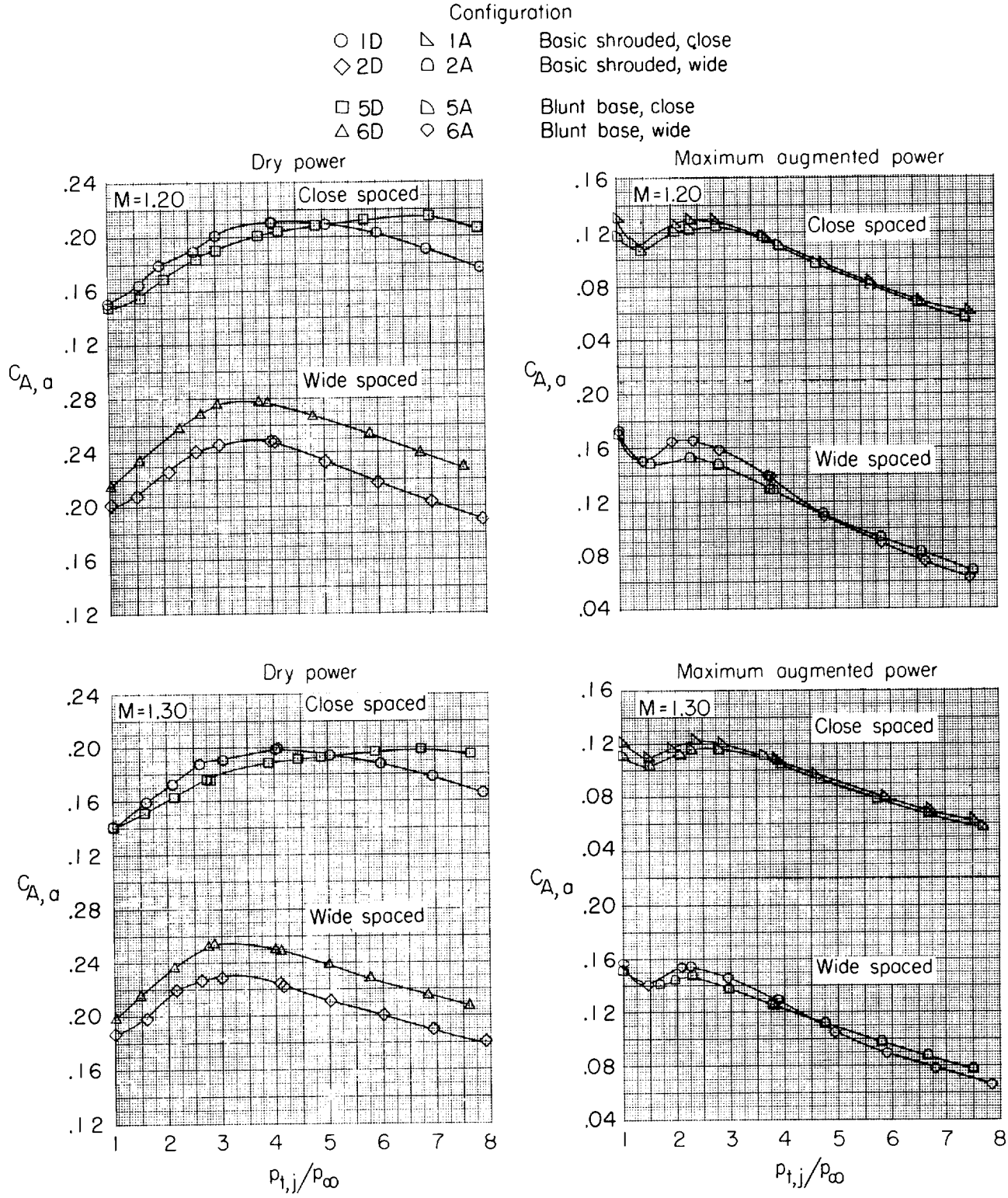

(d) M = 1.20 and 1.30.

Figure 20.- Continued.

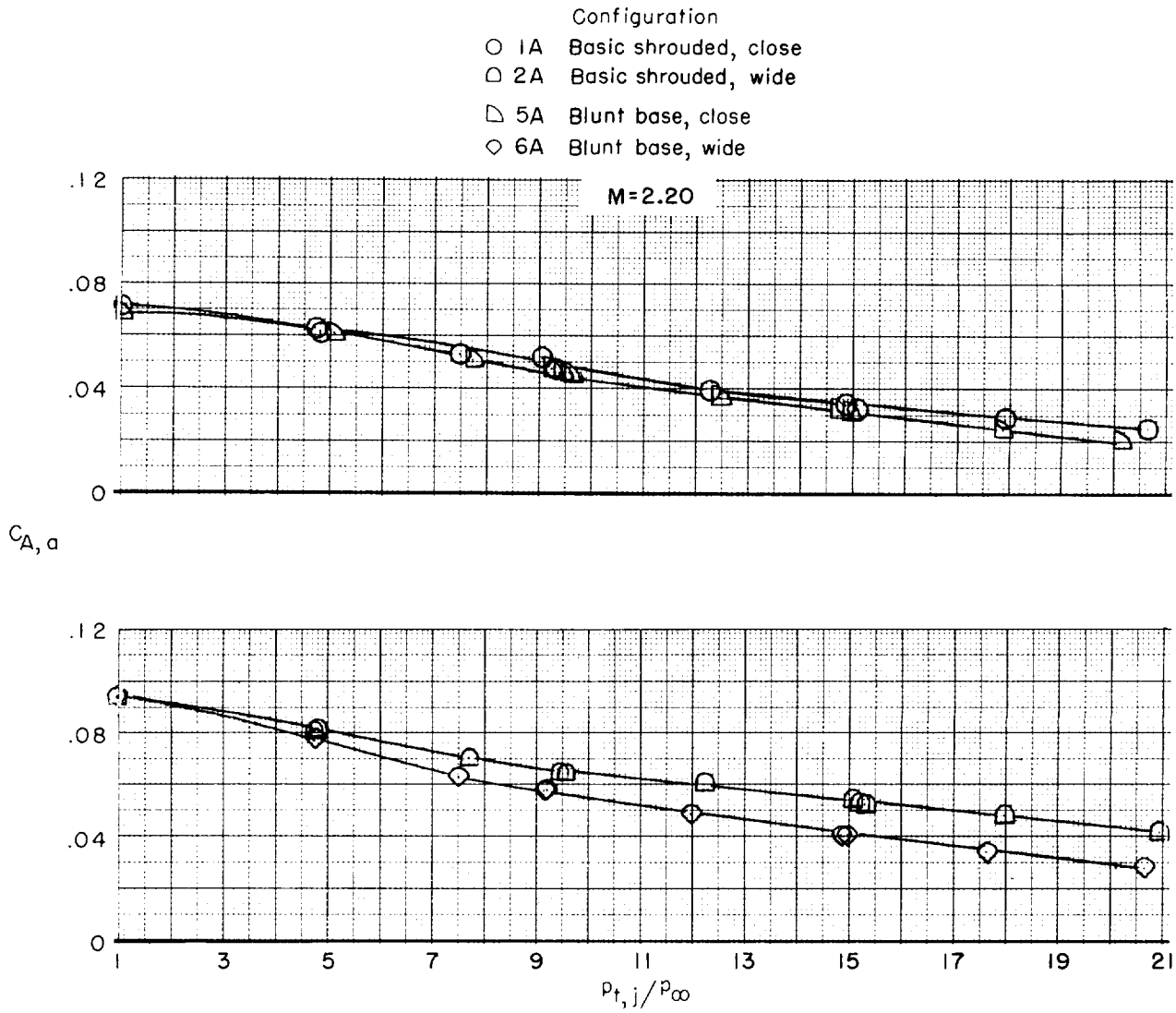

(e) M = 2.20.

Figure 20.- Concluded.

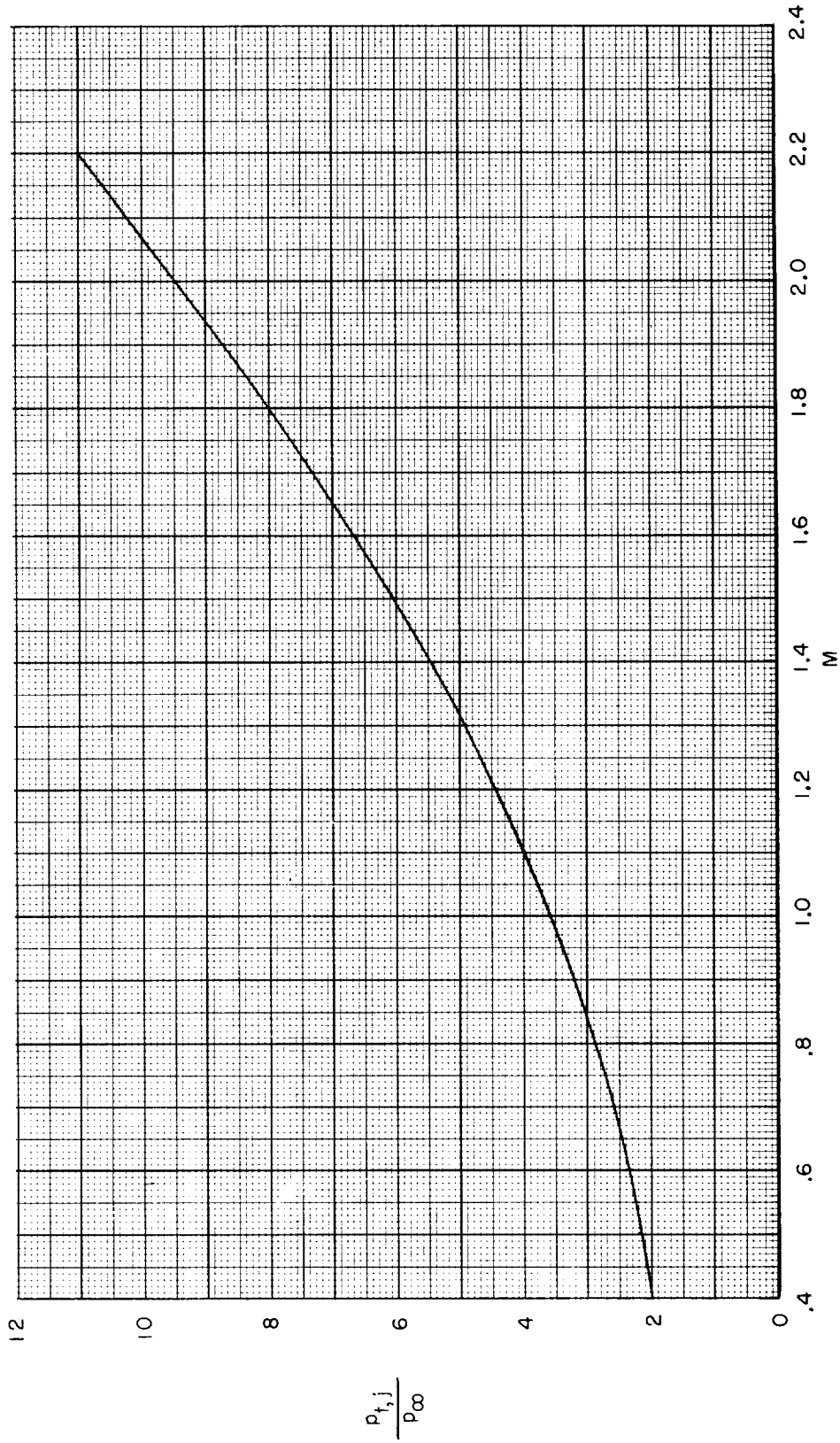

Figure 21.- Typical jet-total-pressure-ratio schedule for a turbofan engine.

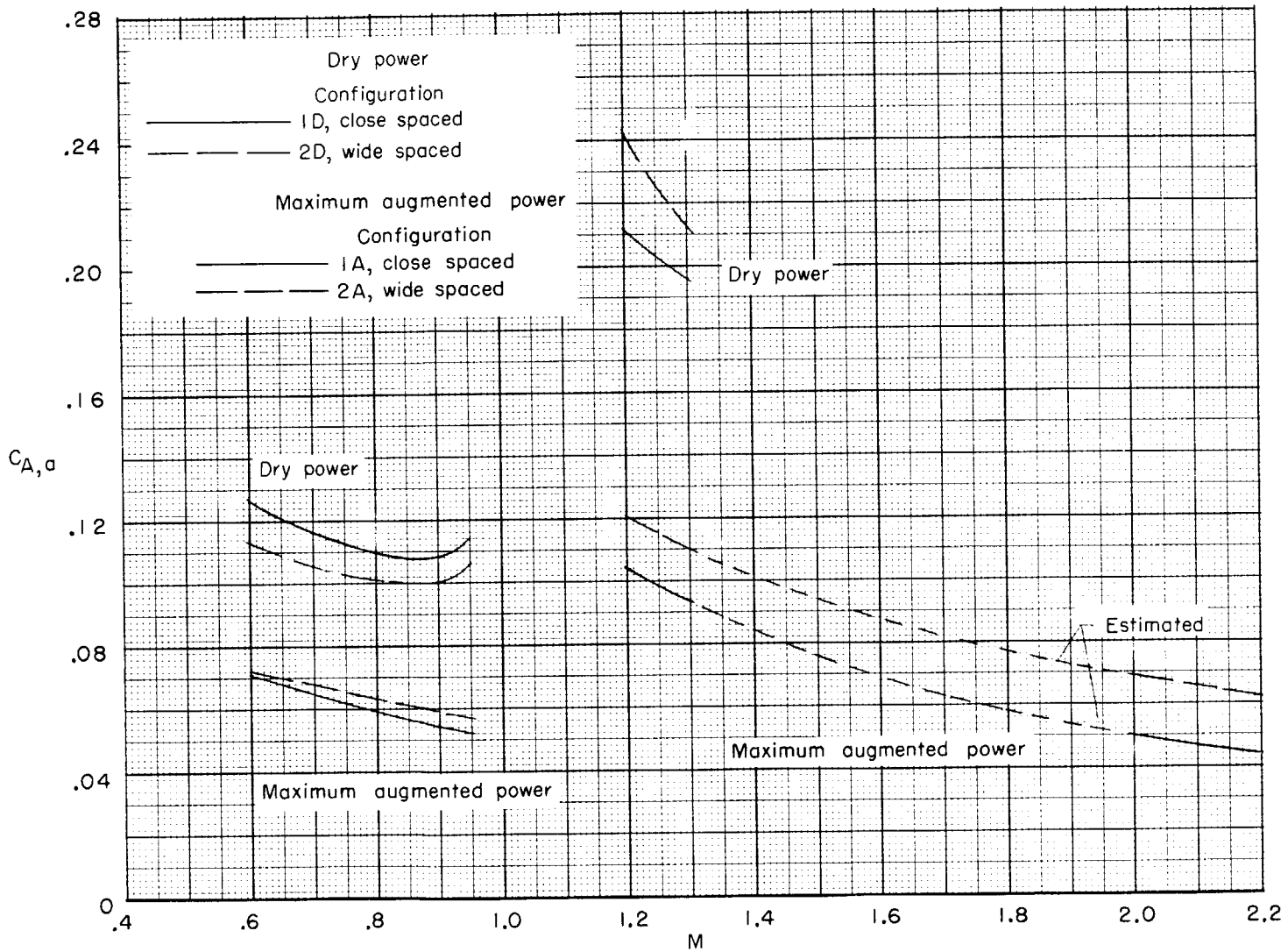

(a) Afterbody configurations 1 and 2.

Figure 22.- Variation of afterbody-axial-force coefficient with Mach number for the scheduled jet-total-pressure ratio.

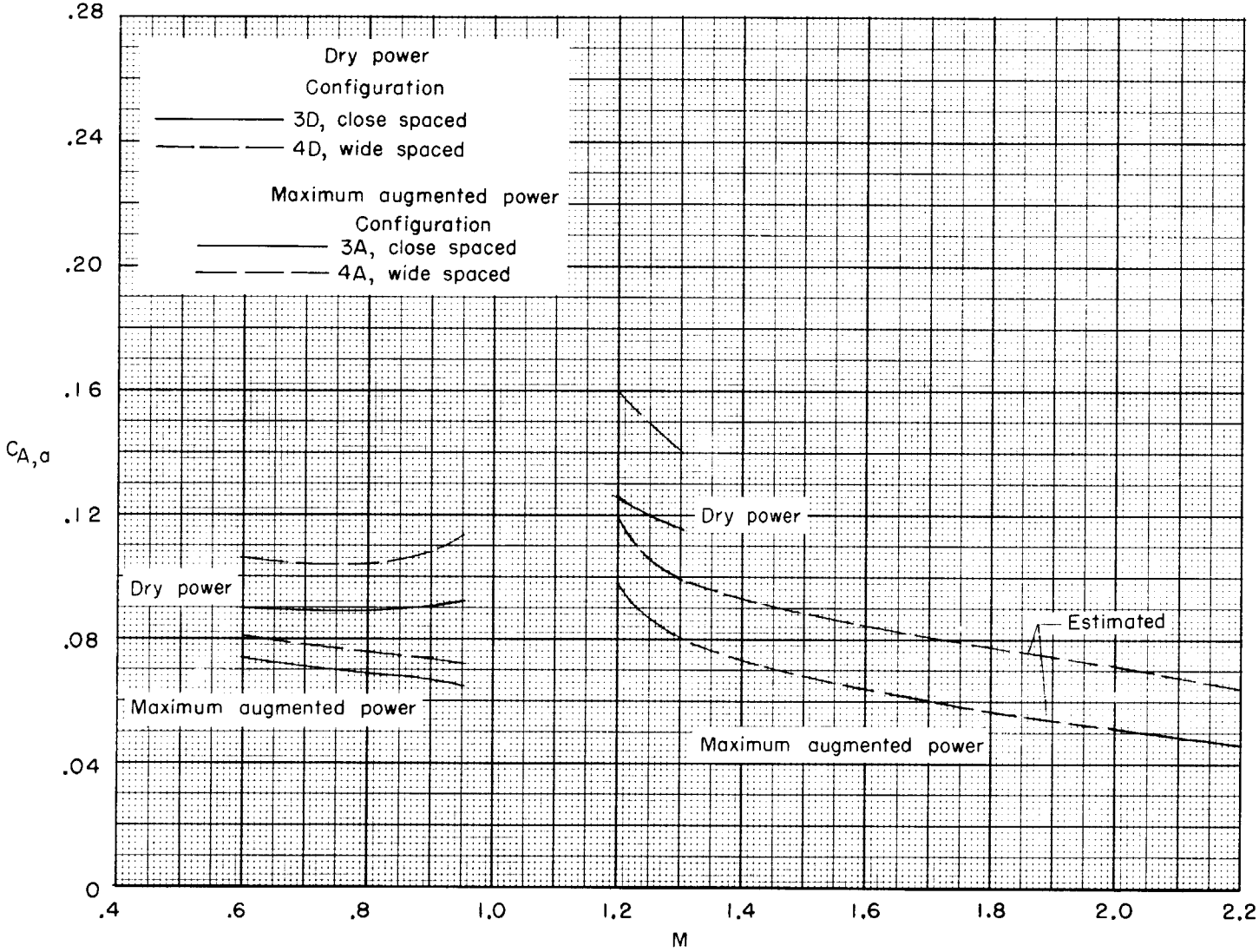

(b) Afterbody configurations 3 and 4.

Figure 22.- Continued.

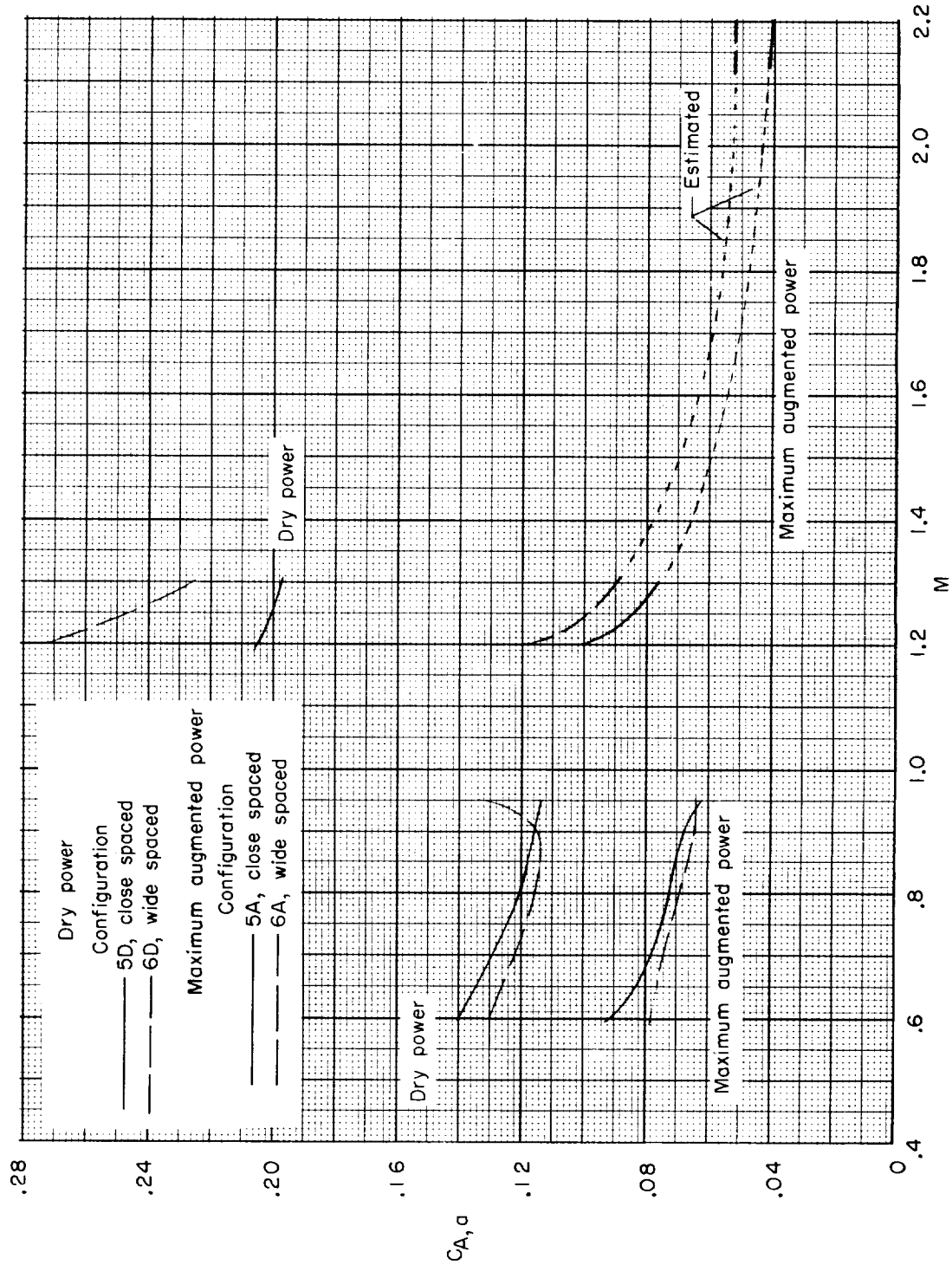

(c) Afterbody configurations 5 and 6.

Figure 22.- Concluded.

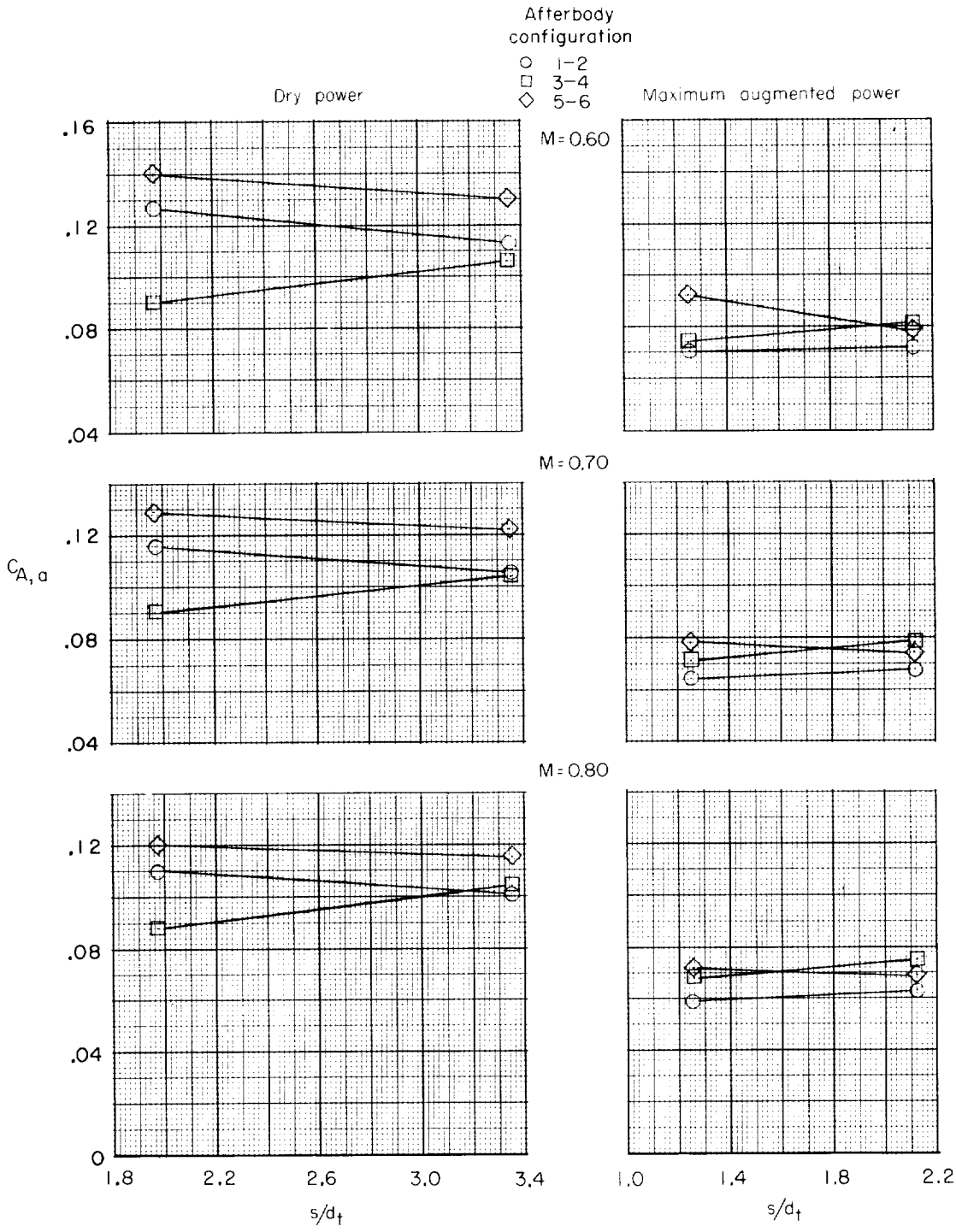

(a) M = 0.60, 0.70, and 0.80.

Figure 23.- Comparison of afterbody axial-force coefficients for spacing ratio s/d_t at several Mach numbers.

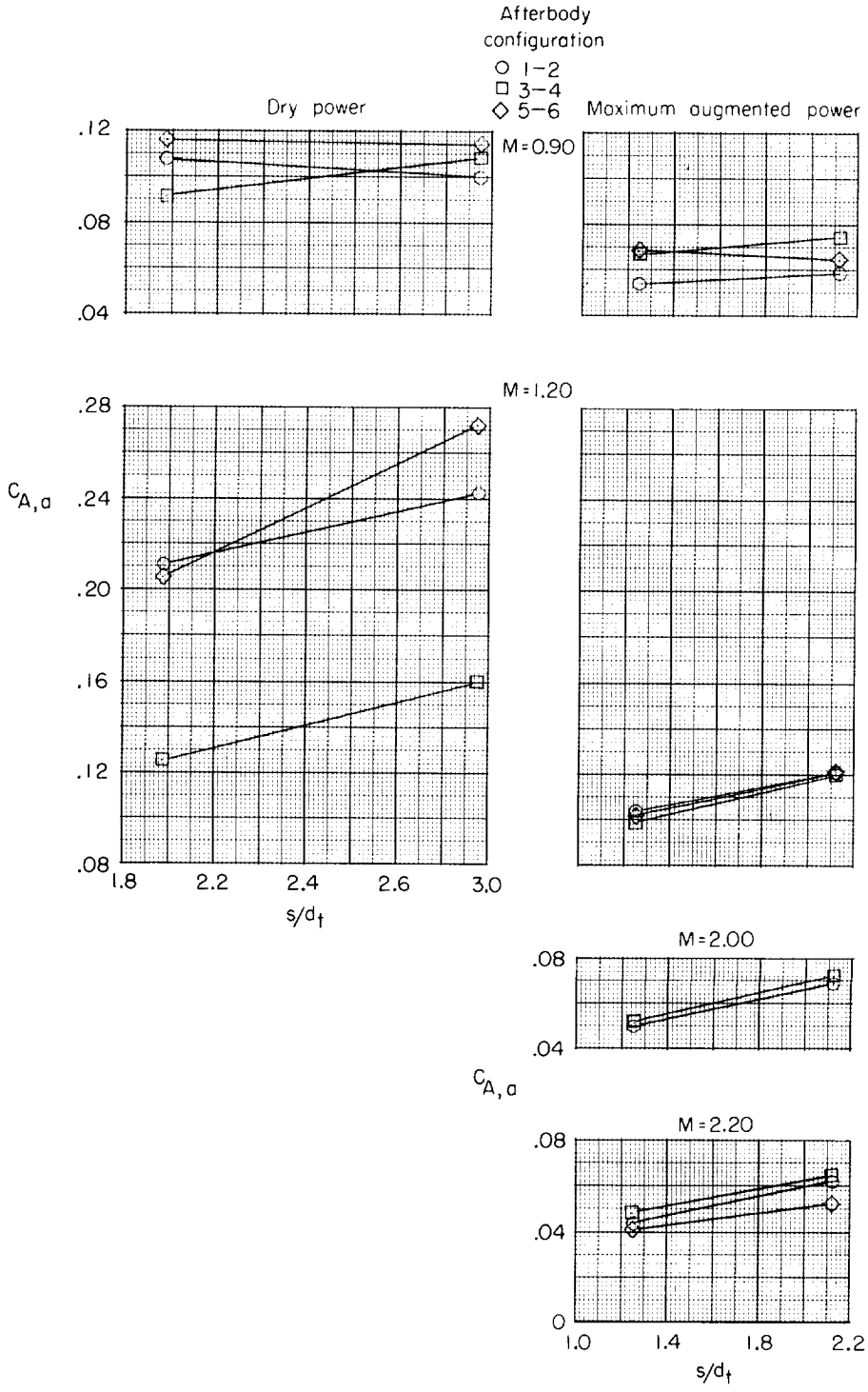

(b) M = 0.90, 1.20, 2.00, and 2.20.

Figure 23.- Concluded.

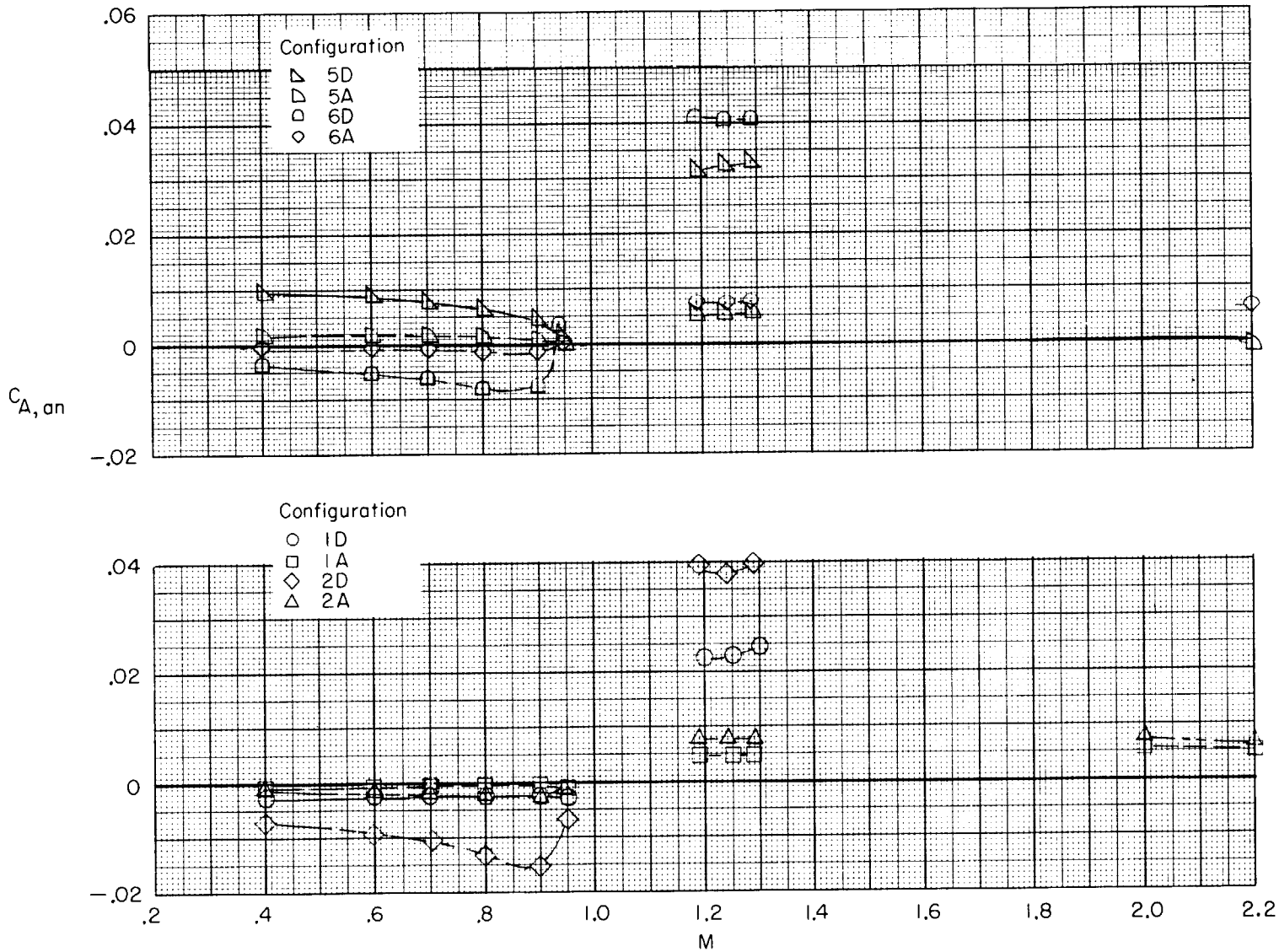

Figure 24.- Variation of axial-force coefficient of nozzle-base annuli $C_{A,an}$ with Mach number for the jet-off condition for afterbody configurations 1, 2, 5, and 6.

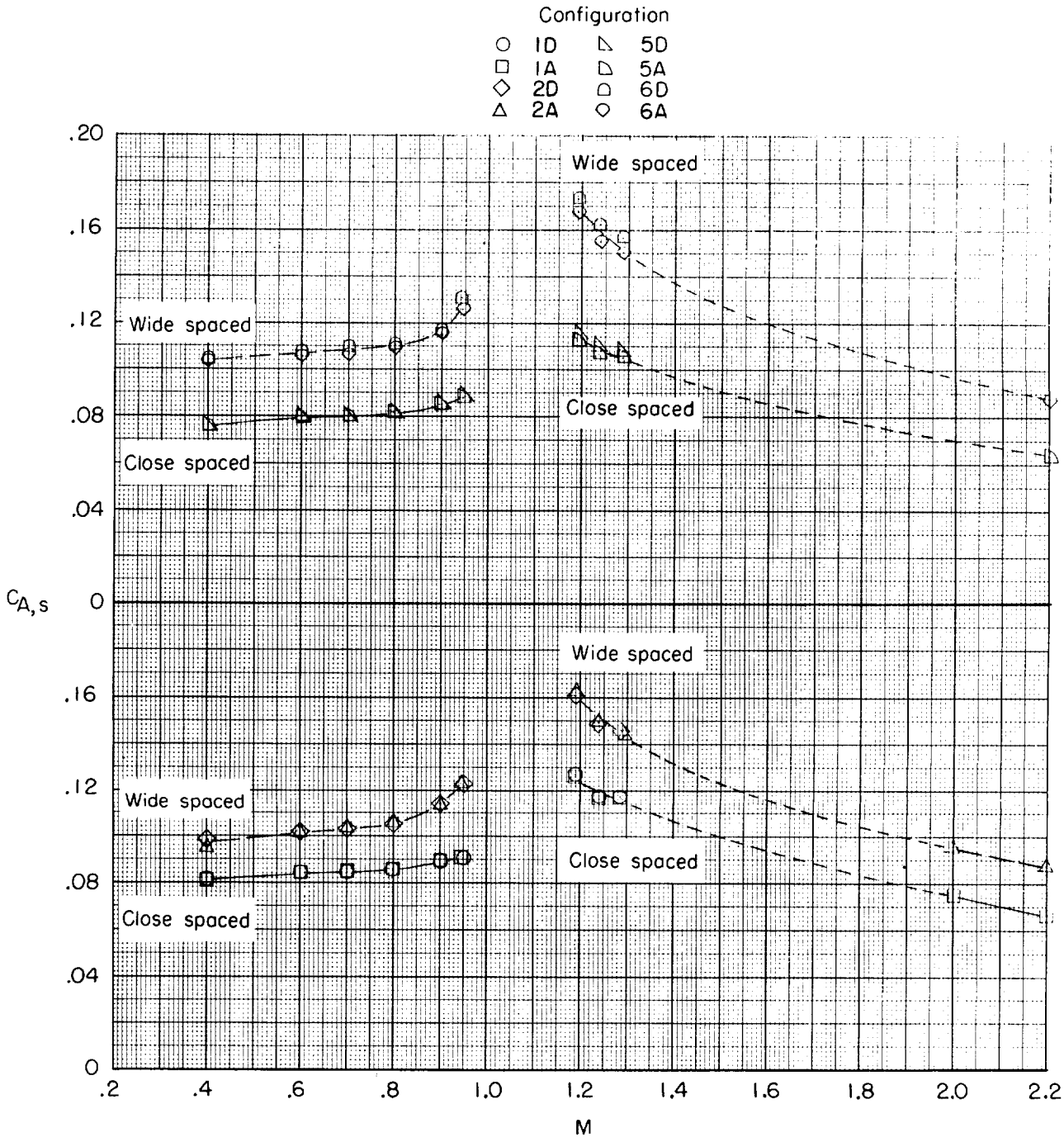

Figure 25.- Variation of shroud axial-force coefficient with Mach number for the jet-off condition for afterbody configurations 1, 2, 5, and 6.

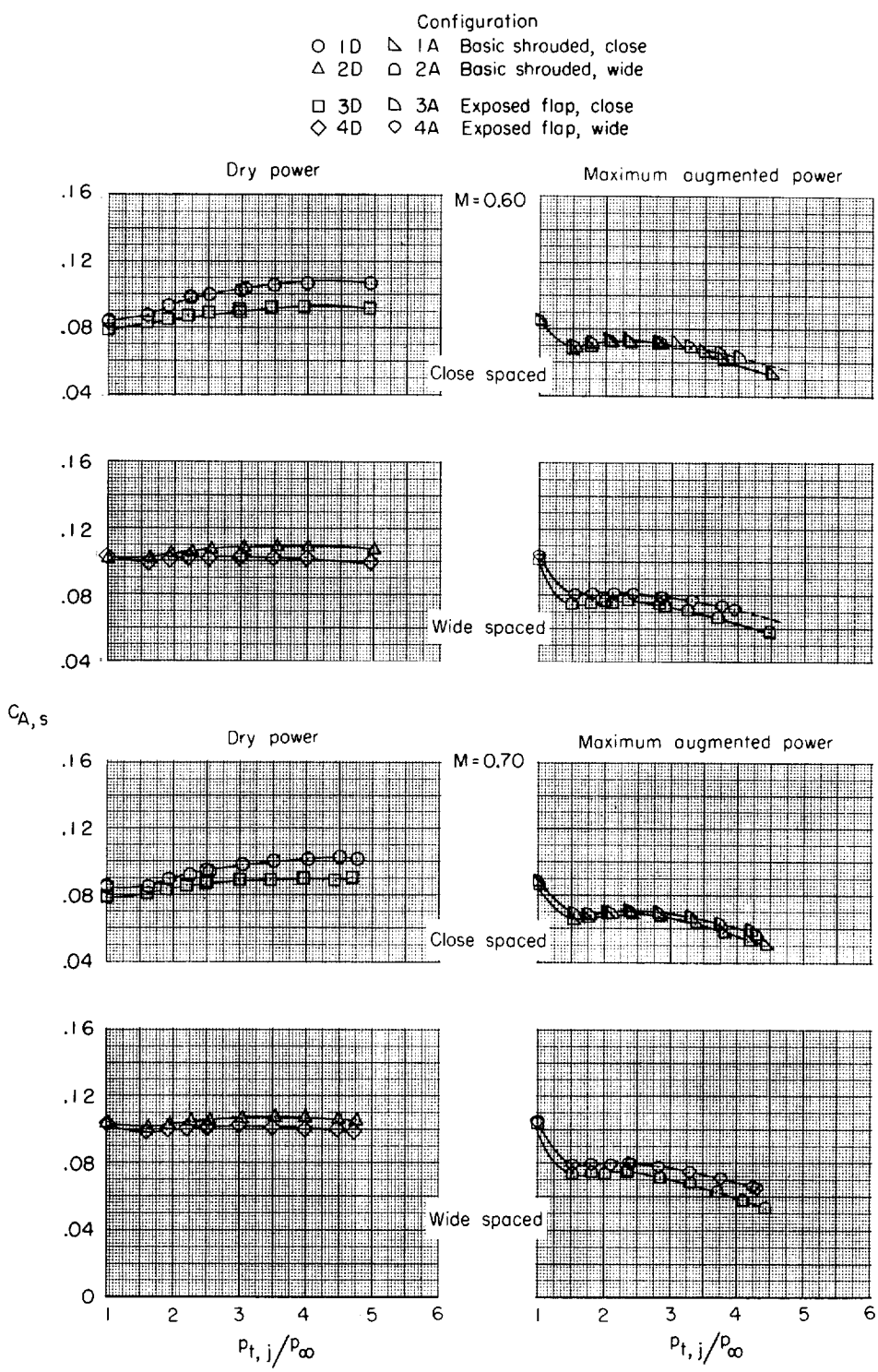

(a) M = 0.60 and 0.70.

Figure 26.- Variation of shroud axial-force coefficient with jet-total-pressure ratio for afterbody configurations 1, 2, 3, and 4.

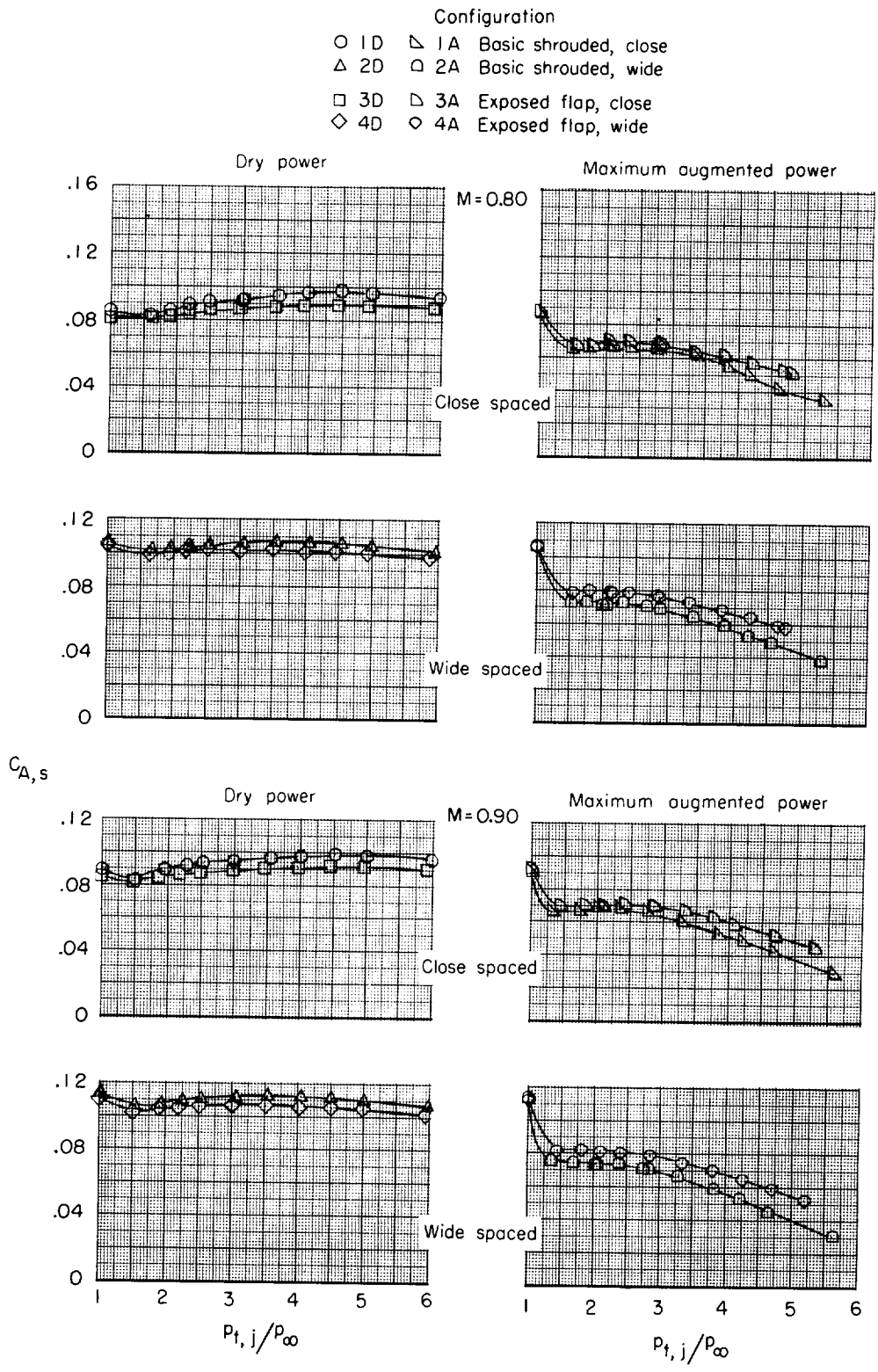

(b) M = 0.80 and 0.90.

Figure 26.- Continued.

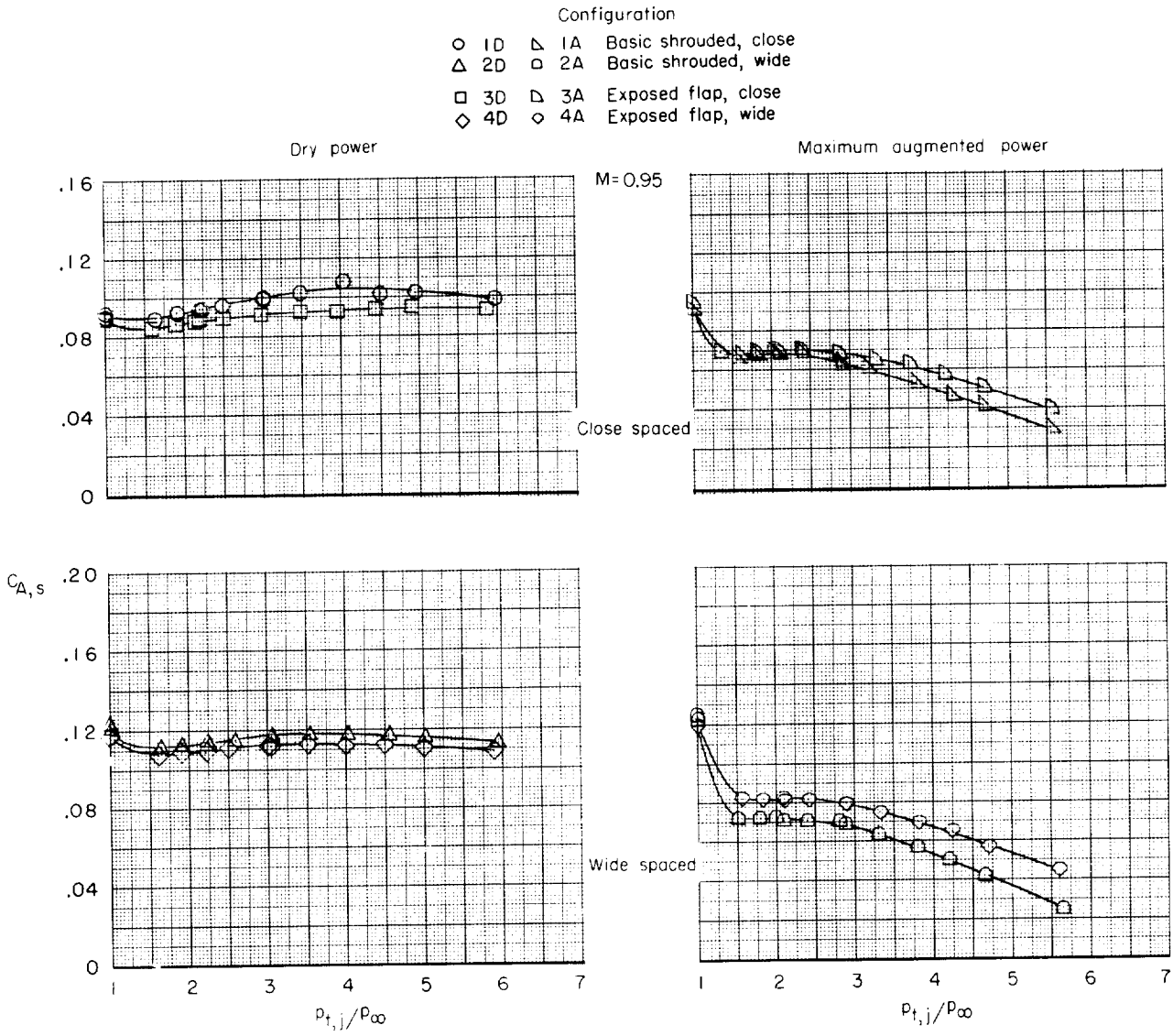

(c) M = 0.95.

Figure 26.- Continued.

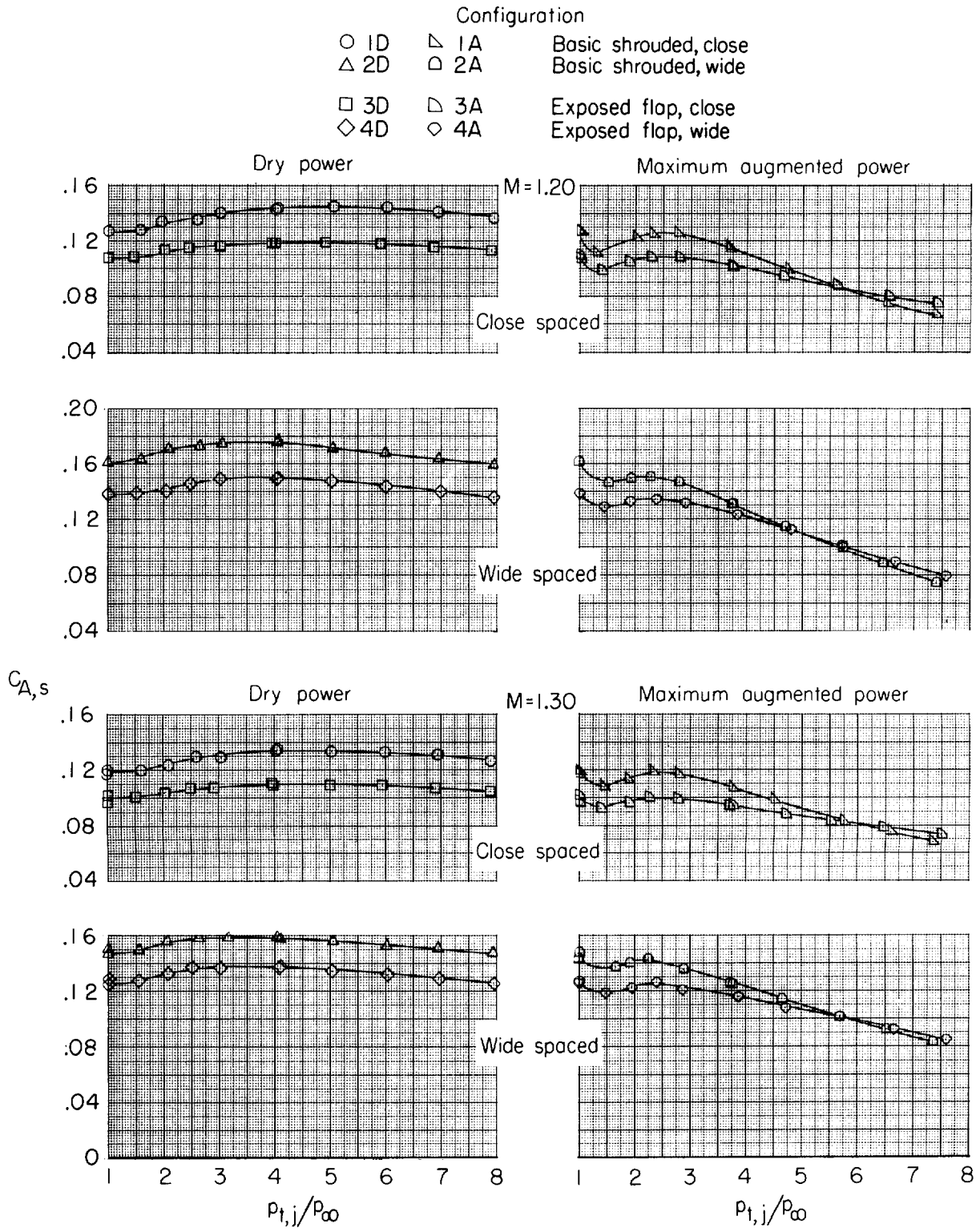

(d) M = 1.20 and 1.30.

Figure 26.- Continued.

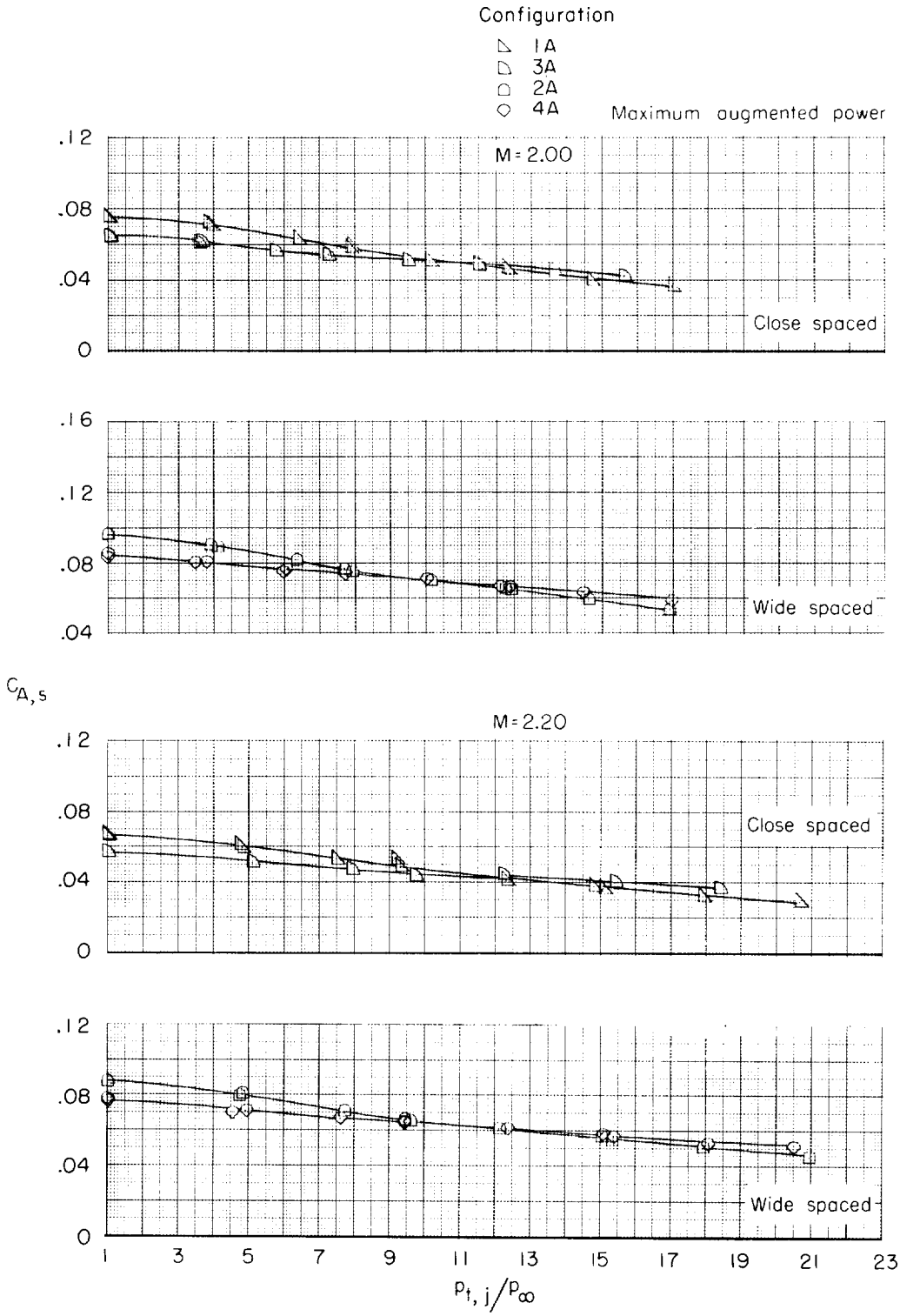

(e) M = 2.00 and 2.20.

Figure 26.- Concluded.

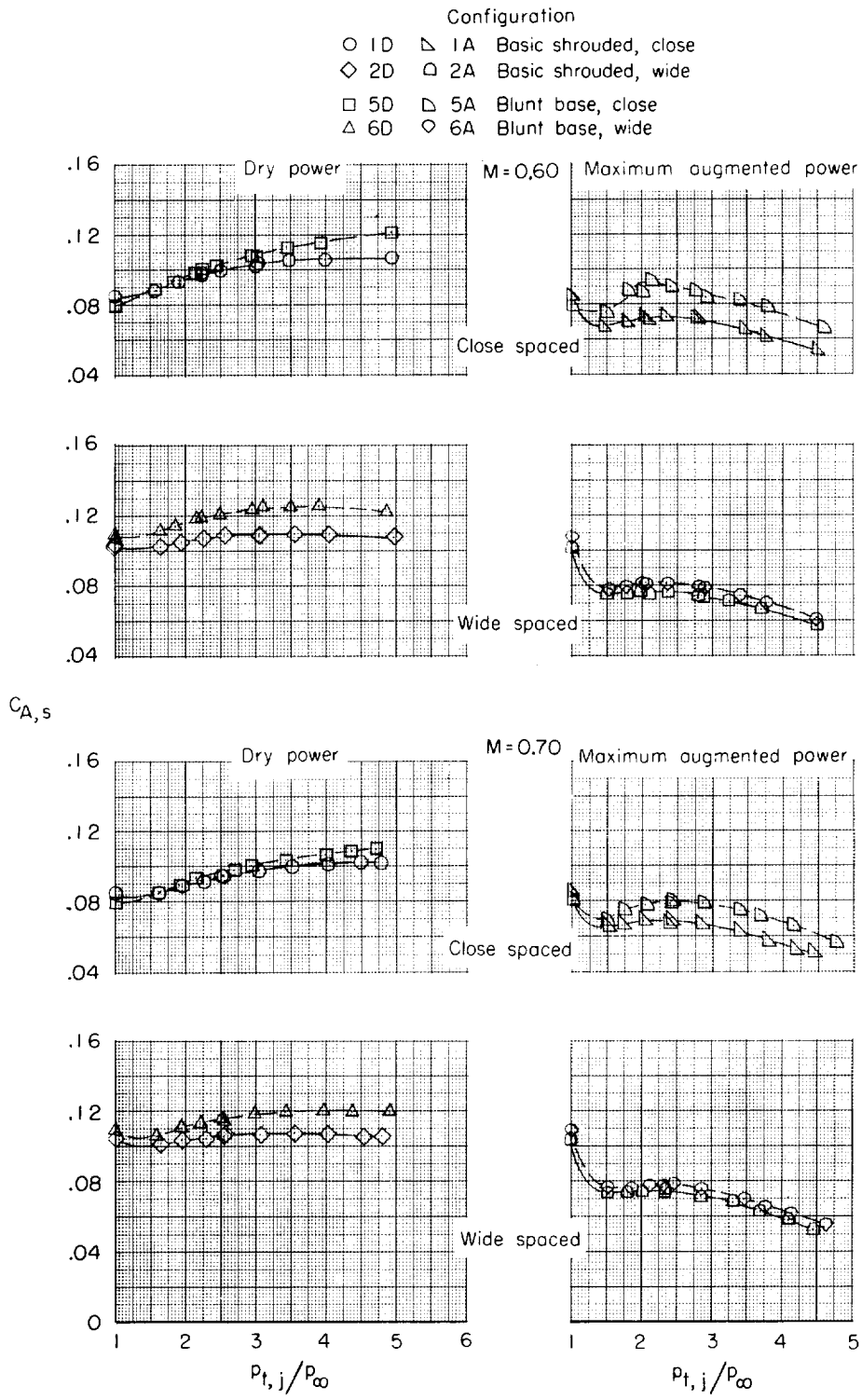

(a) M = 0.60 and 0.70.

Figure 27.- Variation of shroud axial-force coefficient with jet-total-pressure ratio for afterbody configurations 1, 2, 5, and 6.

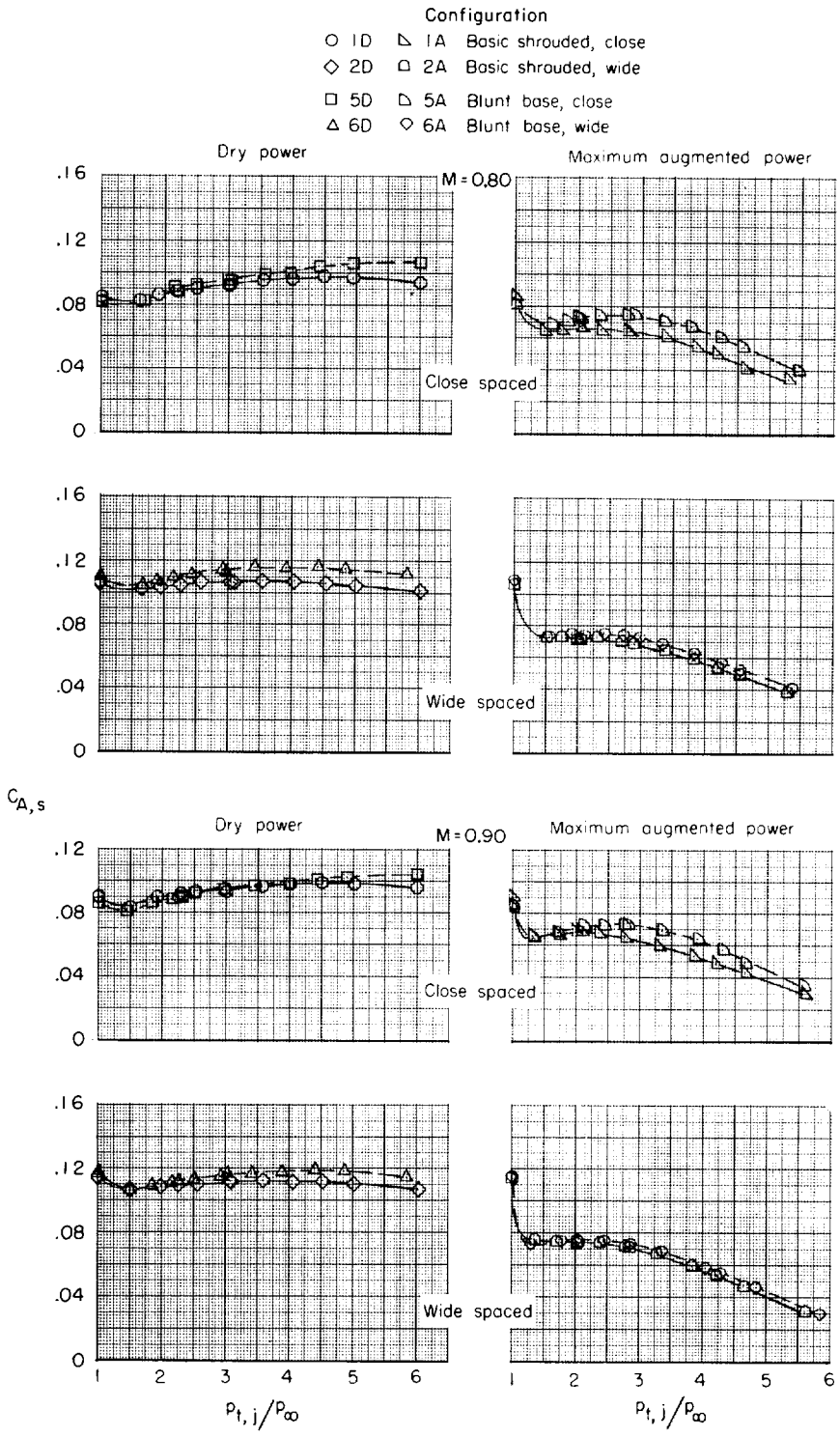

(b) M = 0.80 and 0.90.

Figure 27.- Continued.

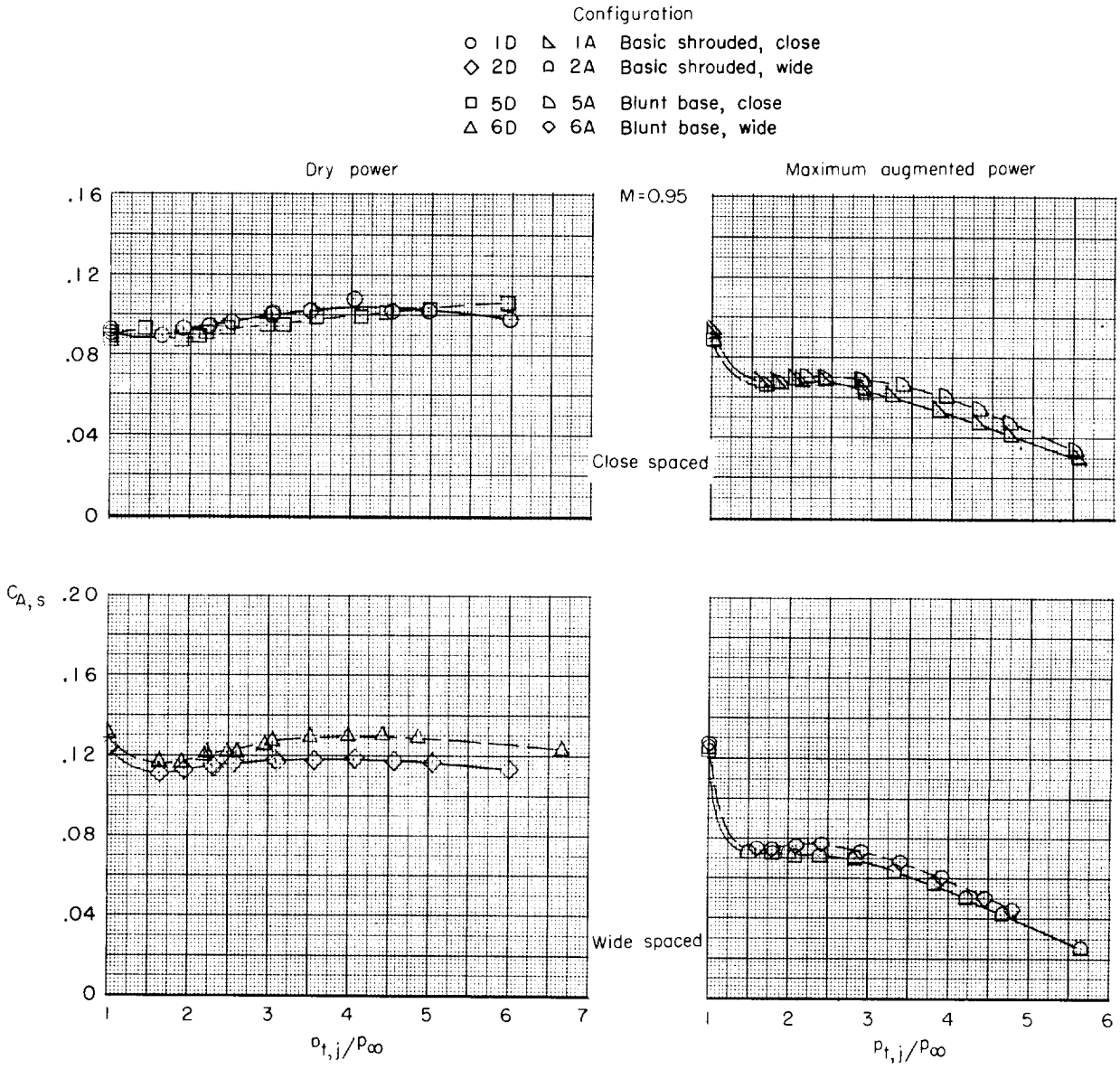

(c) M = 0.95.

Figure 27.- Continued.

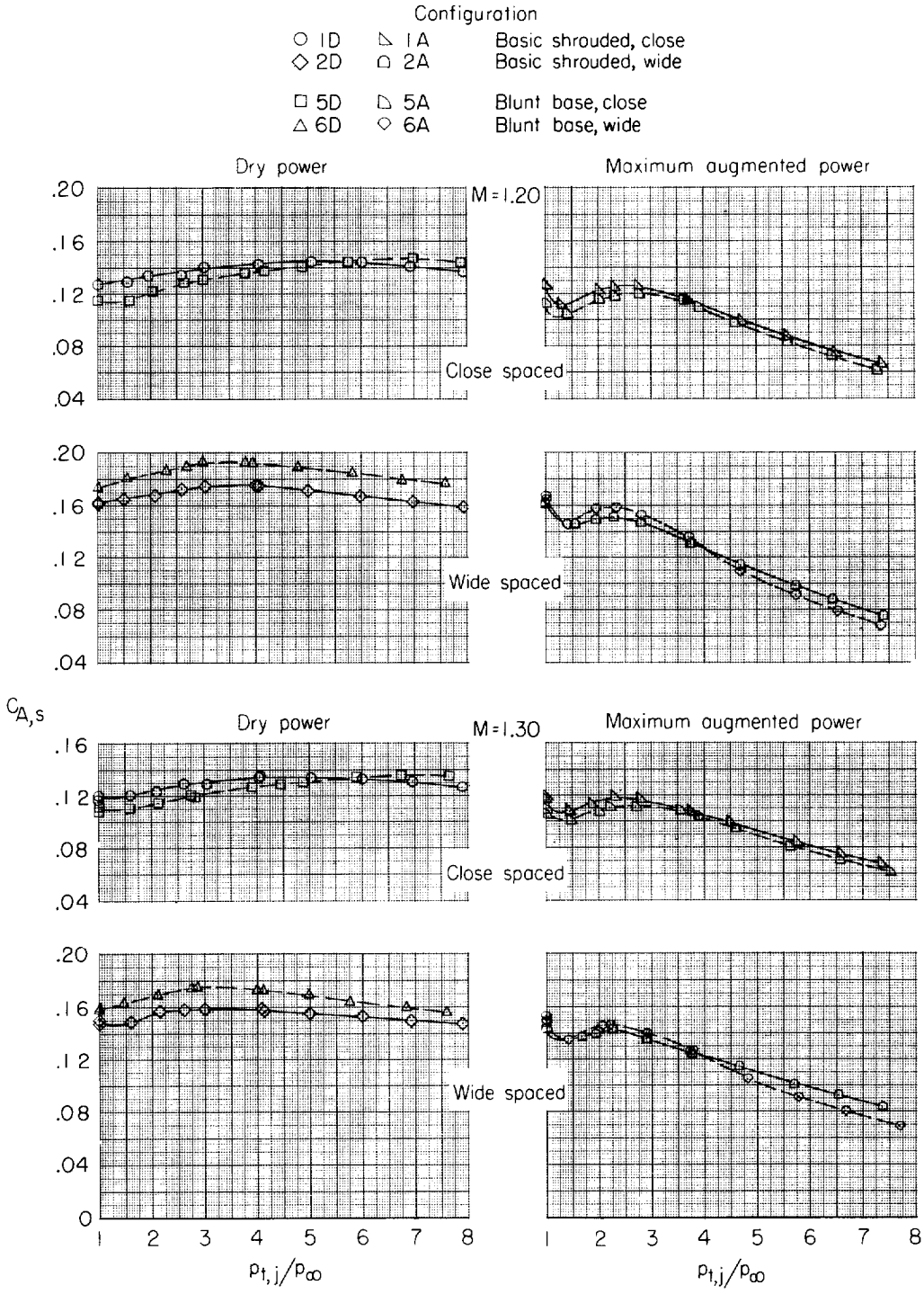

(d) M = 1.20 and 1.30.

Figure 27.- Continued.

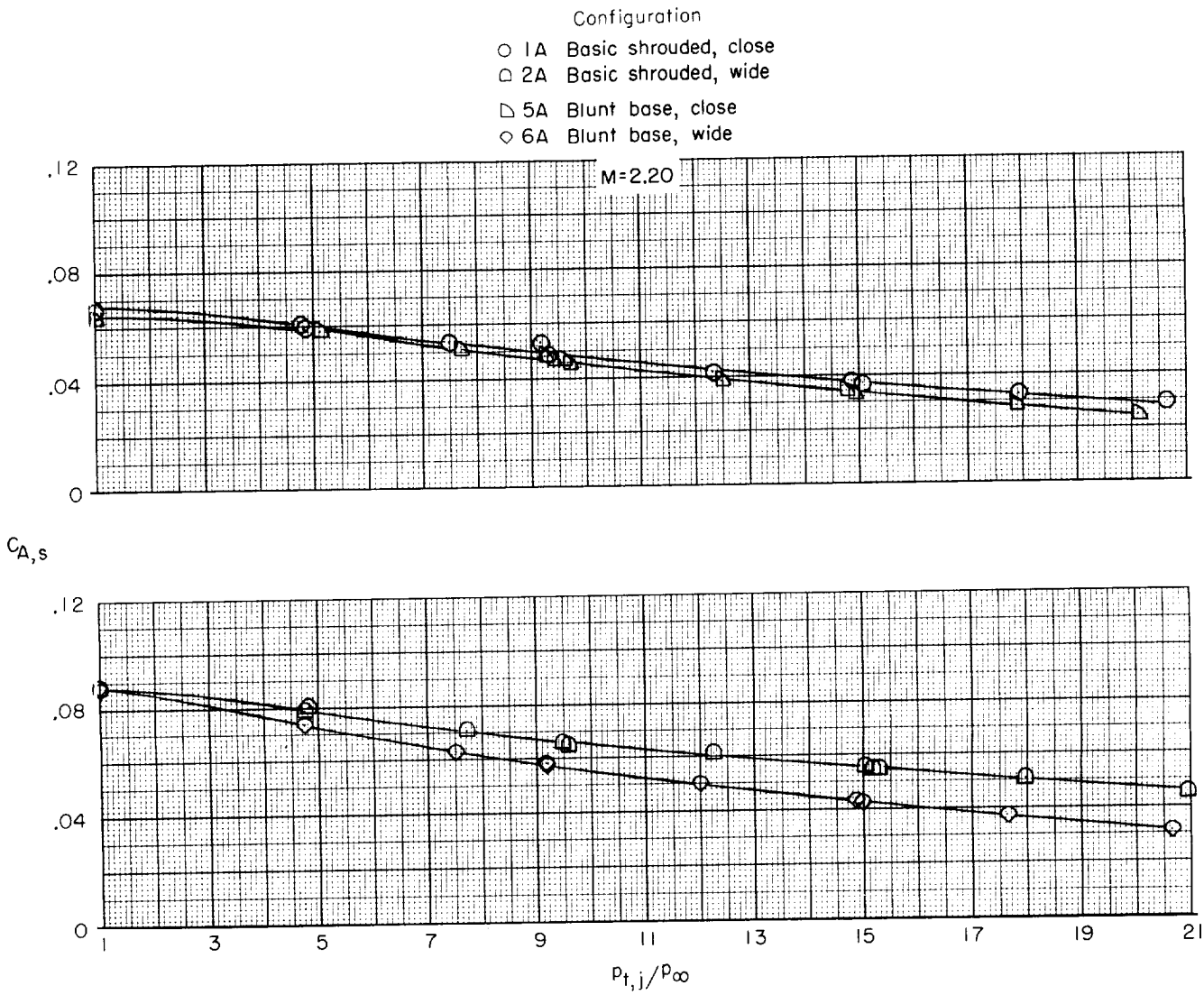

(e) M = 2.20.

Figure 27.- Concluded.

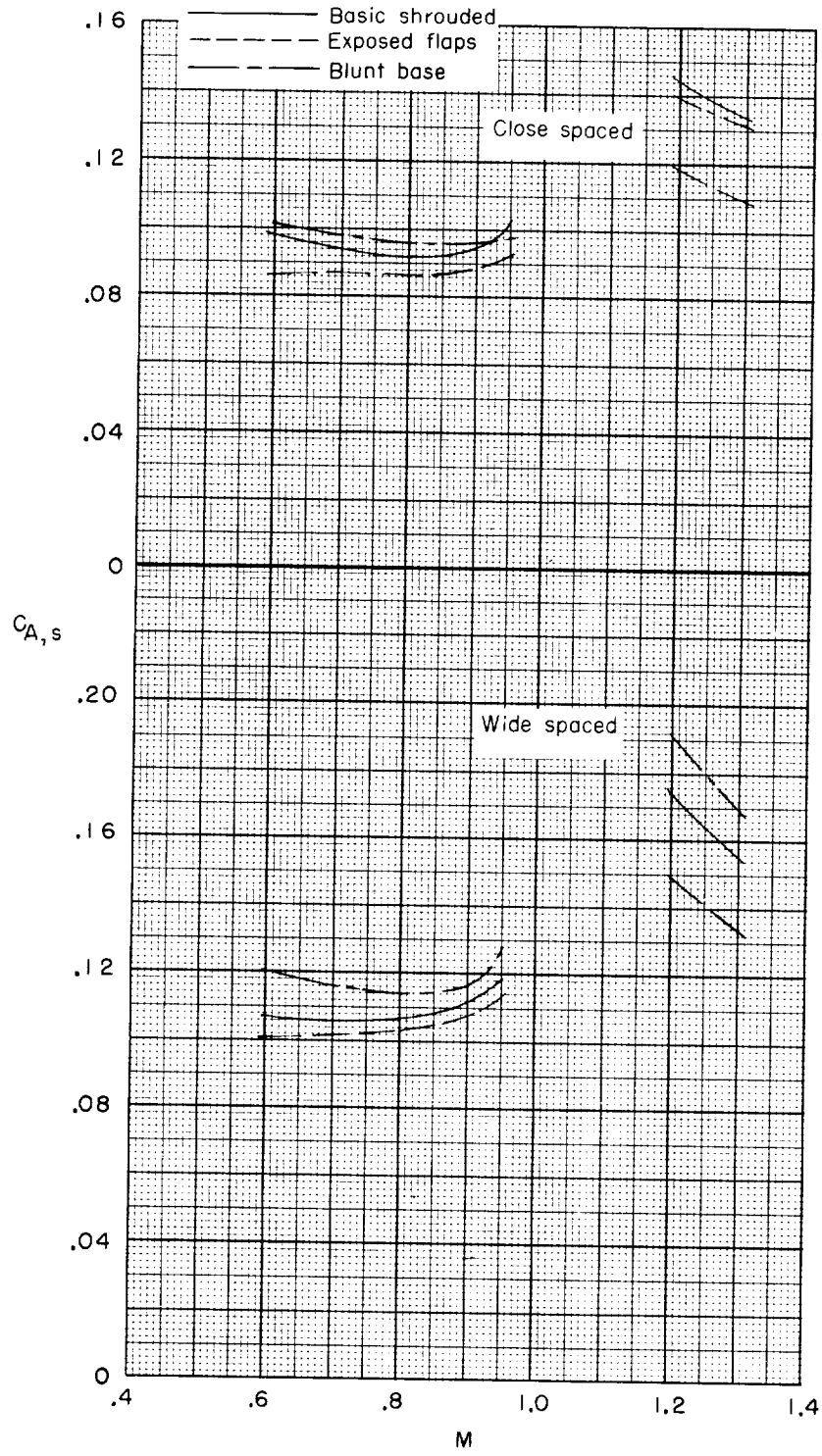

(a) Dry power.

Figure 28.- Variation of shroud axial-force coefficient with Mach number for the jet-pressure-ratio schedule in figure 21.

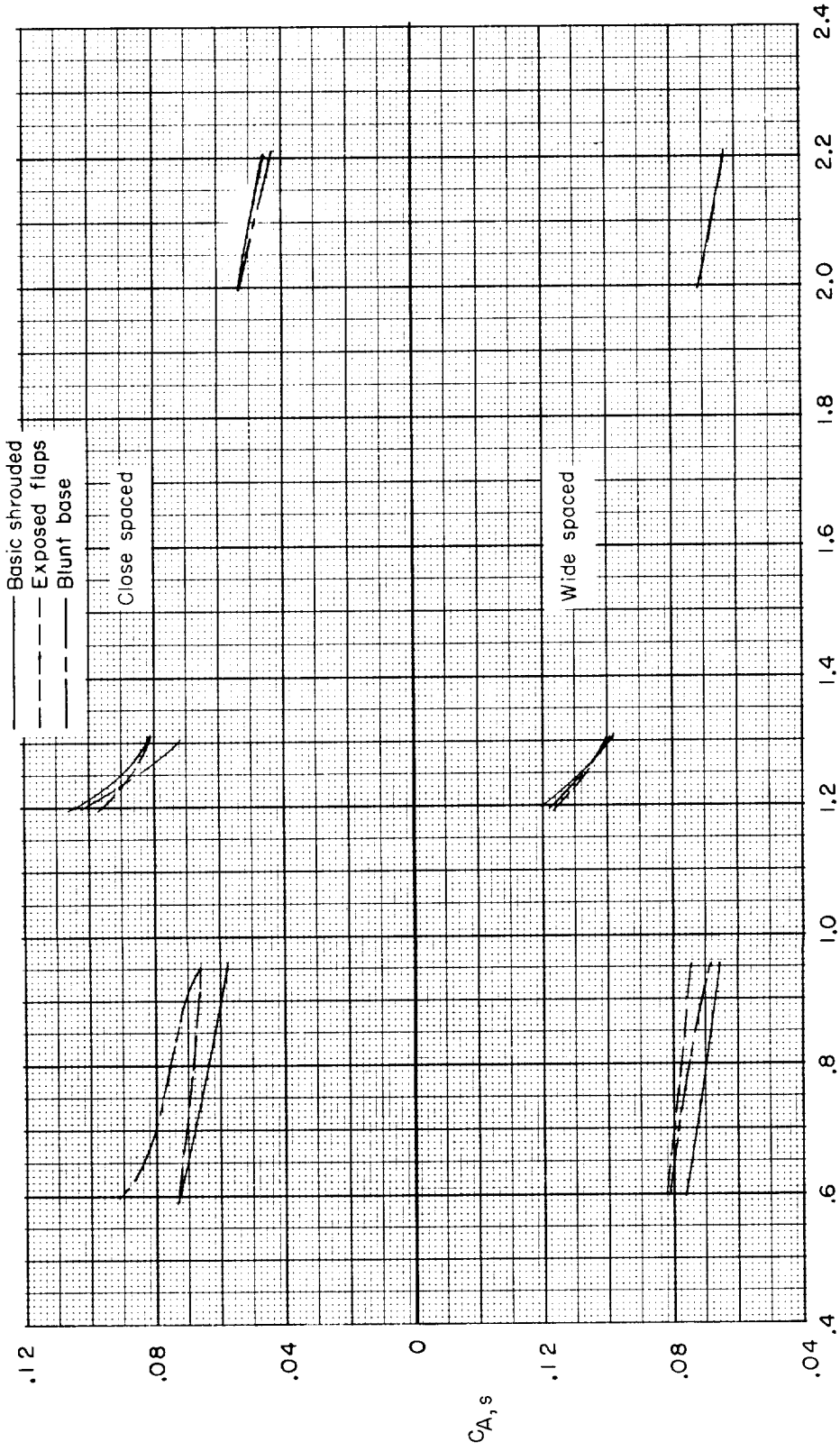

(b) Maximum augmented power.

Figure 28.- Concluded.

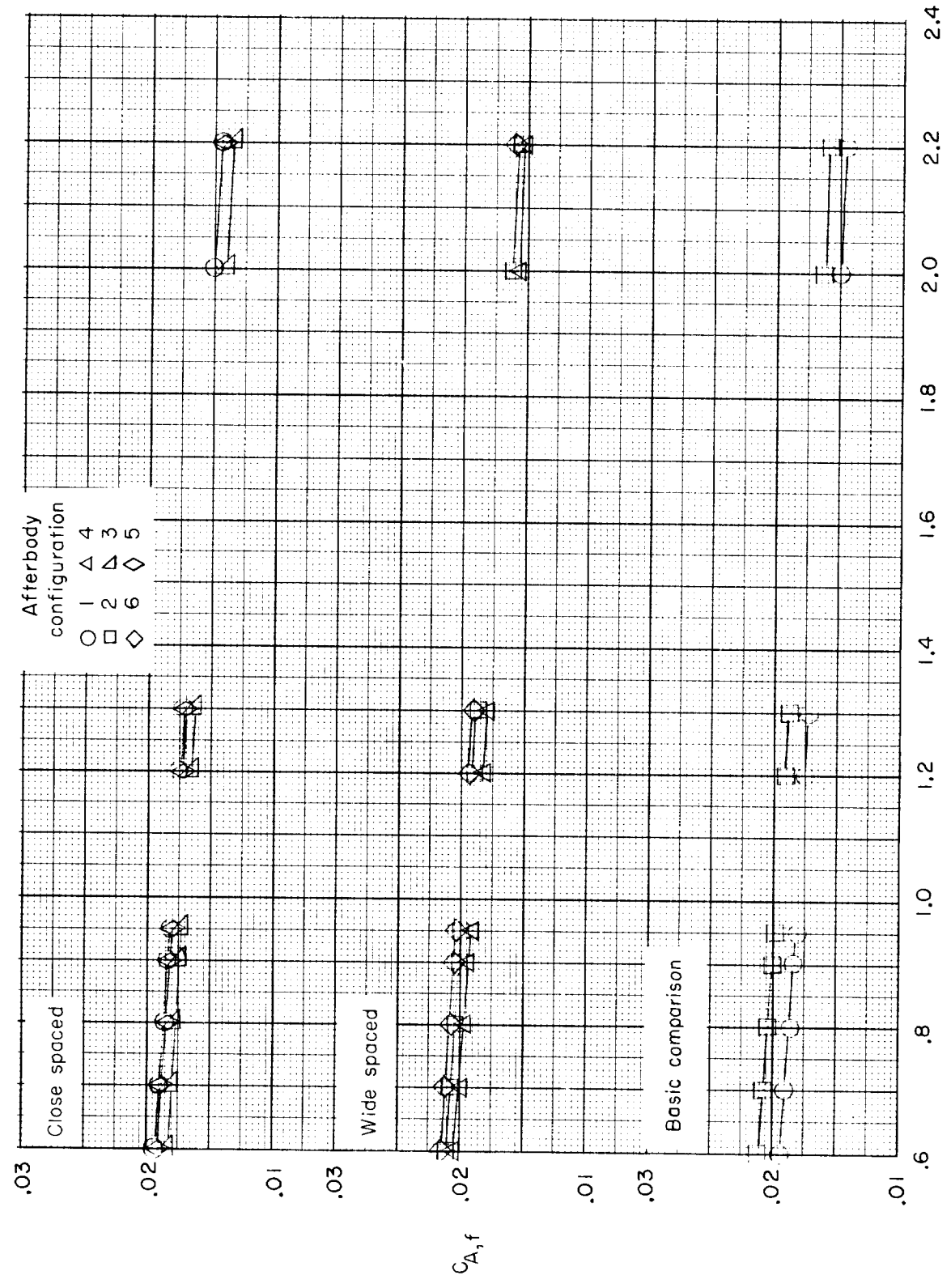

Figure 29.- Variation of calculated skin-friction axial-force coefficient with Mach number and afterbody configuration.

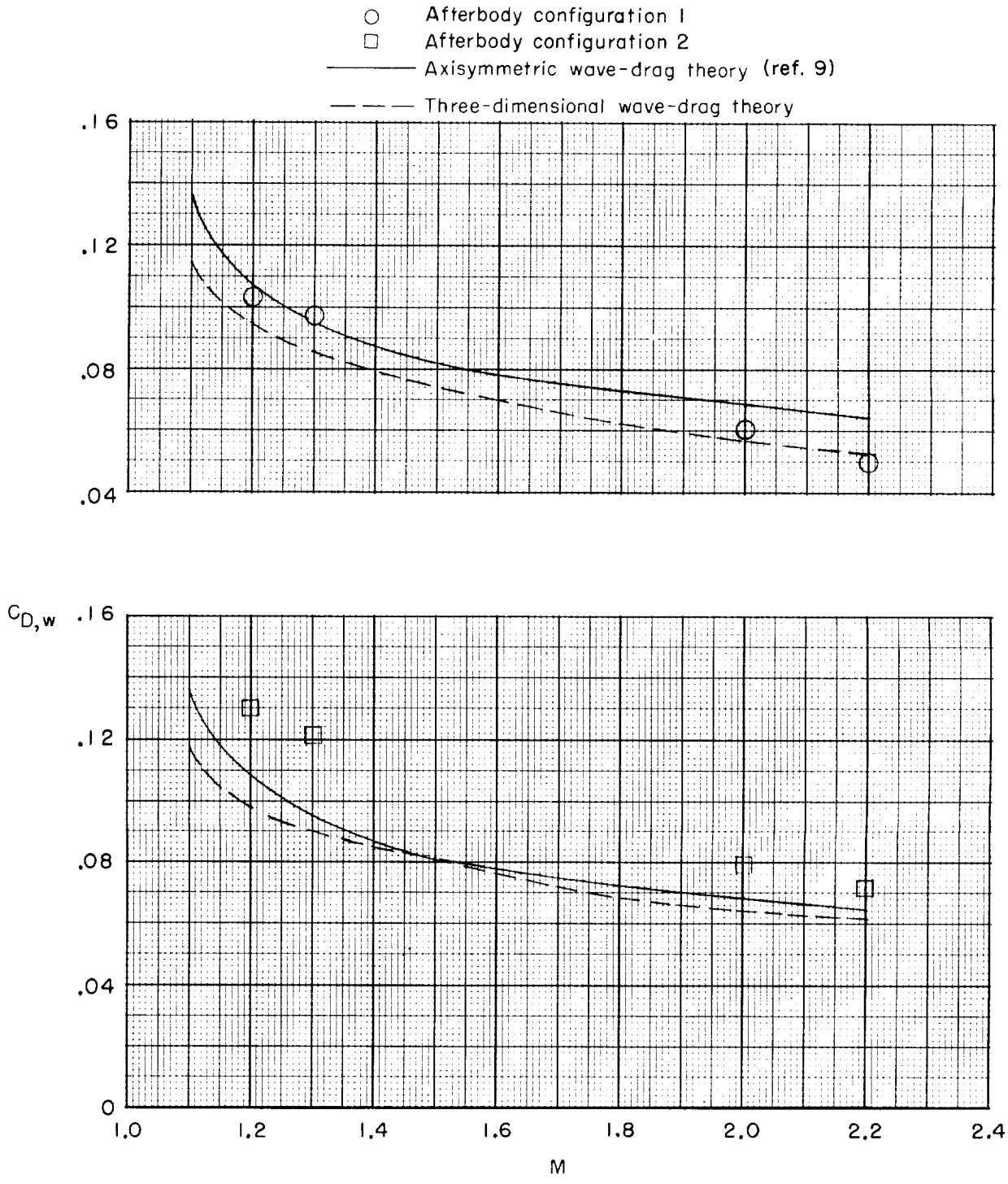

(a) Afterbody configurations 1 and 2.

Figure 30.- Comparison of experimentally and theoretically determined afterbody wave-drag coefficients.

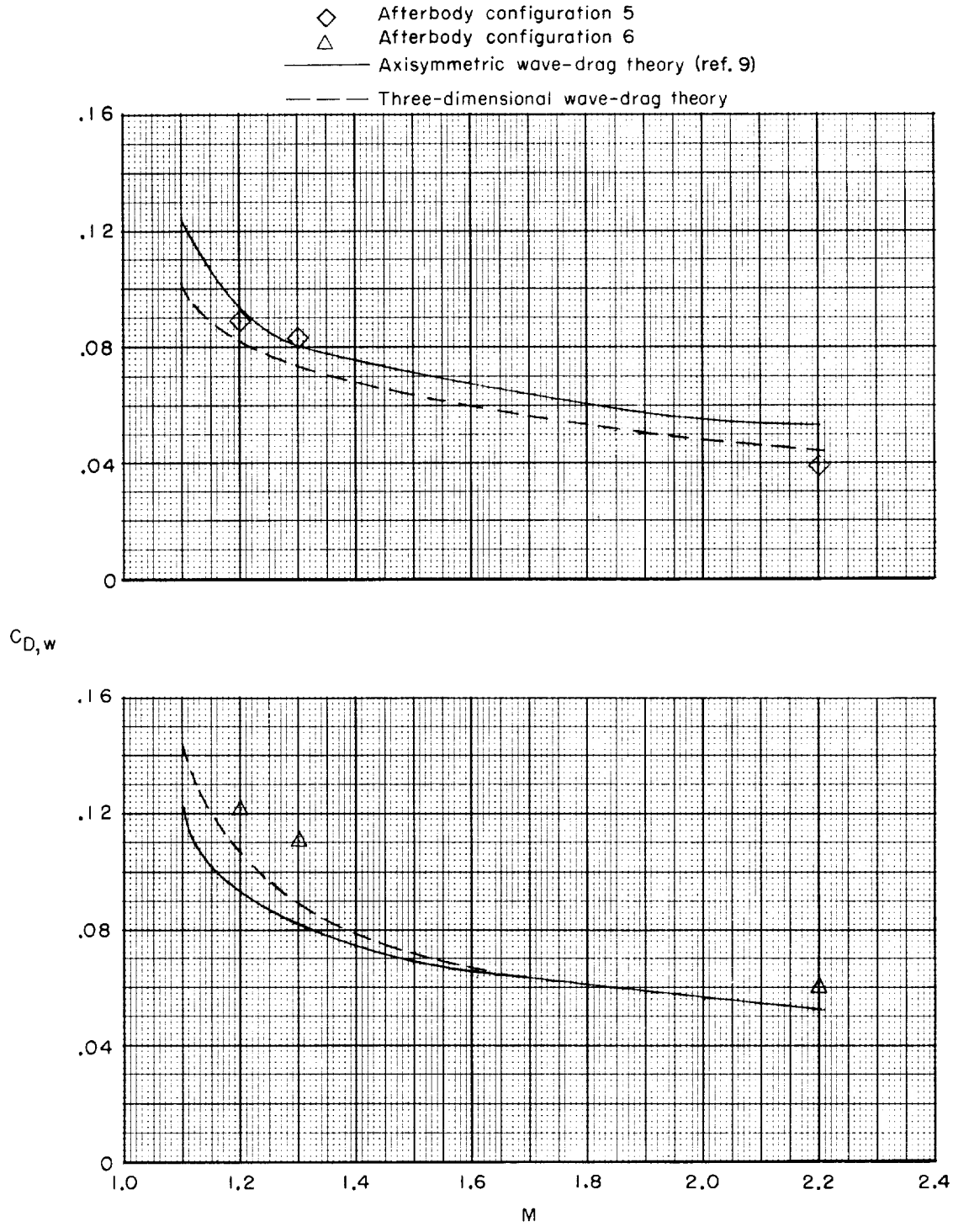

(b) Afterbody configurations 5 and 6.

Figure 30.- Concluded.

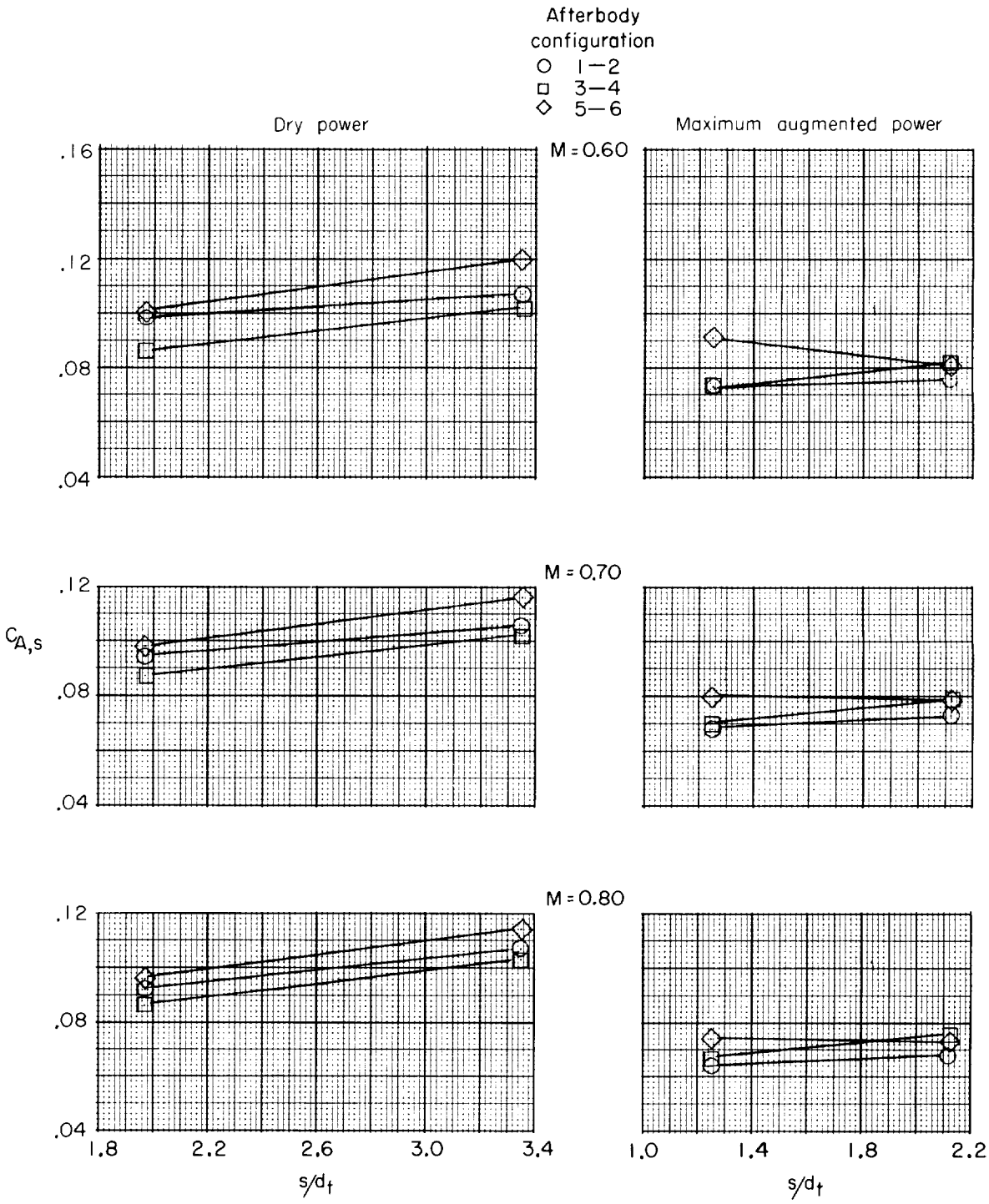

(a) M = 0.60, 0.70, and 0.80.

Figure 31.- Comparison of shroud axial-force coefficient for spacing ratio s/d_t at several Mach numbers.

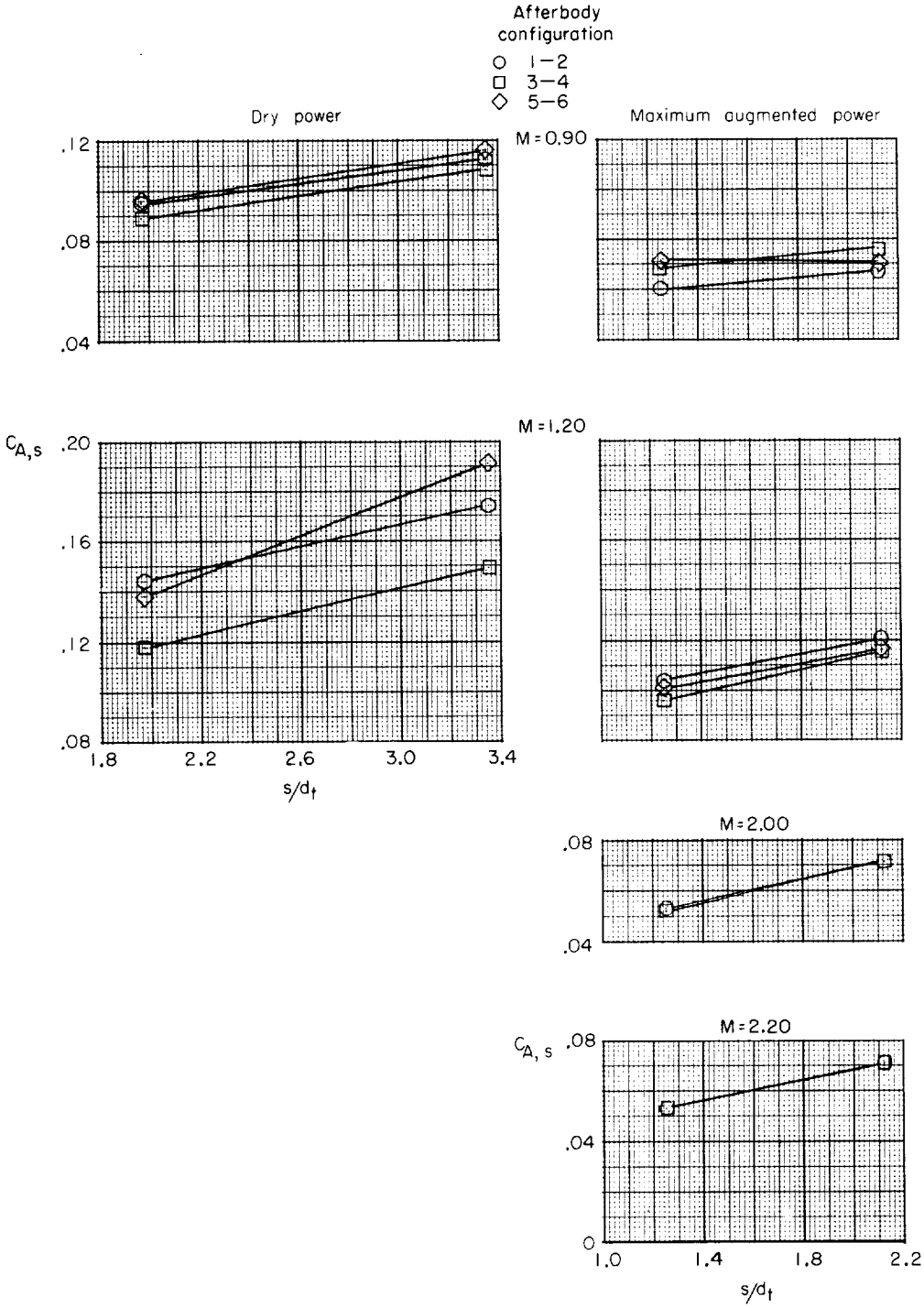

(b) M = 0.90, 1.20, 2.00, and 2.20.

Figure 31.- Concluded.

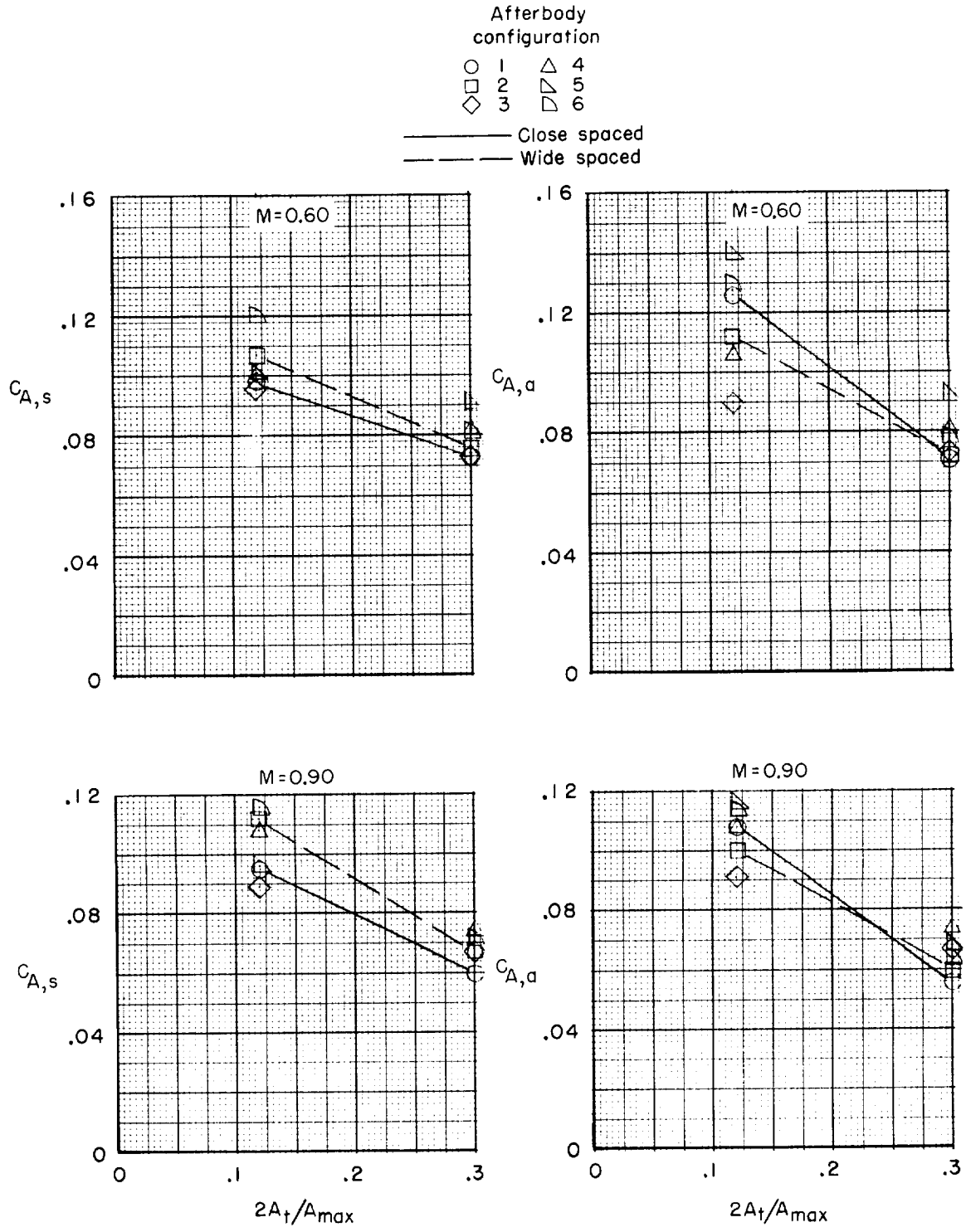

(a) M = 0.60 and 0.90.

Figure 32.- Variation of axial-force coefficients with the power parameter $2A_t/A_{max}$.

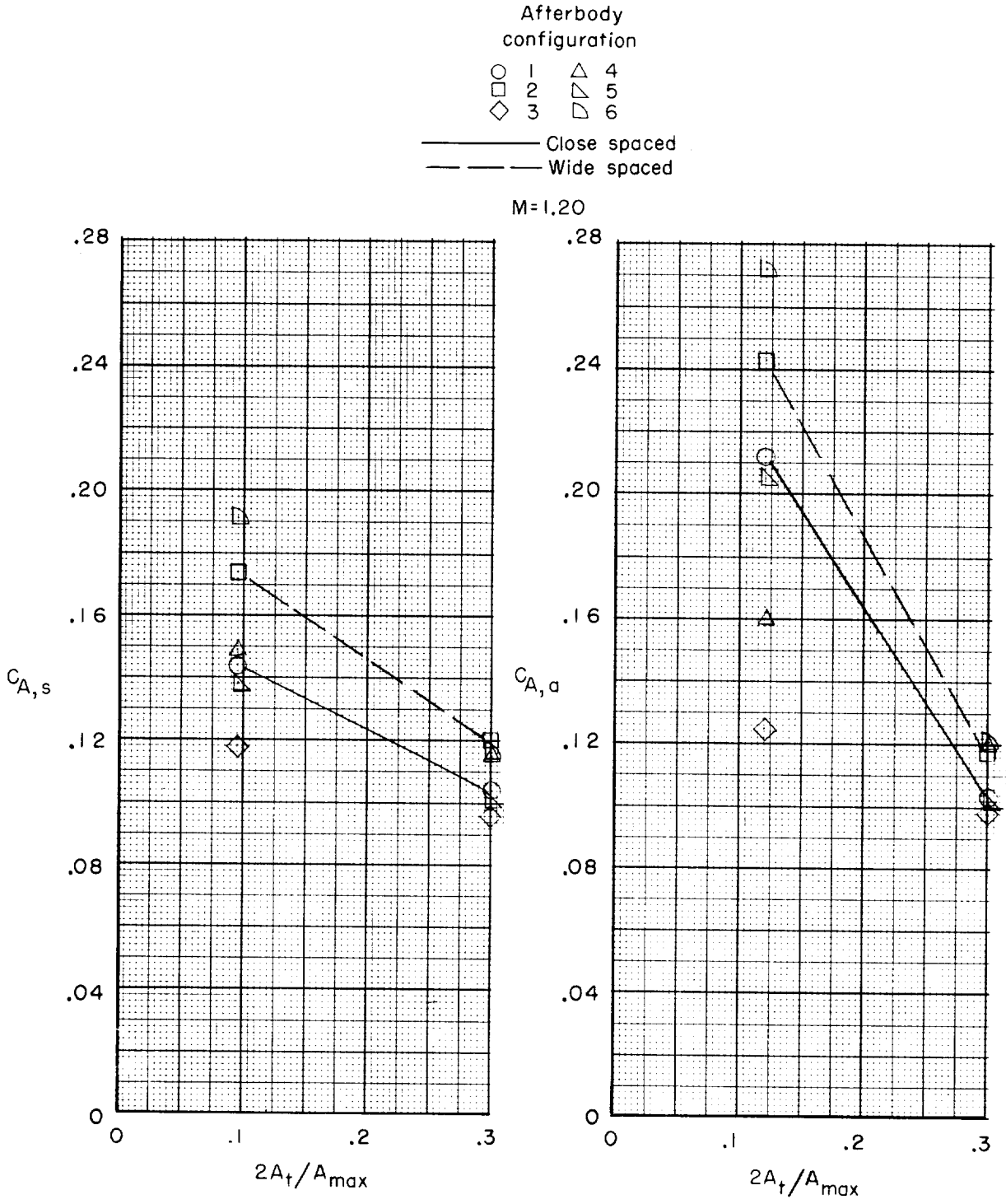

(b) M = 1.20.

Figure 32.- Concluded.

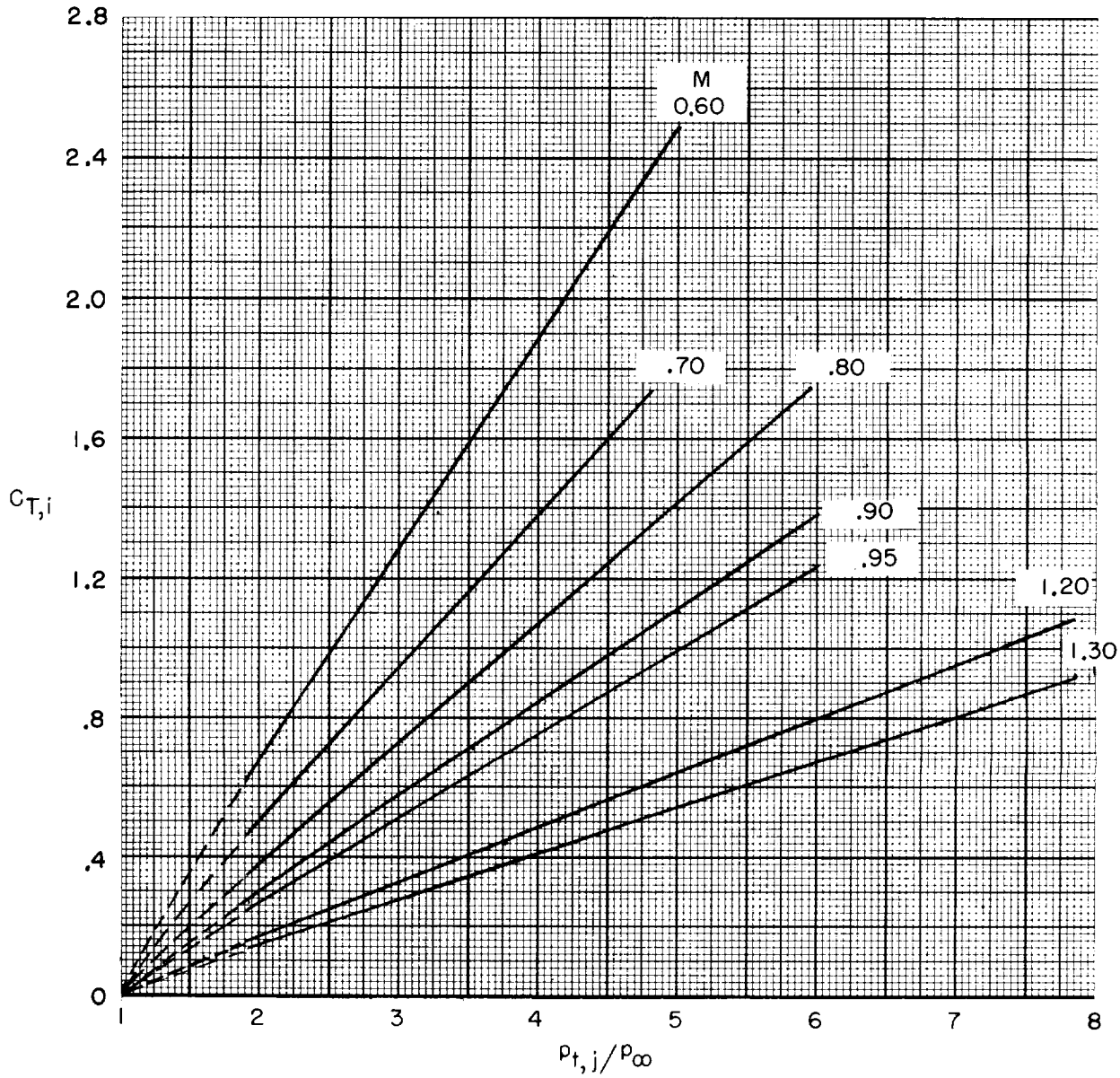

(a) Dry-power setting.

Figure 33.- Variation of aerodynamic ideal-thrust coefficient with jet-total-pressure ratio.

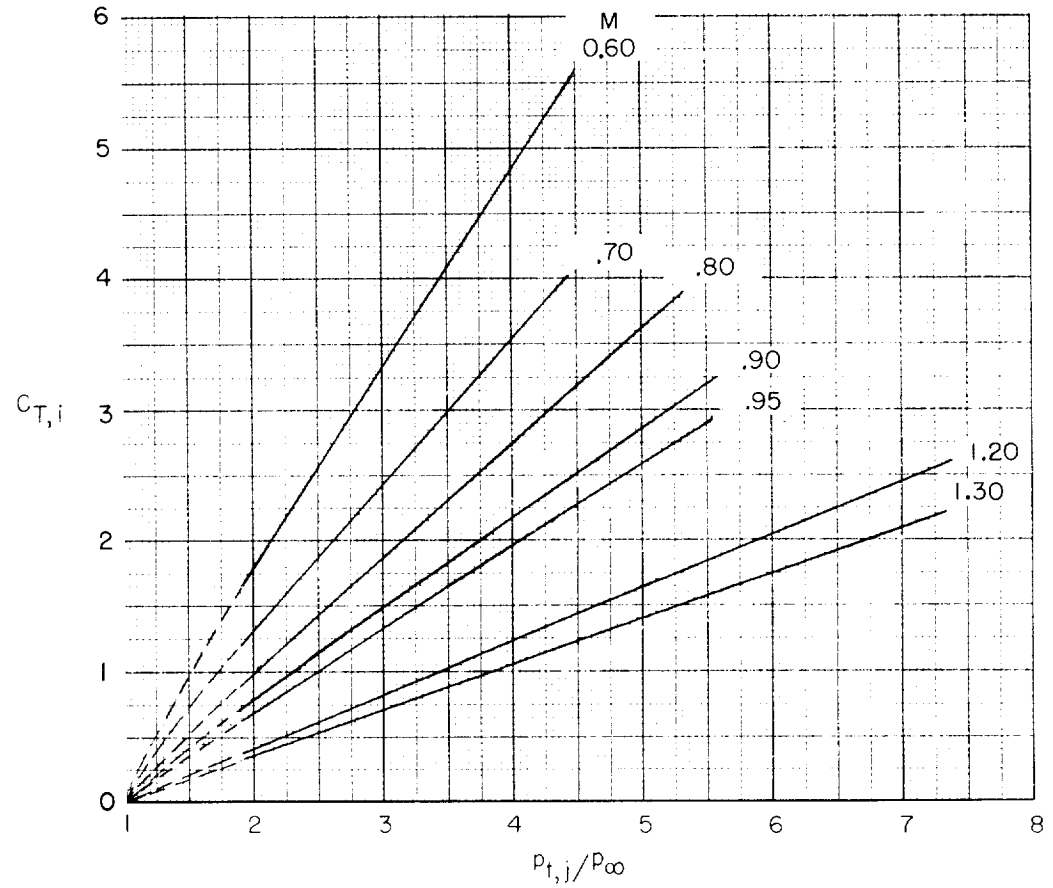

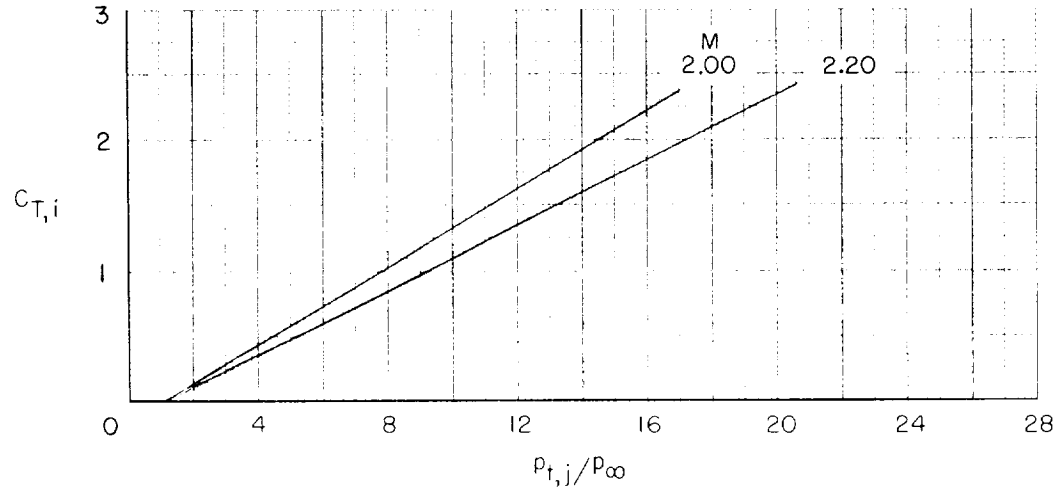

(b) Maximum-augmented-power setting.

Figure 33.- Concluded.

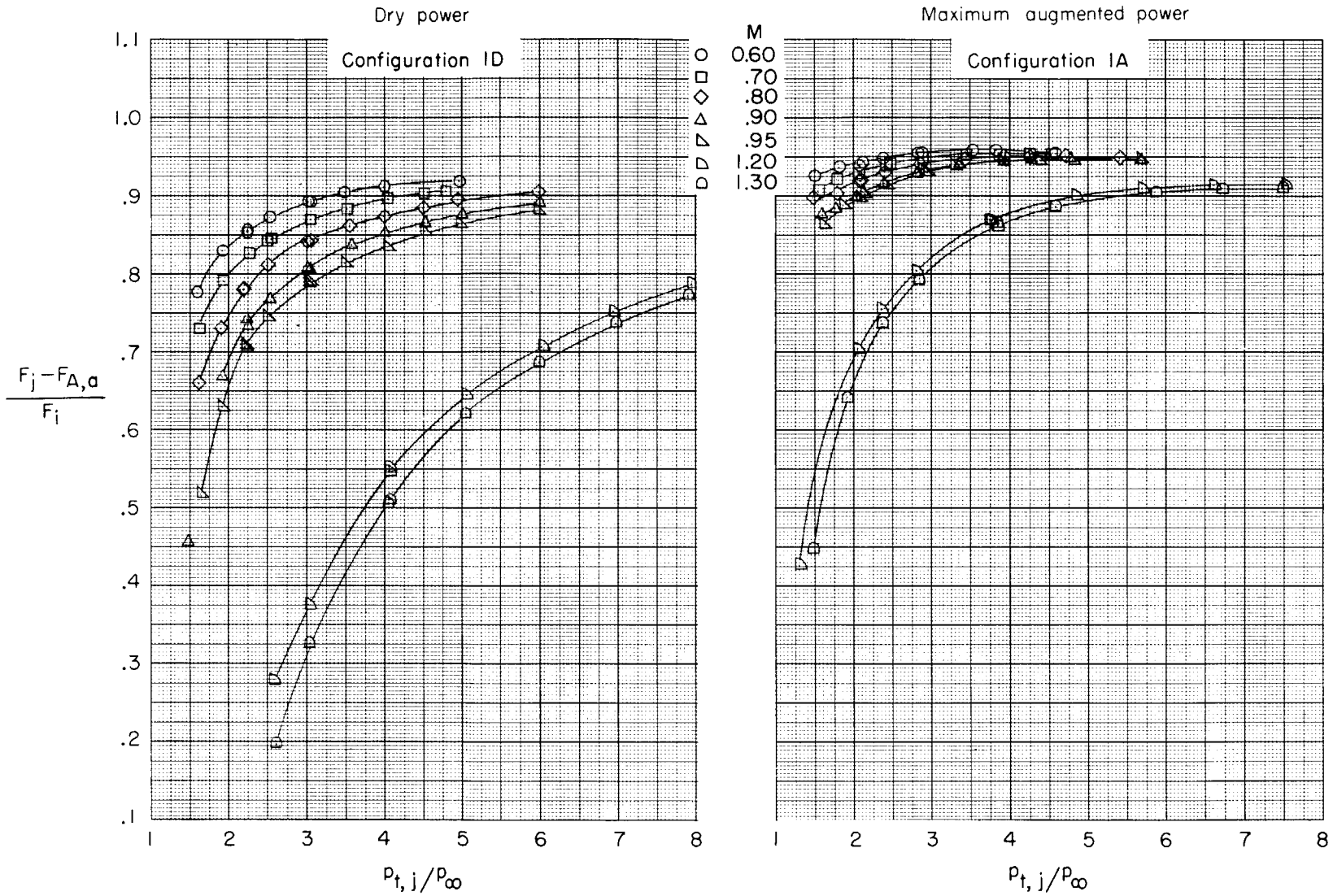

(a) Configurations 1A and 1D.

Figure 34.- Variation of thrust-minus-drag ratio with jet-total-pressure ratio.

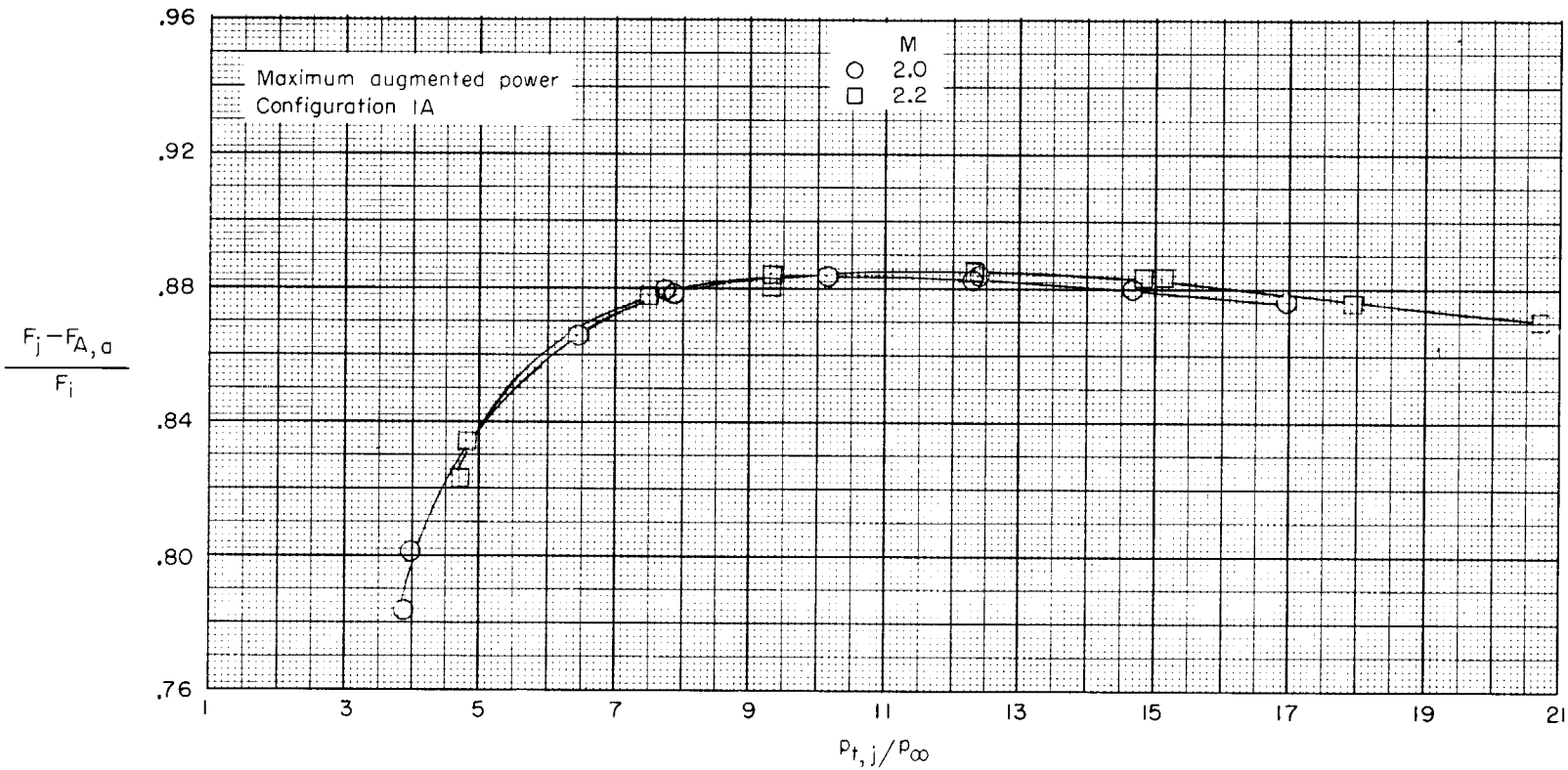

(a) Concluded.

Figure 34.- Continued.

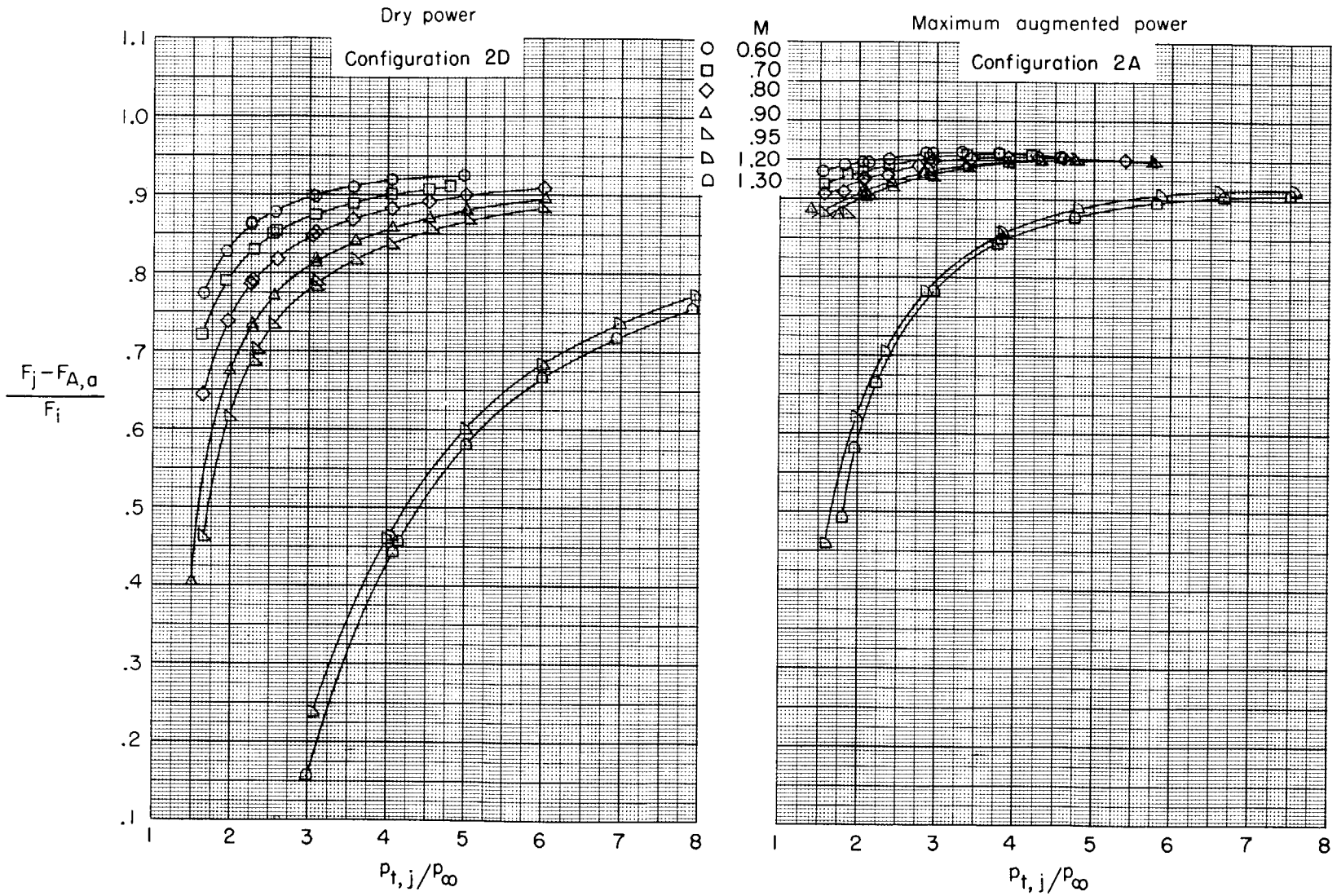

(b) Configurations 2A and 2D.

Figure 34.- Continued.

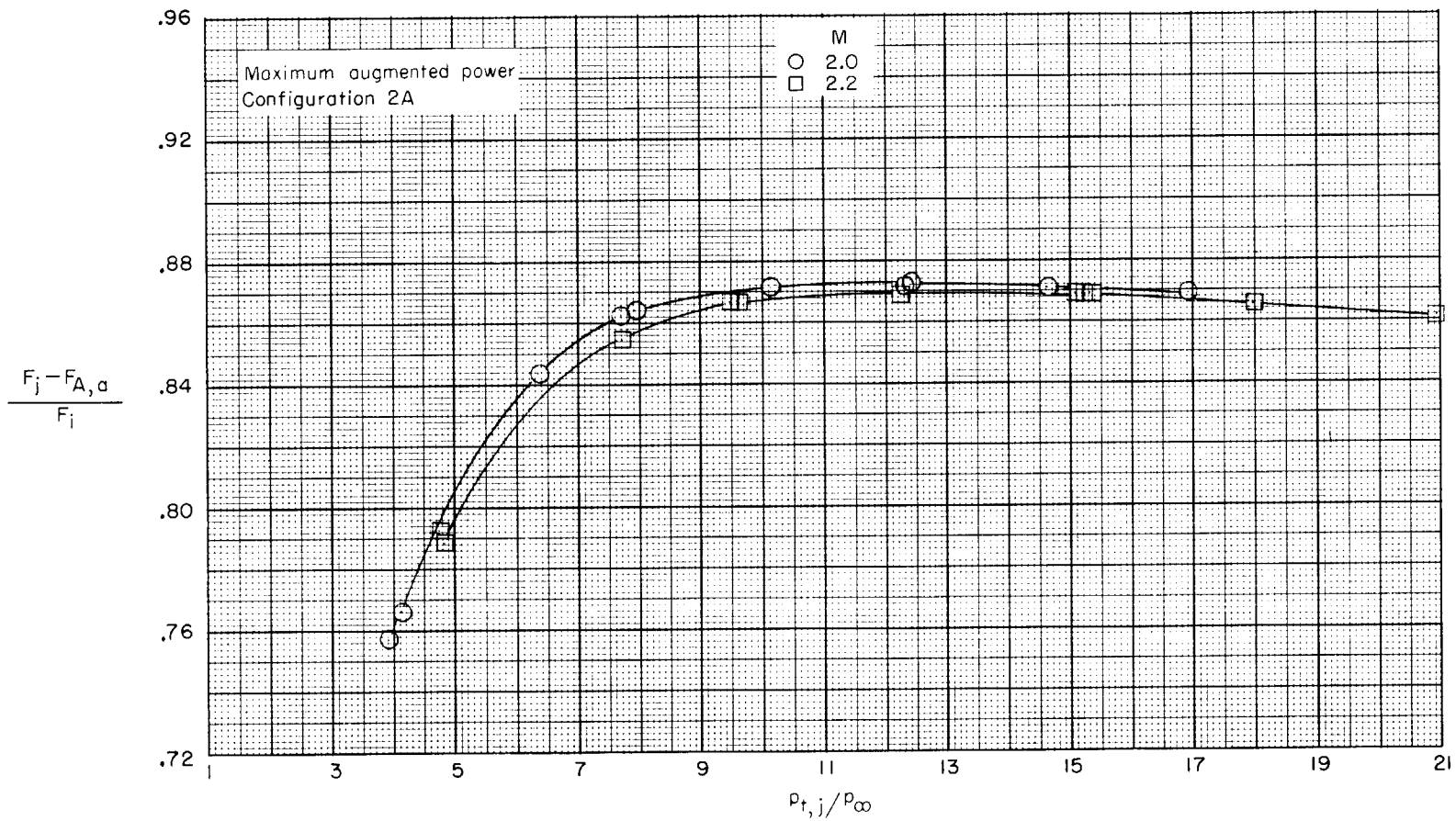

(b) Concluded.

Figure 34.- Continued.

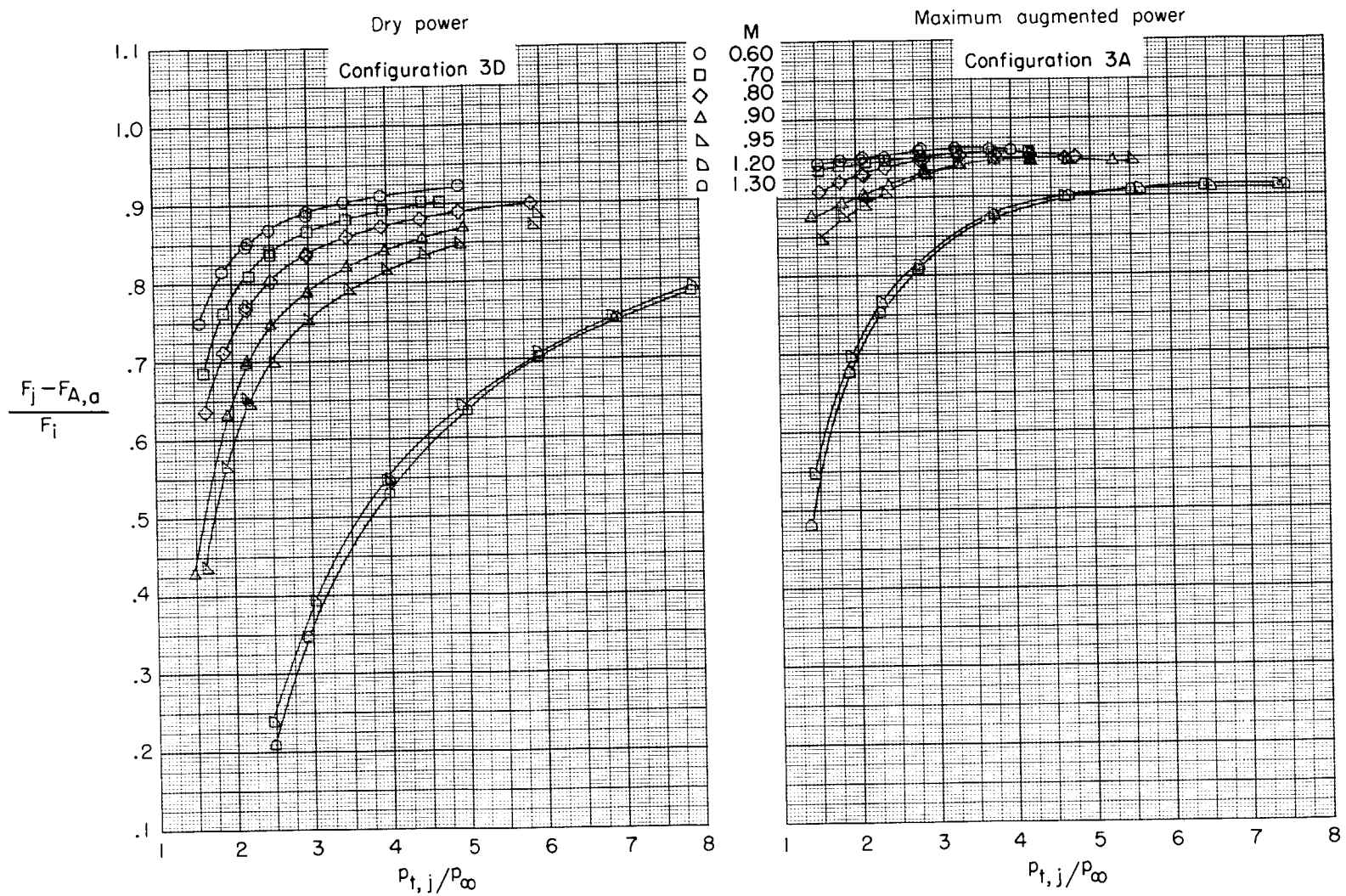

(c) Configurations 3A and 3D.

Figure 34.- Continued.

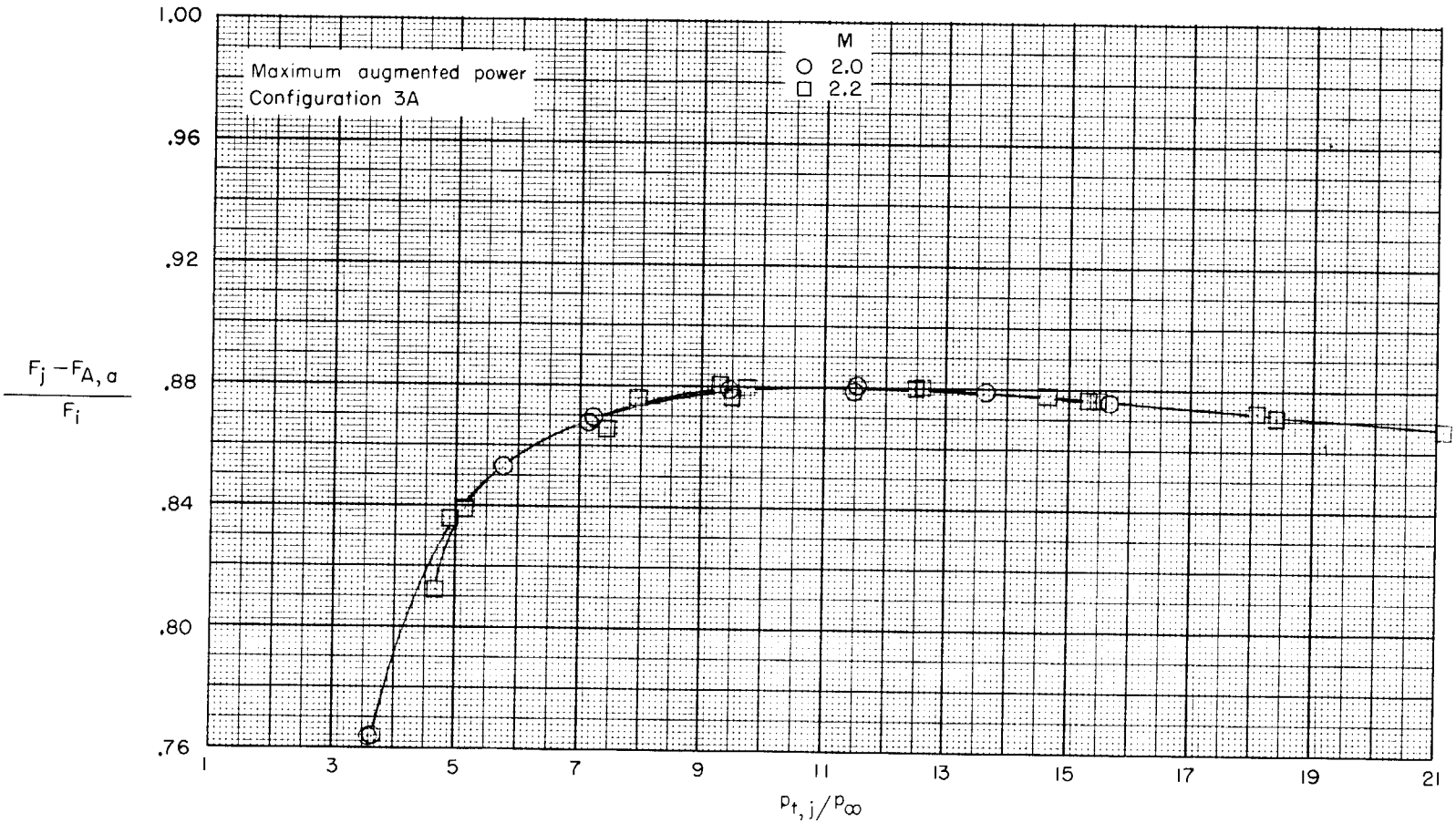

(c) Concluded.

Figure 34.- Continued.

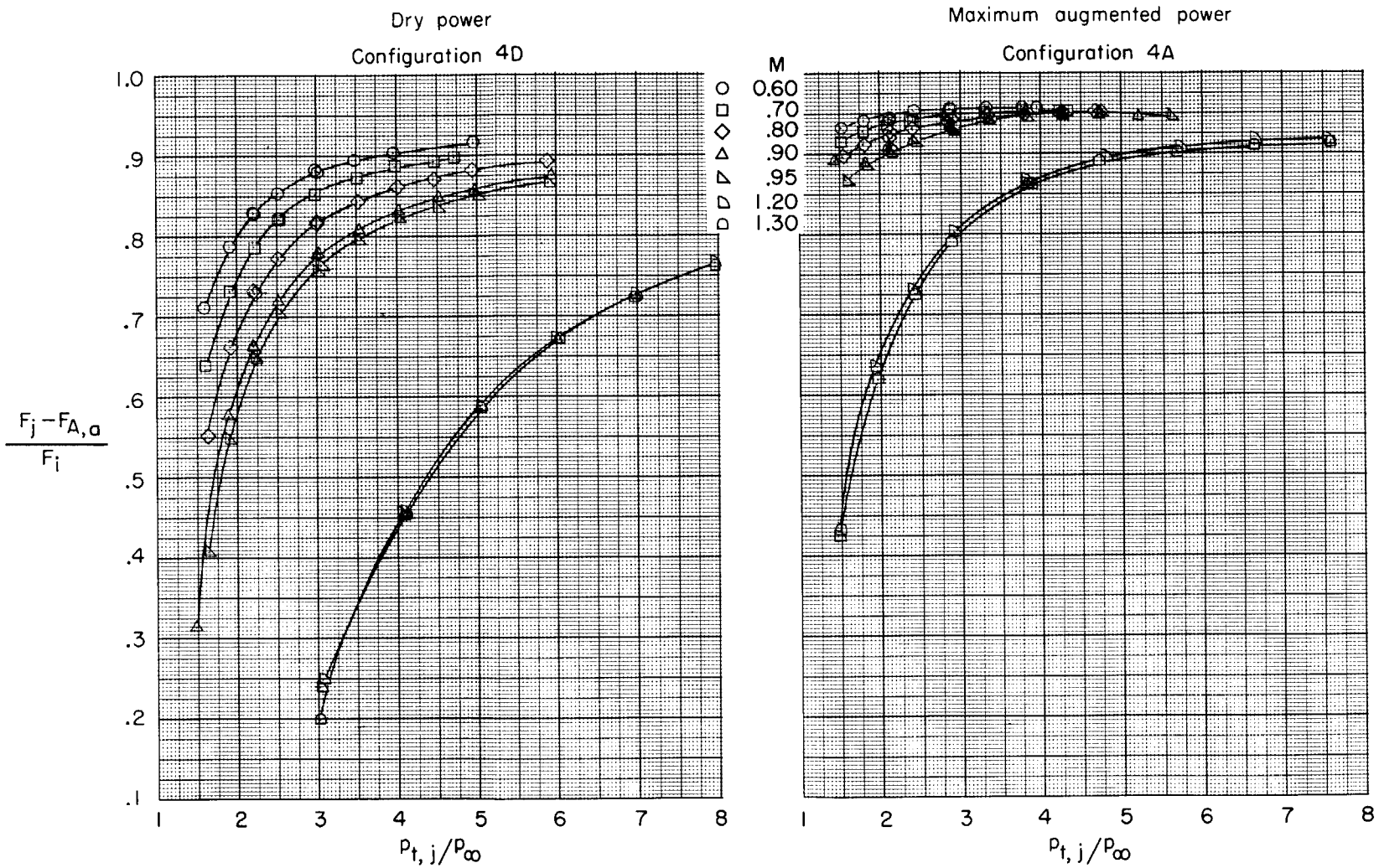

(d) Configurations 4A and 4D.

Figure 34.- Continued.

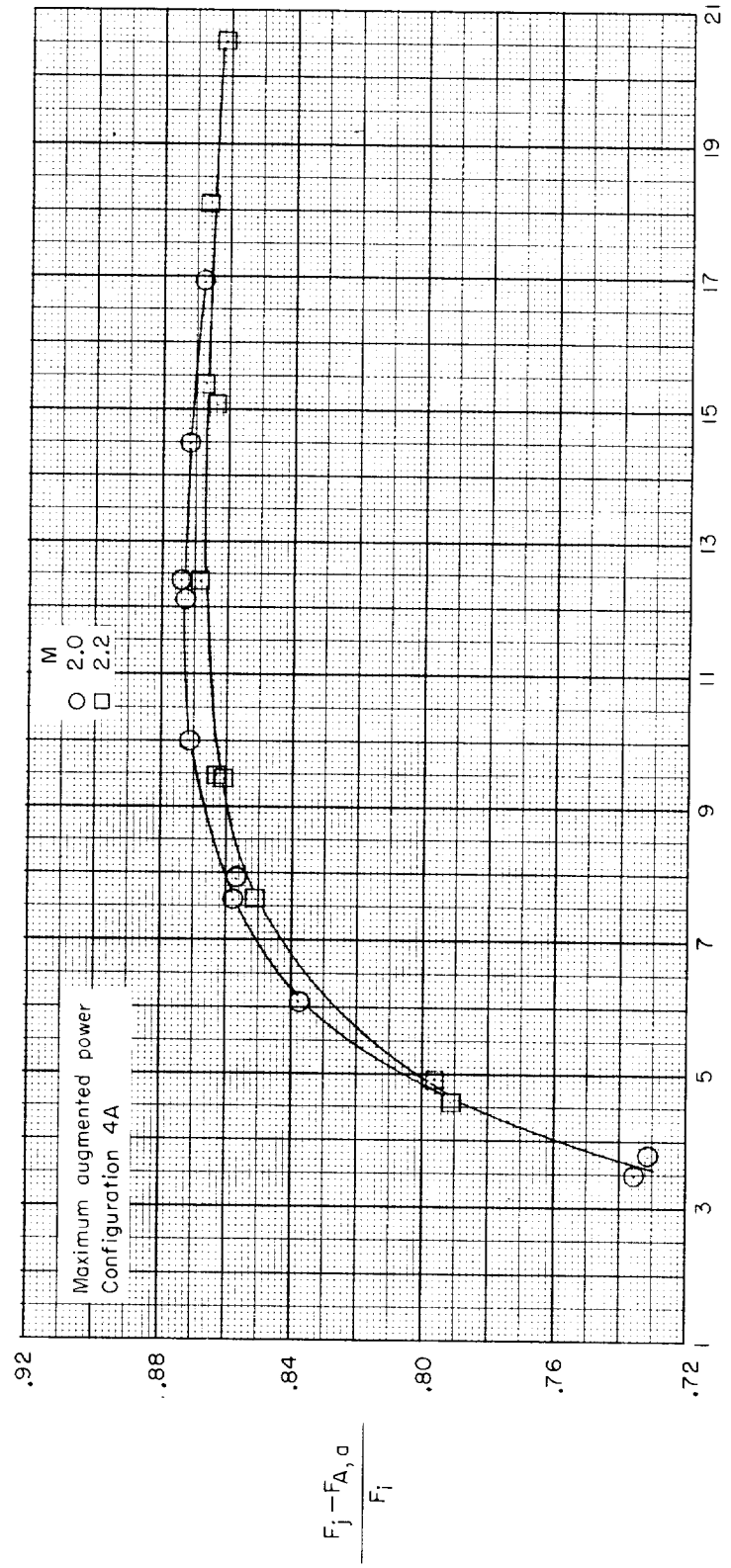

(d) Concluded.

Figure 34.- Continued.

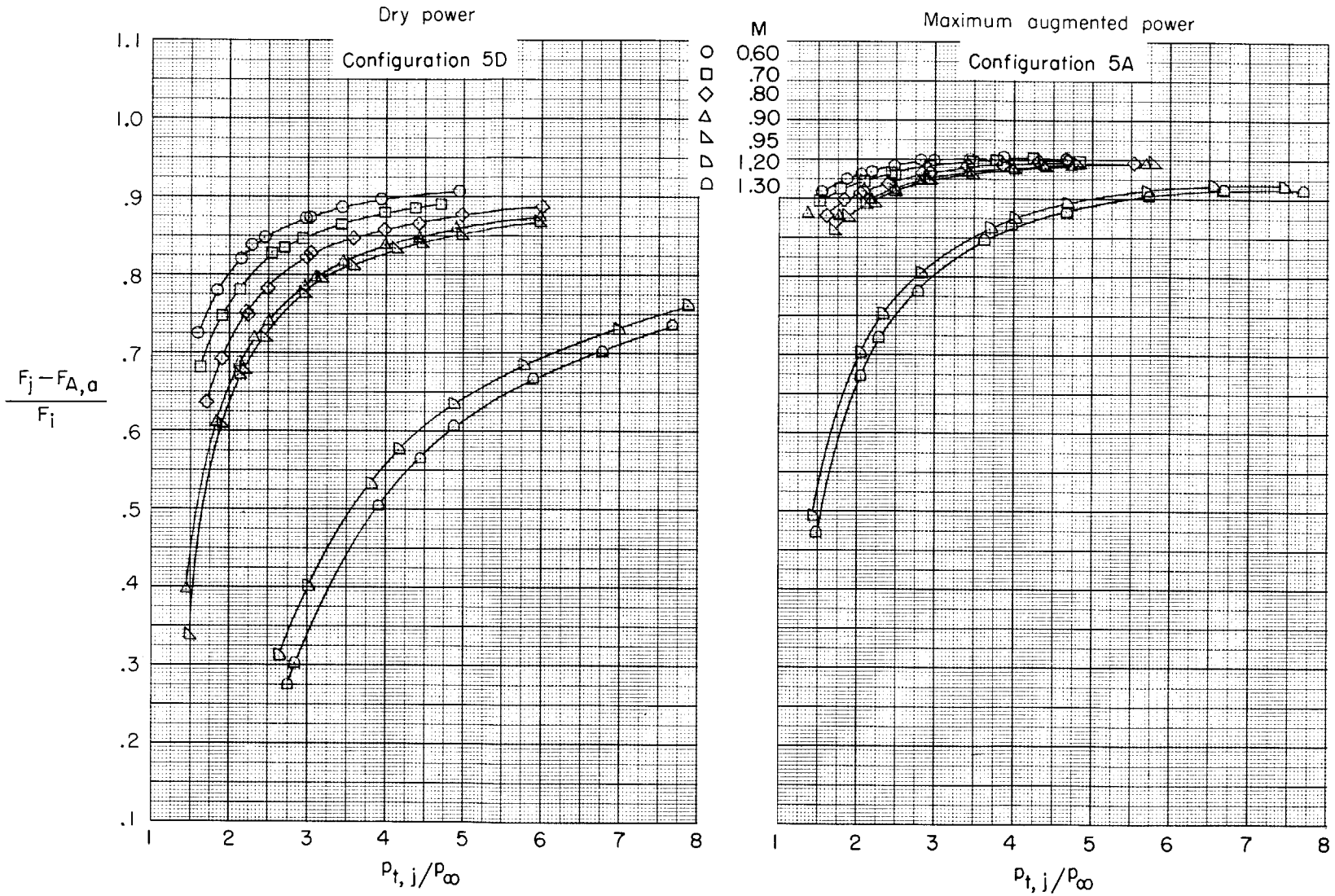

(e) Configurations 5A and 5D.

Figure 34.- Continued.

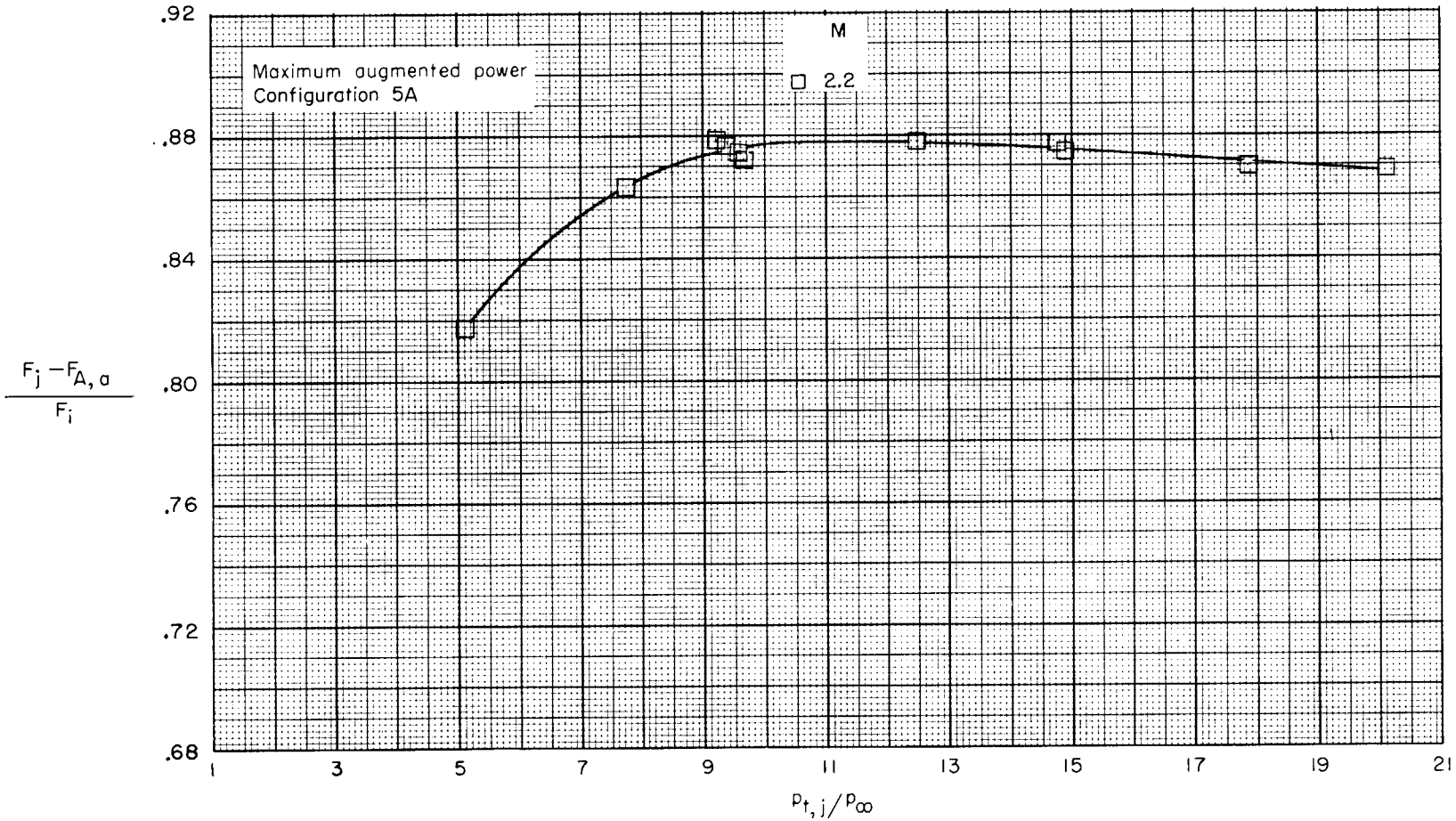

(e) Concluded.

Figure 34.- Continued.

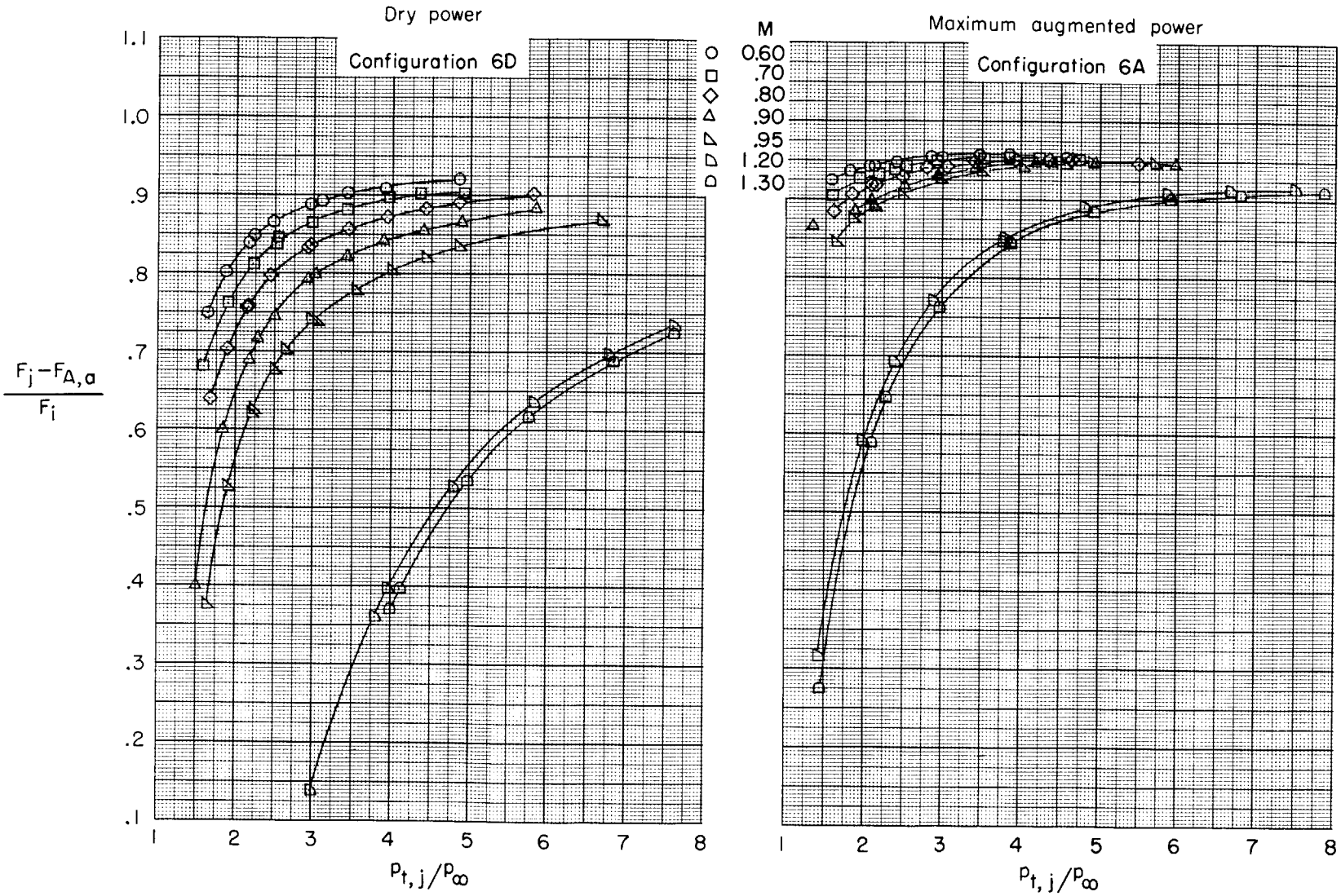

(f) Configurations 6A and 6D.

Figure 34.- Continued.

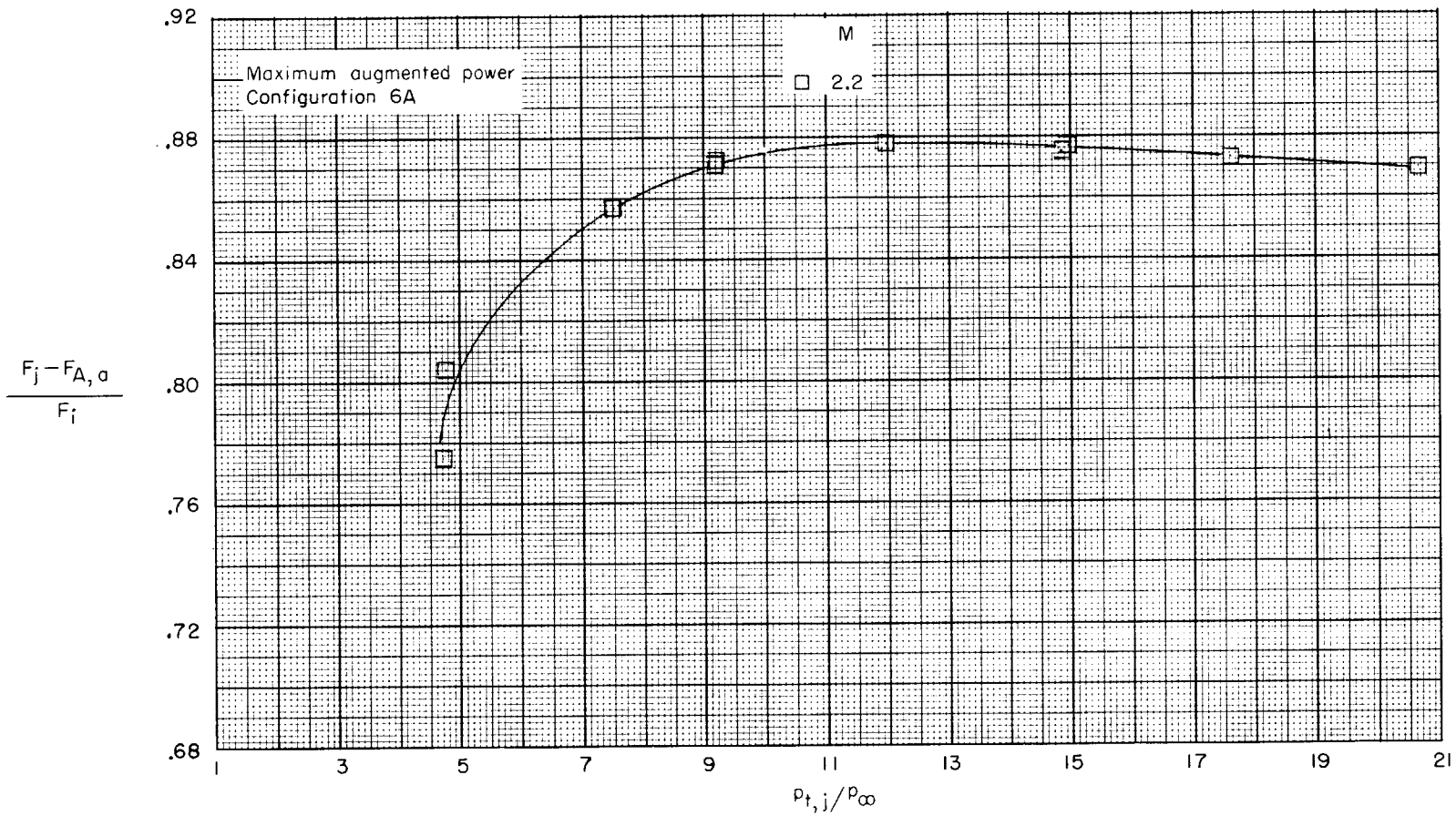

(f) Concluded.

Figure 34.- Concluded.

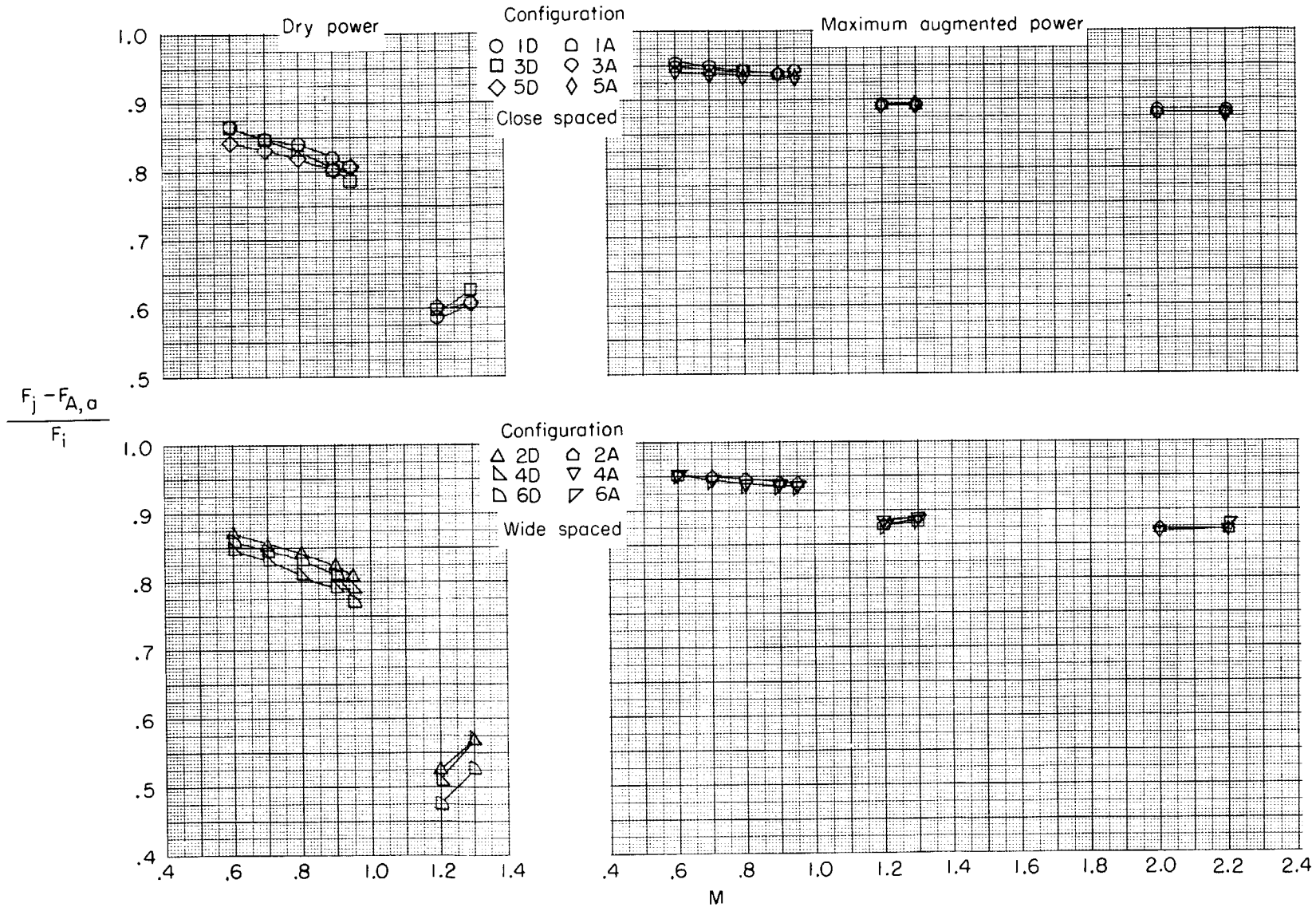

Figure 35.- Variation of thrust-minus-drag ratio with Mach number, power setting, and configuration for typical jet-pressure-ratio schedule.

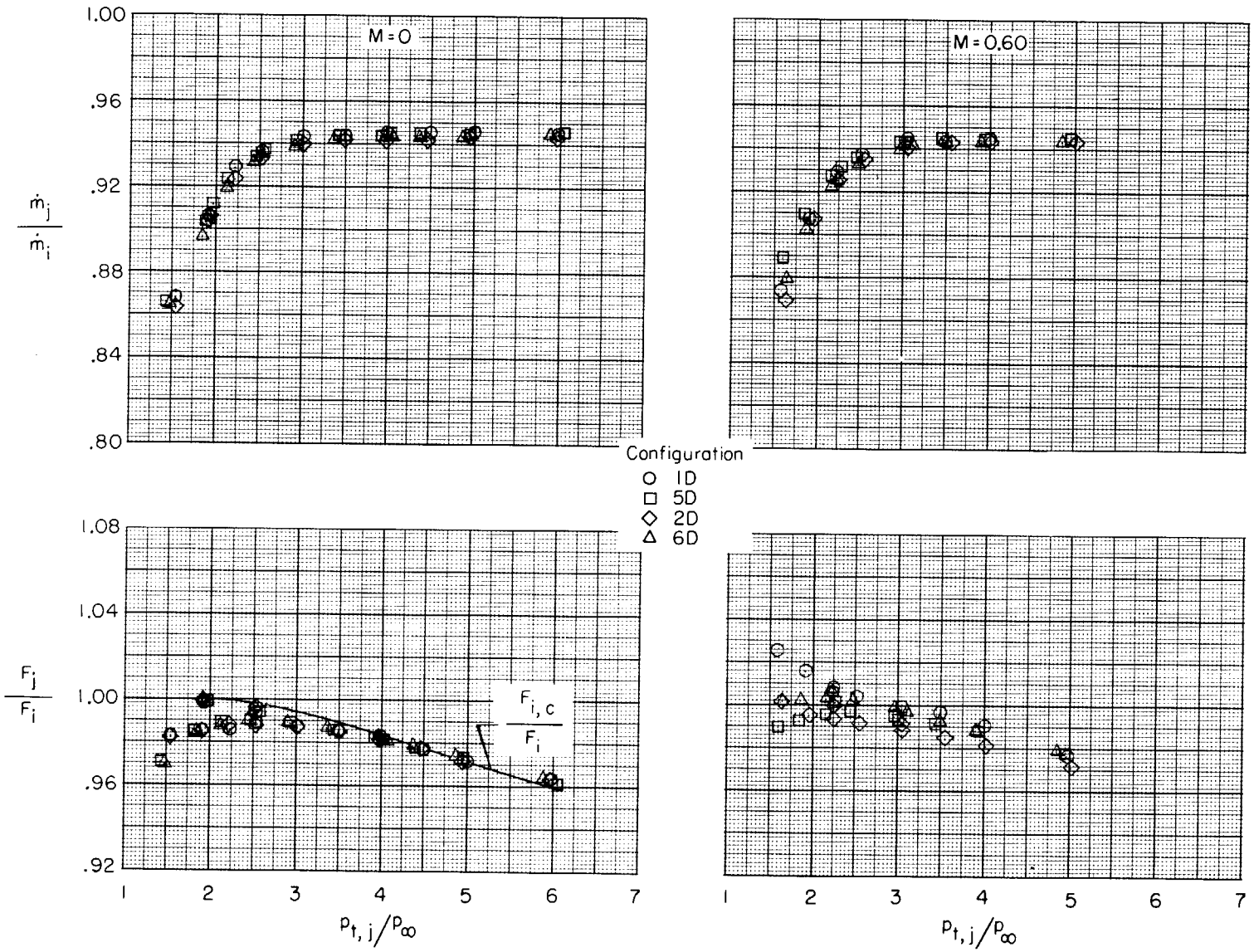

(a) M = 0 and 0.60.

Figure 36.- Internal performance at several Mach numbers for dry-power setting.

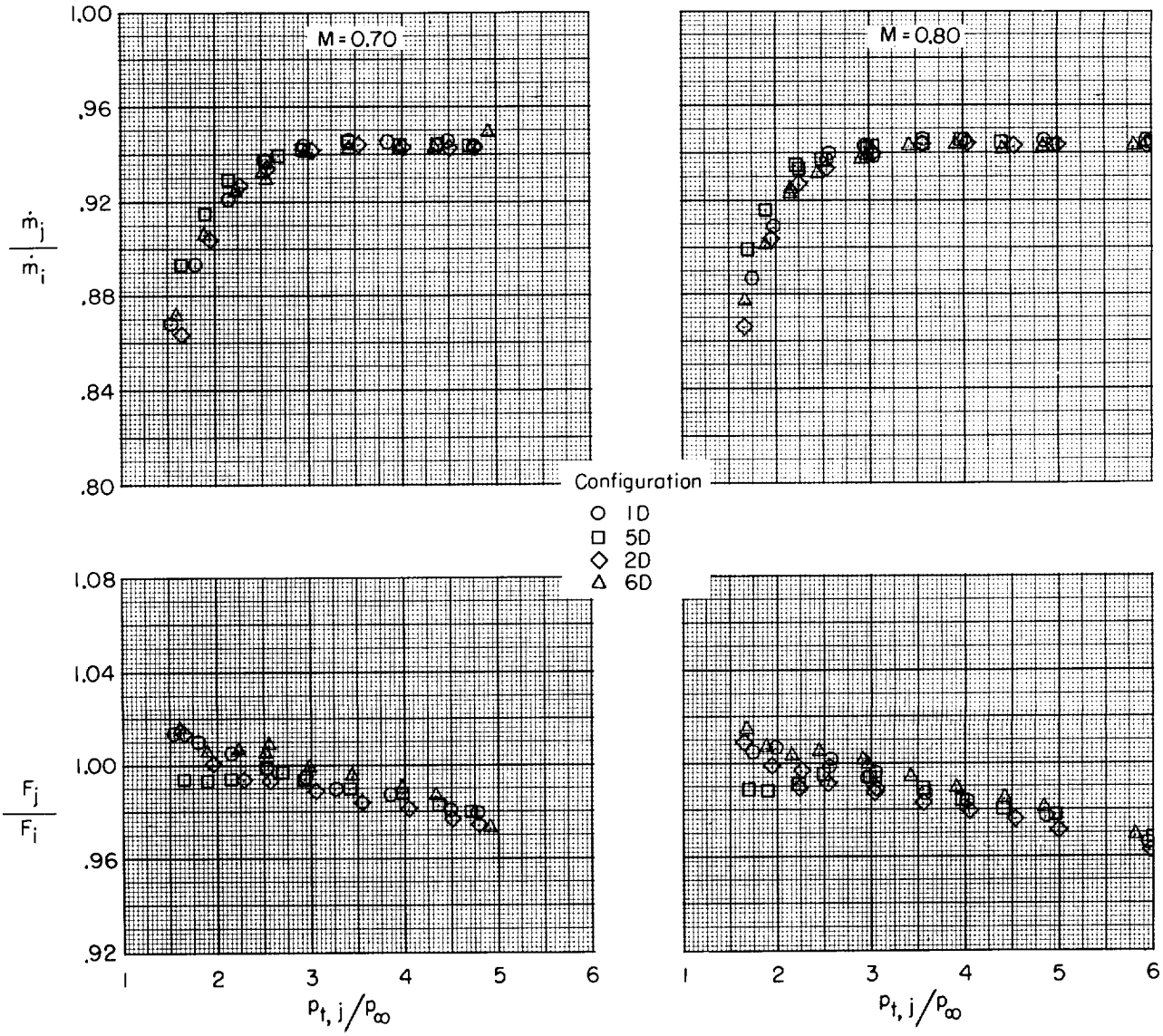

(b) M = 0.70 and 0.80.

Figure 36.- Continued.

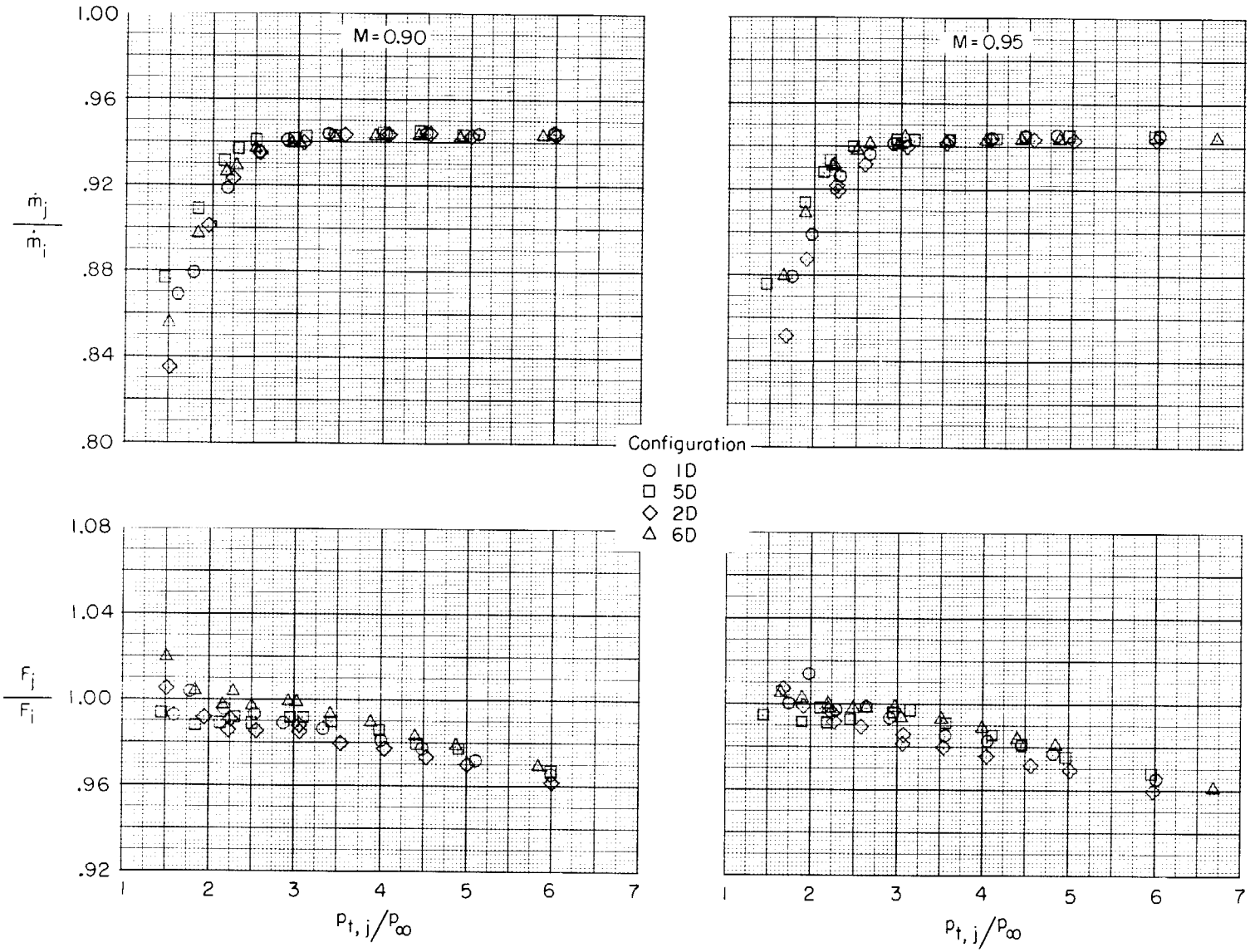

(c) M = 0.90 and 0.95.

Figure 36.- Continued.

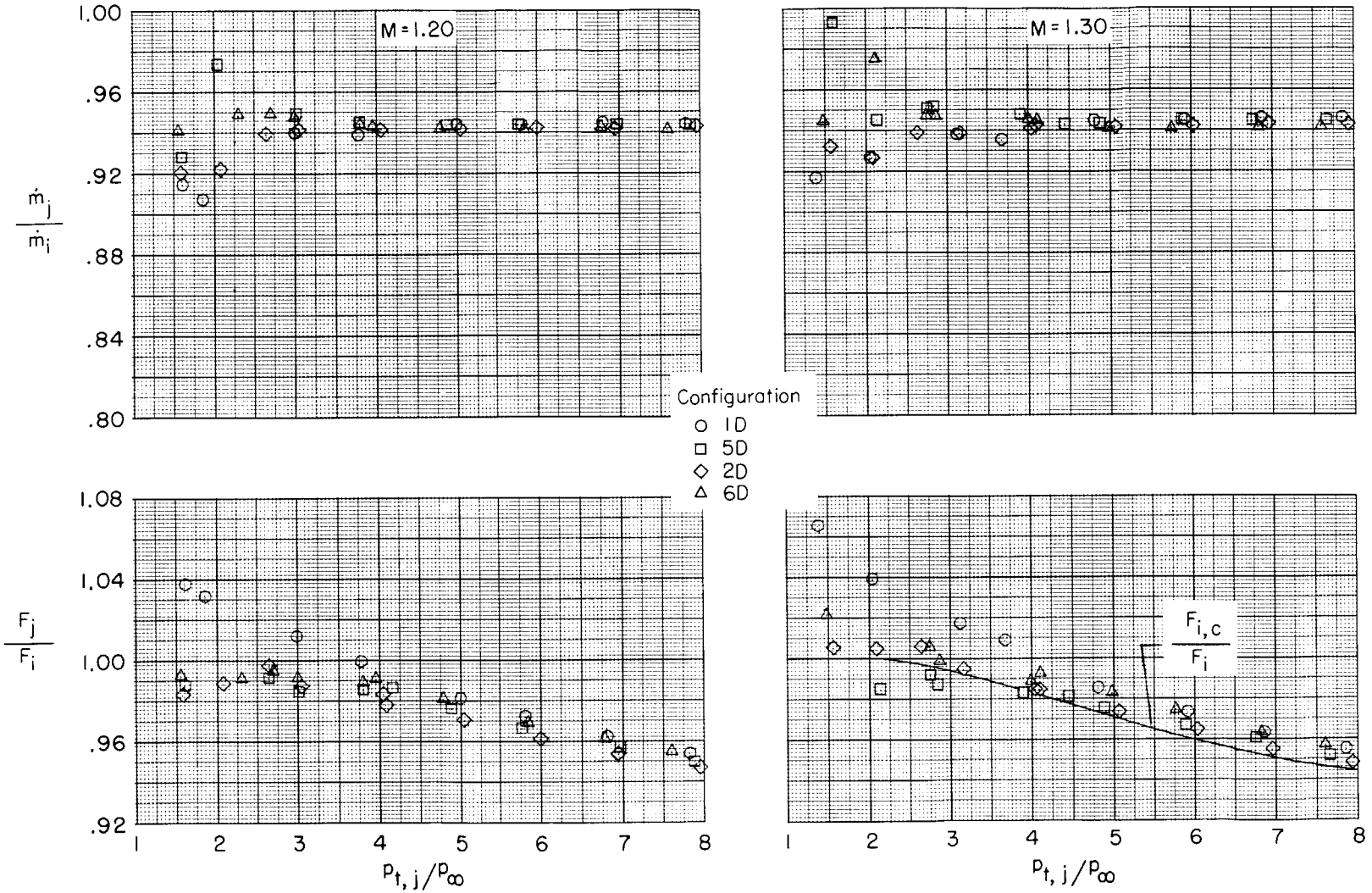

(d) M = 1.20 and 1.30.

Figure 36.- Concluded.

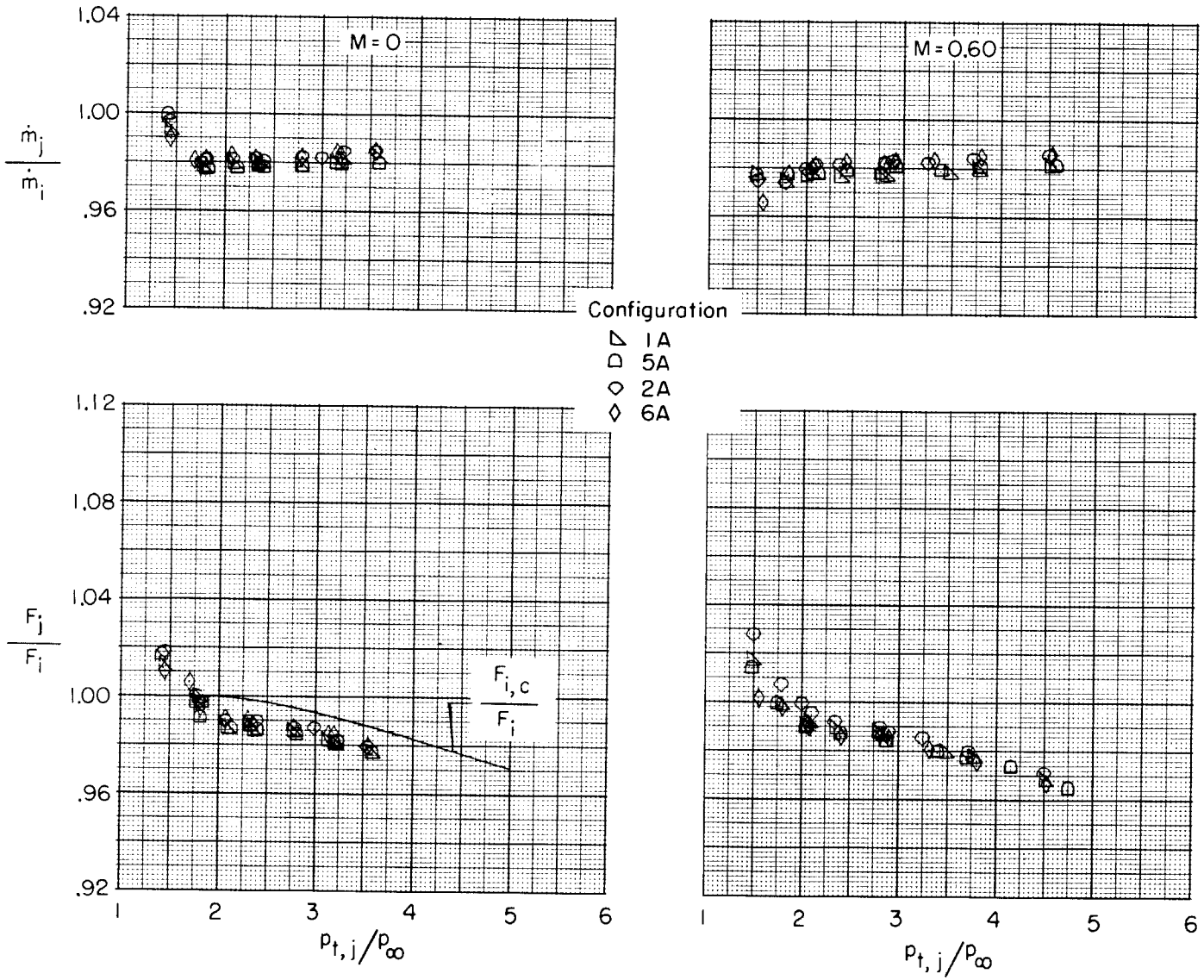

(a) M = 0 and 0.60.

Figure 37.- Internal performance at several Mach numbers for maximum-augmented-power setting.

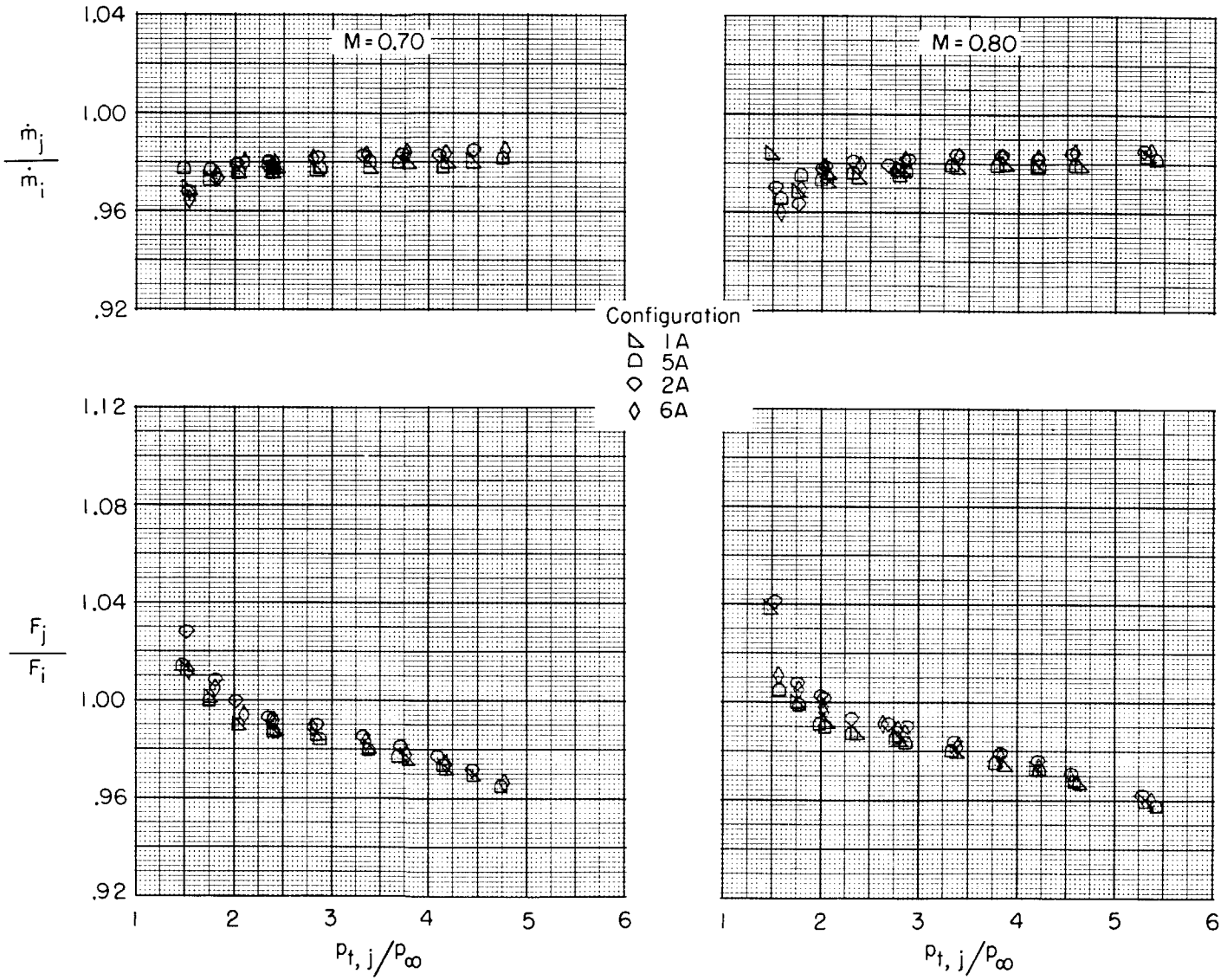

(b) M = 0.70 and 0.80.

Figure 37.- Continued.

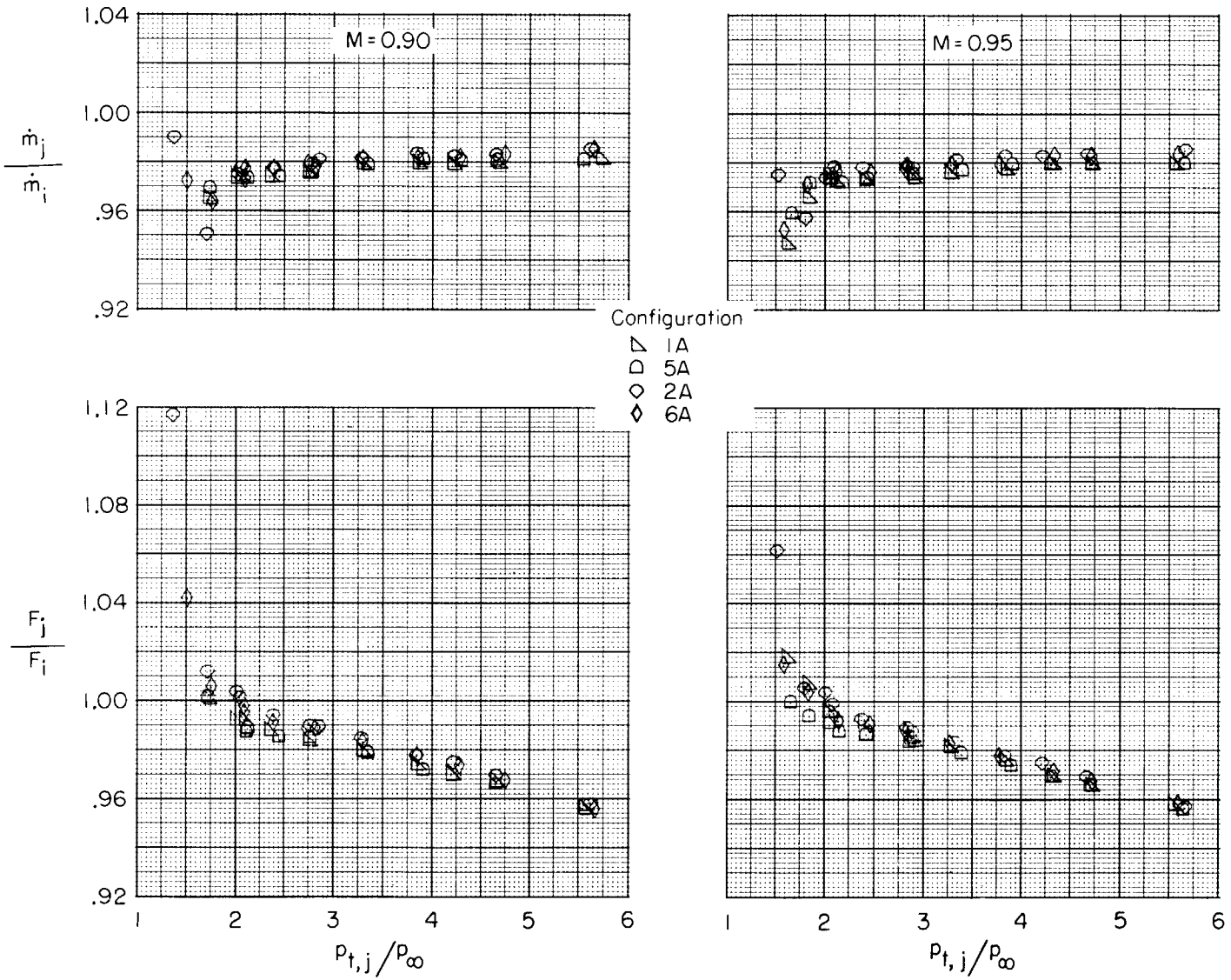

(c) M = 0.90 and 0.95.

Figure 37.- Continued.

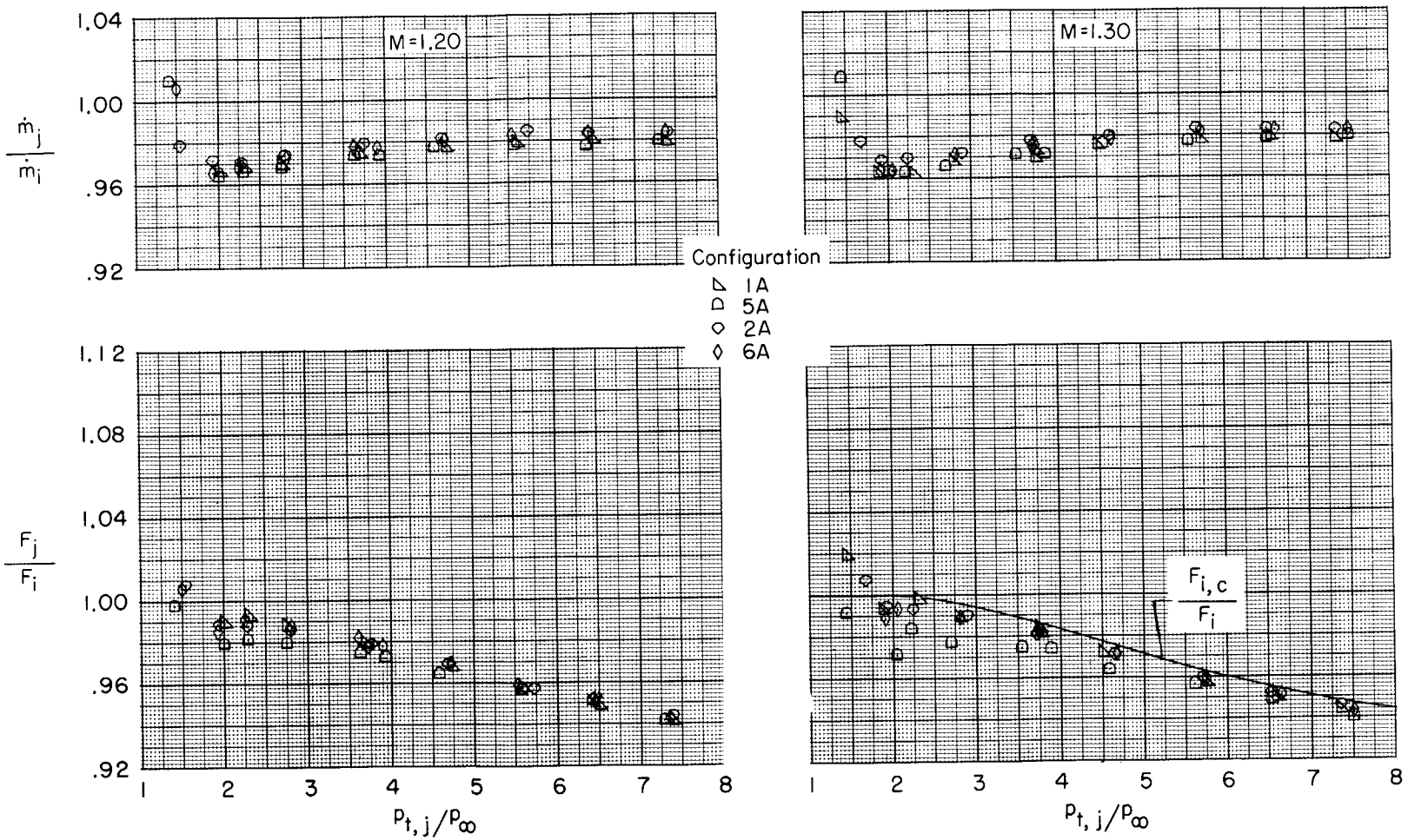

(d) M = 1.20 and 1.30.

Figure 37.- Concluded.

Configuration 1A

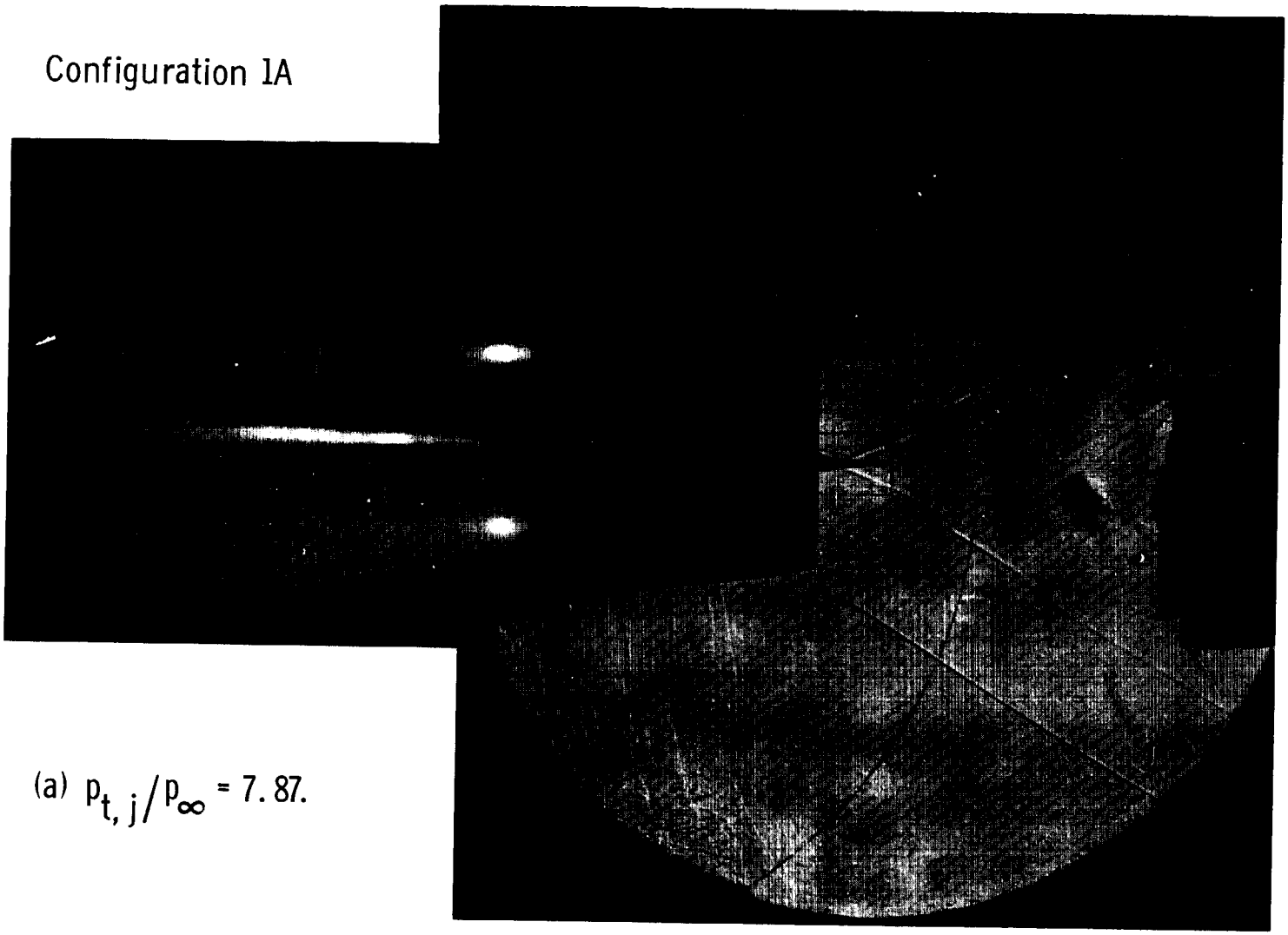

(a) $p_{t,j}/p_{\infty} = 7.87.$

Figure 38.- Shadowgraphs of twin-jet configuration 1A at Mach 2.0.

L-70-1686

Configuration 1A

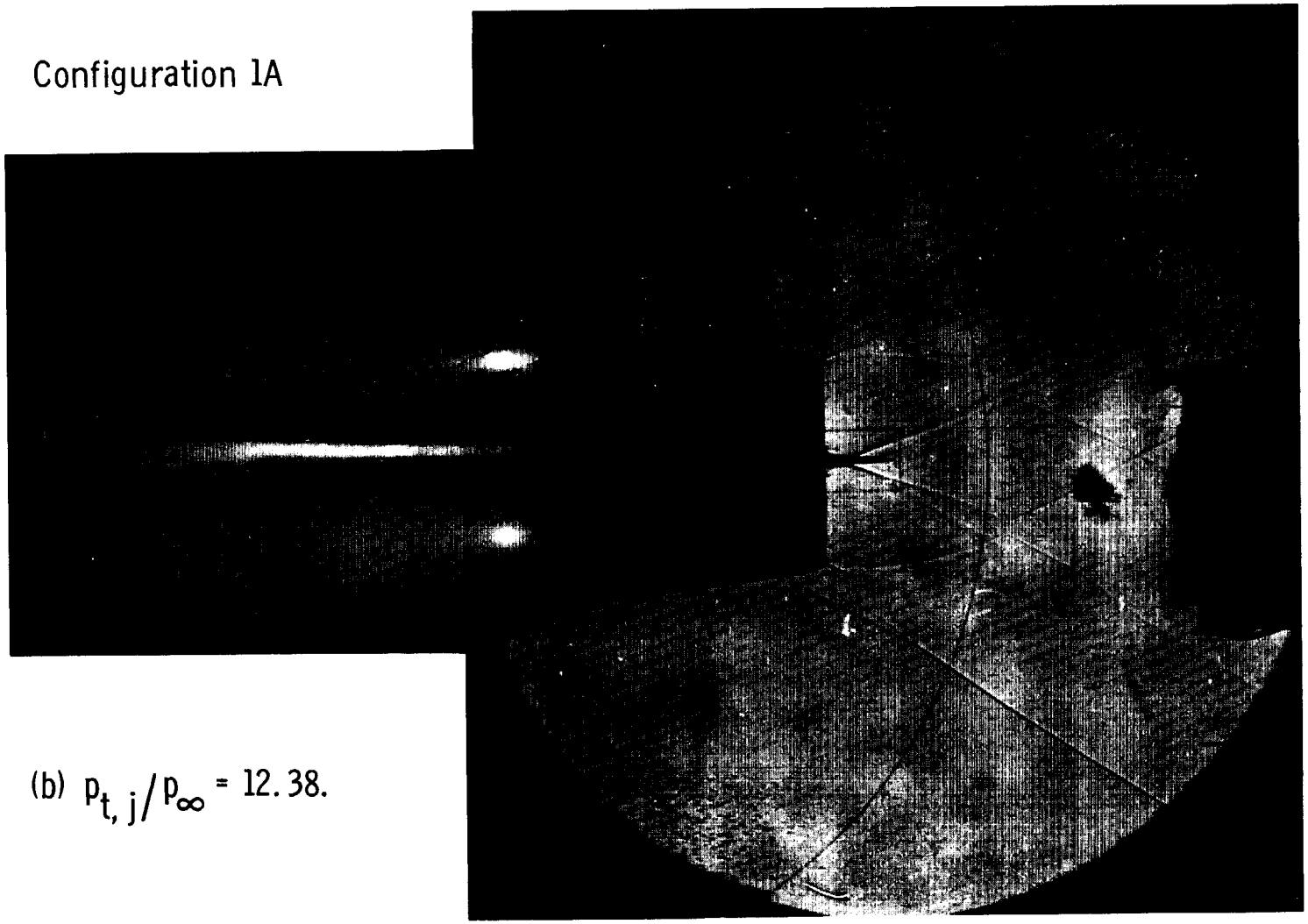

(b) $p_{t,j}/p_{\infty} = 12.38.$

Figure 38.- Continued.

L-70-1687

Configuration 1A

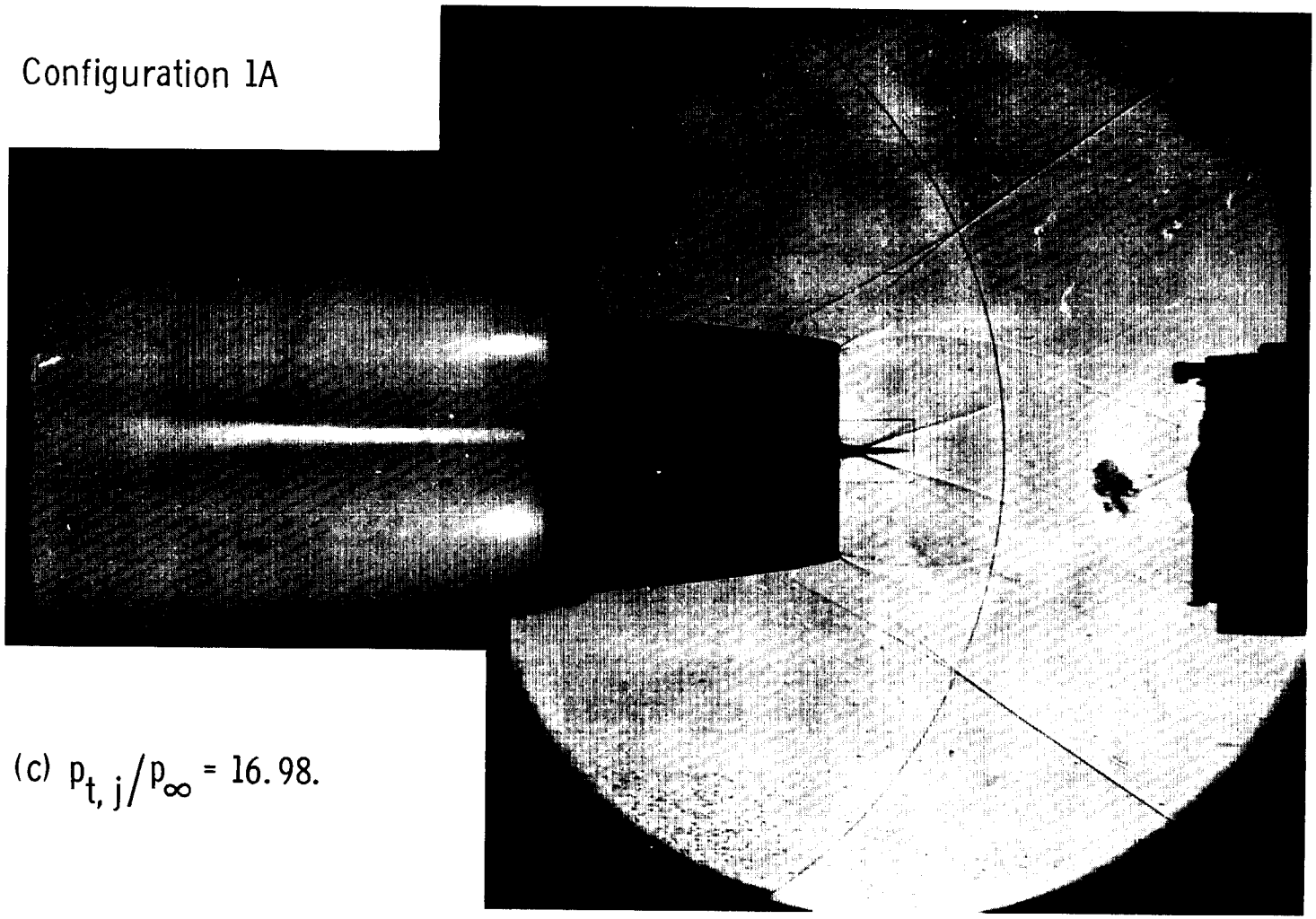

(c) $p_{t,j}/p_{\infty} = 16.98.$

Figure 38.- Concluded.

L-70-1688

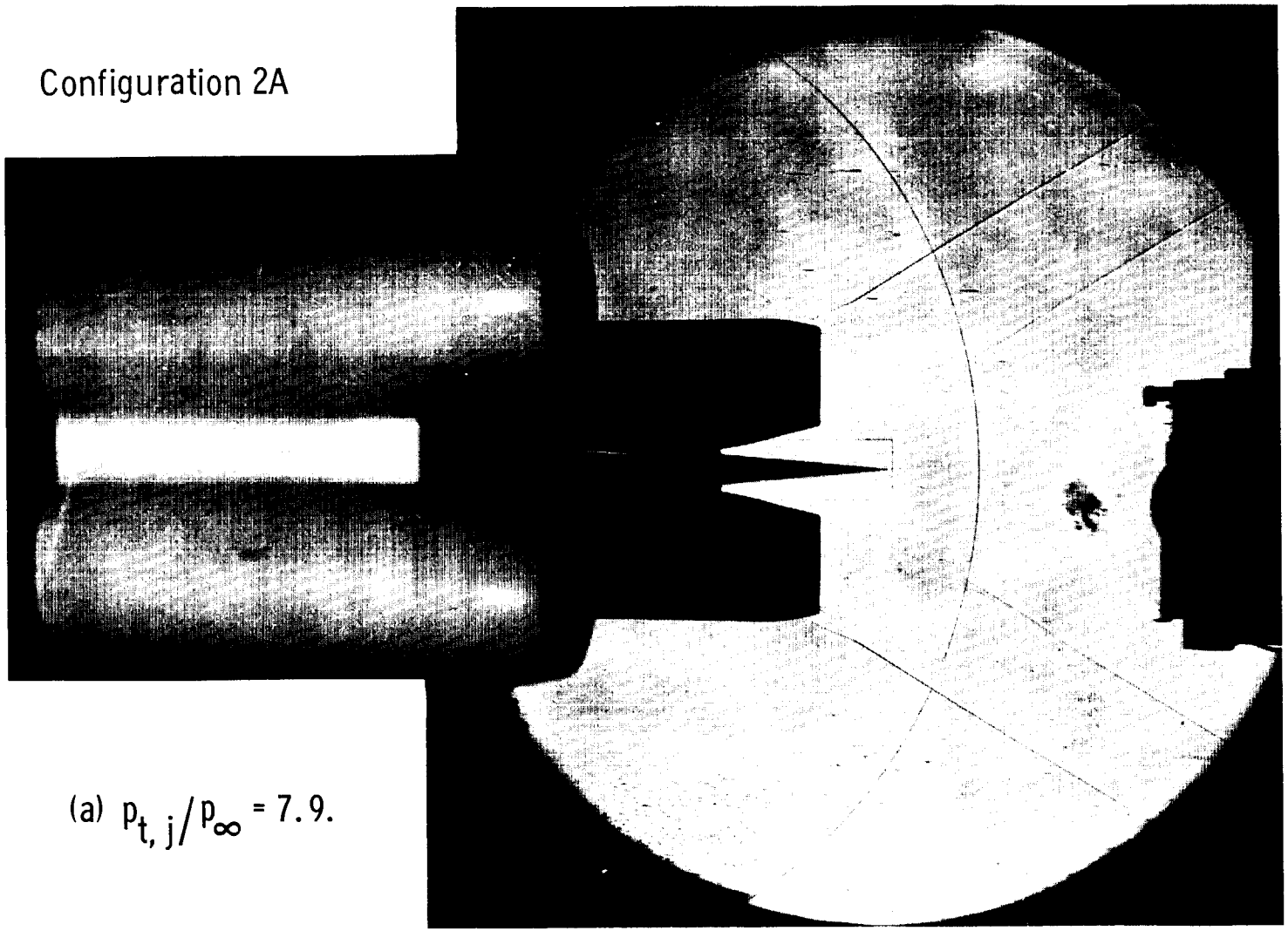

Figure 39.- Shadowgraphs of twin-jet configuration 2A at Mach 2.0. L-70-1689

Configuration 2A

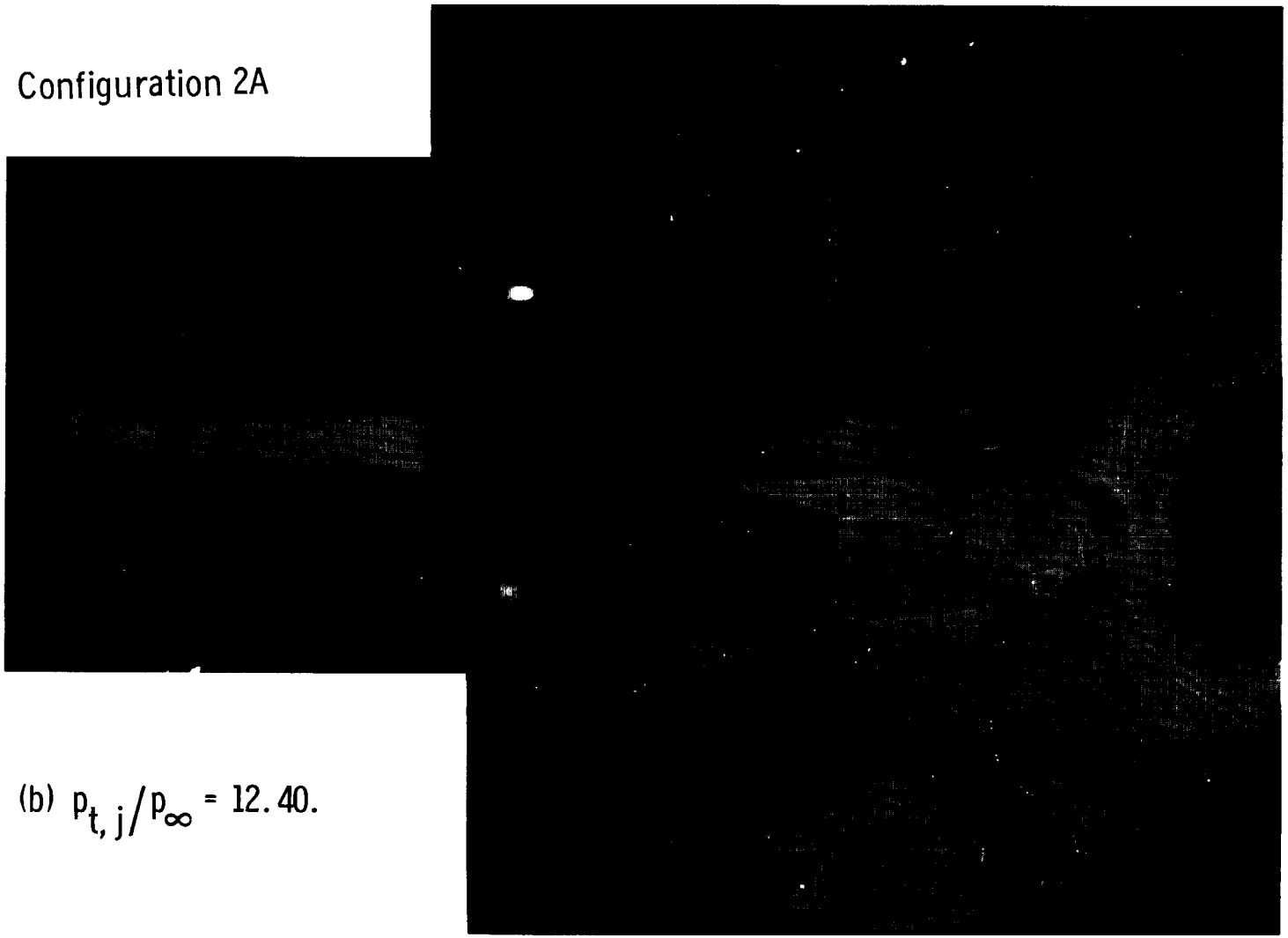

(b) $p_{t,j}/p_{\infty} = 12.40.$

Figure 39.- Continued.

L-70-1690

Configuration 2A

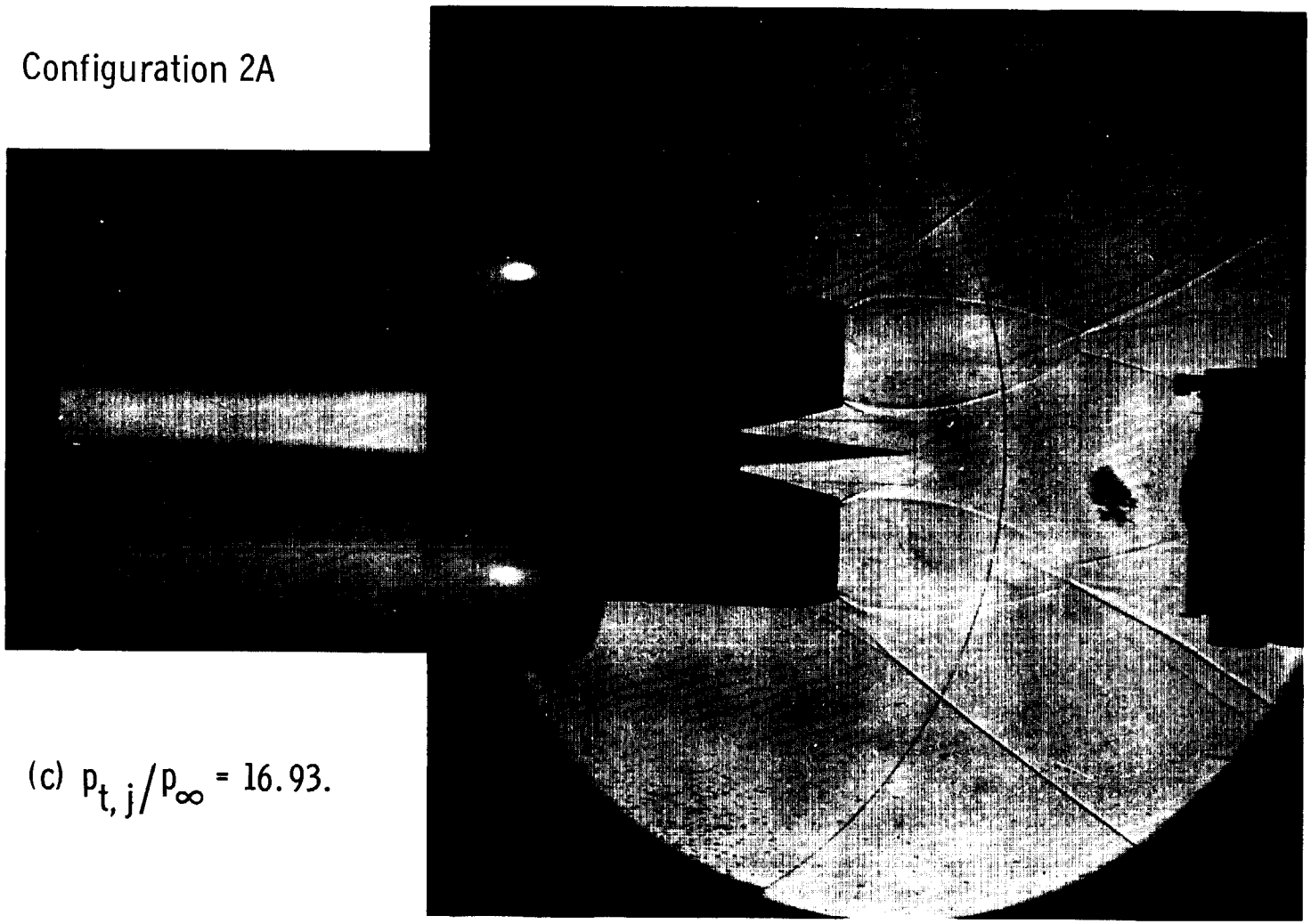

(c) $p_{t,j}/p_{\infty} = 16.93.$

Figure 39.- Concluded.

L-70-1691

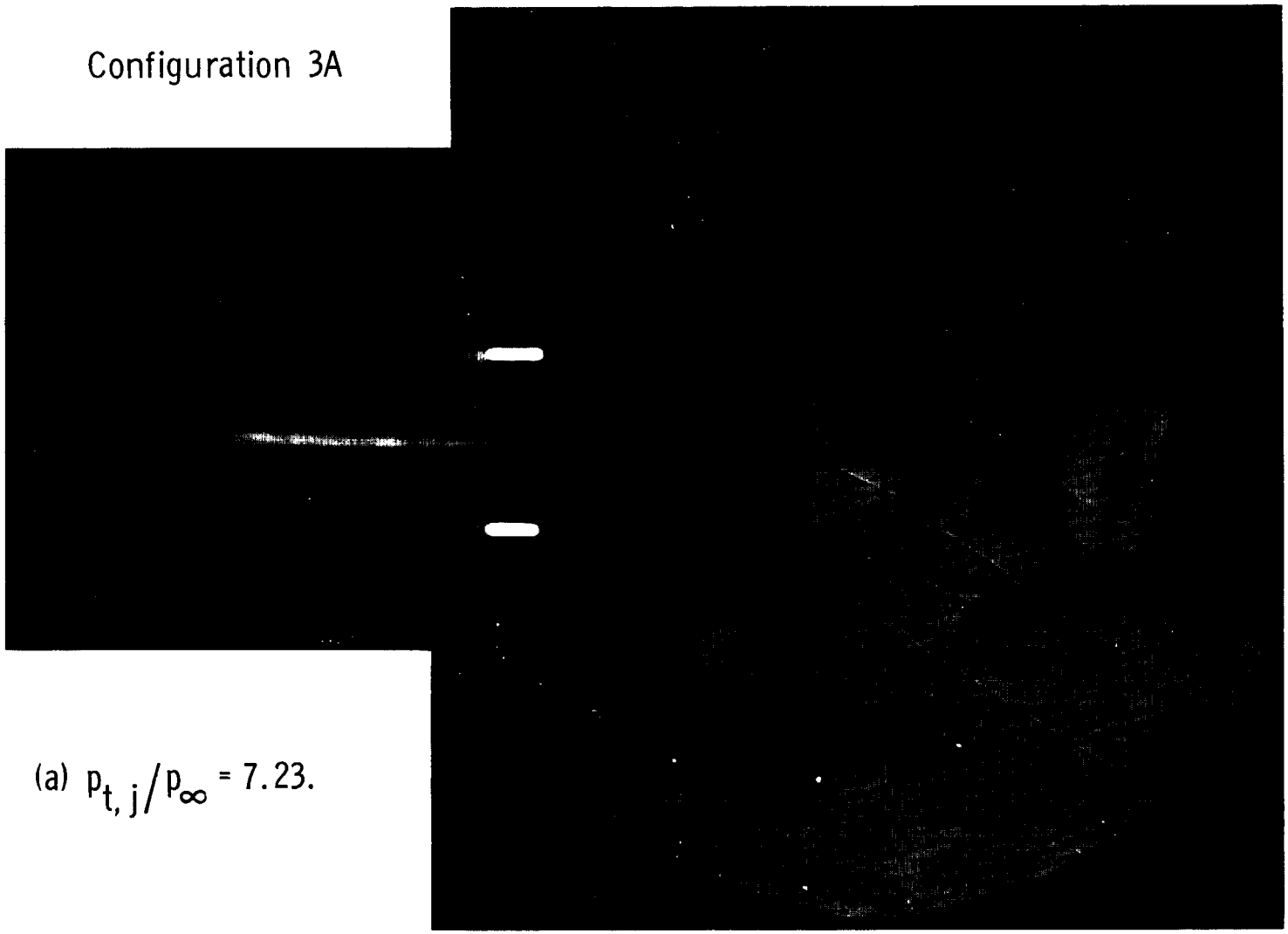

Figure 40.- Shadowgraphs of twin-jet configuration 3A at Mach 2.0.

L-70-1692

Configuration 3A

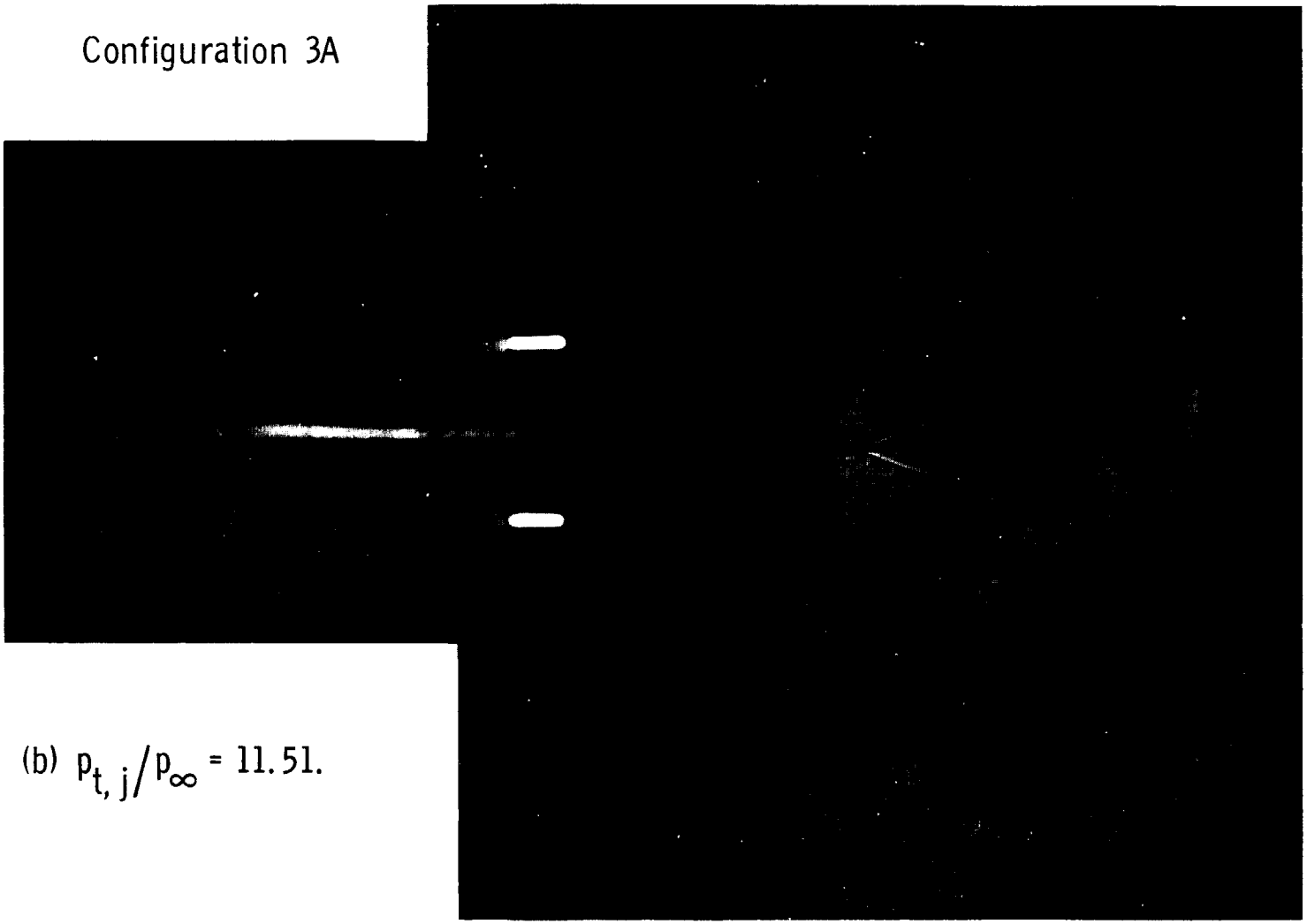

(b) $p_{t,j}/p_{\infty} = 11.51.$

Figure 40.- Continued.

L-70-1693

Configuration 3A

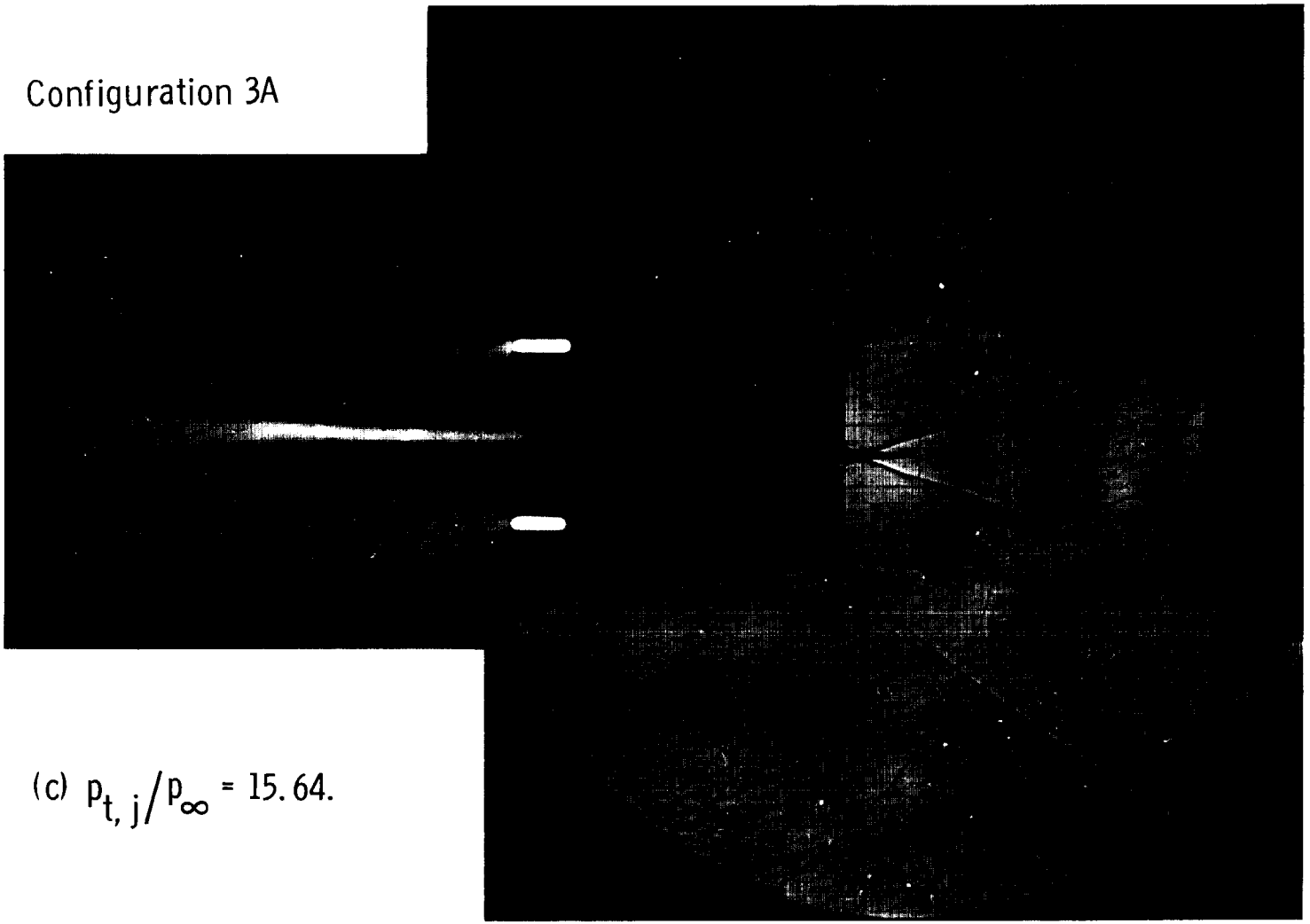

(c) $p_{t,j}/p_{\infty} = 15.64.$

Figure 40.- Concluded.

L-70-1694

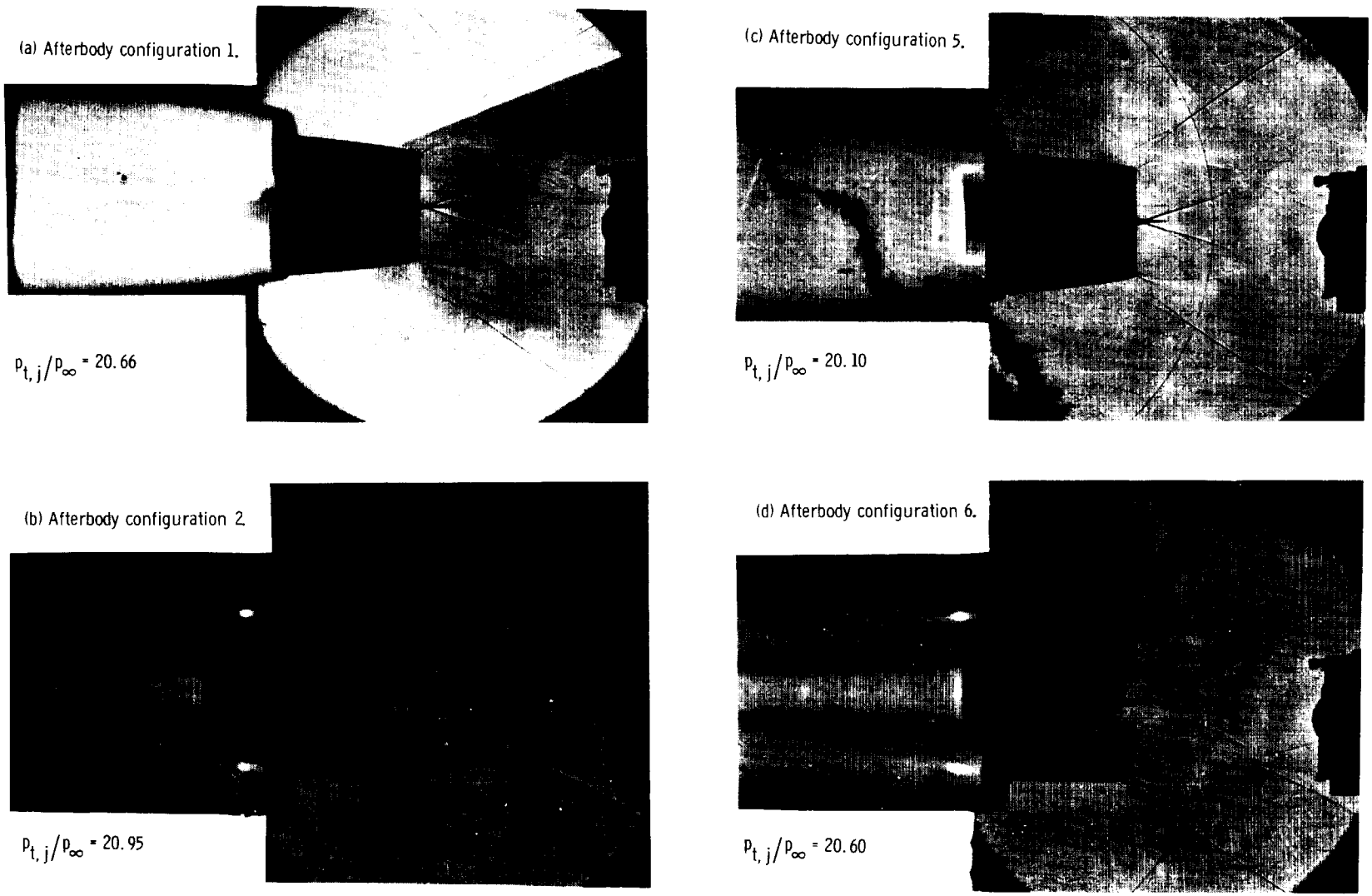

Figure 41.- Shadowgraphs of twin-jet simulator configurations at Mach 2.2.

L-70-1695